

The Alliance of Laboratories in Europe for Education, Research and Technology

ALERT Doctoral School 2026

Experimental Geomechanics for Beginners

Editors:

Nadia Benahmed

Miguel Angel Cabrera

Jelke Dijkstra

Eleni Gerolymatou

Alessandro Tarantino

Alessandro Tengattini

Preface

This volume originates from the ALERT Geomaterials doctoral school "Experimental Geomechanics for Beginners".

Experimental geomechanics provides the foundations for testing, observing, measuring, and interpreting the behaviour of geomaterials and geomechanical processes. Yet performing a good experiment is not trivial at all. The quality of an experiment depends on the entire chain linking the material, the specimen, the apparatus, the sensors, the testing protocol and the acquisition of the resulting data.

The aim of this volume is to provide an accessible introduction to the principles and practice of experimental geomechanics. The chapters begin with the purpose and challenges of geotechnical testing and proceed to the fundamentals of measurement, sensors, calibration, and uncertainty. They then address specimen preparation and triaxial testing, the design and dimensioning of experimental apparatus, and specialised experimental techniques for unsaturated soils. The final chapter broadens the perspective to physical modelling, where abstraction, initial and boundary conditions, dimensional analysis, and similitude become central to the experimental design.

Each chapter stands on its own, but the collection forms a continuous path through the whole experimental process. A common message throughout the volume is that sophisticated equipment alone does not guarantee a good experiment. Reliable and reproducible results require a sound understanding of the assumptions, limitations, uncertainties, and physical principles underlying every stage of the test.

The intended readers are doctoral candidates and young researchers entering experimental geomechanics, as well as practicing engineers wishing to strengthen their understanding of experimental methods.

As always, the PDF of this book can be downloaded free of charge from the ALERT Geomaterials website. ALERT Geomaterials thanks all contributors for the time, materials, and effort invested in crafting this volume.

Ioannis Stefanou
Director of ALERT Geomaterials
ENSTA – Institut Polytechnique de Paris

Contents

Foreword
N. Benahmed, M. Cabrera, J. Dijkstra, E. Gerolymatou,
A. Tarantino, & A. Tengattini 1

Introduction to geotechnical testing
Dijkstra, Jelke & Cheng, Xiaoyang 4

Sensors: fundamentals of measurement and electronics for experimentalists
Tengattini, Alessandro 21

Triaxial Testing of Geomaterials
Benahmed, Nadia 60

Dimensioning and construction of experimental apparatus with examples
Gerolymatou, Eleni, Düsterloh, Uwe & Castellanza, Riccardo 114

Unsaturated soils: experimental techniques
Tarantino, Alessandro 139

Physical modelling: From abstraction to experiment design
Cabrera, Miguel Angel 178

Foreword

The contributions assembled in the present volume proceed from the lectures of the 2026 ALERT Geomaterials Doctoral School with the topic "Experimental Geomechanics for Beginners". The school has been organized by N. Benahmed (INRAE, Aix Marseille University), M. Cabrera (Delft University of Technology), J. Dijkstra (Chalmers University of Technology), E. Gerolymatou A. Tarantino (University of Strathclyde) & A. Tengattini (Université Grenoble Alpes).

Experimental Geomechanics for Beginners is aimed at providing the fundamental understanding required for the experimental study of soils and rocks. The objective is not simply to describe laboratory devices or procedures, but to provide an organized framework for understanding what an experiment measures, how measurement chains are constructed, and how experimental choices determine the physical meaning of the resulting data. The central premise of experimental geomechanics is that the specimen response—already governed by state, history, and coupling - is observed through measurement systems whose outputs must be interpreted with care. Accordingly, experimental competence is not limited to operating apparatus; it requires a coherent understanding of what is measured, how it is measured, and what conclusions are justified.

Geomaterials exhibit behavior that is state- and path-dependent: deformation mechanisms evolve with stress level, drainage condition, saturation state, and initial microstructure (fabric, bonding, cementation). In addition, experimental results depend on applied boundary condition, apparatus characteristics and selected sensors. This makes laboratory testing intrinsically complex, not because it is "difficult by nature", but because the experimental chain links an internal material state to external observations through intermediate transformations: specimen storage, preparation and installation, boundary-condition control, sensor physics, calibration, signal conditioning, data reduction, and interpretation. Each transformation introduces assumptions and potential biases. The resulting data therefore represent an identifiable mapping from an internal physical response to measured variables, and the validity of constitutive or mechanistic inferences depends on the credibility of that mapping

A core contribution of the volume is to frame geotechnical experiments as inference problems. In practice, "measured stress" or "measured strain" are seldom direct measurements of internal fields; instead they are composed quantities inferred from indirect measurement chains. The book emphasizes that metrology and uncertainty analysis are not peripheral to experimental geomechanics: they determine whether differences between specimens reflect material variability or experimental artefacts, and they constrain how model calibration should be performed. The reader is guided

towards understanding systematic versus random error, precision versus accuracy, and the propagation of uncertainty through stress–strain constitutive relations.

The book further develops experimental design as a scientific discipline. The objective of testing - mechanism exploration, theory development and validation, or site investigation and calibration - directly determines the required degree of control, the suitable choice of independent and dependent variables, and the structure of an experimental programme. This includes the use of abstraction and dimensional analysis to relate scaled or simplified representations to prototype behavior, as well as the statistical logic needed to choose replication and factorial or fractional designs when multiple variables interact. In this view, experimental efficiency is not only a matter of time or cost; it is a matter of whether the programme provides discriminating power for the targeted hypotheses

For doctoral-level researchers, these principles offer an essential toolkit: the ability to design experiments that are fit for purpose, to select suitable equipment, to interpret measurements as inferred variables with known limitations, and to report results with traceability and defensible physical meaning. The organizers hope that this book can prove useful as both a methodological guide and a conceptual foundation for experimental geomechanics: a disciplined approach to converting measurements into knowledge.

Eleni Gerolymatou
Technische Universität Clausthal
- on behalf of the organizers -

Introduction to geotechnical testing

Jelke Dijkstra, Xiaoyang Cheng

Chalmers University of Technology, Gothenburg, Sweden

The complexity of most natural soils requires a combination of laboratory and field tests to characterise their response. Furthermore, to fully map the behaviour of these materials, simplified model soils have been developed to isolate certain features and behaviour for further experimental studies and subsequent generalisation in a constitutive model. A large variety of tests have been developed, depending on the scientific questions outstanding and/or the needs in geotechnical engineering practice. This Chapter aims to give an introduction to the purpose and challenges of testing both model soils and natural soils at element and boundary value level in the laboratory and at field scale. As will be further elaborated in the other Chapters of this book, there are many experimental aspects, such as metrology, specimen preparation, design of the apparatus, and the test protocol, that need to be properly addressed to obtain results that are accurate and repeatable.

1 Introduction

Geotechnical testing has been part of the profession since its inception. Terzaghi and his co-workers have already developed various test apparatuses to investigate the response of different soils that helped to formulate the fundamental theories on effective stress and consolidation that we still use today. A rather comprehensive overview of this early work has recently been given in [VH26].

Whilst the importance of testing in geomechanics and geotechnical engineering is undisputed, in recent years the research community has shifted from attempting to develop the near-perfect laboratory test with few sensors and strict control at the boundary of the specimen to simplified tests with less control but unprecedented data from 3D full-field measurement techniques (e.g. X-ray Computed Tomography paired with Digital Volume Correlation). The latter is exemplified by the ALERT Doctoral schools organised in 2012 & 2022 that first introduced and subsequently expanded the need for and opportunities of full-field (image-based) measurement techniques [VHRM$^+$12, AMHD22]. Full-field techniques allow one to overcome limitations in classic geotechnical tests resulting from heterogeneity in sample preparation and the

localisation of failure in a shear band by directly measuring the material response within the material. However, that does not imply that poor test execution can be completely offset by these new measurement techniques, as in most of these approaches, the mechanical stress (and/or) pore water pressures are still measured at the sample boundary. Furthermore, the availability of tomography equipment remains limited and costly, which requires compromises in testing. Therefore, in order to make the best compromise, the experimenter should still have a strong understanding of the basics of testing natural soils and granular model materials.

Another recent development in research is that experimental work has been complemented with virtual experiments that use the Discrete Element Method (DEM) to probe stress paths or initial conditions that are not experimentally accessible, e.g. [AMH02, TZ10]. In the best efforts so far, a Level-Set DEM model is combined with 3D image data from X-ray Computed Tomography (XCT), [KAVA18]. The data is used to build and calibrate a 3D model using the particle level kinematics from time-series data obtained during triaxial tests on a model sand. Subsequently, these models can be used to investigate the material response to loading paths and initial particle configurations that are not possible to apply in the laboratory, but are of importance for the development of constitutive models at the continuum scale [USOA24]. This approach has not yet been successfully replicated for more challenging soils, due to the technical limitations of XCT for imaging fine-grained soils and the challenges of capturing an initial state that represents the fabric in natural soils in DEM. However, these developments show the opportunities offered by the state-of-the-art advanced experimental techniques, and at the same time, illustrate the need for a comprehensive understanding of the test itself.

In geotechnical engineering practice, laboratory and field tests remain an important part of the job. Due to time constraints and general lack of laboratory capacity, the discipline has changed from classic Site Investigation strategies that rely heavily on careful sampling and laboratory testing to developing digital ground models based on in-situ tests, such as the Cone Penetration Test and near-surface geophysical methods, especially in offshore geotechnics. At the same time, engineering projects have become more complex, requiring more advanced numerical analyses, e.g. using the Finite Element Method (FEM, see previous ALERT school [TSP24]). The constitutive models used in those numerical codes need to be calibrated against laboratory data and most commonly the models are effective stress based. Consequently, some tests often used in engineering practice to quickly obtain a measure of (undrained) shear strength are of limited use for the calibration of a constitutive model. Hence, even when performing numerical analyses, it is worthwhile to appreciate the origin of these data and their limitations.

In the following Sections the purpose and context of geotechnical testing will be elaborated and compared, before expanding on the principles of certain testing methodologies. Furthermore, for simplicity ‘geotechnical testing’ and ‘geomechanical testing’ are used interchangeably when the purpose of the test is to quantify the mechanical response of a geomaterial (soils, rock and concrete [VB84]).

2 Why do we need experiments?

Experiments can serve different purposes. The most obvious purpose is to investigate research questions the experimenter might have regarding an unknown or surprising response of the material, whereas in other situations the experiment merely serves to characterise the physical properties that already have been understood and generalised in a theoretical model. The design and execution of experiments aimed at falsification or confirmation of theoretical hypotheses (predictions) are scarce in geotechnics. Among those are laboratory experiments that proved the Mandel-Cryer effect [Man53] for the 3D coupled consolidation problem [GKT63] and the field observation of the critical track velocity predicted by Krylov [Kry95] in high-speed rail near Ledsgård in Sweden [MK00]. Geotechnical testing follows mostly three main categories of experimentation: (i) scientific exploration, (ii) systematic tests for theory development & validation and Site Investigation for design & model calibration. These categories are not restricted to test type; more often than not, multiple test types and protocols are needed.

2.1 Experiments for scientific exploration

Scientific exploration is driven by curiosity about the material response, the possibility of using new methodologies for testing, or, as often is the case, a combination of both, when new experimental methodologies inspire new questions and vice versa. As a result, experiments for scientific exploration are often bespoke, i.e. the experimental methodology has been developed to provoke and characterise a certain mechanism or physical property in a geomaterial for the first time. Primary classic examples are the development of the biaxial test that enabled the study of the localisation of a failure mechanism in a shear band [VGG78] and the creation of the hollow cylinder apparatus for the investigation of the impact of the rotation of principal stresses [HGS83]. These developments are not only at the element level in the laboratory. A major breakthrough for physical model testing was the development of the geotechnical centrifuge that allowed appropriate scaling of the experiments [Tay95] and, more recently, the combination of miniaturised geotechnical test equipment that facilitates operando tests in a tomography instrument. The majority of those bespoke test equipment are only available in a select number of laboratories, due to the complexity of the test and the resources (funds, staff, space) required. Some of those apparatuses fell in disrepair in an unused part of the laboratory after addressing the original scientific question, whilst others have been commercialised.

Model soils, including, but not limited to, kaolin clay, glass ballotini, clean uniformly graded silica sand, are commonly used as a substitute for natural soils. These materials have controlled properties, are easy to procure (no need to go to the field), and are ideally suited to isolate a mechanism of interest. We have better control on the initial conditions of a sample, and certain measurement techniques are enabled. In photoelastic experiments the grains need to be replaced by a photoelastic material that is birefringent before the stress (or more precisely the difference in principal stress

$\sigma_1 - \sigma_2$, see e.g. [DB10] can be quantified. Furthermore, an artificially gap-graded soil, a mixture of the fine and very coarse fraction of soils, enables the study of internal erosion in which the small particles are transported by the pore fluid through the pores between the large grains [KT14]. Another example is the manipulation of the pH of the pore fluid to create an initial fabric in a clay sample that is disperse or aligned, e.g. [PT18].

A combination of skills should be present in the research team, for non-standard scientific experimentation to succeed. Those include the ability to control and measure displacement, stress, and other physical properties on the sample boundary or within the sample (see Chapter 2, 4, 5) to understand the limitations and opportunities of sample preparation to get the best results (Chapter 3) and an understanding of the scaling effects and similitude when designing and executing model tests (Chapter 6). In addition, a laboratory with support staff to help with prototyping (manufacturing and assembly) and instrumentation of parts and equipment is essential, although the latter requirement can be relaxed if the stress levels and accuracy required fall within those that can be reached with contemporary 3D printing and sensing available in the maker community [Ban09].

2.2 Systematic tests for theory development and validation

Most (natural) soils respond differently depending on initial conditions (stress, density), loading history, and applied load (magnitude, direction). Some of the main scientific contributions in the discipline have been based on a series of systematic tests that support and validate the theoretical formulation of a constitutive model that has the ability to predict the observed soil behaviour. The textbook example is Critical State Soil Mechanics (CSSM) [SW68, MW03] that brings together the deformation and strength response in soils via effective stress and the introduction of some state parameters that keep track of the loading history and the density. The model development required systematic testing of a (reconstituted) model soil for various initial conditions (effective stress, density) and loading paths (1D compression, triaxial tests sheared in compression). The test equipment used was not necessarily a big departure from prior research; rather, the systematic use of standard equipment with the aim to formulate a constitutive model was groundbreaking. Performing these types of systematic study requires a large number of tests that capture the full (experimentally accessible) stress space in a controlled manner so that the yield envelope and evolving stiffness can be determined throughout the test. This requires drained stress paths at controlled stress-ratios (deviatoric stress q over mean effective stress p'), which is especially time consuming (months per test) in (natural) soft clays that have very small hydraulic conductivities ($10^{-9}\,\mathrm{m\,s^{-1}}$). Figure 1 Examples for the latter are the experimental probing of the hysteretic behaviour that inspired the bounding surface (bubble) models [ATMW89] and the investigation of anisotropy and structure (fabric + bonding) in natural (soft) soils [LV90, WNKL03].

Additional systematic test protocols have been developed for cyclic loading paths, where instead of probing the incremental stiffness response at element level during

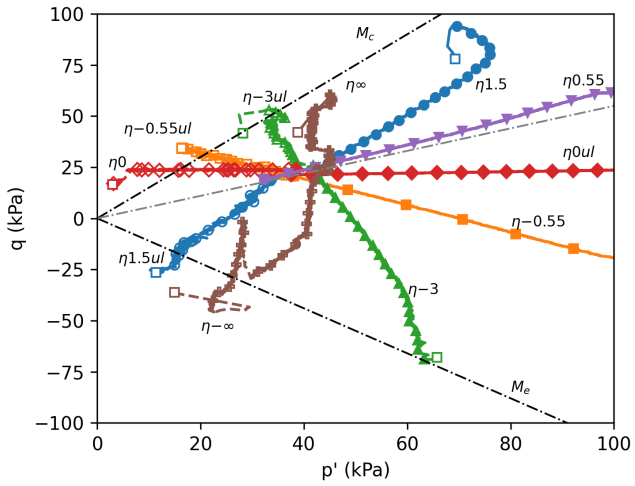


Figure 1: Drained stress probing of a Swedish sensitive clay in an advanced loading triaxial apparatus.

drained stress-probing, the accumulated strains are monitored during a large number of loading cycles with the aim of developing models that directly link the number of loading cycles (with certain initial and loading conditions) to the emerging irreversible deformations and/or excess pore water pressures [Wic05]. Given the many permutations in initial (e.g. void ratio, stress level) and loading conditions (loading amplitude, frequency and average stress level), a very large number of experiments are required. Therefore, this experimental approach is more suitable for developing, calibrating and benchmarking phenomenological constitutive models. Another generalisation is the development of a family of experimentally derived backbone curves which subsequently can be used with a smaller number of additional tests to estimate the cyclic response of a certain soil [And09].

In all those examples the formulation of the test programme is aided by a conceptual or theoretical model with the current understanding of the geomaterial being tested. This informs the type of tests to be executed, the initial and loading protocol to be applied and some ideas on how to organise and plot the results. Most test programmes are based on a series of preliminary tests that help to finalise experimental details. All these steps aid, in case the tests are properly conducted, the quantification of the constitutive response experimentally in a systematic manner. Proper test execution is specific to test type and apparatus, as prescribed in the test protocols (for regular tests codified in international standards) and for non-standard test as documented in the laboratory that developed it.

2.3 Site investigation for geotechnical design & model calibration

Experiments are still important after scientific discovery and model development. In contrast to engineered materials in which properties are controlled during production, the geotechnical engineer faces new site conditions with each project. The site conditions are the result of geological processes that include the impact of humanity (e.g. prior construction activities). In turn, the design of the technical solution depends on the site conditions and the theory and/or models used for design. The observed response guides the engineer in selecting the appropriate models for designs and geotechnical solutions. Burland's triangle (Fig. 2) clearly shows the interplay between these factors and the role of the engineer [Bur08].

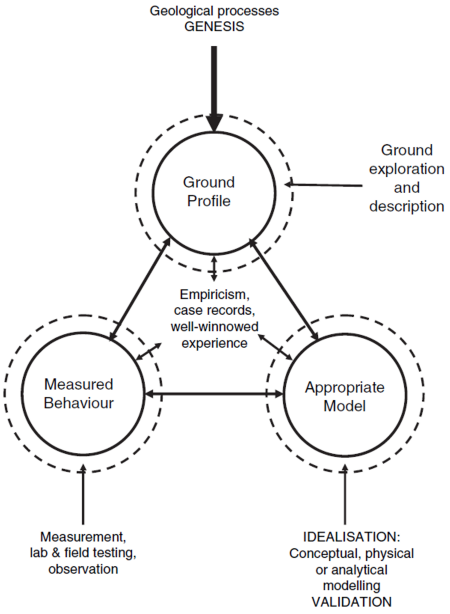


Figure 2: Geotechnical triangle of Burland.

During site investigation the stratigraphy (extent and depth of layers with comparable soil type), hydraulic conditions, and engineering properties of the soil layers need to be determined for subsequent geotechnical design, whereas the complexity of the site and engineering solution dictates the degree of accuracy of the (numerical) model used. The design and execution of a proper site investigation plan is beyond the scope of this school, a good starting point for further reading is [Hun05]. However, in most situations a desk study that collects prior geological and geotechnical data, is combined with in-situ methods that characterise the site-specific ground profile (this can be geophysical methods, cone penetration tests, etc), prior to sampling and laboratory testing. In practice, only in a few cases samples are retrieved for subsequent tests in the

laboratory for characterising index properties and (hydro-)mechanical properties. Irrespective of the resources invested or methods used, uncertainties will always remain, as a site can never be fully characterised, and the site conditions will also change with time. Therefore, as a geotechnical engineer you need to develop the ability to quantify and incorporate the uncertainties in your project.

An important aspect of specifying laboratory tests for the determination of mechanical properties of a soil sample is to consider the initial state (stress level, void ratio of the soil at the site, dimensions), and the selection of a loading path that is representative for the engineering solution. Two main approaches are identified:

1. In the classical approach, the laboratory test is used to overcome the difficulties in predicting the emerging soil behaviour. The (series of) laboratory tests is specified to capture loading conditions of the future structure, subsequently the emerging response (e.g. undrained shear strength) is used in a simplified semi-analytical design approach to predict the stability of a structure (ultimate limit state). A major difficulty is to specify the relevant test conditions (which requires experience), and to apply those on a soil specimen using geotechnical test equipment (most loading paths are not accessible with standard equipment). Furthermore, in complex projects where different load paths emerge at different locations in the underground, a consistent prediction of deformations and stability often is not possible. For pile foundations, laboratory tests are skipped altogether and direct correlations with in-situ tests, such as the Cone Penetration Test are used instead [L$^+$22].

2. A generalised predictive model that is calibrated against experimental data from the specific site can be used, on the premise that the theoretical or numerical model captures the full range of loading paths that can be expected in the engineering problem with sufficient accuracy. The Finite Element Method is an advanced numerical model that is commonly used for advanced geotechnical engineering projects in which the accurate prediction of the (delayed) deformations and emerging stability of a geotechnical structure are essential.

   Most advanced constitutive models have a combination of model parameters that can be directly derived from laboratory data, and some that need to be calibrated with additional test data. A scientifically sound approach for the latter is to use multi-objective optimisation with test results from different kinds of geotechnical tests to arrive at a unique set of model parameters that captures all relevant test data [GSKD17]. This approach requires a model of sufficient accuracy for the soil type and site conditions, as well as knowledge on the bounds of the model parameters (theoretical bounds from the model formulation and experimentally observed extreme values from prior tests).

Perhaps counter-intuitively the specification of tests for the classic design method requires much more knowledge on the expected emerging soil behaviour, and test limitations. In contrast, for a well-designed constitutive model more standardised tests (in terms of loading path and rate) are prescribed. Yet, it is impossible to calibrate an

overly simple model that does not capture the main features of the soil behaviour.

3 Laboratory scale tests

Two types of tests are performed for the (hydro-)mechanical characterisation in the controlled conditions of a laboratory: (i) element level tests and (ii) physical model tests. Element level tests are designed to probe the (hydro-)mechanical response of a soil specimen, whereas in physical model tests the response of a geotechnical system is studied. In addition, a large number of characterisation methods have been developed to quantify index properties (e.g. density, water content, grain size distribution) or more advanced properties (e.g. mineralogical composition, pore size distribution), though those will not be discussed here.

3.1 Element level tests

In an element level test a soil specimen that is carefully prepared from an intact sample of natural soil (clay) or reconstituted from sample material and subsequently subjected to a mechanical or hydraulic load on the sample boundary. The design of the experimental apparatus is such that a uniform condition is maintained within the specimen (up to failure), by applying a controlled load or displacement. At the same time, the response is measured at the boundary, this can be displacements (when applying a load) or stress (total, pore water pressures) when applying a controlled displacement. Most advanced tests have mixed loading conditions (a mixture of load and displacement control). Contemporary researchers argue that uniform conditions are difficult to achieve and instead seek to complement the element test with tomography-scans to acquire 3D image data on the changes in the specimen (e.g. kinematics, density change).

Figure 3 shows a sketch of a large number of element level tests developed over the years. Both monotonic static loads and cyclic loads are applied at small and large amplitude sometimes even a dynamic load (induced accelerations substantially larger than gravitational acceleration g). The test configurations depicted are:

a *Triaxial test.* A cylindrical test specimen with a height that is two times (or more) the diameter is tested in a cell. Triaxial test can be used for all soil types. Many test configurations exist, allowing loads in compression, and extension, as well as controlled stress ratios. A triaxial test allows to control the effective stress to a large degree by using a combination of back pressure and cell pressure (separated by a membrane surrounding the specimen), hence providing an universal apparatus for model development and engineering. The symmetry of sample, however, prevents the proper localisation of shear bands (if that matters to you). Furthermore, there is no possibility of controlling stress rotations (they emerge in the localised shear band). Several design iterations exist, where the Bishop-Wesley design [BW75] is among the most versatile and accurate at low effective stress levels (important for soft soils). An overview of the details of

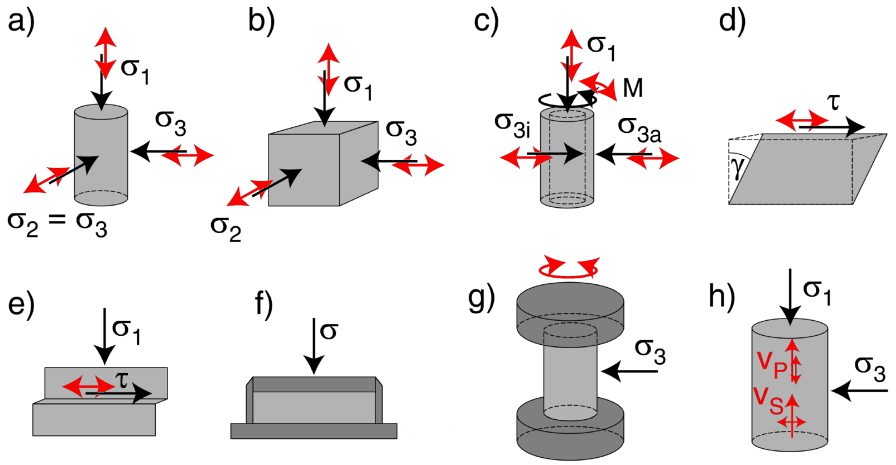


Figure 3: Principal overview of different types of geotechnical tests. Adapted from [Wic05]

executing a triaxial test is given in [Lad16].

b *True triaxial test.* In a true triaxial test, stresses (soft wall) or displacements (fixed wall) are applied on all sides of the specimen. The true triaxial test is a research instrument in few laboratories for studying inherent and (stress) induced anisotropy, as well as incremental stiffness response for general stress state. The failure mechanisms arise more naturally throughout the specimen. The execution of the test is very challenging, especially at large levels of deformation, with issues arising at the corners of the prismatic specimen. Simpler versions exist (fixed and soft wall) where only two axes are controlled (biaxial test). A recent exciting iteration developed for testing rocks has one side available for observing deformations on the sample surface [BL16].

c *Hollow cylinder test.* In a hollow cylinder, the soil specimen is subjected to stress boundaries on both sides of the annulus in addition to a vertical stress and a torsion [HGS83]. It is the only laboratory instrument for controlling the stress rotations in a soil specimen. The latter, however, requires boundary value level interpretation (and control) and the assumption of uniform stress in the annulus. Hollow cylinder testing can be used for all soil types, but most commonly (dry) sands.

d *Direct Simple Shear test.* The DSS test is most commonly performed on cylindrical soil specimens. The intention is to approach the pure shear in the specimen as closely as possible. The DSS test induces rotation of principal stress, but does not control it (in contrast to the hollow cylinder). As opposed to the direct shear test, the specimen is contained in a membrane. Either rings or a

reinforced membrane (wire in the latex) are used to force a shear stress on the vertical sides of the specimen. This traditional test is considered to represent a load case relevant for plane strain failure mechanisms. The uniformity of stress in the specimen is however not guaranteed, hence the emerging strength cannot be associated with a (effective) stress state. Consequently, the results are not useful for anything else than a hand calculation. Despite its many limitations, the DSS test is still surprisingly common in the Nordic countries, including investigating the cyclic response of offshore sediments.

e *Direct Shear test.* In a DST test a cylindrical or prismatic specimen is sheared (horizontal plane) within a split box, by moving the top part whilst fixing the bottom. The shear plane is forced between the top and bottom box. The interpretation of the test is affected by wall friction effects, which can be corrected [KH12]. Similarly to the DSS test, the stress non-uniformity also affects the interpretation of the results, so avoid using DTS for serious probing of soil response. The direct shear test still is very useful for investigating the interface strength and stiffness properties between a structural element (concrete, steel) and a soil, by replacing the soil in the lower box with a solid interface material.

f *1D compression test.* The 1D compression test, or oedometer test, is one of the earliest tests developed to characterise the stiffness and consolidation properties (unloading/reloading stiffness, preconsolidation pressure, consolidation coefficient, creep rate) of primarily soft saturated soils. Cylindrical specimens are cut into a ring and a vertical load (incremental loads or constant rate of strain/displacement) is applied. Modifications of the cell allow for the determination of hydraulic conductivity (falling head test), the horizontal component of consolidation coefficient (radial flow in a Rowe cell) or the coefficeint of earth pressure at rest in normally consolidated condition $K_{0;nc}$ (soft wall oedometer).

g *Resonant column test.* The RC test applies an harmonic small-amplitude torsional load (typically using electromagnetic voice coils) on the top of a cylindrical specimen that is mounted in a cell. For the stiffness response, a frequency sweep with constant load amplitude is applied, and the resulting strain response is measured. In order to obtain damping properties, the decay of energy is measured after a forced loading cycle. Whilst the initial consolidation stress and density of the specimen can be controlled, the test induces complex vibrational modes in the specimen depending on the apparatus. Hence, it is a useful instrument to investigate dynamic soil properties (in general), but linking the results to site specific response remains challenging.

h *Bender element test.* Bender elements are manufactured from a piezoelectric material and generate a very small mechanical actuation (bending of the element) when excited with an electrical voltage (and vice versa - generate an electrical signal when excited with a mechanical wave). The bender elements are used to generate and measure the wave propagation of P-waves and S-waves in a soil specimen. The bender elements are often added to an existing test apparatus (e.g. triaxial test). The results obtained depend on the configura-

tion and orientation of the source and receiver elements. Shear wave velocities are derived from the arrival time and the distance between the bender elements, and are subsequently converted to a (small-strain) shear modulus. The testing is deceptively simple, but notoriously hard to execute and interpret properly, see [LS05] for a primer.

There are many more (geotechnical) tests developed, including but not limited to those developed to test partially saturated soils (e.g. double walled triaxial cell) or large shear displacements (ring shear apparatus), though these are typically research only.

3.2 Physical model tests

Physical modelling is a wonderful tool for scientists and engineers to systematically study the soil response at boundary value level under controlled conditions in the laboratory. A physical model is a scaled model of (part of) the prototype geotechnical system. The purpose of a physical model test is to identify mechanisms, or to systematically study the response of the scaled prototype with different initial and loading conditions. When properly executed, a model test will for example: give insights in often unexpected failure mechanisms, allow to optimise a foundation solution or validate advanced numerical analysis. A physical model test can perhaps be regarded as the laboratory version of Finite Element Analysis (FEA). Ideally, the geometrical scaling should not influence the observed soil behaviour in the model test. Due to the stress and density-dependent strength and stiffness behaviour of the granular media, the stress state and the density state in the model test also need proper scaling, such that a realistic failure mechanism is obtained. It is easily demonstrated from similitude that by increasing the gravitational acceleration g with the same factor N, as the dimensions of the model are reduced compared to the prototype (field conditions), and thus a proper scaling is achieved [Tay95, G$^+$07]. The most well established technique to preserve the stress state (and stress gradient) in the physical model is to place the model in a geotechnical centrifuge. For instance, if a test is executed at 100-g, one centimetre in the model corresponds to one meter in the prototype (field scale). A scaled model test without scaling the gravitational acceleration is denoted as a 1-g test, while a physical model test conducted in the geotechnical centrifuge is called a N-g test. A more detailed breakdown of physical model tests will be elaborated in Chapter 6.

4 Field scale tests

Field scale tests are defined herein as tests performed in-situ in real world conditions, either for characterisation of the subsurface or for a physical model test at 1-g.

4.1 Subsurface sectioning

Several tests have been developed to investigate the composition and engineering properties of the soils in the subsurface. The majority follow the concept of ‘poke

the ground with a stick and measure the response'. Figure 4 provides an overview of many (but not all) methods that have been proposed over the years. Those include standard penetration, cone penetration, dilatometers, pressuremeters, vanes, flat and stepped blades, hydro-fracture, borehole shear, torsional probes, and many others, for a complete overview is referred to [May07] and its cited references. The majority of techniques are designed to measure some form of mechanical resistance and/or the generation of (excess) pore water pressures during penetration or torsion. In contrast to inferring the strength, the in-situ determination of stiffness is much more challenging as the seismic methods only yield the small-strain shear modulus. The dilatometer or pressuremeter measurements remain challenging, and the inferred 'stiffness' from these tests are difficult to correlate to more generalised stiffness properties of the soil. Some of those methods have also been miniaturised for use in physical model tests, such as the Cone Penetration Test, or further developed to obtain a new type of data (e.g., the ROBOCONE p-y module [C$^+$23].

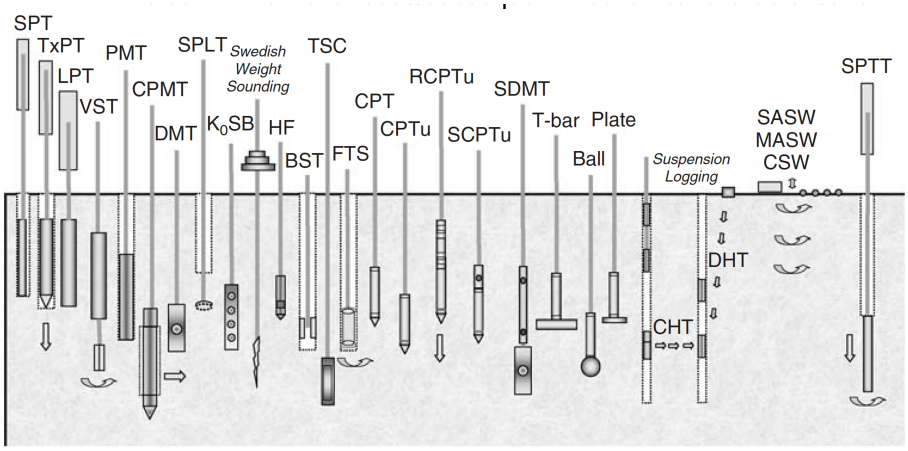


Figure 4: Principal overview of different types of in-situ geotechnical tests. Original Figure from [May07].

4.2 Large scale tests

A large scale test is performed in-situ on a geotechnical structure, and basically is a 1-g test at a scaling factor that is close to the prototype scale at a test site that is well characterised, and has a large number of instrumentation embedded in the soil and on the structure. The challenge here is the control and characterisation of the initial conditions, the sparse instrumentation (compared to the total soil volume to be instrumented), and the small number of tests due to the large expense (typically only one test performed). Interestingly, most industry clients prefer large scale demonstration tests that closely resemble the final technical solution, rather than systematic tests under controlled conditions in a geotechnical centrifuge. However, from a scientific point

of view, the one-off results often have a limited value of offering new insights in the system behaviour.

5 Model soils vs. natural deposits

Natural geomaterials often have a complex geological loading history and are composed of many constituents. The determination of the site conditions and the behaviour of natural soils in itself is very challenging, bringing additional complications ranging from sample disturbance issues and difficulties in specifying initial stress conditions, to long lead times in acquiring material for testing. Therefore, a large number of researchers have resorted to model soils such as kaolin clay powder and uniform clean sand, which is more easily available and well documented (especially when other researchers use material from the same supplier). Furthermore, the researcher can tailor the materials to systematically study the impact of soil composition and morphology, as well as the stress history. Although the emerging responses of these materials are not directly comparable with most (intact) natural soils, these materials helped to elucidate many mechanisms in soil mechanics. The soil fabric in natural soils is one of the most difficult features to capture. Fig. 5, shows that a natural fabric (as maintained by suction during sampling) cannot be recreated in the laboratory, despite a similar initial density and stress state at the start of shearing. The results indicate a completely different response in the intact sample, both peak strength, strain to failure and the volumetric response during shearing.

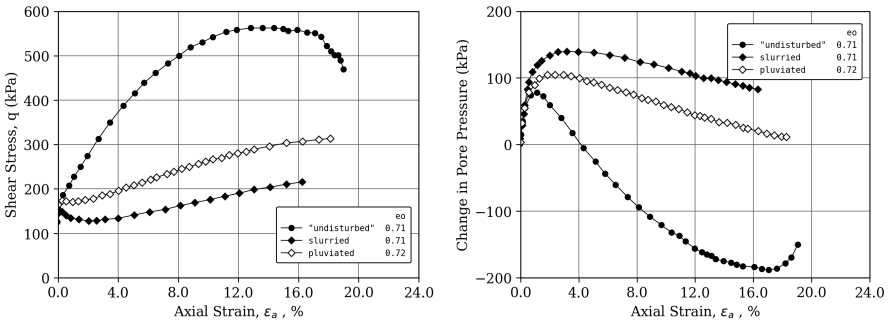


Figure 5: Undrained triaxial test results on silt in its natural and reconstituted state. Replotted from [HDS00].

6 Conclusions

Geotechnical testing is an integral part of the discipline, as part of research and engineering applications. A wide range of geotechnical tests have been developed at laboratory and field scale and only a select few have been briefly discussed. The purpose of the test influences the design of the experimental test setup, the materials used, the test protocol and the experimental programme. Some of those aspects will be elaborated in more detail in the following chapters.

References

[AMH02] F Alonso-Marroquin and H.J. Herrmann. Calculation of the incremental stress-strain relation of a polygonal packing. *Physical Review E*, 66(2):021301, 2002.

[AMHD22] E. Andò, B. Marks, R. Hurley, and J.A. Dijksman. *ALERT Doctoral School 2022: Advanced Experimental Geomechanics*. ALERT Geomaterials, 2022.

[And09] K.H. Andersen. Bearing capacity under cyclic loading—offshore, along the coast, and on land. the 21st bjerrum lecture presented in oslo, 23 november 2007. *Canadian Geotechnical Journal*, 46(5):513–535, 2009.

[ATMW89] A. Al-Tabbaa and D. Muir Wood. An experimentally based bubble model for clay. In *International Symposium on Numerical Models in Geomechanics (3rd: 1989).*, pages 91–99, 1989.

[Ban09] M. Banzi. *Getting Started with arduino*. O'Reilly Media, Inc., 2009.

[BL16] P Bésuelle and P Lanatà. A new true triaxial cell for field measurements on rock specimens and its use in the characterization of strain localization on a vosges sandstone during a plane strain compression test. *Geotechnical Testing Journal*, 39(5):879–890, 2016.

[Bur08] J.B. Burland. Personal reflections on the teaching of soil mechanics. In *Education and training in geo-engineering sciences*, pages 35–48. Taylor & Francis Group London, 2008.

[BW75] A.W. Bishop and L.D. Wesley. A hydraulic triaxial apparatus for controlled stress path testing. *Géotechnique*, 25(4):657–670, 1975.

[C+23] J. Creasey et al. Motivation and demonstration of robotic tooling for ground characterisation: the robocone. In *SUT Offshore Site Investigation and Geotechnics*, pages SUT–OSIG. SUT, 2023.

[DB10] J. Dijkstra and W. Broere. New method of full-field stress analysis and measurement using photoelasticity. *Geotechnical Testing Journal*, 33(6):469–481, 2010.

[G+07] J. Garnier et al. Catalogue of scaling laws and similitude questions in geotechnical centrifuge modelling. *International Journal of Physical Modelling in Geotechnics*, 7(3):01–23, 2007.

[GKT63] E. Gibson, K. Knights, and P.W. Taylor. A critical experiment to examine theories of thrree-dimensional consolidation. In *Proceedings European Conference on Soil Mechanics*, volume 1, pages 69–76, 1963.

[GSKD17] J.-P. Gras, N. Sivasithamparam, M. Karstunen, and J. Dijkstra. Strategy for consistent model parameter calibration for soft soils using multi-objective optimisation. *Computers and Geotechnics*, 90:164–175, 2017.

[HDS00] K. Høeg, R. Dyvik, and G. Sandbækken. Strength of undisturbed versus reconstituted silt and silty sand specimens. *Journal of geotechnical and geoenvironmental engineering*, 126(7):606–617, 2000.

[HGS83] D.W. Hight, A. Gens, and M.J. Symes. The development of a new hollow cylinder apparatus for investigating the effects of principal stress rotation in soils. *Géotechnique*, 33(4):355–383, 1983.

[Hun05] R.E Hunt. *Geotechnical engineering investigation handbook*. CRC Press, 2005.

[KAVA18] R. Kawamoto, E. Andò, G. Viggiani, and J. Andrade. All you need is shape: Predicting shear banding in sand with ls-dem. *Journal of the Mechanics and Physics of Solids*, 111:375–392, 2018.

[KH12] V Kostkanová and I Herle. Measurement of wall friction in direct shear tests on soft soil. *Acta Geotechnica*, 7(4):333–342, 2012.

[Kry95] V.V. Krylov. Generation of ground vibrations by superfast trains. *Applied Acoustics*, 44(2):149–164, 1995.

[KT14] L. Ke and A. Takahashi. Experimental investigations on suffusion characteristics and its mechanical consequences on saturated cohesionless soil. *Soils and Foundations*, 54(4):713–730, 2014.

[L+22] B.M. Lehane et al. Cpt-based axial capacity design method for driven piles in clay. *Journal of Geotechnical and Geoenvironmental Engineering*, 148(9):04022069, 2022.

[Lad16] P.V. Lade. *Triaxial testing of soils*. John Wiley & Sons, 2016.

[LS05] J.-S. Lee and J.C. Santamarina. Bender elements: performance and signal interpretation. *Journal of geotechnical and geoenvironmental engineering*, 131(9):1063–1070, 2005.

[LV90] S. Leroueil and P.R. Vaughan. The general and congruent effects of structure in natural soils and weak rocks. *Géotechnique*, 40(3):467–488, 1990.

[Man53] J. Mandel. Consolidation des sols (étude mathématique). *Géotechnique*, 3(7):287–299, 1953.

[May07] P.W. Mayne. In-situ test calibrations for evaluating soil parameters. In Phoon Tan, editor, *Characterisation and Engineering Properties of Natural Soils–Proceedings of the Second International Workshop on Characterisation and Engineering Properties of Natural Soils: Taylor & Francis*, pages 1601–1652, 2007.

[MK00] C. Madshus and A.M. Kaynia. High-speed railway lines on soft ground: dynamic behaviour at critical train speed. *Journal of Sound and Vibration*, 231(3):689–701, 2000.

[MW03] D. Muir Wood. *Soil Behaviour and Critical State Soil Mechanics*, chapter A particular elastic-plastic model: Cam-Clay, pages 112–138. Cambridge University Press, 2003.

[PT18] M. Pedrotti and A. Tarantino. An experimental investigation into the micromechanics of non-active clays. *Géotechnique*, 68(8):666–683, 2018.

[SW68] A.N. Schofield and P. Wroth. *Critical state soil mechanics*, volume 310. McGraw-hill London, 1968.

[Tay95] R.N. Taylor. *Geotechnical centrifuge technology*. CRC press, 1995.

[TSP24] C. Tamagnini, L. Sanavia, and M. Pastor. *ALERT Doctoral School 2024: Numerical Methods in Geomechanics.* ALERT Geomaterials, 2024.

[TZ10] C. Thornton and L. Zhang. On the evolution of stress and microstructure during general 3d deviatoric straining of granular media. *Géotechnique*, 60(5):333–341, 2010.

[USOA24] J. Ulloa, L. Stainier, M. Ortiz, and J. Andrade. Data-driven micromorphic mechanics for materials with strain localization. *Computer Methods in Applied Mechanics and Engineering*, 429:117180, 2024.

[VB84] P.A. Vermeer and R. de Borst. Non-associated plasticity for soil, concrete and rocks. *Heron*, 29(3):1–64, 1984.

[VGG78] I. Vardoulakis, M. Goldscheider, and G. Gudehus. Formation of shear bands in sand bodies as a bifurcation problem. *International Journal for Numerical and Analytical Methods in Geomechanics*, 2(2):99–128, 1978.

[VH26] G. Viggiani and I. Herle. From oedometer to computed tomography: 100 years of experimental soil mechanics. In Pistrol, Adam, and Schweiger, editors, *Proceedings of the 21st ICSMGE, Vienna, Austria, 14 – 18 June 2026*, pages 21–40. Taylor & Francis Group London, 2026.

[VHRM+12] G. Viggiani, S.A. Hall, E. E. Romero Morales, E. Tudisco, G. Musso, C. Jommi, and J.C. Santamarina. *ALERT Doctoral School 2012: Advanced Experimental Techniques in Geomechanics*. ALERT Geomaterials, 2012.

[Wic05] T. Wichtmann. *Explicit accumulation model for non-cohesive soils under cyclic loading*. PhD thesis, Universität Bochum, 2005.

[WNKL03] S.J. Wheeler, A. Näätänen, M. Karstunen, and M. Lojander. An anisotropic elastoplastic model for soft clays. *Canadian geotechnical journal*, 40(2):403–418, 2003.

Sensors: fundamentals of measurement and electronics for experimentalists

Alessandro Tengattini

Laboratoire 3SR, Université Grenoble Alpes; Institut Laue-Langevin

Experimental geomechanics relies on converting material responses into quantifiable signals through measurement chains. This chapter analyses what underlies these measures and establishes a foundational metrological framework for understanding laboratory sensors. We use a liquid-in-glass thermometer as an illustrative example to introduce the key elements involved in measurement and the assessment of measurement accuracy. We examine the trade-offs between signal sensitivity, operational range, and sensor invasiveness. We clarify the distinction between precision and accuracy, highlighting the pitfalls of Full Scale (% FS) error ratings across narrow measurement windows, and introduce the Test Uncertainty Ratio ($10:1$ *Rule) to assess instrument fitness for purpose. Finally, we provide a structured method for quantifying individual errors contributors into a unified standard uncertainty and describe the mathematical foundation required for formal error propagation through geomechanical constitutive equations.*

1 Elements of Metrology

1.1 Is What You Are Measuring What You Think You're Measuring?

When you step into a laboratory, it is easy to adopt a certain blind faith in your equipment. You glue a strain gauge to a rock core, wire it to a digital data acquisition system, and watch numbers flicker on a screen. The software says $120\ \mu\epsilon$, so you write down that the rock experienced exactly $120\ \mu\epsilon$ of strain. But what do we find when we pull back the curtain on that measurement?

The physical reality is that the rock deformed. Because it deformed, a tiny foil grid glued to it stretched. Because that grid stretched, its electrical resistance changed minutely. Because its resistance changed, a voltage balance across a circuit called a Wheatstone bridge was disrupted. An analog-to-digital converter (ADC) measured

that voltage change, converted it into a binary number, and the software multiplied that number by a calibration factor to print out a number on your screen.

Experimental mechanics is entirely about measuring things. But a foundational philosophical hurdle every experimentalist must overcome is asking the simple, unsettling question: **"Is what I'm measuring truly what I think I'm measuring?"** The unsettling but honest answer is that the vast majority of our measurements are entirely indirect.

1.2 What Can We Measure? Base vs. Composed Quantities

Before we can critique how we measure, we must look at what exists out there to be measured in the physical universe. In science and engineering, we organize our observations into specific dimensions, quantified by standardized units. These can be split fundamentally into **base quantities** and **composed (derived) quantities**.

1.2.1 Base Quantities

Base quantities are the the agreed-on building blocks of metrology. They are not defined in terms of other physical dimensions. Examples include:

- **Length/Dimension:** Measured in meters [m] or angles in degrees [°].
- **Mass:** Measured in grams [g].
- **Time:** Measured in seconds [s].
- **Temperature:** Measured in Celsius [°C] or Kelvin [K].
- **Electric Current:** Measured in Amperes [A].
- **Voltage/Electrical Potential:** Measured in Volts [V].

1.2.2 Composed Quantities

Composed quantities are built by mathematically combining these base dimensions. They describe more complex mechanical behaviors by examining how base quantities interact. For instance:

- **Speed [m/s]:** You cannot directly "see" speed as an isolated baseline unit; you must observe a change in distance (Length) over a specific duration (Time).
- **Volumetric Strain Rate [s^{-1}]:** In geomechanics, this describes how a volume of soil deforms per unit of time, compounding spatial dimensions and time.
- **Stress/Pressure [Pa or N/m^2]:** Composed of mass, length, and time ($kg \cdot m^{-1} \cdot s^{-2}$), representing an internal force distribution over an area.

Understanding this distinction is crucial because when you measure a composed quantity, an error in *any single one* of its underlying base components will fundamentally compromise your final calculated value, as detailed in section 1.8.

1.3 The Anatomy of Indirect Measurements: Law, Device, and Calibration

Since nearly all physical quantities in geomechanics are measured indirectly, we must formalize how an indirect measurement is constructed. Every indirect measurement is not a singular event; it is a three-part chain consisting of a **fundamental law**, a **physical device**, and a **calibration procedure**. If any of these three links is mishandled, the entire measurement fails.

1.4 Anatomy of an Indirect Measurement: The Thermometer Example

To see how these concepts intertwine, let us dissect a deceptively simple device: a classic mercury liquid-in-glass thermometer. It seems straightforward, but its operation relies heavily on a chain of physical assumptions.

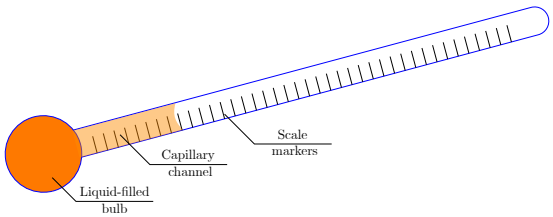


Figure 1: Anatomy of a standard fluid expansion thermometer.

A mercury thermometer consists of three core structural elements: a bulb containing a known fluid mass, a narrow capillary channel, and a graduated scale. The fundamental law governing this tool is the linear thermal expansion of the fluid:

1.4.1 The Law: Non-Linearities in Thermal Physics

In an ideal metrological model, the expansion of a liquid within a container is assumed to be linear. We define the volumetric expansion of the working fluid (ΔV) relative to its initial volume at the reference temperature T_0 as V_0, using a constant coefficient of thermal expansion (α):

$$\Delta V = V_0 \cdot \alpha \cdot \Delta T \tag{1}$$

However, physical laws are rarely linear across wide operational ranges. In reality, the volumetric expansion coefficient β is a function of temperature itself ($\alpha(T)$), introducing higher-order non-linear terms:

$$V(T) = V_0 \left[1 + \alpha(T - T_0) + \beta_2(T - T_0)^2 + \gamma_3(T - T_0)^3\right] \tag{2}$$

For mercury or organic indicator fluids, while α dominates near ambient conditions, the second-order (β_2) and third-order (γ_3) thermodynamic terms become significant

near the fluid's phase boundaries. Furthermore, the glass bulb housing itself undergoes thermal expansion (β_{glass}), meaning the observed displacement proxy relies on the *net differential expansion* ($\beta_{net} = \beta_{fluid} - \beta_{glass}$). If the thermal response of the glass lags behind the fluid during rapid temperature transients, the governing law briefly breaks down, yielding a transient non-linear error.

1.4.2 The Device: Physical Imperfections and Structural Hysteresis

Even if the physical law were perfectly linear, the physical hardware introduces geometric and mechanical distortions that corrupt the signal path:

- **Bore Inhomogeneity:** The capillary channel is assumed to be a uniform cylinder of cross-sectional area A. In manufactured glass, the channel diameter fluctuates along its length. A displacement Δh near the base does not represent the same volumetric step as Δh near the top of the stem:

$$\Delta V = \int_0^h A(z)\, dz \tag{3}$$

- **Meniscus Concavity and Capillary Action:** The interface between the liquid indicator and the internal stem vapor forms a curved meniscus due to surface tension. The contact angle (θ) varies depending on whether the liquid column is rising (advancing contact angle) or falling (receding contact angle). This variable curvature distorts visual alignment with stem markings and exerts capillary pressure variations on the internal fluid column.

1.4.3 Calibration: Benchmark Realization and Environmental Sensitivities

Because no physical device possesses a perfectly straight channel or a linear material law, we must calibrate the instrument against stable, reproducible physical state transitions—traditionally, the freezing point ($0°$C) and boiling point ($100°$C) of water. However, establishing these reference points introduces severe experimental vulnerabilities:

The Ice Point Phase Transition ($0°$C) A standard ice bath relies on the thermodynamic equilibrium between solid ice and liquid water. However, an unrefined ice bath is notoriously unstable:

- **Salinity and Impurities:** The presence of dissolved minerals or salts lowers the freezing point according to the law of freezing-point depression ($\Delta T_f = i \cdot K_f \cdot b$). Even minor chemical contamination of the water bath causes the real transition temperature to drift below $0.00°$C.
- **Thermal Stratification:** If the bath is not continuously agitated, water density anomalies (where water reaches maximum density at $3.98°$C) cause warm water pockets to settle at the bottom while ice floats, creating significant spatial temperature gradients across the thermometer bulb.

The Boiling Point Phase Transition (100°C) The vaporization point of water provides a second fixed point, but it is acutely sensitive to atmospheric pressure (P_{atm}):

- **Barometric and Altitude Sensitivity:** According to the Clausius-Clapeyron relation, the boiling point of water shifts dramatically with changing ambient pressure:
$$\frac{dP}{dT} = \frac{L}{T\,\Delta V_{vap}} \tag{4}$$
At higher elevations or during weather-induced barometric shifts, the actual boiling point drops significantly (e.g., boiling occurs at approximately 96.8°C at an altitude of 1000 m). Without precise barometric pressure correction at the exact moment of calibration, the upper anchor point introduces a significant systematic bias into the scale factor.

To overcome these environmental vulnerabilities, primary calibration laboratories abandon open water baths in favor of sealed **Triple Point of Water (TPW) cells**—where liquid, solid ice, and water vapor coexist in an evacuated, contaminant-free chamber at a fixed thermodynamic constant (0.01°C at 611.657 Pa)—eliminating atmospheric and salinity variations entirely.

1.4.4 How to make it better?: Precision, Accuracy, and the Interplay with Range

OK let's say that now we have mastered our understanding of the laws, the device and the calibration – I still don't know how accurate is my tool and whether it is fit for the specific task at hand!

The Interplay between Measurement Range, Geometry, and Invasiveness A fundamental challenge in sensor design is balancing intrinsic accuracy against operational range and physical invasiveness. To see these trade-offs clearly, consider a designer attempting to improve the sensitivity of a liquid-in-glass thermometer.

The elongation "proxy" (Δh) resulting from a thermal change (ΔT) is governed by the volume of the fluid reservoir (V_0), the net coefficient of thermal expansion (α_{net}), and the cross-sectional area of the capillary tube (A):

$$\Delta h = \frac{\Delta V}{A} = \frac{V_0 \cdot \alpha_{net} \cdot \Delta T}{A} \tag{5}$$

To increase the sensitivity ($\Delta h/\Delta T$) and allow finer resolution readings on the stem scale, a logical design change is to reduce the capillary bore area A. However, altering this single geometric parameter triggers a cascading sequence of physical trade-offs:

1. **Sensitivity vs. Measurement Range:** For a thermometer stem of fixed length L_{stem}, the maximum measurable temperature span ($\Delta T_{max} = T_{max} - T_{min}$) is strictly bounded by the total bore volume:
$$\Delta T_{max} = \frac{A \cdot L_{stem}}{V_0 \cdot \alpha_{net}} \tag{6}$$

Reducing A to amplify sensitivity drastically reduces the operational range (ΔT_{max}). The instrument becomes an ultra-precise "micro-thermometer" capable of measuring tiny temperature variations, but it 'saturates' rapidly outside a narrow thermal window.

2. **Stem Length vs. Mechanical Practicality:** If the wide temperature range must be preserved while keeping the narrow bore area A, the only geometric variable left to expand is the stem length L_{stem}. The thermometer rapidly becomes unwieldy, fragile, and practically impossible to mount inside a standard laboratory cell or triaxial apparatus.

3. **Reservoir Enlargement vs. Thermal Invasiveness:** To avoid an infinitely long stem, the designer might instead consider enlarging the initial fluid reservoir volume (V_0) to yield a larger absolute volume change (ΔV) for a small bore A. However, this introduces the critical issue of **invasiveness**.

   A measurement device should ideally observe a system without altering its energy state. The thermometer bulb possesses a finite heat capacity ($C_{sensor} = m \cdot c_p$), where c_p is the specific heat capacity at constant pressure. When inserted into a small or delicate experimental sample at temperature T_{sample}, heat transfers between the specimen and the probe until thermal equilibrium (T_{eq}) is reached:

$$T_{eq} = \frac{m_{sample}c_{sample}T_{sample} + m_{sensor}c_{sensor}T_{sensor}}{m_{sample}c_{sample} + m_{sensor}c_{sensor}} \tag{7}$$

   Increasing the fluid volume V_0 increases the sensor's thermal mass ($m_{sensor}c_{sensor}$). If the thermometer's heat capacity is significant relative to the test sample, inserting the cold probe drains thermal energy from the specimen, artificially depressing its temperature before the measurement is even recorded.

Thus, every sensor design represents a constrained optimization problem: maximizing signal sensitivity while keeping the instrument compact enough to be non-invasive, and a range sufficiently broad to capture the full mechanical or thermal process under study.

To answer this, we must formally distinguish between precision and accuracy, and evaluate how they scale across the operational range of the instrument.

The Interplay between Precision, Accuracy, and Fitness for Purpose Mastering these trade-offs leads to the core metrological question: **How accurate is this specific tool, and is it fit for the task at hand?** To answer this, we must evaluate how the thermometer's physical limits govern its precision, accuracy, and operational range.

Precision vs. Accuracy in the Stem Returning to our thermometer, precision and accuracy reflect two distinct sources of error:

- **Accuracy (Systematic Bias):** Reflects how close the stem reading is to the absolute thermodynamic ground truth. For instance, if an uncorrected atmospheric

pressure drop at high altitude shifts the upper boiling point calibration mark by $-1.2°$C, every reading across the stem suffers from a systematic calibration bias (β).

- **Precision (Repeatability and Resolution):** Reflects the random noise and physical reading limits (ϵ_{rand}). In our thermometer, precision is set by the physical capillary bore size A and the spacing of the etched scale lines. If A is large, Δh per degree is very small, making it impossible for the human eye to visually resolve variations smaller than $\pm 0.5°$C, regardless of how perfectly calibrated the ice bath was.

Full-Scale Error Traps The choice between a wide-range thermometer (large bore A or long stem L_{stem}) and a narrow-range thermometer (fine bore A) fundamentally alters how error scales. Sensor accuracy is often quoted as a percentage of Full Scale (% FS):

$$U_{abs} = \pm\,(\%\ \text{FS}) \cdot (T_{max} - T_{min}) \tag{8}$$

Consider two competing thermometer choices for a geotechnical thermal testing rig:

- **Option A (Wide-Range General Tool):** Designed with a large bore A to cover a wide range from $0°$C to $200°$C with a rated accuracy of $\pm 0.5\%$ FS. Its absolute uncertainty is fixed at $U_{abs} = 200°\text{C} \times 0.005 = \pm 1.0°$C everywhere along the stem.
- **Option B (Narrow-Range Micro-Thermometer):** Designed with an ultra-fine bore A tailored specifically to track ambient laboratory variations from $15°$C to $25°$C ($\Delta T_{max} = 10°$C) with the same $\pm 0.5\%$ FS accuracy rating. Its absolute uncertainty shrinks to $U_{abs} = 10°\text{C} \times 0.005 = \pm 0.05°$C.

If the experimental objective is to measure a small $2.0°$C thermal disturbance during a soil consolidation test:

- Using Option A yields a relative measurement error of $\frac{\pm 1.0°\text{C}}{2.0°\text{C}} = \mathbf{50}\%$. The measurement is overwhelmed by uncertainty.
- Using Option B yields a relative error of $\frac{\pm 0.05°\text{C}}{2.0°\text{C}} = \mathbf{2.5}\%$. The instrument provides a high-fidelity signal for this specific experiment.

The Fitness-for-Purpose Rule To formalize this decision process, an experimentalist applies the Test Uncertainty Ratio or 10:1 Rule:

$$U_{instrument} \leq \frac{1}{10} \cdot \Delta T_{target,min} \tag{9}$$

By matching the instrument's absolute uncertainty ($U_{instrument}$) to one-tenth of the smallest expected physical change ($\Delta T_{target,min}$), you ensure that your sensor's precision and accuracy are strictly aligned with the target phenomena, avoiding both

the trap of under-resolved measurements and the unnecessary invasiveness of over-designed sensors.

According to international standards, a properly maintained liquid-in-glass thermometer can achieve an uncertainty of $\pm 0.01°\mathrm{C}$ within a narrow 0 to $100°\mathrm{C}$ calibrated range. If one steps outside that range, and the uncertainty widens significantly ($\pm 0.2°\mathrm{C}$ up to $450°\mathrm{C}$) because the physical system loses its predictable structural alignment.

1.5 Elements of Noise: Systematic vs. Random Errors

Every experimental measurement contains a mix of the true signal and unwanted errors. To handle these errors, we must categorize them into **systematic errors** and **random noise**.

Table 1: Comparison of Systematic and Random Errors

Error Feature	Systematic Errors	Random Noise
Definition	Consistent, predictable deviations that bias data in a specific direction.	Unpredictable, chaotic fluctuations that scatter data statistically evenly around a mean value.
Typical Causes	Bad calibration, sensor thermal drift, or flawed experimental assumptions.	Electronic thermal noise, ambient vibrations, or structural signal disturbances.
Statistical Behavior	Does not average out; remains constant regardless of sample size.	Follows a clear statistical distribution, such as a Gaussian or Poisson curve.
How to Fix It	Physical recalibration, proper instrument warm-up, and regular system maintenance.	Accumulating and averaging data over longer periods to mathematically smooth out the noise.

Imagine you are using a digital thermometer that outputs a voltage signal to an Analog-to-Digital Converted (ADC). If the system tells you it reads $2.5\mathrm{V}$, that number is never perfectly static. If you look closely at the raw data, it oscillates slightly.

If those oscillations are **random noise**, they might follow a clean Gaussian bell curve. By oversampling—recording thousands of data points over a few extra seconds—you can mathematically find the true mean and effectively eliminate the noise.

But if that error is **systematic**—say, the electrical cable is long, uncompensated, and heating up due to internal resistance—the signal will slowly and permanently drift in one direction. No amount of statistical averaging will save your data from a systematic

error. You need to physically find the root cause, acknowledge it, and recalibrate your system.

There is no such thing as a perfect measuring tool. There is only a tool that is appropriate for your specific problem, provided you thoroughly understand its range, constraints, and inherent uncertainties.

1.6 Digital vs. Analog Measurements: The Digital Mirage

I know exactly what you are thinking. *"Ah, okay, I see why we have all these headaches with physical limits, non-linear thermal expansion, and surface tension. But that is because a liquid-in-glass thermometer is an old, purely analog device! We live in the era of microchips and digital precision. If I just switch to a digital thermometer, all these messy physical laws disappear, and a computer fixes it automatically."*

It is a comforting thought, but it is a complete mirage.

When you look at a digital thermometer, you are not looking at a fundamentally different way of interacting with the universe. Under the hood, a digital instrument is nothing more than an analog sensor wearing a digital mask. Let us pull apart a digital thermometer—specifically, one utilizing a **thermistor** or a **resistance temperature detector (RTD)**—to see how it actually functions at the technical level by tracing the signal from its physical origin all the way through to Bytes in the computer and to numbers on your screen.

1.6.1 The Digital Chain: From Physical Law to Bits

1. The Transducer Stage and the Wheatstone Bridge Our chain begins with the sensor element itself which alters its fundamental electrical resistance (R) in response to an environmental stimulus. For an RTD or thermistor, the underlying physical law is thermo-resistivity:

$$R(T) = R_0 \left[1 + \alpha(T - T_0)\right] \tag{10}$$

where α is the temperature coefficient of resistance. However, a microchip cannot natively read resistance; it can only read voltage or current. Therefore, we must convert a changing resistance (ΔR) into a changing voltage (ΔV).

Because the resistance variations in experimental mechanics are often incredibly minute - frequently on the order of milliohms (mΩ) - a simple series voltage divider is generally far from adequate. Instead, we employ a **Wheatstone Bridge** configuration. Historically, this current would have passed through a coil suspended in a magnetic field, deflecting a physical needle across a scale—a **galvanometer**. Modern digital systems replace the needle with voltage measurement circuits.

The Wheatstone Bridge (Fig.2) consists of four resistive arms arranged in a diamond topology, powered by a highly stable direct current (V_{in}). The differential output voltage ($V_{out} = V_A - V_B$) is measured across the middle nodes of the diamond. In a standard **Quarter-Bridge configuration**, one arm contains our active sensing

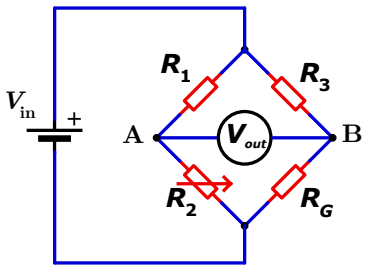


Figure 2: Schematics of a Wheatstone Bridge.

element (R_G), while the other three arms consist of fixed, highly precise reference resistors (R_1, R_2, R_3). The fundamental balance equation governing the differential output voltage is given by:

$$V_{out} = V_{in} \left(\frac{R_G}{R_3 + R_G} - \frac{R_2}{R_1 + R_2} \right) \tag{11}$$

When the system is at rest, the bridge is adjusted to a state of perfect equilibrium where $R_1/R_2 = R_3/R_G$. At this point, the ratio cancels out, yielding $V_{out} = 0$ V. This process is known as **nulling** the bridge. When the physical stimulus deforms or heats the sensor, its resistance shifts to $R_G + \Delta R$. Substituting this into our balance equation demonstrates how the bridge generates a differential voltage:

$$V_{out} = V_{in} \left(\frac{R_G + \Delta R}{R_3 + R_G + \Delta R} - \frac{R_2}{R_1 + R_2} \right) \tag{12}$$

Assuming all reference resistors are matched exactly to the baseline resistance of the gauge ($R_1 = R_2 = R_3 = R_G = R$), the equation simplifies via a first-order Taylor series approximation for small resistance variations ($\Delta R \ll R$):

$$V_{out} \approx V_{in} \left(\frac{\Delta R}{4R} \right) \tag{13}$$

This equation reveals a crucial fact: the output voltage is directly proportional to the fractional change in resistance ($\Delta R/R$). However, it also exposes a dangerous vulnerability: V_{out} scales linearly with V_{in}. If your excitation voltage ripples, surges, or decays, your output voltage shifts proportionally, fabricating a false physical signal out of thin air.

2. The Analog Signal Conditioning Stage (The Amplifier) If a strain gauge experiences a strain of $1000\ \mu\epsilon$, the resulting change in resistance might produce an output voltage V_{out} on the order of a few millivolts (mV), or even microvolts (μV). This raw

analog signal is far too small, and close to the environmental noise floor to be directly processed by an analog to digital converter. If fed directly into a chip, the tiny signal steps would be completely swamped by the internal electronic noise.

To resolve this, the signal must pass through an **Electronic Amplifier**. This is a specialized integrated circuit typically built from multiple distinct operational amplifiers. The primary purpose of the instrumentation amplifier is twofold:

1. **High Input Impedance:** It presents an incredibly high electrical resistance to the Wheatstone bridge (typically in the gigaohm (GΩ) range). This ensures that the amplifier draws virtually zero current from the bridge circuit, preventing it from loading or distorting the analog voltages it is trying to observe.
2. **Common-Mode Rejection Ratio (CMRR):** Because the long cables running from the triaxial cell to the computer act as antennas, they pick up massive amounts of electromagnetic interference (like 50Hz$/60$Hz power line hum). This noise affects both signal lines (V_A and V_B) identically. The instrumentation amplifier acts as a mathematical subtractor, discarding any identical voltage components (*common-mode noise*) while amplifying only the true difference ($V_A - V_B$) by a fixed gain factor G:

$$V_{amplified} = G \cdot (V_A - V_B) \tag{14}$$

The signal is scaled up so that its dynamic range spans several volts (e.g., 0 to 5 V or -10 V to $+10$ V), perfectly matching the optimal input window of the Analog-to-Digital Converter.

3. The Analog-to-Digital Converter: Quantization and Bits Now, the amplified, continuous analog voltage ($V_{amplified}$) arrives at the gates of the Analog-to-Digital Converter (ADC). This chip acts as the final gatekeeper, translating a smooth, continuous physical voltage into a stepped sequence of (binary) bits.

While there are multiple ADC architectures, two dominate experimental engineering: the **Successive Approximation Register (SAR) ADC** (ideal for high-speed dynamic measurements like acoustic emissions) and the **Sigma-Delta ($\Sigma\Delta$) ADC** (ideal for high-resolution, slow geomechanical processes like soil consolidation). To understand how voltage becomes bits, let us examine the elegant logic of a SAR ADC.

A SAR ADC functions like a high-speed binary balance scale. It contains an internal register of n bits, a control circuit, and a precise internal Reference Voltage (V_{ref}), which sets the absolute boundaries of the measurement universe. If $V_{ref} = 5.000$ V, the ADC can only process inputs between 0 V and 5 V.

When a conversion command is triggered, the ADC samples and holds the incoming analog voltage (V_{in}). It then executes a binary search routine, evaluating each bit from the Most Significant Bit (MSB) down to the Least Significant Bit (LSB):

- **Step 1 (Evaluating the MSB):** The controller sets the first bit to 1 and all other bits to 0 (for an 8-bit system, this is binary `10000000`, or decimal 128).

An internal Digital-to-Analog Converter (DAC) turns this binary guess back into a precise internal test voltage exactly equal to half of V_{ref} (2.500 V). A comparator circuit matches this test voltage against our actual input V_{in}. If $V_{in} \geq 2.500$ V, the comparator keeps the MSB set to 1. If $V_{in} < 2.500$ V, the controller drops the MSB to 0.

- **Step 2 (The Next Bit):** The controller moves to the next bit (`x1000000`), generating a new test voltage that splits the remaining half-scale. If our first bit remained 1, the new test voltage rises to $2.500 + 1.250 = 3.750$ V. The comparator evaluates V_{in} against this new threshold, keeping or dropping the bit accordingly.
- **Remaining Steps:** This process repeats sequentially for all n bits. Each step cuts the remaining voltage uncertainty exactly in half. After n iterations, the binary register locks, outputting a stable digital integer code.

The total number of discrete intervals (N) available to map the analog world is defined entirely by the converter's bit depth (n):

$$N = 2^n \tag{15}$$

The absolute smallest voltage change that can trigger a change in the least significant bit—known as the **voltage resolution** or **LSB step size** (ΔV_{LSB})—is calculated as:

$$\Delta V_{LSB} = \frac{V_{ref}}{2^n} \tag{16}$$

If we use an inexpensive 8-bit system ($2^8 = 256$ steps) with a 5 V reference, our step size is:

$$\Delta V_{LSB} = \frac{5.000 \text{ V}}{256} = 0.01953 \text{ V} = 19.53 \text{ mV} \tag{17}$$

If our input voltage is 2.500 V, the ADC outputs the digital integer code 128 (`10000000`). If the physical sample deforms slightly and the voltage creeps up to 2.510 V, the ADC cannot see it! The voltage change (10 mV) is smaller than our LSB step size (19.53 mV). The output integer code stays frozen at 128. The actual physical movement is entirely lost to **quantization error**.

To capture this subtle movement, you must increase the bit depth to a 16-bit architecture ($2^{16} = 65,536$ steps):

$$\Delta V_{LSB} = \frac{5.000 \text{ V}}{65536} = 0.0000762 \text{ V} = 76.2 \ \mu\text{V} \tag{18}$$

With a 16-bit converter, a 10 mV change spans over 130 discrete digital steps, rendering the physical deformation beautifully visible to your logging software.

Yet, this resolution comes at an immediate physical cost. A step size of 76.2 μV is very tiny. If your laboratory cables lack high-quality braided shields, or if the system

shares an electrical ground line with a heavy hydraulic pump motor, the ambient environmental electrical noise floor might easily exceed $500\ \mu$V. In this scenario, your high-resolution 16-bit ADC will spend its time digitizing ambient electrical noise. The last three or four bits of your digital code will dance and oscillate randomly, presenting an illusion of precision that is completely uncoupled from the physical mechanics of your soil sample.

1.6.2 Additional Electronic Vulnerabilities: Self-Heating

Far from liberating you from physical constraints, going digital introduces specific physical issues unique to circuits. To read a resistive sensor, you must pass an electrical current through it. Because the thermistor or strain gauge has electrical resistance (R), it obeys Joule's Law, dissipating power as heat:

$$P = I^2 R \tag{19}$$

By the simple act of trying to measure the temperature, your current is physically heating up the sensor! If your excitation current is too high, or if your soil medium has low thermal conductivity and cannot dissipate this heat, the sensor will measure its own self-heating rather than the environment's true temperature.

Crucially, **digital sensors still require calibration**. The software inside the instrument still relies on fundamental laws (but now several more laws are engaged in the process), and calibration simply applies a mathematical formula to convert a binary integer back to a physical unit value. If the underlying calibration coefficients programmed into that microchip drift over time, your digital display will print out a highly precise, clean, professional-looking number that is completely wrong.

1.7 Analog vs. Digital: Which is Truly Better?

Given these realities, we cannot simply state that digital is superior to analog, or vice-versa. Both approaches have distinct trade-offs that an experimentalist must carefully choose.

The main advantage of digital tracking is its sheer capacity for data logging and speed. In geomechanics, if you are capturing a dynamic seismic wave propagating through a triaxial specimen, or analyzing a high-speed projectile impact, human eyes and paper charts are often useless; you need high-fidelity digital ADCs sampling at tens of kilohertz.

However, analog systems retain an element of mechanical transparency. If an analog pressure dial is sticking due to dirt, you can see the needle jerk. If a digital system suffers from a corrupted calibration file, or a new source of noise appears it will continue to output perfectly smooth, stable, beautifully formatted garbage data, giving you false confidence in a ruined experiment.

Table 2: Architectural Trade-offs Between Analog and Digital Systems

Metric	Analog Instruments	Digital Instruments
Resolution	Infinitely continuous. Limited only by physical optical limits or needle friction.	Discretized steps. Limited strictly by the bit-depth (2^n) of the ADC.
Data Capture	Manual transcription or continuous physical charting (e.g., paper roll plots). Slow.	Automated, ultra-/high speed logging (1 Hz to several kHz). Mass storage.
Noise Susceptibility	Highly vulnerable to mechanical friction, wear, and local environmental parallax errors.	Vulnerable to electrical interference, ground loops, and quantization limits.
Failure Modes	Progressive degradation. Wear happens gradually and can often be seen visually.	Catastrophic or hidden failure. Code can crash, or bits can flip silently without warning.

1.8 Are We Doomed? Error Assessment and Propagation

Looking at this mountain of potential disasters—fluid expansions, structural compliance, electronic noise, quantization limits, and self-heating—it is easy for a student to fall into despair. You might ask: *"If every single component of my measurement chain introduces a structural flaw, are my experimental results completely meaningless? Are we doomed?"*

The answer is -thankfully- **no**.

In experimental mechanics, an error should not be seen as a personal failure or a mistake; it is a fundamental property of the physical universe. Your job as an experimentalist is not to produce a measurement with zero error—that is physically impossible. Your job is to accurately **bound and quantify** that error. A measurement only needs to be small enough that its error boundaries do not obscure the physical phenomenon you are trying to observe. If you are tracking a massive soil settlement of 50 mm, a sensor error of ± 0.1 mm is entirely negligible. If you are tracking a microscopic rock strain of 10 $\mu\epsilon$, that same ± 0.1 mm error is catastrophic.

Quantifying error should not merely be about reading a manufacturer's accuracy tolerance off a datasheet; it requires systematically categorizing every individual source of deviation within the measurement chain. In practice, metrologists classify these sources into two distinct categories: **Type A evaluations**, which are quantified through statistical analysis of repeated observations (such as experimental variance and standard deviation of the mean), and **Type B evaluations**, which are derived from non-statistical knowledge (such as calibration certificates, digital resolution limits, sensor drift tolerances, and environmental bounds). By converting both Type A random scat-

ter and Type B systematic bounds into standardized quantities known as *standard uncertainties* (u_i), we establish a unified numerical foundation. Only when every primary input parameter—whether a force, a temperature, or a length—is expressed with its corresponding standard uncertainty can we step into the mathematical mechanics of tracing how these individual errors combine and amplify across our governing physical laws.

To understand how individual error sources are quantified and combined into a single standard metric, let us analyze a real-world temperature measurement using our calibrated liquid-in-glass thermometer.

Suppose we place our thermometer into a fluid cell during a soil consolidation test and read a temperature of $T_{meas} = 22.4°\text{C}$. To quantify the uncertainty of this single reading, we must evaluate four distinct physical error contributors:

1. **Scale Resolution Limits (δT_{res}):** The stem has etched markings every $0.5°\text{C}$. Assuming a reader can estimate to within half a division, the visual resolution bound is $\pm 0.25°\text{C}$. Assuming a rectangular probability distribution (where any value within the interval is equally likely), the standard uncertainty component is:
$$u_{res} = \frac{0.25°\text{C}}{\sqrt{3}} \approx 0.144°\text{C} \tag{20}$$

2. **Calibration Reference Drift (u_{cal}):** The thermometer was calibrated using a boiling water fixed point at an elevation where atmospheric pressure was not measured directly. Based on local barometric fluctuations during calibration, the systematic uncertainty bound assigned by the calibration certificate is $\pm 0.10°\text{C}$ (normally distributed at a 95% confidence level, $k = 2$):
$$u_{cal} = \frac{0.10°\text{C}}{2} = 0.050°\text{C} \tag{21}$$

3. **Capillary Non-Uniformity (u_{bore}):** Due to minor manufacturing variations in the internal bore diameter $A(z)$, the displacement-to-temperature scale factor drifts slightly across the stem, contributing an estimated uniform error bound of $\pm 0.08°\text{C}$:
$$u_{bore} = \frac{0.08°\text{C}}{\sqrt{3}} \approx 0.046°\text{C} \tag{22}$$

4. **Parallax and Eye Alignment ($u_{parallax}$):** The glass wall thickness introduces a refraction offset if the observer's eye line is not perfectly perpendicular to the fluid meniscus. Repeated positioning trials show a random scatter with a standard deviation of:
$$u_{parallax} = 0.080°\text{C} \tag{23}$$

Combining the uncertainties Because these error sources act independently, and it is unlikely that they will combine in the most unfavorable way in a single measurement, we combine them in quadrature using the Root-Sum-of-Squares (RSS) method to establish the total combined standard uncertainty (u_c):

$$u_c(T) = \sqrt{u_{res}^2 + u_{cal}^2 + u_{bore}^2 + u_{parallax}^2} \tag{24}$$

Substituting our quantified values:

$$u_c(T) = \sqrt{(0.144)^2 + (0.050)^2 + (0.046)^2 + (0.080)^2} = \sqrt{0.0318} \approx \mathbf{0.178}^\circ\text{C} \tag{25}$$

For a standard 95% coverage interval (using a coverage factor $k \approx 2$), the expanded uncertainty is $U = 2 \cdot u_c = \pm\mathbf{0.36}^\circ$C. Thus, our final reported reading is:

$$T = 22.40 \pm 0.36^\circ\text{C} \quad (k = 2,\ 95\%\ \text{confidence}) \tag{26}$$

This example illustrates the core power of error quantification: while the eye might read 22.4°C off the glass, scale resolution (u_{res}) dominates the error budget. If we need to achieve an accuracy finer than $\pm 0.2^\circ$C, investing in a better calibration bath will not help—we must physically reduce u_{res} by choosing a finer-bore stem or upgrading to a digital transducer. With this unified uncertainty metric $u_c(T)$ in hand, we can now proceed to study how such errors propagate through governing physical equations.

OK this is great for single quantity but what about for composed mechanical variables as those in section 1.2.2? How does an error in vertical displacement propagate to our strain computation? This is the domain of **Error Propagation**.

1.8.1 The Mathematical Framework of Uncertainty Propagation

Suppose you are calculating a final experimental quantity, f, which depends on several independently measured physical variables, $x, y, z, \ldots$. Each of these variables is recorded using a specific sensor that carries its own quantified uncertainty (δx, δy, δz, $\ldots$), which you obtained from calibration certificates or statistical noise analysis.

The calculated value is expressed as:

$$f = f(x, y, z, \ldots) \tag{27}$$

If the errors are small, independent, and random, they will not simply add up linearly. Because they are random, there is a strong statistical likelihood that an overestimate in variable x will be partially canceled out by an underestimate in variable y. To reflect this statistically, we use Taylor series expansions to derive the standard **variance formula**, propagating the errors in quadrature:

$$\delta f = \sqrt{\left(\frac{\partial f}{\partial x}\delta x\right)^2 + \left(\frac{\partial f}{\partial y}\delta y\right)^2 + \left(\frac{\partial f}{\partial z}\delta z\right)^2 + \dots} \tag{28}$$

where $\frac{\partial f}{\partial x}$ represents the partial derivative of the function with respect to x. This derivative acts as a sensitivity factor, telling you how heavily an error in that specific sensor scales into your final result.

1.8.2 A Classic Geomechanical Case: Void Ratio Calculation

Let us apply this fundamental equation to a concrete problem every geotechnical engineer faces: determining the initial **void ratio** (e) of a soil specimen. The void ratio represents the ratio of the volume of voids to the volume of solid soil skeletons:

$$e = \frac{V_v}{V_s} = \frac{V_{total} - V_s}{V_s} = \frac{V_{total} \cdot \rho_s}{m_s} - 1 \tag{29}$$

where V_{total} is the total volume of the cylindrical specimen (calculated from its measured diameter d and height h), ρ_s is the known grain density of the solid mineral particles, and m_s is the dry mass of the soil skeleton measured on a laboratory scale.

Let us expand the function completely:

$$e(d, h, m_s) = \left(\frac{\pi d^2 h}{4}\right)\frac{\rho_s}{m_s} - 1 \tag{30}$$

Assume we are testing a soft clay specimen. We use an electronic caliper to measure the dimensions and a laboratory balance to weigh the dry mass. Our instrumentation setup yields the following readings and absolute uncertainties:

- Specimen Diameter, $d = 50.00$ mm $\quad (\delta d = \pm 0.05$ mm$)$
- Specimen Height, $h = 100.00$ mm $\quad (\delta h = \pm 0.10$ mm$)$
- Soil Dry Mass, $m_s = 320.50$ g $\quad (\delta m_s = \pm 0.02$ g$)$
- Mineral Grain Density, $\rho_s = 2.65$ g/cm^3 $= 0.00265$ g/mm^3 (treated as an exact baseline constant for this analysis).

First, let us compute the baseline calculated value for the void ratio:

$$V_{total} = \frac{\pi \cdot (50.00)^2 \cdot 100.00}{4} = 196349.54 \text{ mm}^3$$

$$e = \frac{196349.54 \cdot 0.00265}{320.50} - 1 = 1.62348 - 1 = 0.6235$$

Now, to discover the error boundaries (δe) of our calculated void ratio, we must evaluate the partial derivatives of our function with respect to each independent measurement variable:

$$\frac{\partial e}{\partial d} = \frac{\pi d h \rho_s}{2 m_s} = \frac{\pi \cdot 50.00 \cdot 100.00 \cdot 0.00265}{2 \cdot 320.50} \approx 0.06494 \text{ mm}^{-1} \tag{31}$$

$$\frac{\partial e}{\partial h} = \frac{\pi d^2 \rho_s}{4 m_s} = \frac{\pi \cdot 50.00^2 \cdot 0.00265}{4 \cdot 320.50} \approx 0.01623 \text{ mm}^{-1} \tag{32}$$

$$\frac{\partial e}{\partial m_s} = -\frac{\pi d^2 h \rho_s}{4 m_s^2} = -\frac{196349.54 \cdot 0.00265}{(320.50)^2} \approx -0.005065 \text{ g}^{-1} \tag{33}$$

Now, we feed these sensitivities and our sensor uncertainties into our quadrature propagation formula:

$$\delta e = \sqrt{\left(\frac{\partial e}{\partial d}\delta d\right)^2 + \left(\frac{\partial e}{\partial h}\delta h\right)^2 + \left(\frac{\partial e}{\partial m_s}\delta m_s\right)^2} \tag{34}$$

Let us evaluate each individual error term under the square root to see which sensor is hurting us the most:

- Contribution from diameter error: $(0.06494 \cdot 0.05)^2 = (0.003247)^2 = 1.054 \times 10^{-5}$
- Contribution from height error: $(0.01623 \cdot 0.10)^2 = (0.001623)^2 = 2.634 \times 10^{-6}$
- Contribution from mass scale error: $(-0.005065 \cdot 0.02)^2 = (-0.000101)^2 = 1.026 \times 10^{-8}$

Summing these up and taking the square root:

$$\delta e = \sqrt{1.054 \times 10^{-5} + 2.634 \times 10^{-6} + 1.026 \times 10^{-8}} = \sqrt{1.318 \times 10^{-5}} \approx \pm 0.0036 \tag{35}$$

Our final reported void ratio is therefore:

$$e = 0.6235 \pm 0.0036 \tag{36}$$

Look closely at the individual error contributions under the radical. The contribution from our mass balance scale (10^{-8}) is completely negligible compared to our geometric measurement errors (10^{-5}). Why? Because the caliper can only resolve measurements down to a twentieth of a millimeter, while our laboratory balance is a highly precise device resolving fractions of a milligram.

As an experimentalist, this tells you exactly where your budget and labor should be spent. Buying a more expensive, high-precision mass balance will do absolutely nothing to improve the quality of this experiment. If you want to cut your error in half, you must find a more accurate way to measure the physical diameter of your specimen.

Now that we have established the foundational laws of metrology, electronic signal chains, and how to rigorously handle the errors that come with them, we can step away from abstract principles and examine the real-world hardware used in a typical geomechanics laboratory. In the following chapter, we will discover how LVDTs, potentiometers, strain gauges, and fluid transducers manipulate these laws to capture the behavior of deforming geomaterials.

2 Classical Measurement Instrumentation in Geomechanics

Modern geomechanical testing requires both precise execution of prescribed boundary stress-strain paths. This chapter examines the core sensing and actuation technologies that underpin laboratory testing apparatus. We begin by analyzing classical displacement and load transducers—evaluating linear variable differential transformers (LVDTs), linear potentiometers, bonded foil strain gauges suited for localized microstrain, and multi-axis load cells—focusing on compliance, thermal drift, and signal conditioning. On the actuation side, we contrast the open-loop operation and stalling vulnerabilities of digital stepper motors against the high-torque electrodynamics of continuous DC motors, comparing linear transmissions and fluidic pressure drives (e.g., high-pressure syringe pumps versus continuous peristaltic systems subject to hydraulic pulsation). Bridging sensing and actuation, we detail the architecture of Proportional-Integral-Derivative (PID) servocontrol.

Having established some elements of metrology, and analogical and digital readings, we can step into the laboratory and look at the physical hardware used to test earth materials. Geomechanics presents a uniquely challenging environment for instrumentation. We deal with multiphase materials—solid grains, water, and air—that undergo massive ranges of deformation, from the microscopic, pre-failure elastic straining of stiff rocks to the large, destructive, post-liquefaction flowing of soft soils.

To capture these phenomena, we rely on a classical suite of instruments designed to measure three core mechanical fields: displacement/strain, force, and fluid pressure. This section explores their inner workings.

2.1 Displacement and Strain Measurement

In geomechanics, displacement measurements are broadly split into macro-scale boundary movements (measured externally on the specimen or loading piston) and localized, material deformations (measured locally on the specimen).

2.1.1 Linear Potentiometers

The linear potentiometer is one of the oldest and most intuitively simple electromechanical transducers. It is a direct-contact sensor designed to measure medium-to-

large boundary displacements, such as the vertical axial settlement of a soil specimen in an oedometer or triaxial cell.

1. Mechanical and Electrical Operation The internal architecture of a linear potentiometer (Fig. 3)consists of a stable, uniform resistive track (typically made of conductive plastic or wire-wound elements) and a moving conductive wiper brush attached to an external actuating rod.

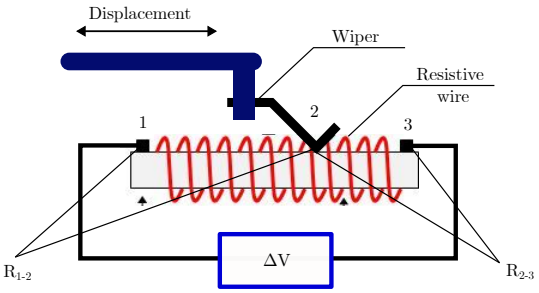


Figure 3: Schematics of a linear potentiometer.

Electrically, the device functions as a variable three-terminal voltage divider. A stable direct current voltage (V_{in}) is applied across the two fixed outer boundaries of the resistive track (Terminal 1 and Terminal 3). The moving wiper brush (Terminal 2) taps into the track at an intermediary position, picking up a local electrical potential. The underlying fundamental law is Ohm's Law combined with the linear geometric distribution of electrical resistance along a uniform path:

$$R_{total} = R_{1-2} + R_{2-3} \tag{37}$$

Assuming the resistive track has a perfectly uniform cross-sectional area and material composition, the resistance from the start of the track to the wiper position (R_{1-2}) scales linearly with the wiper's physical displacement (x) relative to the total electrical stroke length (L):

$$R_{1-2}(x) = R_{total}\left(\frac{x}{L}\right) \tag{38}$$

When connected to an infinite-impedance voltmeter or amplifier channel reading the output voltage (V_{out}) at Terminal 2, zero current flows through the wiper brush. The output voltage simplifies to:

$$V_{out} = V_{in}\left(\frac{R_{1-2}(x)}{R_{total}}\right) = V_{in}\left(\frac{x}{L}\right) \tag{39}$$

By rearranging this equation, we find our direct geometric link:

$$x = L \cdot \left(\frac{V_{out}}{V_{in}}\right) \tag{40}$$

2. Advantages, Disadvantages, and Failure Modes Linear potentiometers are highly favored in industrial testing because they are inexpensive, robust, simple to diagnose, and capable of operating on simple DC power supplies without complex external signal conditioning. Furthermore, they provide a massive dynamic range; a single potentiometer can easily measure strokes spanning from few mm to tens of cm.

However, potentiometers possess a critical flaw for high-precision geomechanics: they are **contact mechanical devices**. The wiper brush must physically rub against the resistive track. This introduces two severe limitations:

- **Mechanical Friction and Spring Force:** The wiper drag exerts a small but finite mechanical resistance on the actuating rod. If you are testing an extremely soft, unconfined clay or a fragile gel, the physical force required to push the potentiometer's internal spring and overcome wiper friction can alter or restrict the specimen's unhindered deformation.
- **Wear and Electrical Noise:** Over thousands of cycles, the physical rubbing scoring the track generates microscopic debris. This debris accumulates, causing the wiper to briefly lift off or lose electrical contact. On your data logging screen, this manifests as sudden, chaotic voltage spikes—mechanical scratching resulting in spurious, sudden displacement steps.

2.1.2 Linear Variable Differential Transformers (LVDTs)

To eliminate the vulnerabilities of physical contact, high-precision laboratory testing relies heavily on the **Linear Variable Differential Transformer (LVDT)**, Fig. 4. The LVDT is an electromagnetic transducer that replaces mechanical contact with magnetic coupling.

1. Internal Mechanical Architecture An LVDT consists of two separate, non-contacting assemblies: a hollow, rigid cylindrical stator housing and a solid, moving ferromagnetic core. The stator housing contains three precisely aligned electrical coils wrapped around a central tube:

- A single **Primary Coil** positioned in the middle, along the axial length.
- Two identical **Secondary Coils** (S_1 and S_2) wound symmetrically on either side of the primary coil.

The moving core is a highly permeable ferromagnetic rod attached to an unmagnetized actuating stem. This core slides freely inside the hollow center of the stator tube without physically touching the internal walls or the electrical coils, creating a completely frictionless mechanical action.

2. Electromagnetic Operation and Signal Chains The LVDT operates entirely on the principles of Faraday's Law of Induction and alternating current (AC) magnetic circuits. The primary coil is driven by an external AC excitation voltage (V_{pri}),

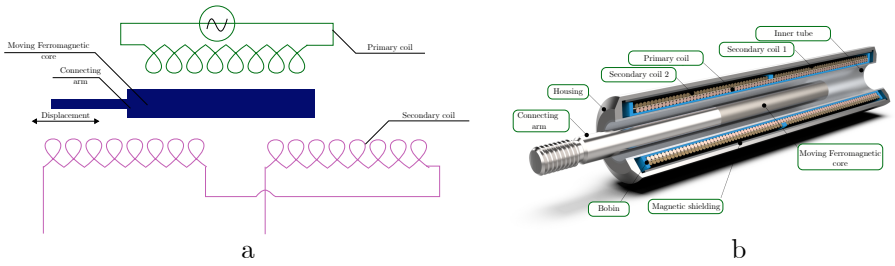


Figure 4: Schematics of a Linear Variable Differential Transformers in 2D(a) and 3D(b).

typically oscillating at a frequency between 1 kHz and 10 kHz:

$$V_{pri}(t) = V_0 \sin(\omega t) \tag{41}$$

This alternating current generates a continuous, fluctuating axial magnetic field inside the tube. The moving ferromagnetic core acts as a highly efficient conduit, capturing this magnetic flux and inductive-coupling it into the surrounding secondary coils (S_1 and S_2). This flux induces alternating voltages across both secondary windings (V_{s1} and V_{s2}).

The two secondary coils are wired together in a **series-opposing configuration**. This means their electrical polarities are inverted, and the total differential output voltage (V_{out}) delivered to the data acquisition system is the absolute subtraction of the two individual signals:

$$V_{out}(t) = V_{s1}(t) - V_{s2}(t) \tag{42}$$

Let us analyze the spatial mechanics of the core's position (x) relative to the center of the device:

- **The Null Position ($x = 0$):** When the core is positioned precisely at the geometric center of the stator, it bridges the primary coil to both secondary coils evenly. The magnetic flux coupled into S_1 is identical to the flux coupled into S_2. Therefore, $V_{s1}(t) = V_{s2}(t)$, and the series-opposing wiring causes the signals to perfectly cancel out:

$$V_{out}(t) = 0 \text{ V} \tag{43}$$

- **Positive Displacement ($x > 0$):** When the core moves upward toward secondary coil S_1, more ferromagnetic mass enters S_1's zone, increasing its magnetic coupling efficiency. Conversely, the core withdraws from S_2, dropping its coupling. Consequently, V_{s1} grows while V_{s2} shrinks, generating a net differential AC voltage wave that is perfectly in-phase with the primary excitation signal.

- **Negative Displacement ($x < 0$):** When the core slides downward toward S_2, the inverse occurs: $V_{s2} > V_{s1}$. The subtraction yields a net differential AC voltage wave that has an identical amplitude to the positive displacement, but its electrical phase is shifted by exactly 180° relative to the primary wave.

To turn these raw AC waveforms into a digital displacement metric, the signal must pass through a conditioning circuit called a **phase-sensitive demodulator**. This circuit tracks both the amplitude of V_{out} (to determine the absolute distance from null) and its phase angle relative to the primary excitation wave (to determine the direction of movement, positive or negative), outputting a smooth, linear DC voltage proportional to displacement.

3. Performance Characteristics in Geomechanics The LVDT is the gold standard for tracking small-strain soil behavior due to its excellent performance properties:

- **Infinite Resolution:** Because there are no discrete steps, wires, or digital bits inside the physical sensor mechanism, the analog magnetic coupling resolution is theoretically infinite. It is bounded entirely by the electronic noise floor of your external amplifier and the bit depth of your analog to digital converter.
- **Frictionless and Non-Destructive:** The lack of physical contact means the sensor exerts zero mechanical resistance on the soil sample, eliminating structural disturbance. Furthermore, if a soil sample undergoes a sudden catastrophic shear failure, the core simply slides violently through the open tube without grinding or destroying any internal mechanical parts.
- **Submersible Capability:** LVDTs can be constructed with specialized enclosures. This allows them to be submerged directly inside high-pressure triaxial water cells (*internal LVDTs*), mounting straight to the specimen's membrane. This eliminates the errors introduced by piston compliance, seal friction, and top-cap tilting that plague external measurements.

The primary trade-off is complexity: LVDTs require expensive AC carrier amplifiers, careful shielding against ambient magnetic fields compared to potentiometers.

2.1.3 Electrical Resistance Strain Gauges

While potentiometers and LVDTs excel at tracking macro-level boundary movements, they cannot capture the localized, micro-scale internal straining of intact rock specimens or structural elements (such as pile walls). For this, we turn to the **bonded foil strain gauge**.

1. The Law of Piezoresistivity and Piezometric Expansion A strain gauge is an ultra-thin, flexible backing material (usually polyimide) supporting a precisely etched, serpentine grid of ultra-fine metallic foil (such as constantan alloy). The gauge is glued directly onto the clean surface of the test specimen using a high-stiffness adhesive (like

cyanoacrylate or epoxy). As the material beneath deforms, the strain is transferred perfectly through the adhesive layer into the foil grid.

The underlying physics combines basic geometry with the law of **piezoresistivity**. Consider a long, straight electrical wire with an initial length l, cross-sectional area A, and material resistivity ρ. Its baseline electrical resistance is:

$$R = \rho \frac{l}{A} \tag{44}$$

When the rock specimen experiences tensile axial strain ($\epsilon = \Delta l/l$), the foil wire stretches, increasing its length to $l + \Delta l$. Concurrently, due to Poisson's ratio (ν_{foil}), the wire's cross-section laterally contracts, shrinking A. Finally, the physical stretching distorts the crystal lattice of the metal alloy, altering its baseline electronic resistivity ($\Delta\rho$). Differentiating the resistance equation yields:

$$\frac{\Delta R}{R} = \frac{\Delta l}{l} - \frac{\Delta A}{A} + \frac{\Delta \rho}{\rho} \tag{45}$$

By substituting the volumetric geometric relations of mechanical strain, we can condense this entire physical multi-stage relationship into a singular, simple metrological scaling constant known as the **Gauge Factor** (GF):

$$\frac{\Delta R}{R} = GF \cdot \epsilon \tag{46}$$

For standard commercial constantan foil gauges, the Gauge Factor is highly stable and typically equals approximately 2.0. This means that if a rock sample experiences a structural strain of $\epsilon = 1000\ \mu\epsilon$ (0.1% deformation), the fractional change in its electrical resistance ($\Delta R/R$) will be exactly 0.002, or 0.2%.

2. The Quarter-Bridge Circuit and Environmental Compensation Because a 0.2% change in resistance is incredibly small, a standard 120Ω strain gauge will only shift by 0.24Ω. To resolve this, the strain gauge must be integrated into the **Wheatstone Bridge** circuit derived in section 1.6.1.

When using a single active strain gauge glued to a specimen, we build a **Quarter-Bridge** network. While highly sensitive to strain, the quarter-bridge possesses a vulnerability: **thermal drift**. The electrical resistance of metal foil changes drastically with shifting temperature due to its thermal coefficient of resistance, completely independent of mechanical strain. If the lab's air conditioning cycles during a long, week-to-month shear test, the bridge will register a large resistance shift, fabricating a completely false strain reading.

To eliminate this systematic environmental error, experimentalists sometimes use a technique called **temperature compensation** via a **Half-Bridge configuration**.

In a half-bridge setup, we introduce a second, identical strain gauge called the **Dummy Gauge** (R_D). This dummy gauge is glued to an identical, unstressed block of the same material and placed immediately adjacent to our active specimen gauge (R_A) so it experiences the exact same thermal environment. We wire the active gauge into Arm 3 of the bridge, and the dummy gauge into Arm 4. Let us look at how the mathematics handles this layout:

$$V_{out} = V_{in} \left(\frac{R_A}{R_A + R_D} - \frac{R_2}{R_1 + R_2} \right) \tag{47}$$

When the temperature shifts by ΔT, both gauges experience an identical thermal resistance bump ($\Delta R_{thermal}$). Simultaneously, the mechanical stress induces an additional resistance change (ΔR_{mech}) strictly within the active gauge. Our terms become:

$$R_A = R + \Delta R_{thermal} + \Delta R_{mech} \tag{48}$$

$$R_D = R + \Delta R_{thermal} \tag{49}$$

Substituting these back into the bridge equation causes the thermal error terms to completely cancel out in the numerator and denominator. The output voltage remains purely a function of ΔR_{mech}. By taking this a step further and placing active gauges on opposite sides of a bending column, you can create a **Full-Bridge configuration**, which actively multiplies your mechanical signal output by four while maintaining perfect thermal cancellation.

2.2 Force Measurement: Load Cells

To link these measured strains to structural stresses, we require force sensors. In geomechanics, the primary device used is the internal or external electronic **Load Cell**.

1. Architectural Design and Mechanical Elements A load cell is essentially a structural spring optimized to measure mechanical force indirectly by measuring strain. Its internal architecture consists of a high-strength, elastic metallic block (typically structural tool steel or high-tensile aircraft aluminum) machined into a specific geometric shape. Common geometries include:

- **Solid Columns:** Ideal for high-capacity applications (50 kN to 1000 kN), where axial compression is measured.
- **S-Beams and Ring Cantilevers:** Designed for lower capacities (10N to 10kN), where the force induces localized bending or shear deformation along an engineered thin web as the one in Fig. 5a.

The elastic metal block is instrumented with four active strain gauges configured into a perfect **Full-Bridge circuit**. The gauges are aligned precisely along the principal stress directions of the element. For a compressive column load cell, two gauges are

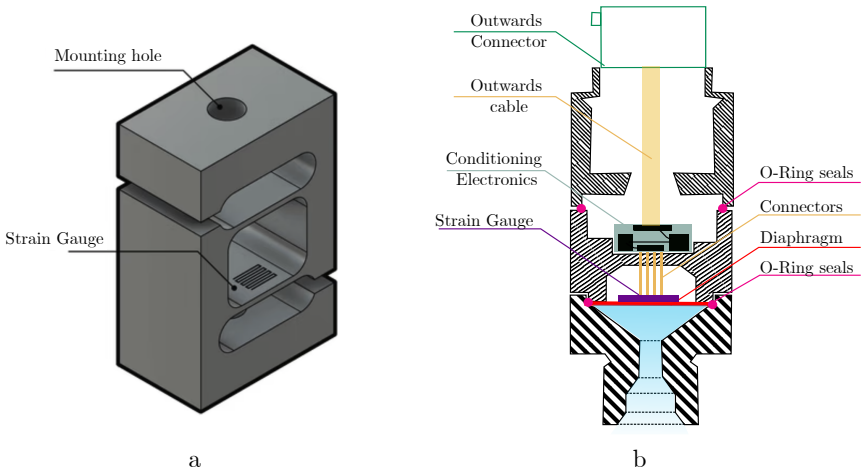


Figure 5: Schematics of a S-beam load cell (a) and of a pressure probe (b).

aligned vertically along the axial compression axis to capture maximum compressive strain ($-\epsilon_a$), while the remaining two gauges are aligned horizontally to capture tensile lateral expansion ($+\nu \cdot \epsilon_a$) due to Poisson's effect.

2. Electrical Output and Sensitivity Scales When an axial force (F) is applied down the loading piston, the metal block deforms elastically according to Hooke's Law:

$$\epsilon_a = \frac{\sigma}{E} = \frac{F}{A \cdot E} \tag{50}$$

where A is the cross-sectional area of the column and E is the Young's Modulus of the metal.

Because the gauges are arranged in a full-bridge configuration where alternating arms experience opposing tensile and compressive strains, their individual fractional resistance steps accumulate constructively. The resulting bridge output voltage scales as:

$$V_{out} = V_{in} \cdot GF \cdot \epsilon_a \cdot (1 + \nu) \tag{51}$$

Substituting our Hooke's Law relation into this equation exposes our complete indirect measurement:

$$V_{out} = \left[\frac{V_{in} \cdot GF \cdot (1 + \nu)}{A \cdot E}\right] \cdot F \tag{52}$$

The terms grouped inside the brackets represent a constant value determined entirely by the geometry, physics, and electronics of the load cell assembly. This constant is

the device's **Sensitivity Factor**. Load cell manufacturers traditionally normalize this value on calibration certificates and express it in units of millivolts of output per volt of input excitation at maximum rated capacity (mV/V). A standard laboratory load cell typically yields a full-scale sensitivity of 2.0 mV/V.

2.3 Fluid Pressure Measurement: Pressure Transducers

Geomechanics is fundamentally dictated by Terzaghi's Principle of Effective Stress: the macroscopic engineering behavior of a soil mass is controlled not by total applied external stresses, but by the difference between total stress (σ) and the internal pore fluid pressure (u) as $\sigma' = \sigma - u$

To track this hidden internal pressure field, we utilize specialized electronic **Pressure Transducers**.

1. Diaphragm Mechanics and Piezoresistive Sensing A modern geotechnical pressure transducer consists of a solid, heavy-walled steel housing containing a thin, flexible, circular metallic sensing diaphragm (Fig. 5b). One face of this diaphragm is exposed to a sealed internal reference chamber (either evacuated to an absolute vacuum or vented to atmospheric pressure), while the opposing face is exposed to the laboratory fluid line or internal pore water.

When the pore fluid pressure (u) increases, it pushes against the exposed face, causing the thin circular diaphragm to bend and bow outward like a flexed structural plate. The mechanical deflection of the diaphragm induces high tensile strains near its clamped edges, and high compressive strains near its geometric center.

To capture this bending, a miniature piezoresistive silicon chip or a set of four metal foil strain gauges is bonded directly onto the dry, protected reference face of the diaphragm. These gauges are wired into a full-bridge array, converting the local structural bending into a linear voltage signal.

2. The Crucial Role of High-Air-Entry Porous Stones In geotechnical testing, a pressure transducer cannot simply be dropped raw into a saturated soil sample. If a clay specimen shears, the solid soil skeleton will press directly against the steel housing, introducing mechanical total contact forces that compromise the fluid pressure reading. Furthermore, soil lines frequently contain dissolved air bubbles.

To isolate the fluid phase from the solid skeleton, pressure transducers must always be coupled to the soil via a **Porous Stone** or a **High-Air-Entry Value Ceramic Filter**.

The porous stone acts as a rigid mechanical shield. Its pore channels are small enough to completely block solid soil grains from passing through and contacting the transducer diaphragm, yet large enough to allow pore water to flow freely across the boundary. This ensures that the water inside the transducer's internal cavity achieves perfect hydraulic equilibrium with the water inside the soil mass.

2.4 Summary of Geomechanical Sensing Technologies

To conclude our overview of laboratory instrumentation, Table 3 provides a summary of the classical transducers analyzed in this section, mapping their physical metrics, underlying laws, and operational boundaries.

Table 3: Comparative Matrix of Classical Geomechanical Sensors

Sensor Type	Measured Quantity	Core Governing Physical Law	Primary Operational Constraint
Linear Potentiometer	Displacement	Linear resistance variation via Ohm's Law	Mechanical friction and physical track wear
LVDT	Displacement	Faraday's Law of Induction via AC coupling	Requires complex AC phase demodulation
Strain Gauge	Local Strain	Piezoresistivity ($\Delta R/R = GF \cdot \epsilon$)	Highly vulnerable to thermal drift
Load Cell	Force	Elastic Hooke's Law combined with Full-Bridge strain	Sensitivity vs. Capacity structural sizing trade-off
Pressure Transducer	Fluid Pressure	Circular diaphragm bending via piezoresistance	Requires strict hydraulic saturation and filtering

Now that we have unpacked the internal electronics and mechanical operations of these point-sensors, we must confront their ultimate limitation: they are single-point measures. A load cell tells you the average total force on a boundary; a strain gauge tells you the strain along a single millimeter of material. However, real soil masses fail along localized, chaotic internal shear bands and complex fracture paths.

3 Action! Actuators, Motors, and Fluidic Drives

Experimental geomechanics is not a passive science; it is fundamentally about "breaking things". To map the constitutive behavior of a soil mass or a rock core, we must actively disturb its state of equilibrium. We compress columns, shear boxes, and inject pore fluids at high pressures. In the previous sections, we analyzed how to look at the material using sensors. In this section, we examine the action part: the electromechanical and fluidic **actuators** that execute these disturbances.

When designing or operating an experimental rig, your choice of actuation determines how precisely you can control either the boundary displacement rate (strain control) or the applied boundary force (stress control). We will dissect the inner workings, internal kinematics, and specific limitations of the motors and pumps that drive modern

testing cells.

3.1 Electromechanical Motors: Stepper vs. DC Motors

Nearly all modern computer-controlled loading frames rely on rotary electric motors to drive a mechanical screw or gear train, transforming rotational torque into linear axial movement and force. To understand how we control these systems, we must first look at the basic physics of how they move.

3.1.1 Stepper Motors: Discrete Open-Loop Rotations

A stepper motor is a synchronous electric motor that divides a full 360° mechanical rotation into a large number of discrete, equal angular increments known as **steps**.

1. Internal Mechanics and Stepping Operation As show in Fig. 6 the internal architecture consists of a central, multi-toothed permanent magnet or iron rotor surrounded by an electromagnets: temporary magnets produced by electric current flowing through a coiled wire, wrapped around a metal core. This phenomenon can be described through Maxwell's equations. The stator ring contains several independent phase coils that can be activated independently.

When a direct current flows through a specific stator coil, it generates a localized magnetic field. The teeth of the permanent magnet rotor are physically pulled into alignment with this active magnetic pole (Fig. 6a). Unlike DC motors (detailed in the next section) that spins continuously under a steady voltage, a stepper motor remains completely frozen in place as long as that single coil remains energized. To make the motor turn, an external electronic **driver** must sequentially switch the power off from the current coil and flash it onto the adjacent phase coil. The magnetic field rotates by a fixed angle, pulling the rotor along with it and making a motor rotate by "a step".

The fundamental law governing its movement is purely geometric and structural:

$$\theta_{step} = \frac{360^\circ}{N_s} \tag{53}$$

where N_s is the number of structural steps built into the motor hardware. A standard industrial stepper motor has 200 rotor teeth, yielding an exact mechanical step angle of:

$$\theta_{step} = \frac{360^\circ}{200} = 1.8^\circ \text{ per step} \tag{54}$$

By chaining together thousands of these discrete digital pulses, the stepper driver can control the total angular displacement purely by counting pulses. The speed is essentially determined in the pause between subsequent steps with a lower boundary (of the delay) determined by the time taken by the system to actually perform the rotation. If you send 200 pulses, the shaft completes exactly one rotation. Because the computer implicitly trusts that the motor moves on every pulse without verifying it using

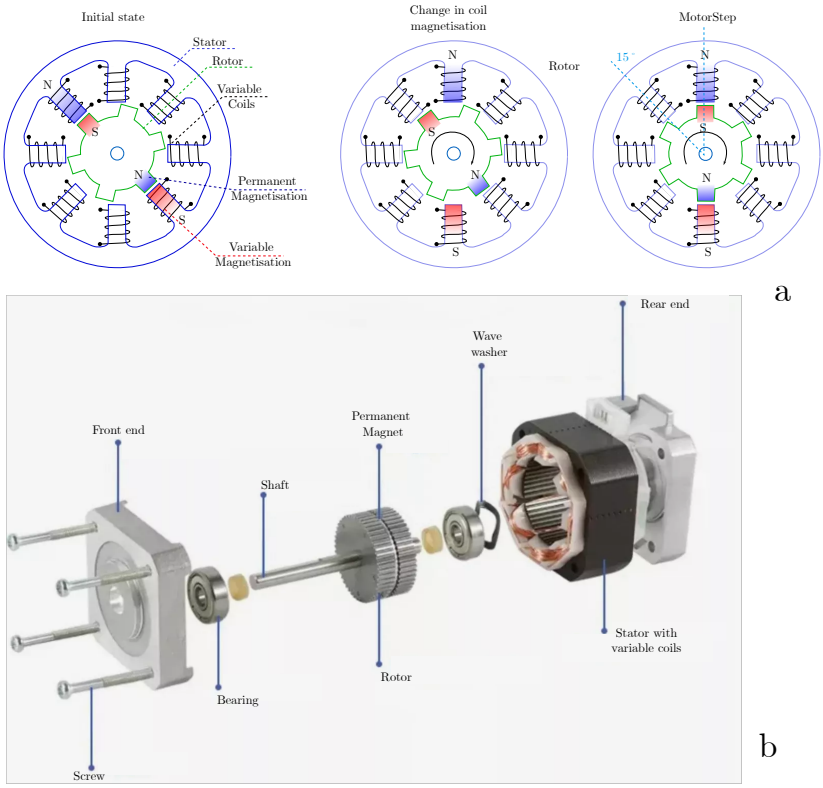


Figure 6: Schematics of a Stepper motor (a) and 3D view (b).

an external sensor, this is known as **open-loop control**. It should be noted that there are strategies to further subdivide the step in sub-steps, by energizing adjacent coils equally (half-step) or asymmetrically (quart-steps and so on).

2. The Issue for Geomechanics: Stall and Lost Steps In geomechanics, we frequently run displacement-controlled shear tests at ultra-slow rates (e.g., 0.001 mm/min) for example to allow pore pressures to dissipate. Stepper motors coupled to high-reduction gearboxes excel at this because they can hold a rock frame perfectly static or step it forward at a very predictable rate.

However, stepper motors have a critical operational vulnerability: **stalling and lost steps**. The torque profile of a stepper motor drops off drastically as its rotational speed increases. More importantly, the motor's hold on its current step position is entirely magnetic. If for example a rock joint locks up, the external mechanical resistance torque (T_{ext}) might exceed the maximum magnetic holding torque (T_{hold}) of the energized stator phase.

When $T_{ext} > T_{hold}$, the rotor slips backward out of magnetic alignment. Because the system is operating open-loop, the microcomputer has no idea a slip occurred. The driver will continue to send digital pulses, blindly assuming the frame is moving forward, while your load frame is completely stalled. Your data log will record a flat displacement line while your software plots false steps.

3.1.2 DC Motors: Continuous Electrodynamic Torque

To overcome the speed boundaries and stall vulnerabilities of stepper motors, high-capacity loading frames turn to **Direct Current (DC) Motors**.

1. Direct Current Motor Mechanics A classical brushed DC motor operates fundamentally on the **Lorentz Force Law**: when a current-carrying conductor coil (the armature or rotor) is placed inside a fixed magnetic field (generated by permanent stator magnets surrounding the housing), the moving electrical charges experience a physical lateral force, as schematized in Fig 7a.

Because the coil is mounted on a central axle, these forces generate a continuous mechanical torque:

$$\tau = K_m \cdot I \tag{55}$$

where I is the electrical current pumped through the windings and K_m is the motor's structural torque constant. Rather than jumping between discrete magnetic teeth, a DC motor spins perfectly smoothly and continuously as long as electricity flows through it. The speed of rotation is directly proportional to the applied voltage (V).

2. The Feedback Necessity A DC motor by itself has no obvious way of controlling displacement. It cannot hold a position, and it cannot maintain a precise slow speed under changing mechanical loads. If the soil sample resists, the motor can slow down and even stop; if the sample yields or liquefies, the motor may violently move forward.

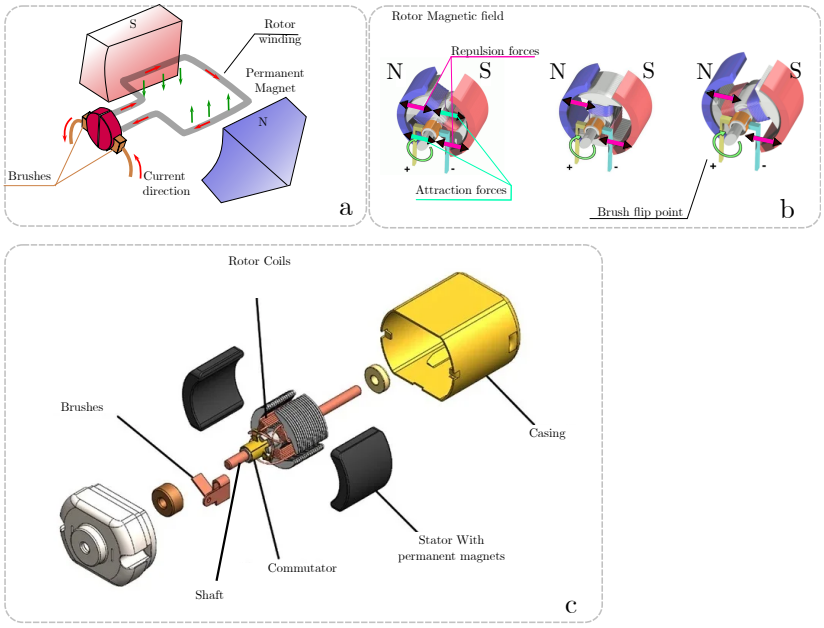


Figure 7: Direct Current (DC) motor: working principle (a) depiction of half a spin, until the magnets are aligned at which point the brushes flip and the current spins in the opposite direction restarting the cycle and (c) 3D scheme.

To turn this continuous, smooth power into a precise laboratory actuator, we do not rely on counting predefined physical steps. Instead, we must couple the motor to a real-time tracking sensor (as the ones we detailed above for example) and govern its voltage using a dynamic control system as detailed in section 3.4. This architecture allows us to precisely dictate displacements, velocities, or forces—even when the motor has no inherent step geometry—by entering the domain of **Servocontrol**, which we will formally explore in a dedicated section below.

3.2 Linear Actuators

To transform the rotary motions of these stepper or DC motors into linear forces required to apply strain to a geomechanical specimen, we channel the torque through a mechanical transmission called a **Linear Actuator**.

The core of a mechanical linear actuator is a precision-machined threaded rod passing through a mating nut assembly as shown in Fig. 8. There are two primary standards used in laboratory engineering:

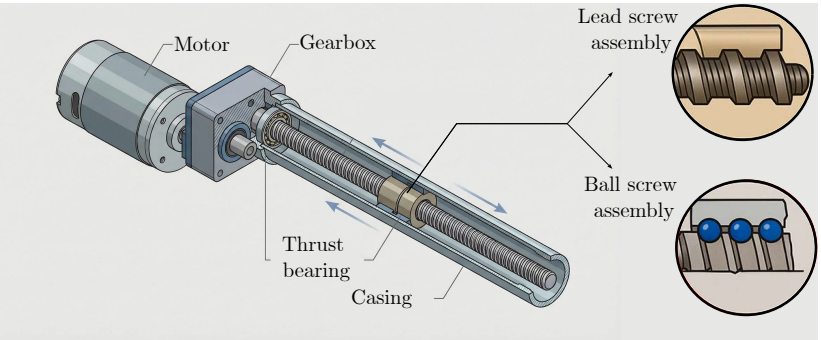


Figure 8: Scheme of a linear actuator with schematics for lead screw and ball screw assemblies.

- **Lead Screws:** These rely on direct sliding friction between the male metal screw threads and a female nut as the one in Fig. 8 top. While inexpensive and often self-locking (preventing the actuator from back-driving when power is cut), they suffer from high internal friction, slow speed limits, and mechanical **backlash**—a tiny dead-zone of play when reversing the direction of travel.
- **Ball Screws:** These replace sliding friction with rolling friction. The nut contains an internal recirculating loop of hardened steel ball bearings (in Fig. 8 bottom) that roll smoothly through the helical grooves of the screw shaft. Ball screws operate at over 90% mechanical efficiency, eliminate backlash completely, and can seamlessly translate low motor torques into higher linear forces (100 kN$+$), making them the gold standard for high-stiffness rock testing machines.

3.3 Fluidic Actuators: Pumps for Pore Pressure Control

Geomechanics requires precise control over fluid volume and fluid pressure inside the specimen's pores. To inject water, gas, or oil into triaxial cells at highly controlled rates, we often rely on two types fluid pump architectures (among the several existing ones).

3.3.1 Syringe Pumps: The Precision Standard

A **Syringe Pump** (or continuous volumetric piston pump) is a displacement device designed for ultra-high-pressure precision fluid control and which can reach pressures of the order of hundreds of MPa.

1. Internal Mechanics and Control As shown in Fig. 9a, this pump consists of cylinder barrel housing a ground, precision-sealed internal piston plunger. The rear of the piston plunger is rigidly attached to a screw linear actuator driven by a high-torque stepper or servo motor.

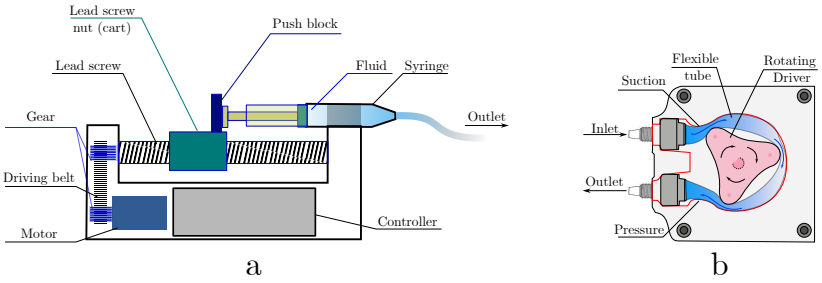


Figure 9: Schematics of a Syringe pump (a) and of a peristaltic Pump (b).

The underlying fundamental law is basic volumetric translation: the volume of fluid displaced (ΔV) is simply the linear travel of the piston (Δx) multiplied by the known cross-sectional area of the cylinder bore (A_{bore}):

$$\Delta V = A_{bore} \cdot \Delta x = A_{bore} \cdot \left(\frac{\theta_{motor}}{360^\circ} \cdot p_{screw} \right) \tag{56}$$

where p_{screw} is the pitch of the ball screw drive.

By measuring the pressure inside the fluid chamber or at the application using a pressure transducer (section 2.3), a digital controller can dynamically adjust the motor's rotation to operate the pump in two distinct control modes:

- **Constant Flow-Rate Mode (dV/dt = constant):** The motor turns at a fixed, immutable speed, injecting fluid into the soil pores at an exact volumetric rate. This is critical for measuring the hydraulic conductivity (permeability) of a clay specimen.

- **Constant Pressure Mode (u = constant):** The controller monitors the fluid pressure transducer. If the pore pressure inside the soil tries to drop due to dilatancy, the motor instantly advances the piston to maintain a perfectly stable, constant boundary pressure. This is essential for simulating groundwater states during long-term consolidation.

The main limitation of a syringe pump is its **finite reservoir capacity**. Once the piston reaches the end of its physical cylinder stroke, the pump must stop, isolate itself from the testing cell using high-pressure valves, and execute a refill cycle, temporarily disrupting continuous flow tests.

3.3.2 Peristaltic Pumps: High Volumetric Flow

When an experiment demands continuous, infinite fluid flow at relatively low pressures—such as simulating long-term internal erosion, piping, or chemical leaching flushing through a large permeameter cell—the finite limits of a syringe pump can be impractical. Instead, we utilize a **Peristaltic Pump** .

1. Mechanical Mechanism A peristaltic pump is a positive-displacement rotary pump that isolates the fluid completely from any moving mechanical parts. The fluid remains trapped inside a flexible, elastic tube looped inside a circular pump casing, as shown in Fig. 9b.

The mechanism relies on a central rotating rotor assembly instrumented with two or more protruding rollers or shoes. As the motor turns the rotor, the rollers press hard against the flexible tubing, completely pinching the tube closed against the outer casing wall. This pinched zone creates a local seal. As the roller travels along the arc of the tube, it physically pushes the trapped pocket of fluid forward ahead of it. When the roller exits the tube arc, the natural elastic spring-back of the tube material causes it to pop open, generating a strong vacuum that draws fresh fluid into the intake side.

2. Metrological Weaknesses: The Pulsation Problem Peristaltic pumps offer massive advantages for environmental geomechanics: because the fluid never touches metal rollers or valves, you can pump highly corrosive chemical brines, acidic contaminants, or muddy, abrasive soil-silt slurries without scratching or corroding your machinery.

However, from a precise metrological perspective, peristaltic pumps possess an architectural drawback: **flow pulsation**. As a roller reaches the end of the circular casing track and lifts off the tubing to return to the start, the pinched zone suddenly opens up. For a fraction of a second, fluid rushes backward into the newly expanded space before the next roller can lock down.

This mechanical transition generates a marked rhythmic fluctuation in fluid velocity and fluid pressure. If you wire a peristaltic pump directly into a delicate triaxial soil specimen, these pressure spikes can become bothersome. To use these pumps safely

in geomechanics, experimentalists might need to integrate inline hydraulic dampeners—such as compliant fluid expansion bladders—to mechanically absorb and smooth out the pulsations before they reach the material core.

3.4 Actuator and Motor Selection Matrix

To conclude this module, Table 4 provides an engineering selection matrix, mapping our primary actuators against their optimal mechanical roles and operational limitations in the laboratory environment.

Table 4: Operational Matrix of Geomechanical Actuators

Actuator Type	Primary Mode	Key Strength	Critical Boundary Limit
Stepper Motor	Open-Loop Rotary	Highly precise discrete angular control at low speeds	Prone to unrecorded structural stalling and lost steps
DC Motor	Continuous Rotary	High-torque, smooth continuous force generation	Requires external sensor feedback loop to behave precisely
Syringe Pump	Positive Fluid Piston	Ultra-high pressure stability; perfect flow control	Capped by finite fluid reservoir volume capacity
Peristaltic Pump	Flexible Tube Roller	Contaminant/slurry immune; infinite flow capability	Generates severe rhythmic hydraulic pressure pulses

4 The Core of Servocontrol: The PID Loop

As we discovered in our motor analysis, while a stepper motor can run blindly in an open-loop configuration, it is highly prone to unrecorded structural stalling. A DC motor, on the other hand, provides smoother force but has no native "geometric awareness". To run a modern geotechnical laboratory—where we must maintain a perfectly constant pore pressure while a sample shears, or cycle an axial load cell along a complex sinusoidal seismic path—we must cross completely into the domain of **Servocontrol**.

A servocontrol system is a closed-loop architecture where an actuator's input is dynamically adjusted in real-time based on sensor data. It allows us to control complex experimental fields (like force or fluid pressure) by constantly reading the error between what we want and what is actually happening. The universal mathematical brain behind this real-time adaptation is the **Proportional-Integral-Derivative (PID) controller**.

4.1 The Anatomy of the PID Equation

Imagine you are controlling a triaxial cell, and you command the system to maintain a constant target axial load of 10 kN (the **Setpoint**, SP). At any given millisecond t, the load cell reads an actual force of 9.2 kN (the **Process Variable**, PV).

The controller's first job is to calculate the absolute system **Error** ($e(t)$):

$$e(t) = SP - PV(t) \tag{57}$$

In this instance, $e(t) = 10\,\text{kN} - 9.2\,\text{kN} = +0.8\,\text{kN}$. The PID controller evaluates this error through three separate mathematical metrics simultaneously to compute the required control output voltage ($u(t)$) sent to the motor driver:

$$u(t) = K_p\, e(t) + K_i \int_0^t e(\tau)\, d\tau + K_d \frac{de(t)}{dt} \tag{58}$$

Let us dissect what each of these three terms physically represents to an experimentalist.

4.1.1 The Proportional Term (K_p): The Present

The Proportional term acts as the immediate muscle of the controller. It multiplies the current error by a fixed tuning gain K_p. If the error is large, the controller delivers a high voltage correction to push the motor harder. If the error shrinks to a tiny fraction, the proportional push relaxes.

The fatal flaw of a purely proportional controller (P-only) is **steady-state error**. Imagine your load frame requires a baseline electrical current just to overcome internal fluid seal friction and compress the cell's top piston. As the actual force approaches the target, the error $e(t)$ approaches zero. Because the error is nearly zero,

the proportional output ($K_p \cdot e$) drops to zero. The motor stops pushing before it ever reaches the setpoint, leaving the system permanently stalled just below the target.

4.1.2 The Integral Term (K_i): The Past

To eliminate steady-state error, we introduce the Integral term. The integral component acts as the system's memory. It continuously sums up (integrates) the accumulation of error over time.

If the system stalls even 0.01 kN below the target for several seconds, the integral term accumulates that persistent small error over thousands of clock cycles. As the area under the error-time curve expands, the integral output grows larger and larger, steadily ratcheting up the voltage to the motor until it breaks through the seal friction and forces the system precisely onto the setpoint.

4.1.3 The Derivative Term (K_d): The Future

The Derivative term acts as an electronic brake. It looks at the rate of change of the error (de/dt).

If the integral and proportional terms are running full throttle to close a large gap, the system will gain massive momentum. As the process variable approaches the target at a high velocity, the derivative term detects that the error is rapidly collapsing (de/dt becomes highly negative). It subtracts a proportional voltage from the motor, damping its movement and braking the actuator smoothly so that it glides onto the target without crashing past it.

4.2 The Challenge of Geomechanical System Tuning

A PID controller is only as good as its tuning constants (K_p, K_i, K_d). In geomechanics, tuning is notoriously difficult because the physical properties of our material under test change drastically during the experiment itself.

Consider a triaxial compression test on a brittle, overconsolidated clay specimen controlled via an axial load cell:

- **Pre-Failure Stiff Behavior:** Before the clay shears, it behaves as a stiff elastic solid. A tiny forward micro-step of the motor piston yields a massive jump in force. In this domain, the system has a high mechanical gain. If your K_p tuning is set too high, the controller will violently over-correct, causing the motor to shake and oscillate wildly around the target.
- **Post-Failure Soft Behavior:** Once the clay reaches its peak strength and breaks along a localized shear band, its stiffness collapses to near zero. Now, the motor must plunge forward aggressively over large distances just to register a tiny increase in force. If you maintain the gentle tuning required for the elastic phase, the controller will become sluggish and completely fail to maintain the target stress path during yielding.

Some modern geotechnical testing systems resolve this by implementing **adaptive tuning profiles**, where the microchip dynamically scales the internal PID parameters based on the current material stiffness calculated by the strain sensors. Understanding these feedback systems ensures that when you see a perfectly flat pressure line or a smooth cyclic wave on your screen, you recognize it not as a static physical event, but as a continuous, high-speed computational battle waged by a silicon chip balancing the physical state of the earth sample.

Triaxial Testing of Geomaterials

Nadia Benahmed

INRAE, RECOVER, Aix Marseille University, France

This chapter provides an integrated overview of triaxial testing of soils and rocks, covering the complete experimental chain from specimen preparation and storage to testing, data reduction, and interpretation. Particular attention is given to specimen characterisation, experimental procedures, measurement corrections, interpretation of mechanical response, and good laboratory practice, with the objective of establishing a consistent framework for obtaining reliable, reproducible, and physically meaningful results.

1 Introduction

The triaxial test is one of the most versatile and widely used laboratory methods for characterising the mechanical and hydro-mechanical behaviour of geomaterials. By allowing the principal stresses, drainage conditions, stress path, and pore-water pressure to be controlled or measured, it provides a comprehensive framework for investigating stiffness, strength, volumetric behaviour, pore-pressure generation, and the evolution of effective stress. The test is therefore widely used both for the determination of engineering parameters and for the investigation and modelling of fundamental soil and rock behavior [BH62] [Lad16] [ISRM07].

The reliability of a triaxial test, however, depends on considerably more than the shearing stage itself. The measured response reflects the entire experimental chain, beginning with sampling or specimen preparation and continuing through storage, dimensional characterisation, installation, saturation, consolidation, shearing, measurement, data reduction, and interpretation. Each stage establishes conditions that influence those that follow, and uncertainties arising from measurement errors, specimen variability, or uncontrolled experimental variations may propagate through the test and ultimately affect the derived mechanical parameters. In particular, differences in initial density, fabric, water content, saturation, stress history, specimen geometry, or disturbance may produce substantial differences in the measured response even when nominally identical loading conditions are subsequently applied.

A rigorous triaxial testing programme must therefore combine careful specimen preparation with accurate dimensional measurements, appropriate control of stress and drainage conditions, reliable instrumentation, and consistent data-reduction procedures. The raw measurements obtained during testing cannot always be interpreted directly as intrinsic material behaviour since specimen geometry, membrane resistance, apparatus compliance, piston friction, hydraulic-system response, boundary conditions, and non-uniform deformation may influence the recorded quantities. The significance of these effects and the associated uncertainties on the material, stress level, drainage condition, loading rate, and strain range is great; appropriate corrections or experimental precautions must therefore be considered when interpreting the results.

This chapter presents an integrated framework for the execution and interpretation of triaxial tests on geomaterials. It first considers specimen preparation, handling, storage, and dimensional characterisation, with particular attention to the preservation or controlled establishment of the initial material state. The fundamental principles and experimental stages of conventional triaxial testing are then described, including initial stress application, saturation, consolidation, and shearing under drained and undrained conditions. The principal measurement corrections and system effects are subsequently examined before addressing the interpretation of stress-strain, volumetric, pore-pressure, and effective stress-path responses, together with the determination of peak, critical-state, and residual strength. Finally, the limitations of laboratory triaxial testing and the requirements of good laboratory practice are considered in order to establish a consistent basis for obtaining reliable, reproducible, and physically meaningful experimental results.

2 Specimen Preparation and Storage

2.1 Overview

Specimen preparation and storage constitute critical stages of any laboratory testing programme, as they directly influence the quality, reliability, and reproducibility of the measured mechanical and hydro-mechanical response. The preparation procedure establishes the initial state of the specimen, including its density, water content, degree of saturation, suction, fabric, stress history, and, where relevant, cementation and bonding. These initial characteristics strongly influence the subsequent stiffness, strength, compressibility, volumetric response, and deformation behaviour observed during testing [HE14] [Lad16].

Geomaterials are inherently heterogeneous and may be highly sensitive to disturbance. Sampling, transportation, trimming, preparation, handling, or storage can alter their fabric, bonding, and hydraulic condition, potentially introducing biases into the measured response and compromising the interpretation of experimental results. The selection of an appropriate preparation technique therefore depends on the material

under investigation (granular soil, cohesive soil, weak rock, or intact rock) as well as on the objectives of the experimental programme and the extent to which in-situ conditions need to be preserved or reproduced

After preparation, appropriate storage and transportation are required to limit further changes before testing. Specimens should be protected from moisture exchange, temperature variations, changes in suction or saturation, and mechanical disturbance. Maintaining controlled conditions throughout this period helps preserve specimen integrity and ensures that laboratory measurements remain representative and comparable across tests.

2.2 Importance of specimen preparation

Specimen preparation should not be regarded as a simple preliminary step to laboratory testing, but rather as a fundamental experimental variable that can significantly influence the measured response. In triaxial testing, for example, the observed behaviour is governed not only by the applied stress path but also by the initial state established during specimen preparation. Relevant parameters include density, particle arrangement (fabric), water content, suction, cementation, stress history, and the degree of disturbance induced during sampling and preparation.

These factors control the subsequent evolution of pore pressure, stiffness, shear strength, volumetric deformation, and failure mechanisms. Consequently, relatively small variations in specimen preparation can produce substantial differences in the measured mechanical response, thereby affecting the reproducibility and comparability of experimental results. Numerous experimental investigations have demonstrated that specimens with similar mineralogical composition, particle-size distribution, and global void ratio may nevertheless exhibit markedly different hydro-mechanical behaviour as a consequence of differences in fabric, particle orientation, and inherent anisotropy.

For granular soils, the initial density is commonly described using the void ratio, e, defined as the ratio between the volume of voids, V_v, and the volume of solids, V_s:

$$e = \frac{Vv}{Vs} \tag{1}$$

The relative density, D_r, is then used to express the current state of packing relative to the limiting states of the soil:

$$D_r = \frac{e_{max} - e}{e_{max} - e_{min}} \tag{2}$$

where e_{max} and e_{min} the maximum and minimum void ratios, respectively.

Although relative density provides a convenient macroscopic measure of the initial packing state, it does not uniquely define the internal structure of a granular specimen.

Specimens having the same relative density may possess different particle arrangements, contact networks, and fabric anisotropies depending on the preparation method.

For this reason, specimen preparation must be carefully standardised and comprehensively documented. The selected procedure should establish an initial state that is either representative of field conditions or appropriate for the specific experimental objective. Preparation parameters should be kept as consistent as possible between specimens, while storage and handling procedures should minimise any alteration of the established state prior to testing, thereby improving the reproducibility and comparability of experimental results.

2.3 Granular soils

The preparation of granular soil specimens is a critical aspect of laboratory testing, as the deposition method directly influences the initial fabric, density, and anisotropy of the material. Unlike cohesive soils, whose natural structure may be preserved through careful sampling, reconstituted granular soils derive their mechanical behaviour largely from the manner in which particles are assembled within the specimen. The deposition process governs the spatial arrangement and orientation of particles and the resulting contact network, thereby defining an initial fabric that constitutes an important state variable, one that plays a role in controlling mechanical behaviour at least as fundamental as conventional descriptors such as void ratio or relative density. This highlights that specimen preparation should be regarded not merely as a laboratory procedure, but as an integral part of the initial state of the material.

Different deposition methods are available for the reconstitution of granular soil specimens including moist tamping, dry pluviation through air and water pluviation (Figure 1). The choice of preparation method should be consistent with the objectives of the testing programme and, where relevant, with the field deposition processes and conditions that the laboratory specimens are intended to reproduce. Careful control and documentation of specimen preparation are also essential for ensuring reliable comparisons between independent studies and for the robust calibration and validation of constitutive models, since variations in initial fabric might otherwise be incorrectly attributed to intrinsic material properties rather than to differences in the initial microstructure.

2.3.1 Moist tamping

Moist tamping is one of the most widely used techniques for preparing granular soil specimens, particularly for achieving very loose to loose initial states on the one hand, and when a controlled range of densities is required, on the other hand. The dry soil is first mixed with a small, controlled amount of water, typically 3–10% by mass, and

then placed into the specimen mould in successive layers. Each layer is lightly compacted with a tamping device until the target thickness or density is reached. The added water generates capillary forces between particles, providing temporary stability to the soil skeleton and allowing very loose specimens to be reconstituted and handled without significant collapse during preparation.

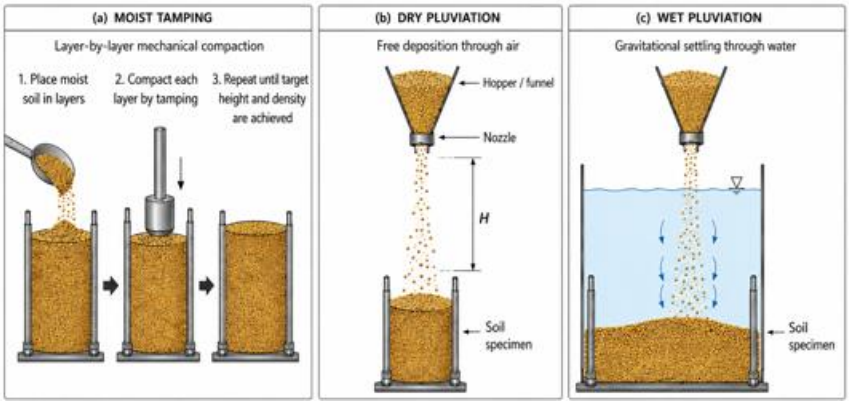


Figure 1: Schematic representation of the main specimen preparation methods of granular materials (Author-generated schematic with AI assistance).

The fabric produced by moist tamping is strongly influenced by the initial moisture content, layer thickness, tamping energy, and number of tamping blows applied to each layer. The presence of water during preparation promotes the formation of particle aggregates through capillary forces, resulting in an aggregated fabric with relatively large inter-aggregate pores (macropores). This characteristic pore structure may result in a heterogeneous distribution of voids within the specimen. Moreover, the successive placement and compaction of individual layers may introduce distinct interlayer interfaces, particularly when the preparation procedure is not carefully controlled.

Consequently, specimens prepared by moist tamping may exhibit a mechanical response different from that of specimens prepared by depositional techniques such as dry or wet pluviation, even at comparable relative densities. Differences in peak strength, dilatancy, and strain-softening behaviour have been associated with variations in particle arrangement, aggregation, pore-size distribution, and contact structure rather than with density alone. For this reason, the preparation procedure should be carefully controlled and documented to ensure consistency and reproducibility between specimens.

A widely used refinement of the basic technique is the under-compaction method [Lad78], in which lower layers are deliberately compacted to a density slightly below the target value, to compensate for the additional densification imparted by the compaction of subsequent layers placed above them. This procedure produces a markedly

more uniform density profile throughout the specimen height and is now considered good practice whenever moist tamping is used for research purposes.

2.3.2 Dry pluviation

Dry pluviation, also referred to as air pluviation or sand raining, consists of depositing dry granular material into a specimen mould by allowing particles to fall freely through air from a controlled height. The soil is typically introduced through a funnel, nozzle, or purpose-built pluviation device (Figure 2), and the resulting density is controlled primarily through the drop height, particle flow rate, nozzle opening, and deposition area. These parameters govern the velocity and trajectory of the particles during deposition and therefore influence the packing arrangement and initial fabric of the specimen.

A major advantage of dry pluviation is its capacity to produce relatively uniform specimens with good repeatability, provided the deposition parameters are carefully controlled. Unlike layer-by-layer compaction methods, particles are deposited continuously, which reduces the formation of pronounced horizontal interfaces. The resulting fabric is nevertheless not perfectly isotropic, as particle orientation and contact arrangement may develop preferential directions associated with the deposition process.

Dry pluviation is widely used in fundamental experimental research because the preparation procedure can be systematically controlled and reproduced. It is particularly valuable for studies in which the influence of density and fabric on mechanical behaviour must be isolated, as well as for constitutive-model calibration and comparison between independent experimental programmes. However, the fabric generated by air pluviation does not necessarily reproduce all natural depositional environments, and its suitability should therefore be assessed with respect to the geological or engineering conditions under investigation.

2.3.3 Wet pluviation

Wet pluviation involves depositing granular material through a column of water, allowing the particles to settle under submerged conditions before accumulating and forming the specimen. In a typical procedure, dry soil is introduced into a water-filled mould or column, and particle motion during settling is influenced by fluid drag, buoyancy, and interaction with previously deposited grains, in contrast to dry pluviation, where such hydrodynamic effects are absent. This method produces a fabric that more closely resembles naturally deposited alluvial, marine, or hydraulically placed sediments, making it particularly relevant for studies of offshore foundations, hydraulic structures, and soil liquefaction.

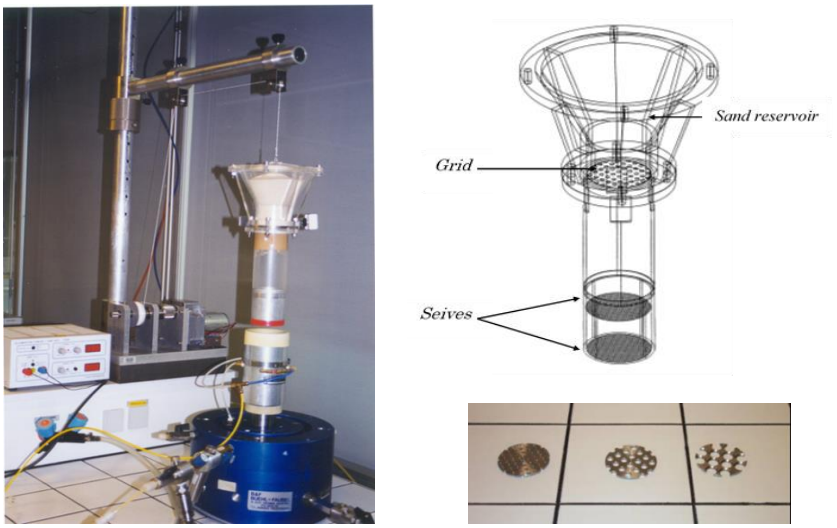


Figure 2: View of sand pluviation device with lifting system. Adapted from [Ben01].

Because the deposition process involves limited direct mechanical disturbance of the developing soil skeleton, it can reproduce particle arrangements more repre-sentative of gravitational sedimentation than mechanical compaction techniques. However, wet pluviation requires careful control of the deposition conditions. Settling velocity depends on particle size, density, and shape, so segregation may occur in broadly graded soils. Achieving a precisely prescribed target density can also be more challenging than with dry pluviation or mechanical compaction. Despite these limitations, wet pluviation remains an effective means of producing saturated granular specimens with a depositional fabric more representative of naturally sedimented soils.

2.3.4 Comparison of the three preparation methods

The three methods considered above differ primarily in the mechanism by which particles are introduced and rearranged within the specimen. Moist tamping relies on layer-by-layer mechanical compaction; dry pluviation produces the specimen through free deposition through air; and wet pluviation relies on gravitational settling through water. These differences directly affect particle orientation, contact distribution, density uniformity, and the degree of fabric anisotropy developed during preparation (Table 1). Experimental evidence has shown that differences in fabric and fabric anisotropy can significantly affect the hydro-mechanical response of granular soils, including stiffness, peak strength, dilatancy, strain localisation, the onset of instability, and resistance to liquefaction [MSC77] [VN88].

Consequently, even when two specimens are prepared at the same relative density, with identical mineralogical and granulometric characteristics, they may nevertheless exhibit markedly different stress–strain and volumetric responses because the underlying particle-scale structure is not identical (differences in particle orientation and contact distribution) (Figure 3 and 4).

Table 1: Comparison of granular soil specimen preparation methods.

	Moist tamping	**Dry pluviation**	**Wet pluviation**
Mechanism	Layer-by-layer mechanical compaction	Free-fall deposition through air	Gravitational settling through water
Fabric & anisotropy	Heterogeneous fabric, layered, anisotropic (depends on compaction technique)	Relatively homogeneous, isotropic (low depositional anisotropy)	Relatively uniform, close to natural depositional fabric
Density uniformity	Moderate (improved with under-compaction)	High (risk of segregation if non uniform material)	High (most uniform)
Typical use	Low to medium density specimens Lower target densities	-Medium to dense density specimens -Air pluviation for clean granular soils	-Medium to high density specimens -Saturated or near-saturated specimens

2.4 Cohesive soils

The preparation of cohesive soil specimens differs fundamentally from that of granular soils, because the mechanical and hydro-mechanical behaviour of fine-grained materials is governed not only by density and stress state, but also by their natural structure, particle arrangement, bonding, natural cementation, degree of overconsolidation, and hydraulic condition. In particular, the fabric of clay particles, physico-chemical interactions between particles, and the degree of saturation can strongly influence stiffness, shear strength, compressibility, creep behaviour, and volumetric response.

For natural cohesive soils, specimen preparation should therefore aim to preserve the in-situ structure and stress history as far as practicable. Sampling, trimming, handling, and storage procedures must minimise disturbance, since changes in particle arrangement, bonding, water content, or stress state can significantly modify the measured response. The distinction between intact, remoulded, and reconstituted specimens is consequently fundamental, as each represents a different initial soil structure and serves a different experimental purpose.

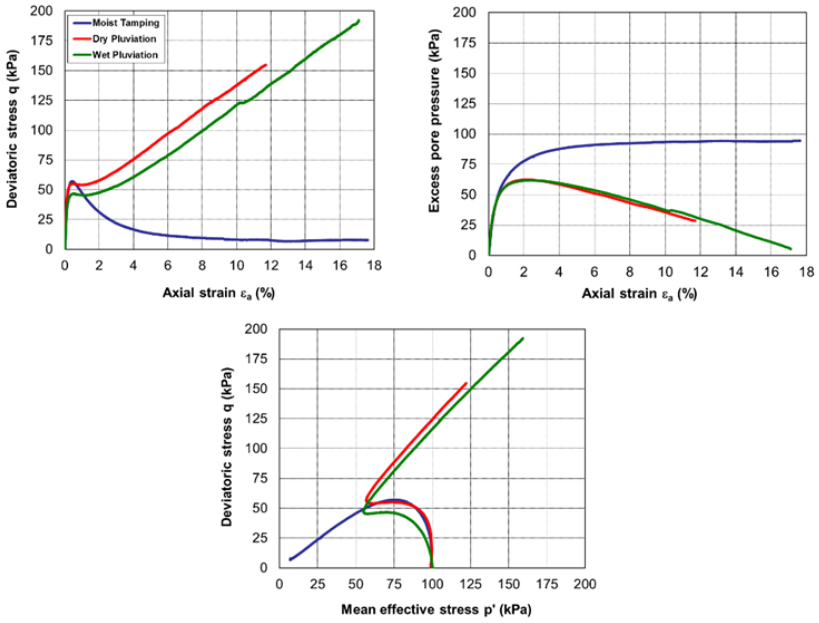


Figure 3: Influence of specimen preparation method on the undrained mechanical response of Hostun sand (σ_c=100kPa, D_r=3%) [Ari12].



(a) (b) (c)

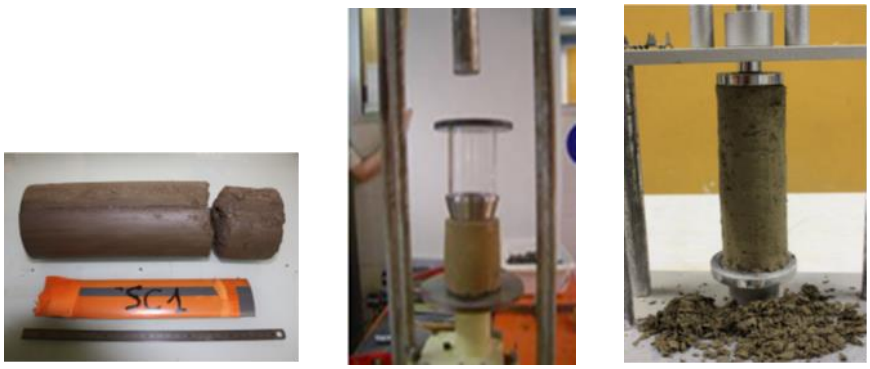
Figure 4: Scanning Electron Microscope images of Hostun sand showing two different structures: (a) macropores and aggregates (moist tamping); (b) macropores and aggregates (zoom); (c) regular stack (dry pluviation) [Ben04].

The appropriate preparation method should be selected according to the objectives of the testing programme. Testing of high-quality undisturbed (intact) specimens is generally required when the objective is to characterise the behaviour of a natural deposit, whereas remoulded or reconstituted specimens may be preferable for establishing a controlled reference response or investigating fundamental constitutive behaviour. Deliberately destructured specimens can similarly be used to examine the influence of natural bonding and fabric on the transition from structured to unstructured behaviour.

2.4.1 Intact specimens

Intact specimens are primarily used to characterise the in-situ mechanical and hydro-mechanical behaviour of natural deposits. They are prepared from high-quality undisturbed field samples with the objective of preserving the natural soil fabric, bonding, structure, water content, and stress history as much as possible. Sampling is first carried out using suitable thin-walled or piston samplers to minimise disturbance during extraction. Once recovered, the sample is carefully removed from the sampler and immediately sealed to limit moisture loss and changes in suction. In the laboratory, the sample is inspected for visible cracks, fissures, or other signs of disturbance before the test specimen is prepared. The specimen is then cut and trimmed progressively to the required diameter and height using sharp and appropriate trimming tools, while avoiding excessive pressure, vibration, or manipulation that could disturb the natural structure (Figure 5). The final dimensions are measured, and the specimen is weighed to determine its initial density and water content. It is then transferred carefully into the testing apparatus, with minimal handling, and subjected to the required testing conditions.

Throughout sampling, transportation, storage, and preparation, the specimen is protected from drying, temperature variations, vibration, and unnecessary handling. Nevertheless, even high-quality sampling cannot completely eliminate disturbance, as stress relief during extraction and subsequent trimming and handling may induce swelling, microcracking, changes in suction, and partial degradation of the natural structure. Such disturbance can modify the measured stiffness, strength, compressibility, and volumetric response, and may therefore result in deviations from the true in-situ behaviour. The degree of disturbance should consequently be assessed and minimised throughout the sampling and preparation process. The quality of an intact specimen should ultimately be evaluated in relation to the extent to which its natural structure and stress state have been preserved.



(a) (b) (c)

Figure 5: Preparation of intact specimen: (a) intact core soil; (b) piston sampling; (c) trimming specimen in the frame. Adapted from [BFB13].

2.4.2 Remoulded specimens

Remoulded specimens are prepared by destroying the natural soil structure through thorough mixing and mechanical disturbance, generally at or close to the natural water content. The soil is first gently broken down to eliminate natural aggregates and fabric, bonding, fissuring, and geological structure, while retaining the fundamental mineralogical and particle-size characteristics of the soil. It is then thoroughly mixed until a homogeneous material is obtained. If necessary, the water content is adjusted to the target value by adding water gradually and mixing carefully to ensure uniform moisture distribution. The prepared soil is subsequently placed into the specimen mould and compacted or formed to the required dimensions and density before testing (Figure 6). During preparation, particular attention is given to achieving a uniform water content and eliminating remaining intact lumps or natural structural features.

Compared with intact specimens, remoulded soils generally exhibit lower stiffness and peak strength, higher compressibility, and more ductile stress–strain response. The magnitude and nature of these differences depend on factors such as soil type, stress history, bonding characteristics, and initial state. Remoulded specimens are consequently used in comparative studies to isolate the effects of structure and bonding, and to investigate the transition from structured to destructured soil behaviour.



(a) (b) (c)

Figure 6: Preparation of remoulded sample from disturbed soil. (a) disturbed soil; (b) cut into small pieces; (c) reconstitution by compaction inside Plexiglas mold. Adapted from [BFB13].

2.4.3 Reconstituted specimens

Reconstituted specimens are prepared by thoroughly mixing soil with water to form a homogeneous slurry or paste, which is then consolidated under controlled one-dimensional or isotropic loading conditions until the desired density and stress state are achieved. This reconstitution process eliminates, to a large extent, the effects of natural deposition, cementation, bonding, and stress history, replacing them with a controlled, reproducible initial fabric.

Reconstituted specimens are particularly important in fundamental studies of fine-grained soils and within the framework of Critical State Soil Mechanics, where reproducible initial conditions are required to investigate the intrinsic behaviour of the soil skeleton. By removing the effects of natural structure and geological history, reconstitution facilitates the identification of fundamental relationships between stress state, density, pore pressure, and deformation.

A commonly adopted approach to reconstitute specimen is slurry deposition (Figure 7). In this technique, dry fine-grained soil is mixed with de-aired water, typically to a water content between 1 - 1.5 times the liquid limit, w_L to form a homogeneous, air-free slurry (degassing if necessary). This is then poured into a consolidometer and subsequently consolidated under controlled conditions until the target vertical effective stress is reached, establishing a well-defined initial void ratio and effective stress. The consolidated block is then extruded, and a cylindrical specimen is trimmed from it for triaxial, direct shear, or other laboratory testing, where it is saturated, reconsolidated to the desired stress state, and subjected to loading.

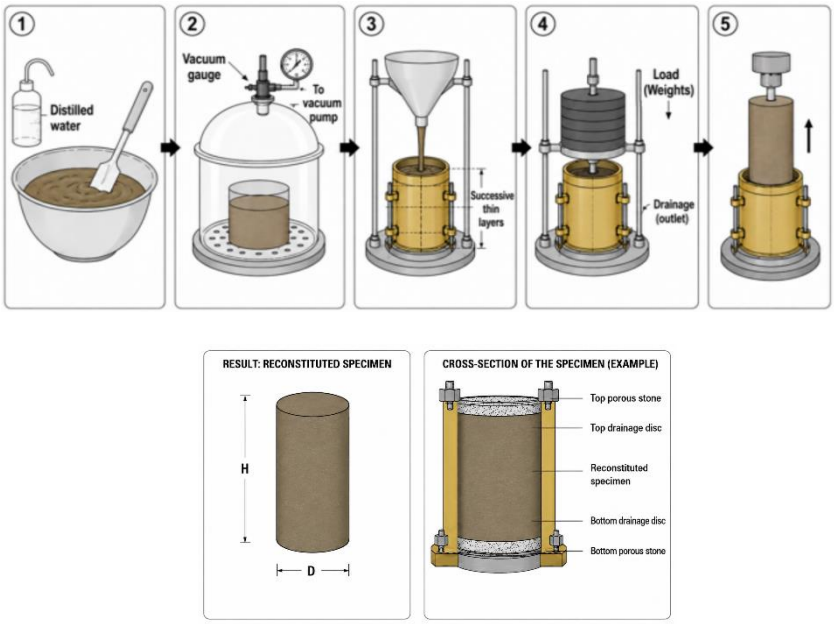


Figure 7: Schematic representation of a typical slurry-deposition procedure for reconstituted fine-grained specimens, including (1) mixing, (2) vacuum de-airing, (3) layered placement, (4) consolidation, and (5) extrusion. Note: The dimensions of the specimen, D and H, depend on the test and the mold used (Author-generated schematic with AI assistance).

This slurry-consolidation approach eliminates natural soil structure and bonding, produces highly reproducible specimens with a uniform initial void ratio and known

stress history, and provides a well-defined reference state for constitutive modelling, making it excellent for calibration and widely adopted in Critical State Soil Mechanics research. Its main limitations are that it does not reproduce the natural fabric of intact soils, one-dimensional consolidation may induce anisotropy, and the process can be time-consuming for low-permeability clays. Despite these limitations, this method is considered the standard approach for preparing reconstituted reference specimens intended for high-quality, advanced geotechnical laboratory testing, and is particularly well suited to clays and silts where the objective is a reproducible fabric and well-defined initial state.

2.5 Rock specimens

The preparation of rock specimens requires a level of precision generally higher than that for soils, since brittle materials are particularly sensitive to geometric imperfections, pre-existing microcracks, and loading boundary conditions. Small deviations in specimen dimensions, end parallelism, or surface flatness can produce non-uniform stress distributions, directly affecting measured stiffness, strength, dilatancy, and fracture behaviour. Damage introduced during coring, cutting, or grinding may likewise alter the initial microstructure and bias the results. Specimen preparation must therefore be carried out under controlled conditions and in accordance with relevant testing standards, using strict geometrical tolerances to ensure uniform stress distribution during testing [ISRM07].

Rock specimens are commonly obtained by diamond coring, followed by precision cutting and end grinding to produce cylindrical specimens with controlled dimensions, typically a height-to-diameter ratio of about 2:1 for standard uniaxial and triaxial compression tests. Specimen ends should be sufficiently flat and parallel to ensure uniform contact with the loading platens. Throughout preparation, excessive heating, vibration, and mechanical impact must be avoided, as these can initiate or propagate microcracks and artificially reduce the measured strength and stiffness.

Specimen orientation relative to bedding planes, foliation, schistosity, joints, veins, or other geological discontinuities must also be carefully considered, as these features can induce pronounced mechanical anisotropy and strongly influence the failure mechanism. Orientation should be selected and documented according to the testing objectives, and where anisotropic behaviour is of interest, specimens may be prepared at several orientations relative to the dominant geological fabric.

Prior to testing, specimens should be visually inspected for cracks, inclusions, and other defects, and stored under controlled environmental conditions to preserve their initial moisture content, saturation, and mineralogical or structural integrity, particularly for weak, porous, weathered, or partially saturated rocks. Natural heterogeneities should also be considered in relation to specimen dimensions; for the specimen to provide a representative material response, the characteristic size of these heterogeneities should generally remain small relative to the specimen size.

The dominant preparation requirements depend on the type of geomaterial being investigated. For granular soils, the focus is on controlling the initial density and particle-scale fabric, which strongly influence stiffness, dilatancy, and shear strength. For cohesive soils, preserving the natural structure and stress history while minimising sampling and handling disturbance is essential for obtaining representative mechanical properties. For rocks, accurate specimen geometry, appropriate specimen orientation, and preservation of the initial microcrack and defect structure are paramount. Inadequate preparation may introduce stress concentrations or artificial damage, potentially leading to premature failure and significant bias in the measured mechanical response.

2.6 Specimen Storage and Transportation

Once prepared or retrieved from the field as an intact/undisturbed sample, specimens must be preserved in a state as close as possible to their initial condition until testing. The main precautions generally recommended are:

- Moisture and suction control: sealing the specimen (e.g., with wax, plastic film, or an impermeable membrane) to prevent evaporation or moisture ingress, which may alter suction and effective stress, particularly in unsaturated specimens.
- Temperature control: storing specimens in a temperature-controlled room or refrigerator to minimise temperature-induced volume changes and, where relevant, biological or biochemical activity and chemical reactions in treated soils such as MICP-cemented specimens.
- Mechanical protection: minimising vibration and shock during handling and transport, which may disturb the soil fabric, particularly in loose, weakly bonded, or lightly cemented materials.
- Duration of storage: limiting the time between preparation/sampling and testing, and systematically recording storage duration, since prolonged storage may allow changes in the specimen state due to processes such as consolidation, moisture redistribution, carbonate precipitation or recrystallisation, and ongoing biological or chemical reactions.
- Labelling and traceability: systematically recording preparation date, storage conditions and duration, and any observed anomalies, to ensure traceability and facilitate the interpretation of experimental results, particularly when deviations or outliers may be related to storage and handling rather than to the intrinsic behaviour of the material.

Overall, specimen preparation and storage should be regarded as fundamental experimental variables that directly influence the reliability, reproducibility, and scientific interpretation of geomechanical testing, rather than as a purely procedural step.

3 Measurement of Specimen Dimensions

3.1 Introduction

Accurate determination of specimen dimensions is a fundamental requirement for obtaining reliable mechanical parameters from triaxial testing. The initial specimen geometry (height, diameter, and volume) forms the basis for calculating the stress and strain variables used to characterise the material response. Consequently, uncertainties in these measurements propagate directly into the calculated axial stress, deviatoric stress, axial strain, and volumetric strain, potentially introducing systematic errors into the resulting stress–strain relationships and derived constitutive parameters [BH62] [HE14] [Lad16].

The measurement procedure should be adapted to the characteristics of the geomaterial under investigation. Granular soils, cohesive soils, and rocks present different challenges owing to differences in surface regularity, stiffness, deformability, and sensitivity to handling. In addition, specimen geometry may change during installation and initialisation of the test. For example, the application of vacuum to stabilise an unsaturated granular specimen prior to cell pressurisation can induce a small radial contraction accompanied by an increase in specimen height. Such changes should be recognised and incorporated into the definition of the initial test geometry.

3.2 Importance of accurate dimension measurement

Accurate and reproducible measurement of specimen geometry is an essential component of the initial specimen characterisation and should be performed using a clearly defined measurement protocol. Specimen geometry directly enters the calculation of the principal mechanical variables obtained from a triaxial test. The cross-sectional area is required to determine the applied axial and deviatoric stresses, while the initial specimen height provides the reference length for calculating axial strain. Similarly, the initial specimen volume is required to determine volumetric strain from the measured volume change.

For a cylindrical specimen, the initial cross-sectional area is given by:

$$A_o = \frac{\pi D_O^2}{4} \tag{3}$$

where D_o is the initial specimen diameter.

The initial specimen volume is then:

$$V_o = A_o H_o \tag{4}$$

where H_o is the initial specimen height.

Unlike random measurement noise, dimensional errors introduce systematic bias into the calculated stress and strain variables. An error in specimen diameter affects the calculated cross-sectional area and therefore directly influences the stress measurement. An error in specimen height affects the calculated axial strain, while uncertainty in the initial volume propagates throughout the volumetric strain calculation. These errors may subsequently influence the interpretation of contractive or dilative behaviour, the identification of characteristic stress states, and the determination of critical-state and constitutive parameters.

3.3 Measurement of granular soil specimens

Granular soil specimens require particular attention because their geometry may be modified during preparation, handling, and installation. Following specimen preparation, the diameter should be measured at several equally spaced locations around the circumference (typically three positions) and at multiple elevations. Measurements around the circumference are used to assess non-circularity, while measurements at different heights provide information on possible taper or local variations in diameter. The specimen height should similarly be determined along the specimen axis (typically three positions), using a vertical calliper or a suitable reference system associated with the loading cap and base (Figure 8). The mean diameter and height should be reported together with an appropriate measure of dispersion (e.g. standard deviation) to quantify the variability of the measurements. Measurements should be performed carefully to avoid compressing or otherwise disturbing loose granular specimens.

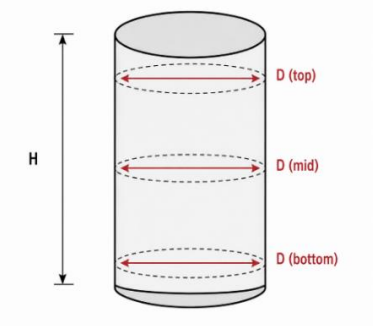
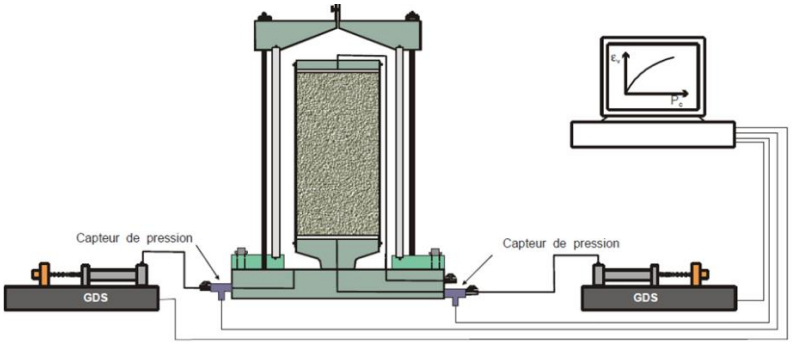


Figure 8: Multi-level diameter and height measurement scheme used to account for non-circularity and taper of the specimen.

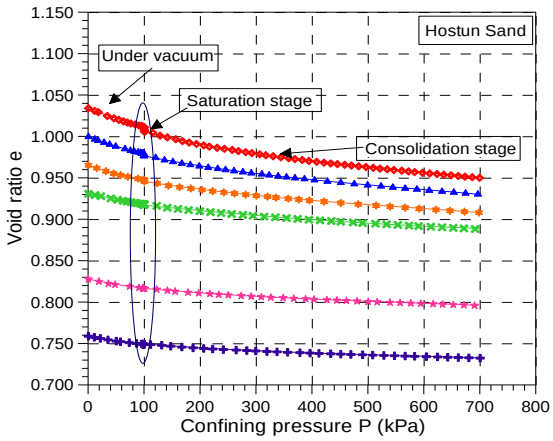
For specimens prepared by pluviation or moist tamping, a small vacuum is frequently applied before installation to provide temporary lateral support while the membrane is fitted and the triaxial cell is assembled. Although the applied vacuum is generally small, it may induce a slight radial contraction and corresponding axial extension of the specimen. Consequently, the dimensions measured after vacuum application may differ from those measured under stress-free conditions. The geometry adopted as the

initial reference state should therefore be clearly defined and consistently used in subsequent calculations.

The specimen volume may also be determined indirectly using a calibrated volume-change system, such as a burette or pressure–volume controller, or specific volume change device (Figure 9). Such systems allow continuous measurement of volume changes during the test and are particularly useful during large-deformation experiments, when direct measurement of specimen geometry is no longer practical. The accuracy of a volume-change system depends on appropriate calibration of the measuring device and the associated tubing and pressure system: system compliance, temperature variations, trapped air, and the compressibility of the measurement fluid may all contribute to the measured volume change and should therefore be quantified and corrected where necessary. Calibration should be performed under conditions representative of the intended test range.



(a)



(b)

Figure 9: Volume change measurements (void ratio) of specimen during initial stress application, saturation and consolidation (a) schematic representation of the volume change cell; (b) typical calibration curves obtained on Hostun sand [Ben01].

3.4 Measurement of Cohesive Soil and Rock Specimens

Characterising the geometry of cohesive soil and rock specimens follows the same fundamental principles but requires additional consideration of specimen shape, surface condition, and end geometry. The diameter should be measured at several elevations, typically near the top, middle, and bottom of the specimen, with measurements repeated along different orientations. This procedure allows deviations from ideal cylindrical geometry, including taper and non-circularity, to be identified and quantified.

For soft cohesive soils, particular care is required because contact with the loading platens and end restraint during shearing can produce local deformation and a barrel-shaped profile even before significant axial loading has occurred. Consequently, a single diameter measurement at mid-height tends to overestimate the mean specimen diameter (and therefore underestimate the calculated stresses). Multiple measurements should therefore be used to obtain a representative cross-sectional area.

Rock specimens may exhibit geometric irregularities resulting from coring, cutting, and grinding. The flatness and parallelism of the specimen ends are particularly important, because imperfect contact with the loading platens can generate non-uniform stress distributions. The dimensions of rock specimens must then be measured at multiple locations and orientations, and the end surfaces should be checked for compliance with the relevant testing standard.

Small deviations from ideal specimen geometry can produce local stress concentrations, particularly near the specimen ends, and may influence the initiation and propagation of failure. These effects are especially relevant for brittle rocks and highly structured or heavily overconsolidated cohesive soils, where localised cracking or shear-band formation may be sensitive to stress concentrations.

3.5 Error propagation in dimension measurements

Uncertainty in specimen dimensions propagates directly into the calculated stress and strain variables. Since the cross-sectional area depends on the square of the specimen diameter,

$$A = \frac{\pi D^2}{4} \tag{5}$$

The relative uncertainty in area is approximately twice the relative uncertainty in diameter:

$$\frac{\Delta A}{A} \approx 2 \frac{\Delta D}{D} \tag{6}$$

Thus, a 1% uncertainty in diameter produces approximately a 2% uncertainty in the calculated cross-sectional area and, consequently, a similar relative uncertainty in the calculated axial stress when the applied load is known accurately.

In contrast, uncertainty in specimen height affects axial strain approximately linearly. For small deformations,

$$\varepsilon_a = \frac{\Delta H}{H_o} \tag{7}$$

where ΔH is the change in specimen height and H_0 is the initial height. The relative influence of height uncertainty therefore becomes particularly important when the measured deformation is small.

Uncertainty in the initial volume affects the calculation of volumetric strain in the same way throughout the test. This is particularly important because volumetric behaviour provides a key basis for interpreting the contractive and dilative tendencies of soils, determining critical-state parameters, and calibrating constitutive models. Differences in constitutive parameters obtained across laboratories do not stem solely from genuine material variability, but also from differences in how specimen geometry is measured and how volume calibration is carried out. For these reasons, dimensional measurements should not be treated as purely geometric observations, but as a source of experimental uncertainty that propagates through the entire data-reduction process. Measurement resolution, repeatability, calibration procedures, and estimated uncertainty should be documented alongside the experimental results. Establishing a consistent dimensional measurement protocol is essential for ensuring the reliability and comparability of triaxial test data.

4 Triaxial Test Procedure

4.1 Introduction

The triaxial test is one of the most versatile and widely used laboratory tests in geotechnical engineering for investigating the stress–strain and strength behaviour of soils and rocks under controlled loading conditions. The specimen is subjected to two independently controlled principal stresses, an all-round confining pressure and an axial load, which together allow a wide range of stress paths to be reproduced under axisymmetric conditions [BH62] [Lad16].

Depending on the objectives of the investigation, different testing procedures may be adopted. The three principal frameworks, namely the Unconsolidated Undrained (UU), the Consolidated Undrained (CU), and the Consolidated Drained (CD), differ primarily in the consolidation and drainage conditions imposed before and during shearing. These differences determine whether the measured response is interpreted in terms of total or effective stresses, and they govern the suitability of each test for particular engineering applications.

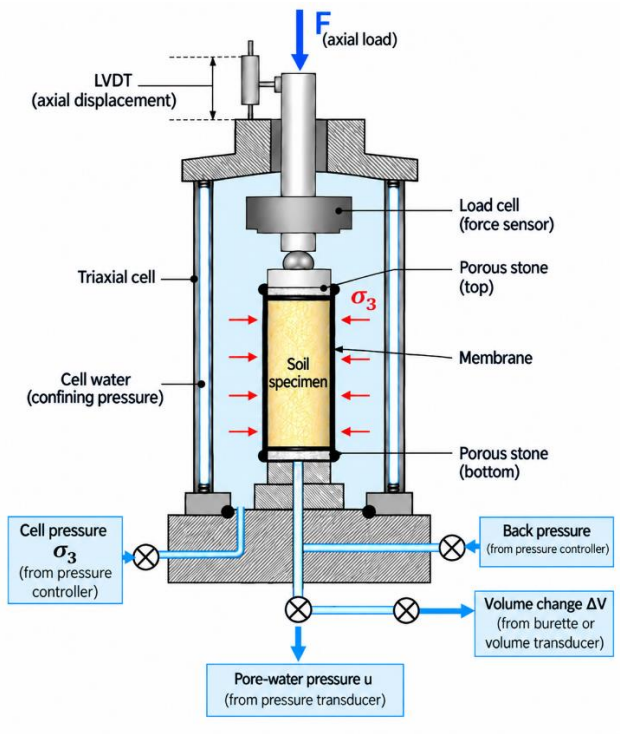
Carrying out a triaxial test involves a carefully controlled sequence of experimental stages, each of which establishes the conditions required for the next. These stages

include specimen installation, initial stress application, saturation, consolidation to the target effective stress, and shearing. Because errors introduced during one stage may propagate into subsequent stages and cannot always be corrected retrospectively, the reliability of a triaxial test depends not only on the accuracy of the instrumentation but also on the careful and consistent execution of each experimental step.

4.2 Fundamentals of triaxial test

The triaxial test is conventionally carried out on a cylindrical specimen enclosed in a flexible and impermeable rubber membrane and installed between a top cap and a bottom pedestal inside a triaxial cell (Figure 10). Three main loading and pressure-control systems are typically involved: the cell-pressure system, which applies an isotropic confining pressure, σ_3, to the specimen through the surrounding cell fluid; the axial loading system, which applies an axial load through the loading ram or piston that passes through the top of the cell and bears down onto the specimen; and the back-pressure system, which controls the pore-fluid pressure through the specimen drainage lines. Because the cell pressure is transmitted through the cell fluid, it acts hydrostatically and uniformly around the specimen while the axial load can be varied independently. Axial deformation is typically measured with a displacement transducer associated with the loading piston. The specimen drainage lines, connected through the base and/or top cap, enable pore-water pressure, u, to be measured or controlled and, under drained conditions, allow water expelled from or absorbed by the specimen to be measured using a volume-change device or burette, thereby providing an estimate of the specimen volume change. In an undrained test, the drainage valves are closed so that no water is allowed to leave or enter the specimen; for a fully saturated specimen, this corresponds approximately to constant-volume conditions, while changes in pore-water pressure are measured using a pressure transducer. The combination of cell pressure and axial loading defines the total stress state, whereas the pore-water pressure governs the corresponding effective stress state. Although u is not a third independent total stress component, its measurement and control are fundamental to the interpretation of saturated triaxial tests.

The principal quantities directly controlled or measured during a triaxial test are the applied cell/confining pressure, axial load, axial displacement, and either specimen volume change or pore-water pressure, depending on the drainage condition. These measurements are subsequently used to determine the relevant stress and strain variables, including deviator stress, axial strain, volumetric strain, and, where pore-water pressure is measured, the corresponding effective stresses. The combination of controlled loading and drainage conditions with independent measurements of deformation, volume change, and pore-water pressure makes the triaxial test particularly suitable for characterising the constitutive response of geomaterials and for determining parameters used in constitutive models.



(a)



(b)

Figure 10: (a) Schematic representation of a conventional triaxial test apparatus and its main loading and pressure-control systems (author-generated with AI assistance); (b) Photography of triaxial cell with mechanical frame.

Under conventional triaxial conditions, the cell pressure acts equally in the two radial directions, resulting in equal intermediate and minor principal stresses, $\sigma_2 = \sigma_3$. The axial principal stress, σ_1, is varied independently through the applied axial load, by applying an additional stress increment, the deviator stress, q, in the vertical direction such that:

$$\sigma_1 = \sigma_3 + q \tag{8}$$

which can equivalently be written as:

$$q = \sigma_1 - \sigma_3 \tag{9}$$

By independently controlling the confining pressure and axial loading, a range of stress paths can be imposed under axisymmetric conditions

In the field, a soil element may generally be subjected to three different principal stresses ($\sigma_1, \sigma_2, \sigma_3$). However, the conventional triaxial apparatus imposes an axisymmetric stress condition and consequently cannot independently control all three principal stresses. The intermediate principal stress σ_2, is therefore equal to either the minor or the major principal stress, depending on whether triaxial compression or extension is considered. In triaxial compression, the axial stress corresponds to the major principal stress, σ_1, with $\sigma_1 > \sigma_2 = \sigma_3$, whereas in triaxial extension, it corresponds to the minor principal stress, σ_3 with $\sigma_1 = \sigma_2 > \sigma_3$ (Figure 11).

Extension does not imply that the specimen is subjected to tensile axial stress. Instead, it is achieved by reducing the axial stress relative to the radial stress. Thus, the axial stress is the major principal stress in triaxial compression and the minor principal stress in triaxial extension. In both cases, the stress state remains axisymmetric, but the relative magnitudes of the axial and radial stresses are reversed [BH62] [Lad16].

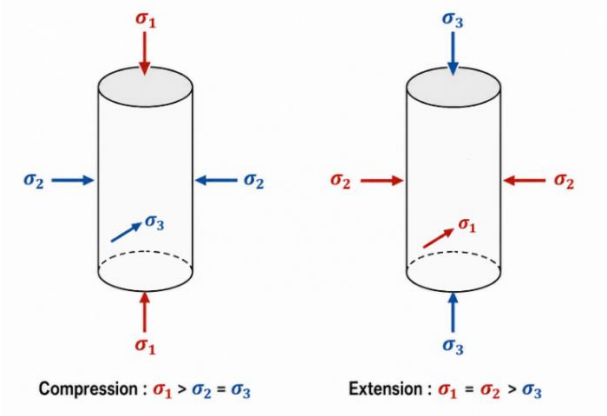


Figure 11: Principal stress conditions in conventional axisymmetric triaxial compression and extension.

4.2.1 Effective stress principle

For saturated soils, the stresses applied externally to the specimen do not correspond directly to the stresses carried by the soil skeleton. The mechanical response of the soil is governed by the effective stresses, which account for the pore-water pressure within the specimen (Figure 12). According to Terzaghi's effective stress principle,

$$\sigma' = \sigma - u \tag{10}$$

where σ is the total normal stress, u is the pore-water pressure, and σ' is the corresponding effective normal stress. For a conventional axisymmetric triaxial compression test, the effective principal stresses are therefore:

$$\sigma_1' = \sigma_1 - u \tag{11}$$

$$\sigma_3' = \sigma_3 - u \tag{12}$$

where σ_1' and σ_3' are the major and minor principal effective stresses, respectively.

Since pore-water pressure acts equally in all directions, it cancels when the principal stress difference is calculated. Consequently, the deviatoric stress may be expressed equivalently in terms of total or effective stresses:

$$q = \sigma_1' - \sigma_3' = \sigma_1 - \sigma_3 \tag{13}$$

In contrast, the mean effective stress is directly dependent on pore-water pressure, and is defined as:

$$p' = \frac{\sigma_1' + 2\sigma_3'}{3} = \frac{\sigma_1 + 2\sigma_3}{3} - u \tag{14}$$

This distinction between total and effective stress is fundamental to the interpretation of triaxial tests. In particular, changes in pore-water pressure during undrained loading modify p' and therefore the effective stress path, even when the externally applied total stresses are prescribed. The $p' - q$ framework subsequently provides a convenient basis for describing consolidation, shearing, and critical-state behaviour.

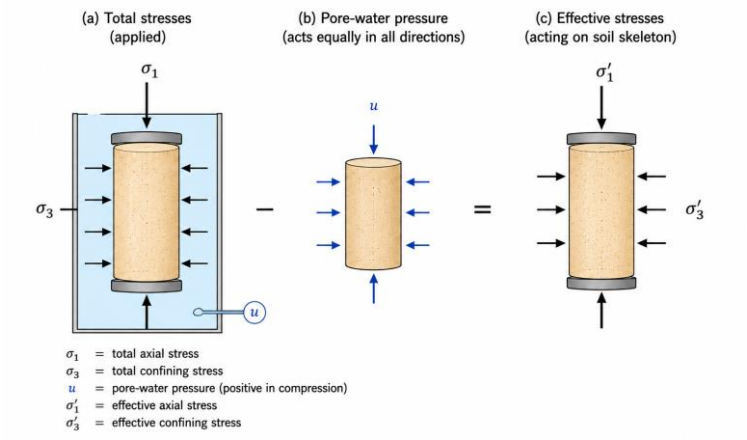


Figure 12: Schematic representation of total stress, pore-water pressure, and effective stress in a conventional axisymmetric triaxial test (Author-generated schematic with AI assistance).

4.3 General sequence of a triaxial test

A conventional triaxial test comprises a sequence of controlled stages, with the precise sequence depending on the material, drainage conditions, and objectives of the experimental programme. Each stage establishes the state required for the subsequent phase and therefore contributes directly to the quality and reproducibility of the final measurements:

- **Specimen installation**: establishes the initial geometry and ensures appropriate alignment within the triaxial cell, while minimising seating and membrane-related effects.
- **Initial stress application**: establishes a prescribed stress state and allows the specimen to reach mechanical equilibrium. For specimens maintained under vacuum during demoulding, cell pressure is applied before the vacuum is progressively released to preserve specimen stability and minimise changes in effective stress.
- **Saturation**: performed when the effective-stress behaviour of a saturated specimen is to be investigated; the objective is to minimise the amount of compressible air remaining within the pore space.
- **Consolidation**: generally required after saturation, since the application of back pressure modifies the total and pore-water pressures within the specimen; restores the target effective stress and dissipates any excess pore pressure generated during saturation.

- **Shearing**: the specimen is sheared under prescribed drainage and loading conditions, while axial load, displacement, cell pressure, pore-water pressure, and volume change are continuously monitored.

The test procedure is an integrated sequence of interdependent operations rather than a series of independent steps. The reliability of the measured response depends on the consistent execution of every stage. Inadequate specimen installation, incomplete saturation, insufficient consolidation, or an inappropriate shearing rate may introduce systematic errors that affect the measured stiffness, strength, pore-pressure response, and deformation characteristics [HE14] [Lad16] [ISO18].

4.4 Initial stress application / consolidation

Following specimen installation, an initial confining pressure is applied to establish stable stress conditions before saturation. At this stage, the objective is not to consolidate the specimen to its final target effective stress state, but rather to maintain specimen stability and establish a controlled initial stress condition for the subsequent saturation procedure. The applied cell and pore-water pressures are controlled to maintain an appropriate initial effective confining stress, as defined in Section 4.2. This stress is generally maintained at a relatively low prescribed value during the subsequent application of back pressure. Careful control of this effective stress is important to minimise unintended changes in specimen volume, structure or stress state before the main consolidation stage.

Once the initial stress condition has been established, the specimen proceeds to saturation, during which back pressure and cell pressure are progressively increased while the prescribed effective stress is maintained.

4.5 Saturation

Complete saturation is a prerequisite for any triaxial test intended to investigate effective-stress behaviour of saturated soils. Even relatively small quantities of entrapped air can substantially increase the compressibility of the pore-fluid system, thereby affecting pore-pressure generation and the reliable interpretation of effective-stress response. Achieving a high degree of saturation therefore represents one of the most critical stages of the testing procedure [BH62] [BL73].

Saturation is generally achieved through three successive operations. First, carbon dioxide may be circulated through the specimen to displace the air occupying the pore space; because CO_2 is considerably more soluble in water than atmospheric air, any residual gas can subsequently dissolve more readily. The specimen is then flushed with de-aired water prepared under vacuum to minimise dissolved gases entering the pore network. Finally, back pressure is progressively increased while maintaining a constant effective stress, typically by increasing the cell pressure simultaneously with the back pressure. This promotes the dissolution of remaining gas bubbles into the

pore water according to Henry's law, and progressively increases the degree of saturation. The magnitude of the required back pressure depends on the soil type and initial degree of saturation and may commonly reach several hundred kilopascals (typically ranging from about 200 to 500 kPa) [BL73] [HE14].

The effectiveness of saturation is evaluated using Skempton's pore-pressure coefficient, *B*-value, defined as the ratio between the induced pore-pressure increment and the applied confining-pressure increment under undrained conditions [Ske54]:

$$B = \frac{\Delta u}{\Delta \sigma_3} \tag{15}$$

Where Δu is the increase in pore-water pressure resulting from an increment of $\Delta \sigma_3$ in cell pressure under undrained conditions. Values approaching unity indicate that the specimen is essentially fully saturated. For most laboratory investigations, a minimum value of $B \geq 0.95$ is considered acceptable for soils, although slightly lower values may be justified for stiff clays or intact rocks, where complete elimination of microscopic air bubbles is considerably more difficult. Because saturation quality strongly influences pore-pressure development, undrained stiffness, and liquefaction behaviour, the achieved *B*-value should always be reported together with the test results, rather than assuming complete saturation solely from the applied back pressure. A sufficiently high *B*-value also supports the assumption of negligible specimen volume change during undrained loading, which is important for estimating the evolving specimen cross-sectional area and, consequently, for the accurate calculation of deviator stress [Ske54] [ISO18].

4.6 Consolidation

Following saturation, the specimen is consolidated to the effective stress state required at the start of shearing. During this stage, drainage is permitted and the cell pressure and, where applicable, axial stress are adjusted relative to the applied back pressure to establish the target effective stresses. Excess pore-water pressures are allowed to dissipate and the specimen volume is monitored until an appropriate equilibrium criterion is satisfied. The effective stress state and density attained at the end of consolidation therefore define the initial conditions for the subsequent shearing stage [HE14] [Lad16] [ISO18].

Two principal consolidation procedures are commonly employed, isotropic consolidation and anisotropic consolidation. Isotropic consolidation is characterised by equal principal effective stresses in all directions, resulting in a hydrostatic effective stress state. In the $p' - q$ stress plane, this condition corresponds to $q = 0$, and the consolidation path therefore develops along the p' axis (Figure 13). This procedure is widely used in fundamental laboratory investigations and Critical State Soil Mechanics because of its simplicity and reproducibility. In contrast, anisotropic consolidation involves unequal principal stresses and is applied to reproduce more closely the stress conditions experienced by natural soil deposits or engineering structures. Since many

geomaterials develop anisotropic fabric and stress history during deposition, anisotropic consolidation may provide a more representative initial state for advanced constitutive modelling and practical engineering analyses. The selected consolidation path should therefore be consistent with the intended field representation and the objectives of the experimental programme.

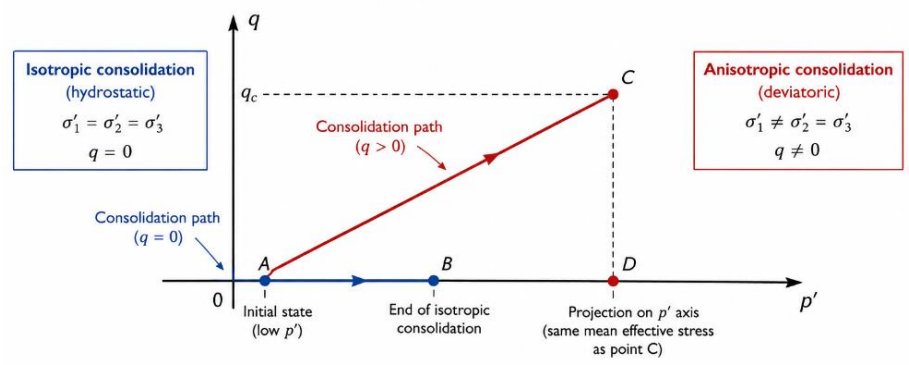


Figure 13: Consolidation paths in the p′−q stress plane: isotropic (q=0) and anisotropic (q≠0) consolidation.

Adequate consolidation is essential to ensure that the effective stress state at the beginning of shearing corresponds to the intended testing conditions. Insufficient consolidation may result in an inappropriate initial effective stress, residual excess pore-water pressure, or an unintended specimen density, which can subsequently affect the measured stress–strain response and complicate comparisons between specimens. The end of consolidation should therefore be established using appropriate criteria based on the rate of volume change, pore-pressure dissipation, or other relevant equilibrium indicators [ISO18] [HE14].

4.7 Shearing stage

The shearing stage is the principal loading phase of the triaxial test, during which the mechanical response of the specimen is investigated from the effective stress state established during consolidation. Axial loading is applied while the confining pressure is controlled according to the prescribed stress path, and the resulting axial load and axial deformation are recorded continuously, together with pore-water pressure for undrained tests or volume change for drained tests. Shearing is continued until the required failure criterion, target strain, or sufficiently large-strain condition has been reached. The different measurements are subsequently used to determine the evolution of deviatoric stress, axial strain, effective stress, and the associated volumetric or pore-pressure response [ISO18] [Lad16].

Axial loading can be applied under either stress-controlled or strain-controlled conditions. Strain-controlled loading is commonly adopted in laboratory investigations because it provides direct control of the deformation rate and enables the complete response to be captured, including peak strength, strain softening, and post-peak behaviour where strain softening may occur. The selected strain rate is particularly important because it must be compatible with the drainage conditions and the hydraulic characteristics of the specimen.

The drainage boundary condition imposed during shearing has a fundamental influence on the measured response [ISO18] [ASTM4767] [ASTM7181**]** [ASTM2850]:

- In a **Consolidated Undrained (CU)** test, drainage is prevented during shearing, so changes in specimen volume are suppressed and loading generates changes in pore-water pressure. Measurement of pore-water pressure therefore allows both the total and effective stress path to be determined throughout shearing.
- In a **Consolidated Drained (CD)** test, drainage is permitted and shearing must proceed sufficiently slowly for excess pore-water pressures to remain negligible; the resulting volume change can then be measured directly.
- In an **Unconsolidated Undrained (UU)** test, neither consolidation nor drainage is permitted, and the response is conventionally interpreted in terms of total stress.

5 Measurement Corrections

5.1 Introduction

The measurements recorded during a triaxial test do not directly represent the intrinsic mechanical response of the tested material. Recorded signals may be influenced by specimen geometry, boundary conditions, the testing apparatus, instrumentation, and other experimental artefacts. Consequently, the raw measurements obtained from load cells, displacement transducers, pressure controllers, volume-change devices, and pore-pressure sensors require appropriate interpretation and, where necessary, correction before reliable stress-strain relationships and constitutive parameters can be derived [BH62] [Lad16].

5.2 Necessity of measurement corrections

Conventional triaxial data reduction is generally based on a number of idealised assumptions, including homogeneous specimen deformation, accurate transmission of the applied load, negligible apparatus deformation, reliable pore-pressure transmis-

sion, and negligible mechanical resistance from the membrane. In practice, these assumptions are only approximations. As shearing proceeds and the specimen deforms, its geometry evolves, the loading system undergoes elastic deformation, friction may affect load transmission, the membrane may contribute to the measured resistance, and the hydraulic system may influence pore-pressure and volume-change measurements. If these effects are neglected, systematic errors may be introduced into the calculated stress and strain variables and, consequently, into the parameters derived from them. Their relative importance depends on the material, stress level, drainage conditions, strain range, and characteristics of the testing system. For example, apparatus compliance is particularly important when evaluating stiffness at small strains, whereas changes in specimen geometry and non-uniform deformation become increasingly significant at larger strains. Membrane resistance may influence the measured strength, particularly at low effective stresses, while hydraulic-system effects may affect pore-pressure and volume-change measurements. Corrections should therefore be selected according to the expected magnitude of each source of error and the level of accuracy required by the experimental programme.

5.3 Cross-sectional area correction

During axial compression, the specimen geometry changes continuously. In particular, the cross-sectional area generally increases as the specimen height decreases. Since deviatoric stress is calculated from the measured axial load and the current specimen area, use of the initial cross-sectional area throughout the test introduces an error that increases progressively with axial strain.

For a saturated specimen sheared under undrained conditions, the total specimen volume may be assumed to remain approximately constant. With axial compressive strain taken as positive, the corrected cross-sectional area may therefore be estimated as:

$$A_c = \frac{A_o}{(1-\varepsilon_a)} \tag{16}$$

where A_o is the initial cross-sectional area and ε_a is the axial strain.

For drained tests, the constant-volume assumption does not apply because the specimen is free to undergo volumetric deformation. The current area must therefore be determined by accounting for both axial and volumetric strains. For a sign convention in which compressive volumetric strain is positive:

$$A_c = A_o \frac{(1-\varepsilon_v)}{(1-\varepsilon_a)} \tag{17}$$

where ε_v is the volumetric strain. The adopted sign convention should be stated explicitly because alternative conventions may lead to a different algebraic form.

The corrected deviatoric stress is subsequently calculated from:

$$q = \frac{P}{A} \tag{18}$$

where P is the axial deviatoric load transmitted to the specimen. The corresponding major principal total stress is $\sigma_1 = \sigma_3 + q$ and, where pore-water pressure is measured, the effective principal stresses may then be obtained using the effective-stress relationships introduced in Section 4.2.

Neglecting changes in specimen geometry can produce increasingly significant errors as deformation develops. This is particularly important for specimens undergoing substantial volumetric deformation and for tests extending to large axial strains. The specimen geometry should therefore be updated throughout shearing whenever accurate stress-strain relationships are required. Particular attention is required when the specimen deviates significantly from an approximately cylindrical shape, for example because of barrelling, necking, or strain localisation, since conventional area-correction relationships based on uniform deformation may then become inaccurate.

5.4 Membrane correction

The latex membrane enclosing the specimen provides hydraulic isolation while allowing the externally applied cell pressure to be transmitted to the specimen. Because the membrane possesses finite stiffness, however, it also resists deformation of the specimen during shearing. The membrane resistance may influence both the axial and radial stresses acting on the specimen and therefore introduces an additional mechanical contribution to the measured response. Its influence is generally negligible for stiff materials tested under high confining pressures, but can become significant for loose sands, soft clays, low effective confining stresses, and specimens subjected to large radial strain, potentially increasing the measured peak strength and altering the apparent post-peak response.

In conventional triaxial data reduction, membrane resistance is often accounted for using a simplified correction applied directly to the measured principal stress difference [HG52]. For approximately constant-volume conditions, the membrane correction may be expressed as:

$$\Delta q_m = \frac{4E_m t_m}{D_c}\varepsilon_a \tag{19}$$

and the corrected deviatoric stress is obtained from:

$$q_{corr} = q_{meas} - \Delta q_m \tag{20}$$

where E_m is the Young's modulus of the membrane, $t_m$is the membrane thickness, D_c is the specimen diameter at the end of consolidation (i.e. at the start of shearing), and ε_a is the axial strain. This simplified correction recognises that part of the resistance measured during shearing may originate from deformation of the membrane rather than from the specimen itself.

More rigorous formulations treat the axial and radial contributions of membrane resistance separately. Considering the membrane as a thin elastic cylindrical shell, circumferential membrane tension associated with radial deformation produces an additional radial traction at the specimen boundary. For radial expansion, the magnitude of this membrane-induced radial stress may be represented in simplified form as:

$$\Delta\sigma_{3,m} = \frac{2E_m t_m}{D}|\varepsilon_r| \tag{21}$$

where D is the current specimen diameter at the considered stage of shearing and ε_r is the corresponding radial strain. The distinction between D_c and D is made because D_c refers to the reference specimen geometry at the start of shearing, whereas D accounts for the evolving specimen geometry during deformation.

In the expression above, $\Delta\sigma_{3,m}$ is defined as the positive magnitude of the additional compressive radial stress generated by membrane tension during radial expansion. The use of $|\varepsilon_r|$ avoids ambiguity where a compression-positive strain convention is adopted, for which radial expansion corresponds to a negative radial strain.

The corresponding corrected radial effective stress may then be written as:

$$\sigma'_{3,corr} = (\sigma_c - u) + \Delta\sigma_{3,m} \tag{22}$$

Where σ_c is the applied cell pressure and u is the measured pore-water pressure. The radial membrane contribution is particularly relevant when accurate determination of both q and p' is required, because an error in the radial effective stress propagates directly into both stress invariants.

The simplified correction to the principal stress difference and the separate radial-stress expression represent different levels of approximation. They should therefore be applied within the assumptions of the selected membrane-correction framework rather than combined indiscriminately, as this may result in double-counting of the membrane contribution. Where accurate effective stress paths or critical-state parameters are required, a consistent formulation that resolves the axial and radial membrane contributions should be adopted.

The magnitude of the membrane effect depends on membrane thickness and stiffness, specimen dimensions, strain level, and deformation mode. At large strains, barrelling, membrane wrinkling, and strain localisation may progressively invalidate the assumptions underlying simplified elastic membrane corrections. The selected correction procedure should therefore be consistent with the observed specimen deformation, the required level of accuracy, and the objectives of the experimental programme.

5.5 Axial deformation and system compliance correction

Axial displacement measured externally does not correspond exclusively to deformation of the specimen, but also to elastic deformation of the testing apparatus itself. The load frame, loading piston, load-measurement assembly, cell walls, specimen-

platen interfaces, drainage system, and other structural components all undergo small elastic deformations under load, which contribute to the measured axial displacement. If these contributions are not accounted for, specimen axial strain may be overestimated and the corresponding stiffness underestimated.

System compliance becomes particularly important in the small-strain range where the displacement associated with apparatus deformation may be comparable to, or even greater than, that of the specimen itself. System compliance may be characterised using an appropriate calibration procedure which is generally performed using a rigid reference specimen whose deformation is negligible compared with that of the testing system. The resulting compliance relationship is then subtracted from experimental measurements to estimate the true specimen deformation. Alternatively, local deformation transducers mounted directly on the specimen can substantially reduce the influence of apparatus compliance and bedding effects. Accurate deformation measurement and compliance correction is particularly important when determining small-strain elastic parameters such as the Young's modulus, E_o, and shear modulus, G_o.

5.6 Ram friction and load measurement

The loading piston passes through seals separating the pressure chamber from the external loading system. Friction is generated at these seals during piston movement, which may cause the force measured by an external load cell to differ from the axial force actually transmitted to the specimen.

The measured axial force may be represented as the combination of the specimen force and the contribution associated with piston friction. When the friction force is defined as a positive resistance to the imposed piston movement, the corrected specimen force may be expressed as:

$$P_{corr} = P_{meas} - P_f \tag{23}$$

Where P_{meas} is the axial force indicated by the external load-measurement system and P_f is the corresponding piston-friction contribution. The corrected deviatoric stress can subsequently be calculated as:

$$q_{corr} = \frac{P_{corr}}{A} = \frac{P_{meas} - P_f}{A} \tag{24}$$

Where A is the corrected specimen cross-sectional area.

The magnitude of piston friction depends on the piston and seal configuration, lubrication, cell pressure, direction of piston movement, and loading rate. Consequently, P_f should preferably be determined from an appropriate calibration performed under conditions representative of the actual test. In general, the friction correction may be represented by a calibration relationship of the form:

$$P_f = f(\delta, \dot{\delta}, \sigma_c, direction) \tag{25}$$

where $\delta \; and \; \dot{\delta}$ denote piston displacement and velocity, respectively, and σ_c is the applied cell pressure. If calibration demonstrates that friction is approximately constant over the relevant range of movement, a constant value of P_f may instead be adopted.

The influence of piston friction is particularly important during cyclic or load-reversal testing because the direction of friction changes when the direction of piston movement is reversed. This behaviour may introduce artificial hysteresis into the measured force–displacement response if it is not adequately accounted for. Therefore, where an external load cell is used, periodic friction-calibration tests should be performed to quantify and correct this additional resistance.

Several approaches are available to minimise the effect of piston friction. Modern research triaxial systems often employ an internal load cell positioned within the triaxial pressure chamber and close to the specimen. Because the axial force is measured downstream of the piston seals, the contribution of seal friction is largely excluded from the measured specimen force.

5.7 Pore pressure system corrections

Reliable pore-pressure measurement is essential for the determination of effective stresses in triaxial testing. In practice, the measured pore pressure may be influenced by the compressibility of the hydraulic system, entrapped air, tubing flexibility, and the response characteristics of the pressure transducer. These effects can attenuate or delay the transmission of pressure changes between the specimen and the transducer, causing the recorded pore pressure to differ from that developing within the specimen.

The influence of the measurement system becomes particularly important during rapid undrained or cyclic loading, where pore pressure may vary rapidly with time. Any error or delay in the measured pore pressure directly affects the calculated effective stresses and may therefore influence the interpretation of effective stress paths and cyclic or liquefaction behaviour.

Unlike some of the corrections discussed in the preceding sections, pore-pressure measurement errors are preferably minimised through appropriate system preparation and calibration rather than corrected retrospectively. Drainage and pressure-measurement lines should be thoroughly saturated, entrapped air minimised, and pressure transducers appropriately calibrated. Where rapid loading is involved, the dynamic response of the hydraulic measurement system should also be sufficiently fast relative to the imposed loading rate.

5.8 Large strain and non-uniform deformation effects

As deformation progresses to large strain levels, the assumption of homogeneous specimen deformation underlying the conventional area correction described in Section 5.3 becomes progressively less representative. The specimen may cease to deform uniformly, while strain localisation and shear-band development can produce highly heterogeneous stress and strain distributions. Consequently, the assumption of a homogeneous cylindrical specimen becomes increasingly inappropriate [BG65].

While deformation remains reasonably uniform, the corrected cross-sectional area still provides an appropriate global measure, but its physical representativeness decreases as non-uniform deformation develops. In particular, end restraint at the specimen–platen interfaces may promote radial non-uniformity and lead to the development of a barrel-shaped specimen. Consequently, the specimen diameter may vary considerably with height, as illustrated in Figure 14. Under these conditions, a diameter measured at mid-height may exceed the equivalent average specimen diameter and therefore should not necessarily be regarded as representative of the entire specimen cross-section.

At larger strains, deformation may become further concentrated within localised zones or shear bands. The resulting stress and strain fields are then highly heterogeneous, and global measurements of axial displacement, specimen volume, and applied force no longer provide a complete description of the local material response. Consequently, stresses and strains calculated using conventional homogeneous-specimen assumptions should be interpreted as global or equivalent quantities, rather than as direct measures of the local conditions within the deforming specimen.

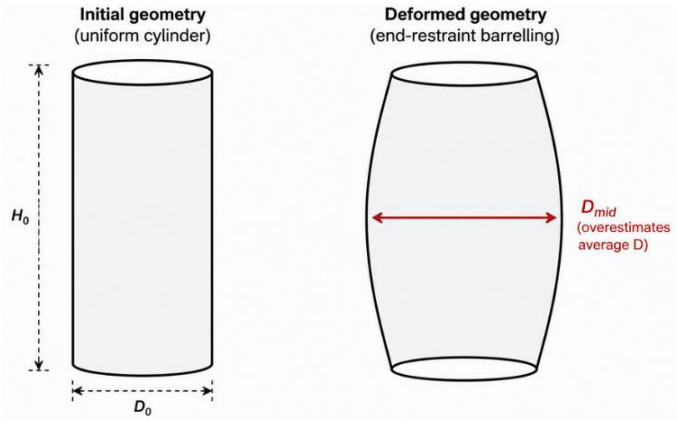


Figure 14: Effect of end restraint on specimen shape: uniform initial geometry versus barrel-shaped deformation, which causes a mid-height diameter measurement to overestimate the average specimen diameter.

Local deformation transducers, radial measurements at multiple elevations, or optical measurement techniques can provide additional information on the evolution of specimen geometry and the development of strain localisation. Such measurements are particularly valuable for characterising post-peak response and identifying the transition from relatively homogeneous deformation to localised failure.

Large-strain measurements nevertheless remain important for investigating failure mechanisms, post-peak behaviour, residual strength, and the evolution towards an ultimate or critical-state condition. However, once substantial barrelling or strain localisation has developed, conventional corrections based on homogeneous deformation cannot fully reconstruct the local stress and strain fields. Data obtained in this regime should be interpreted with caution, particularly when used for constitutive-model calibration based on homogeneous deformation assumptions.

5.9 Relative importance of measurement corrections

The significance of the measurement corrections and system effects discussed in the preceding sections depends on the tested material, stress level, drainage conditions, deformation range, loading rate, measurement configuration, and objectives of the experimental programme. Their relative importance therefore varies between tests, and not all corrections necessarily require the same level of consideration (Table 2).

Cross-sectional area correction is relevant throughout triaxial compression because specimen geometry evolves during loading. Membrane resistance becomes particularly significant when the membrane stiffness is non-negligible relative to the strength or confining stress of the specimen, as may occur for soft soils, loose granular materials, and tests conducted at low effective confining stresses. System compliance is particularly important when accurate deformation and stiffness measurements are required, especially at small strains. Ram friction primarily affects force measurements obtained using external load cells, whereas pore-pressure measurement and hydraulic-system effects become increasingly important during rapid or cyclic undrained loading, when the response time of the pressure-measurement system may influence the recorded pore-pressure response.

The relevance and magnitude of each effect should therefore be evaluated with respect to the specific testing conditions and the parameters to be derived from the experimental results. Corrections should be based, where possible, on appropriate calibration or independently characterised system properties. Applying corrections without establishing their relevance may introduce unnecessary assumptions, whereas neglecting a significant measurement effect may introduce systematic bias into the calculated response.

Table 2. Summary and relative importance of measurement corrections and system effects in triaxial testing.

Correction or system effect	Primary influence	Particularly important for
Cross-sectional area	Calculated deviatoric stress	All triaxial compression tests, particularly at increasing strain
Membrane resistance	Deviatoric and radial stress; p′–q stress path	Soft soils, loose granular materials, low effective confining stresses
System compliance	Measured axial deformation and calculated stiffness	Small-strain response and stiffness/modulus determination
Ram/piston friction	Measured axial force and deviatoric stress	Systems using external load cells; cyclic or load-reversal tests
Pore-pressure measurement and hydraulic-system effects	Measured pore pressure and effective stress path	Rapid and cyclic undrained loading
Large-strain/non-uniform deformation	Representativeness of calculated global stresses and strains	Large-strain, post-peak, and localised deformation

Measurement corrections therefore form an integral part of triaxial data reduction rather than a separate post-processing step. A consistent correction framework improves the reliability of the calculated stress and strain variables and is particularly important when experimental results are used to determine constitutive parameters, compare different materials or specimen-preparation procedures, or calibrate and validate constitutive models.

6 Interpretation, Limitations & Good laboratory practice

6.1 Introduction

The interpretation of triaxial test results extends beyond the direct examination of measured stress–strain curves. It involves translating experimental observations into meaningful strength, stiffness, volumetric and critical-state parameters while accounting for the imposed stress path, drainage conditions, initial specimen state and uncertainties introduced throughout the testing chain procedure, including specimen preparation, testing and data reduction.

Triaxial interpretation is therefore inherently condition-dependent. The measured response reflects not only the mechanical characteristics of the geomaterial, but also the specific conditions under which the test was performed and the data generated. Particular attention should be given to the assumption of stress and strain uniformity. While the specimen response may initially be interpreted in terms of approximately homogeneous material behaviour, the development of heterogeneity or strain localisation, such as a shear band, causes the measured global response to increasingly reflect the behaviour of the specimen as a structure and the associated boundary conditions. In this regime, interpretation of the intrinsic material behaviour becomes a boundary-value problem, and global stress–strain measurements may no longer provide a direct representation of the local constitutive response.

Rigorous interpretation should therefore consider the specimen state, testing conditions, measurement methodology, and laboratory-scale limitations. Good laboratory practice is essential to ensure that the resulting data are reproducible, comparable, and suitable for constitutive model calibration.

6.2 Interpretation of triaxial results

6.2.1 Stress–Strain response

The stress–strain response provides the primary indication of the mechanical evolution of a specimen during shearing, as illustrated in Figure 15. Its interpretation in terms of material behaviour relies on the stress and strain fields remaining sufficiently homogeneous within the specimen. At small strains, the response is generally stiffness-dominated and may be approximately quasi-linear over a limited strain range, although soil stiffness is inherently strain-dependent. With increasing axial strain, progressive yielding and irreversible deformation develop, followed by the mobilisation of shear strength. Depending on the material, initial state, stress history, drainage conditions, and effective confining stress, the subsequent response may involve progressive strain hardening, the development of a distinct peak strength followed by strain softening, or a gradual approach towards a large-strain condition [SW68] [Woo90] [Lad16].

Under drained conditions, dense granular materials and overconsolidated soils commonly develop a pronounced peak strength associated with particle interlocking and dilatancy, followed by strain softening towards a large-strain condition. Loose granular materials and normally consolidated soils more commonly exhibit progressive strain hardening without a pronounced peak, although the response also depends on the effective confining stress and the initial state relative to the critical-state condition. The maximum deviatoric stress, when present, therefore represents a state-dependent peak rather than a unique material constant.

Under undrained conditions, the stress–strain response can differ substantially because the volumetric tendency of the soil influences the evolution of effective stress

through pore-pressure generation. Dense or overconsolidated specimens may exhibit continued strain hardening towards critical state and do not necessarily develop the peak-and-softening response commonly associated with drained dilative behaviour. Conversely, loose and strongly contractive specimens may develop an undrained peak followed by pronounced strain softening and, under sufficiently contractive conditions, a flow-type or static-liquefaction response [Cas69] [Pou81].

The stress–strain curve should therefore not be interpreted in isolation. Its mechanical significance becomes clearer when considered together with the volumetric or pore-pressure response and the corresponding effective stress path, as discussed in the following sections.

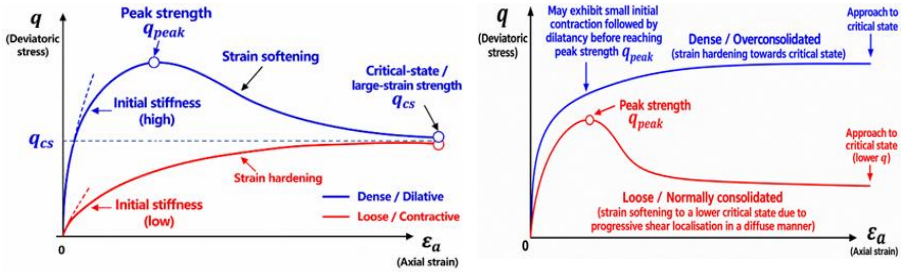


Figure 15: Schematic deviatoric stress–strain responses under (a) drained and (b) undrained condition illustrating dense and loose behaviour.

6.2.2 Volumetric and pore-pressure response

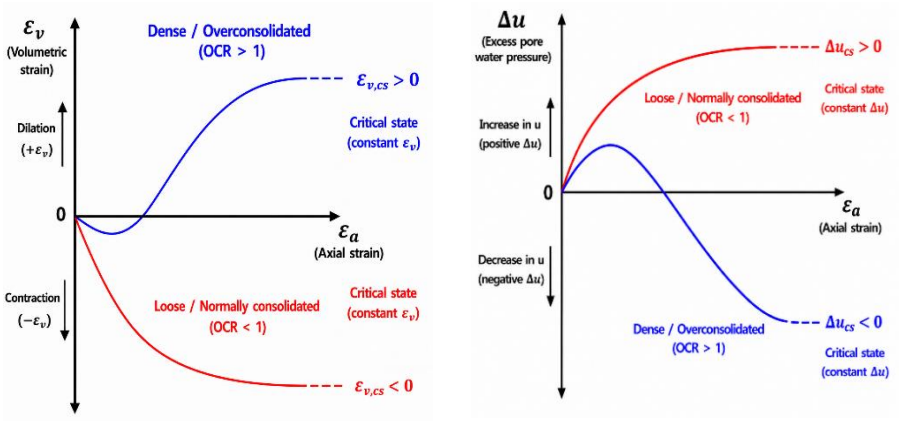
The volumetric response of a soil during shearing is governed by its tendency to contract or dilate and provides essential information for interpreting its state-dependent behaviour. Under drained conditions, this tendency is expressed directly as a change in specimen volume. Contractive behaviour produces a decrease in volume, whereas dilative behaviour produces an increase in volume. Dense or overconsolidated specimens may initially contract before reaching a transition from contraction to dilation, while loose or normally consolidated specimens generally exhibit a predominantly contractive response [SW68] [Woo90].

Under undrained conditions, overall volume change is prevented and the same contractive or dilative tendency is instead reflected in the generation of excess pore-water pressure. A contractive tendency generally generates positive excess pore-water pressures ($\Delta u > 0$), resulting in a reduction in mean effective stress p'. Conversely, the development of a dilative tendency causes the pore pressure to decrease and may result in negative excess pore pressure ($\Delta u < 0$) relative to the initial condition, thereby increasing the mean effective stress p' during shear. Dense or overconsolidated specimens may initially generate positive excess pore pressure during the initial contractive phase before the onset of dilation causes the pore-pressure trend to reverse.

Loose or normally consolidated specimens, by contrast, generally maintain a contractive tendency and consequently generate positive excess pore-water pressure during monotonic undrained shearing (Figure 16).

Drained volume change and undrained pore-pressure generation can therefore be regarded as different manifestations of the same underlying volumetric tendency. This relationship is fundamental to the interpretation of triaxial results. Contraction observed during drained shearing is generally associated with positive pore-pressure generation under undrained conditions for a comparable initial state, whereas dilation is associated with decreasing pore pressure and may ultimately result in negative excess pore pressure. The magnitude and evolution of these responses depend on factors including initial density or void ratio, effective confining stress, stress history and fabric.

As the specimen approaches critical state, the tendency for further volumetric change progressively diminishes. At critical state, the specimen undergoes continuous deformation at an approximately constant stress ratio and constant specific volume, with the corresponding pore-pressure response reaching a stable condition (Figure 16). The implications of these volumetric and pore-pressure responses for the evolution of mean effective stress and the p′–q stress path are discussed in Section 6.2.3.



(a) (b)

Figure 16: Schematic illustration of (a) volumetric response under drained conditions and (b) corresponding excess pore-water-pressure response under undrained conditions during triaxial shearing for dense and loose specimens.

6.2.3 Effective Stress Paths

The effective stress path provides a particularly useful representation of the evolution of the stress state during triaxial shearing. Using the stress variables p' and q defined

previously, the trajectory followed by a specimen in $p' - q$ space describes the combined evolution of mean effective stress and deviatoric stress. This representation complements the stress–strain, volumetric, and pore-pressure responses discussed in the preceding sections [SW68] [Woo90].

The effective stress path depends strongly on the imposed loading and drainage conditions. Under drained conditions, excess pore-water pressure generated during shearing is allowed to dissipate, and the effective stress path is governed primarily by the externally imposed stresses. Under undrained conditions, by contrast, pore-water pressure evolves during shearing and directly modifies the effective stress state. Consequently, drained and undrained specimens may follow markedly different effective stress paths even when subjected to similar external loading conditions.

6.2.3.1 Drained effective stress paths

During a conventional consolidated-drained (CD) triaxial compression test performed at constant cell pressure, drainage is permitted and excess pore-water pressure is allowed to dissipate. If the cell pressure and back pressure remain constant during shearing, the minor principal effective stress σ_3' is constant. Consequently, the deviatoric stress:

$$q = \sigma_1' - \sigma_3' \tag{26}$$

increases as axial loading proceeds, while the mean effective stress:

$$p' = \sigma_3' + \frac{q}{3} \tag{27}$$

The drained effective stress path therefore follows a characteristic trajectory towards increasing p′ and q. For constant σ_3', its idealised slope in the $p' - q$ plane is:

$$\frac{dq}{dp'} = 3 \tag{28}$$

This relationship describes the imposed stress path but does not imply that specimens with different initial states exhibit identical mechanical responses. Dense and loose specimens tested under the same effective confining stress may initially follow similar paths in $p' - q$ space while exhibiting markedly different stress-strain and volume-change behaviour. A dense specimen may mobilise a pronounced peak strengh associated with dilation and subsequently strain softening, whereas a loose specimen may remain predominantly contractive and progressively harden towards its large-strain condition.

The drained effective stress path must then be interpreted together with the evolution of axial and volumetric response. In particular, the position or direction of the stress path alone does not by itself indicate whether the specimen is contracting or dilating.

6.2.3.2 Undrained effective stress paths

The interpretation is fundamentally different under consolidated-undrained (CU) conditions because drainage is prevented and pore-water pressure evolves during shearing. Changes in pore-water pressure directly modify the effective stresses and, consequentely, the mean effective stress p'. The effective stress path is therefore governed by the interaction between applied deviatoric loading and pore-pressure generation. Its shape and direction provide important information regarding the contractive or dilative tendency of the soil and the evolution of its effective stress state during shearing.

A **loose or strongly contractive specimen** generally generates positive excess pore-water pressure ($\Delta u>0$) causing p' to decrease. Its effective stress path consequently moves towards lower mean effective stress as shearing progresses. If the contractive response is sufficiently strong, p′ may decrease rapidly and the specimen may develop an undrained peak followed by pronounced strain softening. In highly contractive materials, this behaviour may be associated with flow-type instability or static liquefaction [Cas69] [Pou81]..

A dense or overconsolidated specimen may also initially generate positive excess pore pressure as a result of an initial contractive tendency, causing the effective stress path to move towards lower p'. As the soil develops a dilative tendency, however, the rate of pore-pressure generation decreases and the pore pressure trend may reverse, and subsequently fall. The effective stress path then turns towards increasing p'. This reversal is an important indication of the transition from contractive to dilative behaviour under undrained conditions, and is called phase transformation.

The contrasting trajectories of loose/contractive and dense/dilative specimens illustrate why effective stress paths should be interpreted together with the corresponding pore-pressure and stress–strain responses. In particular, the evolution of p' reflects the changing pore-pressure response and provides insight into the state-dependent behaviour of the specimen throughout undrained shearing.

Unconsolidated-undrained (UU) tests provide more limited information for effective stress-path interpretation because they are conventionally performed and interpreted in total-stress terms. Unless reliable pore-water-pressure measurements and sufficient information on the initial effective stress state are available, their use within an effective-stress or critical-state framework is therefore limited.

6.2.3.3 Relationship with the critical state

Within the Critical State Soil Mechanics framework, specimens with different initial states and volumetric tendencies may follow markedly different stress paths but ultimately tend towards a common critical-state condition, represented in $p' - q$ space by the Critical State Line (CSL) (Figure 17). The CSL therefore provides a useful large strain reference for interpreting the evolution of the effective stress path. Under

undrained conditions in particular, differences in contractive or dilative tendency influence pore-pressure evolution and hence the direction of the effective stress path. The stress path should therefore be interpreted together with the corresponding stress–strain, volumetric-strain, and pore-pressure responses rather than in isolation.

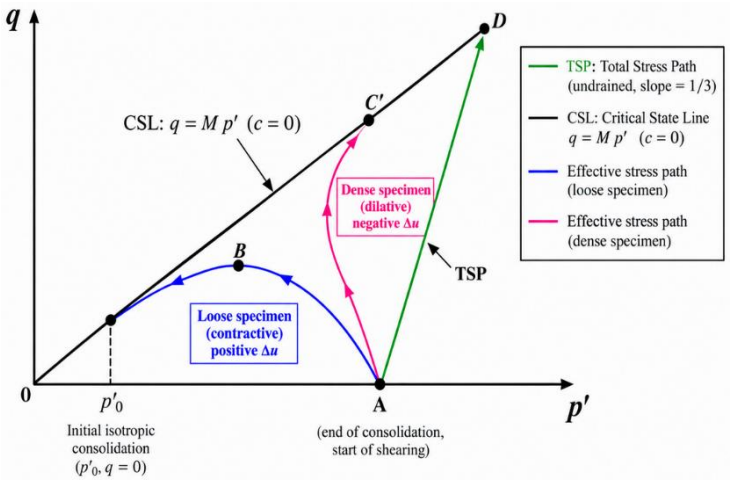


Figure 17: Schematic effective stress paths for drained (CD) and undrained (CU) triaxial compression in p′–q space, together with the Critical State Line.

The interpretation of stress path should therefore not be based solely on whether it intersects or approaches a particular strength line. Its shape, direction, and evolution should be considered together with the corresponding $q - \varepsilon_a$ response and either the $\varepsilon_v - \varepsilon_a$ response for drained tests or the $\Delta u - \varepsilon_a$ response for undrained tests. Taken together, these representations provide a coherent description of the state-dependent evolution of the specimen during shearing. The physical definition and quantitative description of peak, critical-state, and residual strength are presented in Section 6.3.

6.3 Strength definitions: Peak, Residual, and Critical State

6.3.1 Peak strength

Peak strength corresponds to the maximum shear resistance mobilised during a particular loading path. In conventional triaxial compression, it is commonly associated with the maximum deviatoric stress (q_{peak}), although the corresponding effective stress state should also be considered because the value of q alone does not uniquely define the stress ratio at failure [Woo90] [Lad16].

Peak strength is strongly state-dependent. It is influenced by initial density or void ratio, effective confining stress, stress history, fabric, cementation or bonding, drainage conditions, and loading history [BJ85]. Consequently, peak strength should not generally be regarded as a unique intrinsic material constant.

For granular soils under drained shearing, the development and magnitude of peak strength depend strongly on the initial density and effective stress level, with pronounced peak strength in dense soils being closely associated with dilatancy and particle interlocking. As shearing proceeds, the constrained rearrangement of particles produces an additional resistance associated with dilation. The resulting peak friction angle may therefore exceed the critical-state friction angle ($\varphi'_{peak} > \varphi'_{cs}$). After the maximum resistance has been mobilised, continued rearrangement reduces the contribution of the initial dense structure and the response may soften towards the critical-state condition.

For structured, cemented, or bonded soils, a pronounced peak can also arise from bonding and fabric structure. Post-peak softening may then reflect progressive destructuration or bond degradation rather than dilatancy alone.

Under undrained conditions, peak strength requires a different interpretation because contractive or dilative tendencies modify pore pressure and therefore effective stress. A loose, strongly contractive soil can develop a pronounced undrained peak followed by rapid strain softening as positive excess pore pressure reduces mean effective stress. Consequently, such a peak should be interpreted together with the pore-pressure response and effective stress path.

6.3.2 Residual strength

Residual strength refers to the limiting shear resistance mobilised after very large displacement, typically after the original soil structure has been substantially altered and a persistent shear surface has developed [Ske85]. It should be distinguished from both post-peak and critical-state strength.

This distinction is particularly important for fine-grained soils containing platy clay minerals where large shear displacement may progressively align particles along the shear surface, reducing the mobilised friction angle below the critical-state value ($\varphi'_r < \varphi'_{cs}$). It is therefore relevant to reactivated landslides, pre-existing slip surfaces, faults, and old shear zones, where stability may be governed by an already developed shear fabric rather than by the intact peak strength.

Conventional triaxial tests are generally well suited to characterising peak behaviour and to approaching critical-state conditions, but they may not be ideal for obtaining a fully developed residual strength because of limited axial displacement and strain localisation.

6.3.3 Critical state strength

Critical-state strength has a different physical meaning from both peak and residual strength. Within Critical State Soil Mechanics, the critical state corresponds to the condition in which the soil continues to deform at constant stress and constant specific volume under drained condition or constant excess pore-water pressure under undrained condition [RSW58] [SW68] [Woo90].

In $p' - q$ space, critical states for a given material are represented by the Critical State Line (CSL):

$$q = Mp' \tag{29}$$

where M is the critical-state stress ratio, and represents the slope of the CSL. For a given friction angle, M depends on the intermediate principal stress, therefore the slope is different in compression and in extension.

For triaxial compression, the critical-state stress ratio is related to the critical-state friction angle φ'_{cs} by:

$$M_c = \frac{6\ sin\ \varphi'_{cs}}{3-sin\ \varphi'_{cs}} \tag{30}$$

For triaxial extension:

$$M_e = \frac{6\ sin\ \varphi'_{cs}}{3+sin\ \varphi'_{cs}} \tag{31}$$

Critical-state strength therefore provides a large-strain reference that is distinct from the state-dependent peak strength mobilised earlier during shearing. For a given soil under specified loading conditions, it characterises the resistance associated with continued deformation after the effects responsible for peak strength, such as dilatancy or initial structure, have diminished.

Critical state is fundamentally defined by both stress and volume conditions. In the $v - \ln p'$ plane, critical states are commonly represented by a relationship of the form:

$$v = \Gamma - \lambda \ln p' \tag{32}$$

where Γ defines the position of the critical-state line and λ its slope in the $v - \ln p'$ representation. The $p' - q$ and $v - \ln p'$ relationships represent complementary projections of the critical-state framework.

6.3.4 Relationship with Mohr–Coulomb strength parameters

The Mohr–Coulomb failure criterion provides one of the most widely used engineering representations of soil shear strength. In effective-stress terms, the shear stress at failure is expressed as [Woo90] [Lad16] [Atk07]:

$$\tau_f = c' + \sigma_n' tan\varphi' \tag{33}$$

where c' is the effective cohesion intercept, φ' is the effective friction angle, and σ_n' is the effective normal stress acting on the failure plane. The criterion therefore represents shear strength through a linear relationship between normal effective stress and shear resistance over a selected stress range (Figure 18 and 19).

In triaxial testing, the Mohr–Coulomb parameters are generally determined from a series of specimens sheared at different effective confining stresses rather than from a single stress–strain curve. A representative failure condition is selected for each test, and the corresponding principal effective stresses are used to construct Mohr circles and determine a common failure envelope.

For conventional triaxial compression, the principal effective stresses at the selected failure condition are $\sigma_{1,f}'$ and $\sigma_{3,f}'$ and the Mohr circle has centre:

$$C = \frac{\sigma_{1,f}' + \sigma_{3,f}'}{2} \tag{34}$$

and radius:

$$R = \frac{\sigma_{1,f}' - \sigma_{3,f}'}{2} \tag{35}$$

The tangent envelope to the set of the Mohr circles provides an engineering estimate of c' and φ' . These parameters therefore depend partly on the criterion used to define the selected failure states.

The choice of failure condition is particularly important when interpreting triaxial results. If the failure states are selected at the maximum mobilised resistance, the resulting envelope represents peak strength, and the corresponding friction angle may be denoted φ_{peak}'. For dense or dilative granular soils, peak strength includes the additional resistance associated with dilatancy and particle interlocking, and may therefore exceed the critical-state friction angle ($\varphi_{peak}' > \varphi_{cs}'$).

If, instead, the stress states reached at critical state are used, the resulting envelope represents critical-state strength, and the corresponding friction angle φ_{cs}'. This distinction is important because peak and critical-state parameters represent different physical conditions and should not be used interchangeably. Unlike peak strength, critical-state strength does not include the transient enhancement of resistance associated with dilatancy and particle interlocking. It therefore provides a more consistent large-strain reference for characterising the material.

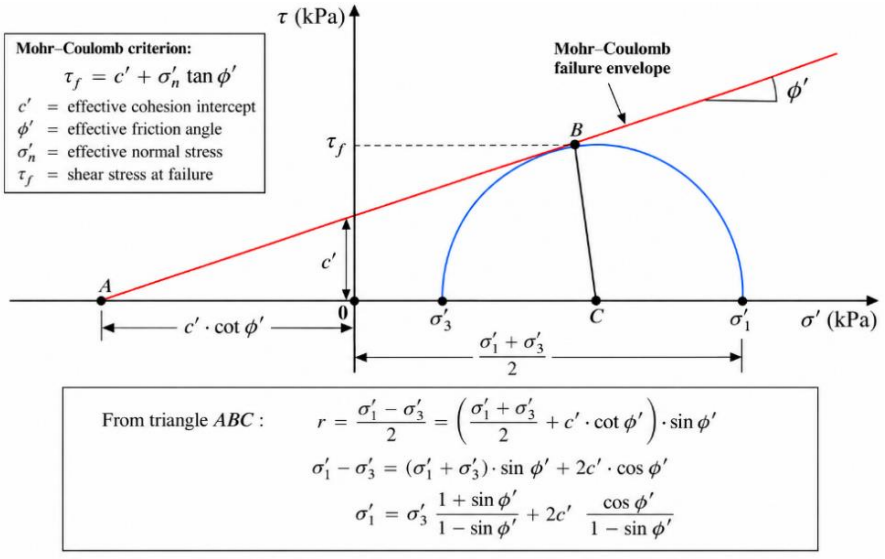


Figure 18: Mohr circle corresponding to a selected failure state in conventional triaxial compression and the associated Mohr–Coulomb failure envelope.

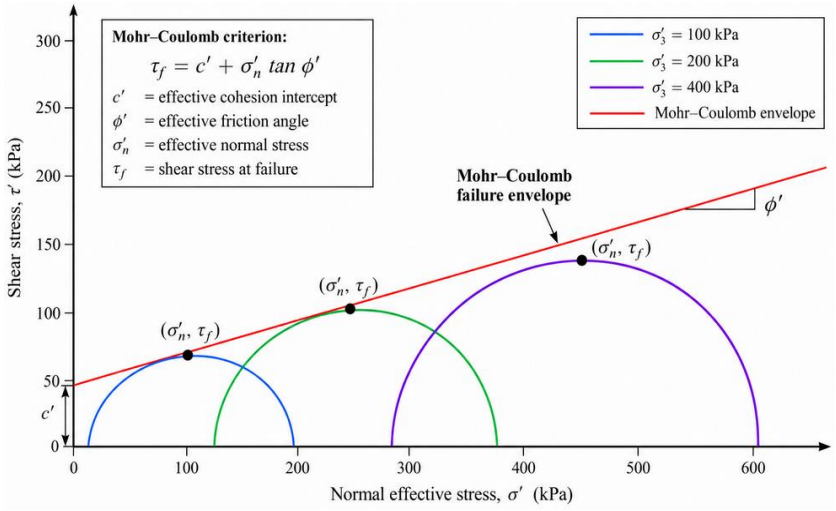


Figure 19: Mohr circles at failure for three confining pressures and the corresponding Mohr–Coulomb strength envelope.

For granular soils, the critical-state envelope is commonly expected to have no effective cohesion intercept, and pass approximately through the origin in effective-stress space, such that:

$$c'_{cs} \approx 0 \tag{36}$$

and consequently:

$$\tau_{cs} = \sigma'_n tan\varphi'_{cs} \tag{37}$$

An apparent non-zero effective cohesion intercept obtained from peak-strength data should therefore be interpreted with caution. When peak strengths obtained at different confining stresses are fitted using a linear Mohr–Coulomb envelope over a limited stress range, a non-zero intercept may arise even for an essentially cohesionless granular material. This may result from curvature of the actual strength envelope, stress-dependent dilatancy, the selected range of confining stresses, or experimental scatter. Accordingly, an apparent c' obtained from a linear regression should not automatically be assigned a direct physical meaning.

For genuinely structured, cemented, or bonded soils, however, a non-zero intercept may reflect real contributions from bonding or structure. Even in these materials, the resulting parameters should be interpreted with respect to the stress range and strain level over which they were determined, because progressive destructuration during shearing may modify the mobilised strength.

An equivalent representation of Mohr–Coulomb strength relationship can be expressed in $p' - q$ space.

For conventional triaxial compression, the Mohr–Coulomb failure criterion becomes:

$$q_f = \frac{6c' cos\varphi'}{3-sin\varphi'} + \frac{6p'_f sin\varphi'}{3-sin\varphi'} \tag{38}$$

Thus, a series of selected triaxial failure states can be represented by a straight line in $p' - q$ space.

For a cohesionless material ($c' = 0$), this reduces to:

$$q_f = Mp'_f \tag{39}$$

With:

$$M = \frac{6\ sin\varphi'}{3-sin\ \varphi'} \tag{40}$$

At critical state, $\varphi' = \varphi'_{cs}$, giving:

$$q_{cs} = M_{cs} p'_{cs} \tag{41}$$

which corresponds to the Critical State Line introduced in Section 6.3.3.

This relationship demonstrates that the Mohr–Coulomb and Critical State Soil Mechanics provide related but distinct descriptions of soil strength. As shown in the previous section, the critical-state stress ratio is directly related to the critical-state friction angle, φ_{cs}, thereby linking the Critical State Line to the Mohr–Coulomb strength criterion. The principal difference lies in their scope: Mohr–Coulomb provides a practical engineering representation of shear strength at a selected condition over a specified effective stress range, whereas Critical State Soil Mechanics places strength within a broader framework that also accounts for the soil state and its evolution in stress–volume space during shearing.

The critical-state framework therefore provides a basis for understanding both the strength mobilised during shearing and why specimens with different initial states may exhibit different stress–strain, volumetric, and peak-strength responses while tending towards a common critical-state relationship at large strains.

For the interpretation of experimental results, it is therefore essential to specify whether reported values of c' and φ' correspond to peak, critical-state, or another explicitly defined strength condition, together with the effective stress range over which they were determined. Reporting a single value of φ' without identifying the associated strength definition may obscure important state-dependent behaviour and lead to inappropriate comparison between tests.

6.4 Influence of experimental conditions

Parameters derived from triaxial testing can be significantly affected by the experimental conditions. Incomplete saturation may lead to erroneous interpretation of undrained strength and stiffness. Failure to account for changes in specimen cross-sectional area generally leads to overestimation of deviator stress and stress ratios at large axial strains, while neglecting membrane resistance may lead to overestimation of the measured shear strength, particularly for soft or weak materials tested at low effective stress levels. Failure to correct for apparatus compliance underestimates small-strain stiffness, particularly when external displacement measurements are used. The choice of deformation-measurement system can therefore substantially influence stiffness parameters. Finally, strain localisation at large deformation produces non-representative post-peak responses that should not be used for constitutive calibration.

These effects demonstrate that reported constitutive parameters cannot be interpreted independently of the experimental procedure. Comparisons between datasets should therefore consider not only material characteristics, but also specimen preparation, saturation, consolidation, loading rate, instrumentation, and data-reduction procedures.

6.5 Experimental limitations

6.5.1 Boundary effects

Friction and restraint at the specimen–platen interfaces restrict lateral deformation near the specimen ends and may generate non-uniform stress and strain distributions. With increasing deformation, this restraint can contribute to barrelling and influence the location and development of strain localisation. Lubricated or specially designed end platens can reduce end restraint, but the associated interface behaviour should still be considered when interpreting measured strength and deformation patterns, particularly where localisation or highly non-uniform deformation occurs [BG65].

6.5.2 Scale effects

Laboratory specimens represent only a limited volume of the natural geomaterial and may not fully capture field-scale heterogeneity. Scale effects become particularly important when the characteristic particle size or structural features are large relative to the specimen dimensions, a limitation especially relevant for coarse gravels, rockfill materials, and structured geomaterials containing large inclusions or aggregates. If the specimen dimensions are insufficient to represent an appropriate Representative Elementary Volume (REV), the measured response may depend strongly on specimen size and particle-scale or structural configuration.

6.5.3 Strain localisation

At large strains, deformation tends to concentrate within narrow shear bands, typically a few grain diameters thick, rather than remaining uniformly distributed throughout the specimen. Once localisation develops, global strain measurements represent an average response that may differ substantially from the local deformation within the shear zone. Post-localisation stress–strain behaviour therefore becomes increasingly dependent on specimen geometry, boundary conditions, and localisation characteristics. Such data remain valuable for studying failure and post-peak response, but should be used cautiously for continuum constitutive calibration when the adopted model assumes homogeneous deformation.

6.5.4 Time-dependent behaviour

The mechanical response of geomaterials may depend on loading rate and test duration. Fine-grained soils can exhibit creep, consolidation and rate effects, while granular and structured materials may also show rate dependence under particular conditions. In CD tests, the shearing rate must be sufficiently low to allow pore-pressure

dissipation and maintain the intended drained condition; in CU tests, the selected rate must permit representative pore-pressure measurement while maintaining the intended undrained boundary condition. Differences in loading rate and test duration should consequently be considered when comparing results obtained from different testing conditions or experimental programmes.

6.6 Good laboratory practice (GLP)

Reliable triaxial testing requires repeatability, consistency and traceability throughout specimen preparation, saturation, consolidation, shearing, measurement and data reduction. Where failure envelopes or constitutive parameters are required, testing over an appropriate range of confining stresses, with appropriate replication, is essential for obtaining robust results [ISO18] [HE14] [Lad16].

A complete experimental record should document the variables required to reconstruct the specimen state, stress path, measurement configuration and data-reduction procedure. A recommended minimum record is summarised in Table 3.

Instrumentation quality is equally critical. It should be routinely calibrated and verified. Load cells require regular calibration, pore-pressure systems should be fully saturated, free of entrapped air (purged) and checked for adequate response time, and volume-change systems should be independently validated and, where necessary, temperature compensated. For small-strain stiffness measurements and advanced constitutive modelling, local strain measurements are strongly recommended, because they reduce the influence of apparatus compliance, and specimen–platen bedding effects [HE14] [Lad16].

Table 3. Recommended minimum information for triaxial test documentation and quality control.

Stage	**Information to document**
Specimen	Preparation method; dimensions; initial void ratio e_0; water content w; degree of saturation Sr where relevant
Saturation	Saturation procedure; back pressure; achieved B-value
Consolidation	Consolidation stress path; target and achieved effective stresses; OCR where relevant; final specimen state
Shearing	Drainage condition; loading path; axial strain rate; test duration
Instrumentation	Load, displacement, pore-pressure and volume-change measurement systems; calibration information
Corrections	Cross-sectional area, membrane, compliance, ram-friction and other data-reduction corrections applied
Final condition	Failure mode; localisation; specimen geometry and relevant post-test observations
Quality control	Repeatability, calibration checks and relevant estimates of experimental uncertainty

Good laboratory practice ultimately provides the link between experimental procedure and interpretation. The reliability of constitutive parameters depends not only on the theoretical framework and interpretation methods used to derive them, but also on the quality, traceability and representativeness of the measurements from which they are obtained.

7 Conclusions

Triaxial testing provides a powerful experimental framework for characterising the mechanical and hydro-mechanical behaviour of soils and rocks under controlled stress and drainage conditions. Its principal strength lies not only in the determination of conventional strength parameters, but also in its ability to investigate the coupled evolution of stress, deformation, volume change, and pore-water pressure over a prescribed loading path. When interpreted within an effective-stress framework, these measurements provide insight into state-dependent behaviour, including contraction and dilation, strain hardening and softening, pore-pressure generation, stress-path evolution, and the approach towards critical-state conditions.

The quality of this interpretation depends fundamentally on the initial state and experimental history of the specimen. Specimen preparation, sampling disturbance, storage, initial density and fabric, water content, saturation, stress history, and dimensional characterisation should therefore be regarded as integral components of the experiment rather than as preliminary operations. Similarly, saturation, consolidation, drainage conditions, and shearing rate must be selected and controlled consistently with the objectives of the test. The triaxial procedure is an interconnected sequence in which the quality of each stage influences the reliability of the subsequent response.

Reliable interpretation also requires recognition of the difference between the measured response and the intrinsic material response. Changes in specimen geometry, membrane resistance, system compliance, ram friction, hydraulic-system effects, and large-strain non-uniform deformation can introduce systematic biases into calculated stresses and strains. Their relative importance varies with the material and testing conditions, and corrections should therefore be applied on the basis of their physical relevance and appropriate calibration rather than as an automatic post-processing procedure. At large strains, where barrelling or strain localisation develops, conventional homogeneous-specimen assumptions become progressively less representative and calculated stresses and strains should be interpreted as global or equivalent quantities.

The interpretation of triaxial results must consequently remain closely linked to the imposed stress path, drainage condition, and initial specimen state. Stress-strain curves should be considered together with volumetric or pore-pressure responses and effective stress paths, while reported strength parameters should be associated explicitly with the condition at which they were determined. Peak, critical-state, and residual strengths represent different physical conditions and should not be used interchangeably. Similarly, Mohr-Coulomb parameters provide a practical engineering representation of strength over a selected stress range, whereas the critical-state framework

provides a broader description relating stress, volume, initial state, and the evolution of material behaviour.

Ultimately, a technically successful triaxial test is not defined solely by the completion of a prescribed loading programme, but by the traceability, consistency, representativeness, and interpretability of the entire experimental process. Appropriate specimen preparation, calibrated instrumentation, controlled testing procedures, justified measurement corrections, systematic documentation, and critical interpretation are therefore equally important. Good laboratory practice provides the link between these elements and ensures that the parameters derived from triaxial testing can be used with confidence for comparison between materials, constitutive-model calibration and validation, and geotechnical engineering analysis.

References

[Ari12] M. Aris, N. Benahmed, and S. Bonelli. *Experimental Geomechanics: A Laboratory Study on the Behaviour of Granular Material Using Bender Elements.* European Journal of Environmental and Civil Engineering, 16(1):97–110, 2012.

[ASTM7181] ASTM International. ASTM D7181-20 — *Standard Test Method for Consolidated Drained Triaxial Compression Test for Soils*. ASTM International, West Conshohocken, PA, 2020.

[ASTM4767] ASTM International. ASTM D4767-11(2020) — *Standard Test Method for Consolidated Undrained Triaxial Compression Test for Cohesive Soils*. ASTM International, West Conshohocken, PA, 2020.

[ASTM2850] ASTM International. ASTM D2850-26 — *Standard Test Method for Unconsolidated-Undrained Triaxial Compression Test on Cohesive Soils.* ASTM International, West Conshohocken, PA, 2026.

[Atk07] J. H. Atkinson. *An Introduction to the Mechanics of Soils and Foundations*. McGraw-Hill, 2007.

[Ben01] N. Benahmed. *Comportement mécanique d'un sable sous cisaillement monotone et cyclique : application aux phénomènes de liquéfaction et mobilité cyclique*. PhD thesis, École Nationale des Ponts et Chaussées, 2001.

[Ben04] N. Benahmed, J. Canou, and J. C. Dupla. *Initial Structure and Static Liquefaction Properties of Sand.* Comptes Rendus Mécanique, 332(11):887–894, 2004.

[BFB13] S. Bonelli, R. Fell, and N. Benahmed, "Concentrated Leak Erosion," in *Erosion in Geomechanics Applied to Dams and Levees*, S. Bonelli and F. Nicot, eds., ISTE Ltd and John Wiley & Sons, 2013, pp. 271–342.

[BG65] A. W. Bishop and G. E. Green. *The Influence of End Restraint on the Compression Strength of a Cohesionless Soil*. Géotechnique, 15(3):243–266, 1965.

[BH62] Alan W. Bishop and D. J. Henkel. *The Measurement of Soil Properties in the Triaxial Test*. 2nd edition, Edward Arnold, London, 1962.

[BJ85] K. Been and M. G. Jefferies. *A State Parameter for Sands*. Géotechnique, 35(2):99–112, 1985.

[BL73] D. K. Black and K. L. Lee. *Saturating Laboratory Samples by Back Pressure.* Journal of the Soil Mechanics and Foundations Division, ASCE, 99(SM1):75–93, 1973.

[Bol86] M. D. Bolton. *The Strength and Dilatancy of Sands*. Géotechnique, 36(1):65–78, 1986.

[BW75] A. W. Bishop and L. D. Wesley. *A Hydraulic Triaxial Apparatus for Controlled Stress Path Testing*. Géotechnique, 25(4):657–670, 1975.

[Cas69] G. Castro. *Liquefaction of Sands*. PhD thesis, Harvard University, Cambridge, MA, 1969.

[HE14] K. H. Head and Roger J. Epps. *Manual of Soil Laboratory Testing, Volume 3: Effective Stress Tests*. 3rd edition, Whittles Publishing, 2014.

[HG52] R. J. Henkel and G. D. Gilbert. *The Effect of the Rubber Membrane on the Measured Triaxial Compression Strength of Clay Samples*. Géotechnique, 3(1):20–29, 1952. DOI: 10.1680/geot.1952.3.1.20.

[ISO18] ISO. ISO 17892-9:2018 — *Geotechnical Investigation and Testing. Laboratory Testing of Soil — Part 9: Consolidated Triaxial Compression Tests on Water Saturated Soils.* International Organization for Standardization, Geneva, 2018.

[ISRM07] R. Ulusay and J. A. Hudson, eds. *The Complete ISRM Suggested Methods for Rock Characterization, Testing and Monitoring: 1974–2006*. ISRM Turkish National Group, Ankara, Turkey, 2007. ISBN: 978-975-93675-4-1.

[Lad16] Poul V. Lade. *Triaxial Testing of Soils*. John Wiley & Sons, 2016. DOI: 10.1002/9781119106616.

[Lad78] R. S. Ladd. *Preparing Test Specimens Using Undercompaction*. Geotechnical Testing Journal, 1(1):16–23, 1978.

[LV90] S. Leroueil and P. R. Vaughan. *The General and Congruent Effects of Structure in Natural Soils and Weak Rocks*. Géotechnique, 40(3):467–488, 1990.

[MSC77] J. P. Mulilis, C. K. Chan, and H. B. Seed. *The Effects of Method of Sample Preparation on the Cyclic Stress-Strain Behavior of Sands*. Report No. EERC 75-18, Earthquake Engineering Research Center, University of California, Berkeley, 1977.

[Pou81] S. J. Poulos. *The Steady State of Deformation*. Journal of the Geotechnical Engineering Division, ASCE, 107(GT5):553–562, 1981.

[Row62] P. W. Rowe. *The Stress-Dilatancy Relation for Static Equilibrium of an Assembly of Particles in Contact*. Proceedings of the Royal Society of London. Series A, 269:500–527, 1962.

[RSW58] K. H. Roscoe, A. N. Schofield, and C. P. Wroth. *On the Yielding of Soils.* Géotechnique, 8(1):22–53, 1958. DOI: 10.1680/geot.1958.8.1.22.

[Ske54] A. W. Skempton. *The Pore-Pressure Coefficients A and B*. Géotechnique, 4(4):143–147, 1954. DOI: 10.1680/geot.1954.4.4.143.

[Ske85] A. W. Skempton. *Residual Strength of Clays in Landslides, Folded Strata and the Laboratory*. Géotechnique, 35(1):3–18, 1985.

[SW68] Andrew N. Schofield and C. Peter Wroth. *Critical State Soil Mechanics*. McGraw-Hill, London, 1968.

[VN88] Y. P. Vaid and D. Negussey. *Preparation of Reconstituted Sand Specimens. In Advanced Triaxial Testing of Soil and Rock*, ASTM STP 977, pages 405–417. ASTM International, Philadelphia, 1988.

[Woo90] David Muir Wood. *Soil Behaviour and Critical State Soil Mechanics*. Cambridge University Press, Cambridge, 1990.

Dimensioning and construction of experimental apparatus with examples

Eleni Gerolymatou[(a)], Uwe Düsterloh[(a)], Riccardo Castellanza[(b)]

[(a)] *Technische Universität Clausthal*
[(b)] *Universitá degli Studi Biccoca*

The aim of the present chapter is to provide a brief overview of the function and dimensioning of experimental apparatus, looking at the topic from the hardware point of view. Two examples are selected for presentation. The first is the triaxial machine, being the means of performing the most widely used tests. Its mode of function, the parts of which it consists and the load carried during testing by each of the parts are discussed. An example of dimensioning for a triaxial machine intended for relatively small rock specimens is presented and the selection of materials is discussed. The underlying considerations are mostly linked to the avoidance of yielding under load of the machine parts. Seals, gaskets and sensors are not discussed. The second apparatus presented is a soft oedometer ring in two variations. The type of apparatus is selected because it combines stability considerations with sensitivity of measurement, which also depends on the used sensors. It is therefore particularly interesting from a didactic point of view, while at the same time being very simple from a geometrical one.

1 Introduction

Laboratory testing in soil and rock mechanics serves for the characterization of material parameters, such as strength and stiffness. It allows the measurement of hydraulic, mechanical and thermal properties. Such quantities can be used as input for analysis and design, for the calibration of constitutive models and as input for numerical calculations, for example with the finite element or the discrete element method. Another significant contribution of laboratory testing is to the understanding of mechanical behavior and its hydraulic, thermal and chemical couplings. It allows the investigation of material behavior under clearly defined boundary conditions, thus supporting the development and validation of models and theories and testing hypotheses about con-

stitutive behavior and failure criteria. In essence, laboratory testing underpins both fundamental understanding and practical design in soil and rock mechanics, by delivering quantifiable, controlled, and reproducible information about geomaterial behavior that cannot be obtained from theory or field observation alone.

The properties of geomaterials vary widely. The permeability of soils and rocks can range from 10^{-7} m^2 to 10^{-19} m^2 [Bea72], ranging over 12 orders of magnitude. The strength of soils can be as low as tenths of kPa [Wag13], while the strength of hard rock can reach hundreds of MPa [Shi81]. In order to succeed in acquiring reliable measurements, it is as a result necessary to dimension experimental apparatus with the span of measured material properties in mind.

The objective of the present chapter is to explain the basic principles of dimensioning experimental devices by means of providing examples. The content is not only addressed to those intending to construct such devices, but also to those wishing a better understanding of the working principles of experimental devices.

Only quasi-static triaxial tests are discussed, not including measurement and control of pore water pressures. Dynamic tests are also not covered. The focus is placed on the mechanical design. The hydraulics and pneumatics, as well as the precision of the measurement system are briefly touched upon.

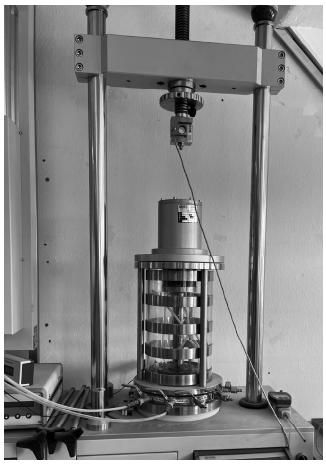
2 Standard triaxial apparatus

Arguably the most common experimental setup in geomechanics is the triaxial apparatus. Depending on the requirements, large variations in construction occur, as shown in figure 1. A further variation not depicted here is the Hoek cell [HF68].

A standard triaxial apparatus consists of several parts, all of which should be dimensioned for a range of stresses and displacements, specimen size and, potentially, the type of control planned. A typical triaxial setup is shown in figure 2. The specific apparatus was designed for the testing of rock specimens, but, though the dimensions may vary, the parts are the same for soil testing.

The specimen is protected by a sleeve or membrane and placed between the loading plates, via which the axial load is applied. The sleeve is usually a polymer tube, whose aim is to protect the specimen from ingress of the confining fluid. The loading plates as a rule consist of a metal, commonly stainless steel for soil testing and hardened steel for rock testing. Figure 3 shows a prepared claystone specimen in a transparent viton sleeve. The loading plates are in position, the specimen is instrumented for local measurements of the axial and radial strain and the triaxial cell has not yet been closed. The depicted setup is an MTS 815 apparatus at the Karlsruhe Institute of Technology.

The central part of the machine is the triaxial cell, a cylindrical chamber in which the specimen is placed in order to apply the confining pressure. The cell is filled prior to testing with the confining fluid, which may be air, water or, most commonly, oil. The pressure of the confining fluid may be controlled over a pump directly, via a piston



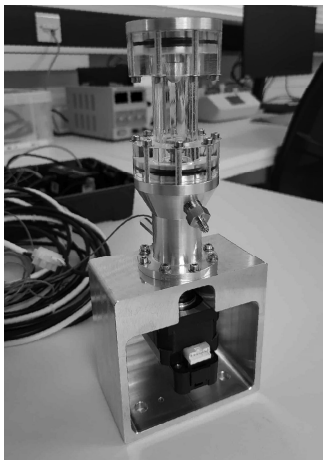
(a) Triaxial apparatus for testing soils constructed in 1998 by the producer Wille Geotechnik, TU Clausthal



(b) Triaxial apparatus for rock for specimens with a diameter of up to 150 mm dimensioned by Prof. U. Düsterloh TU Clausthal



(c) Large scale triaxial apparatus for specimens with a diameter of 750 mm dimensioned by Prof. Düsterloh, TU Clausthal



(d) Mini triaxial apparatus for the testing of soils in tomographs designed for specimens with a diameter of 10 mm, Durham University

Figure 1: Different types of triaxial machines.

or using a linear actuator, with the second method being the most common one. The cell itself may consist of varying materials. The most common choices are safety glass or acrylic with steel bands for soil or steel for rock. The role of the cell is to withstand the pressure of the confining fluid without permanent deformation or failure

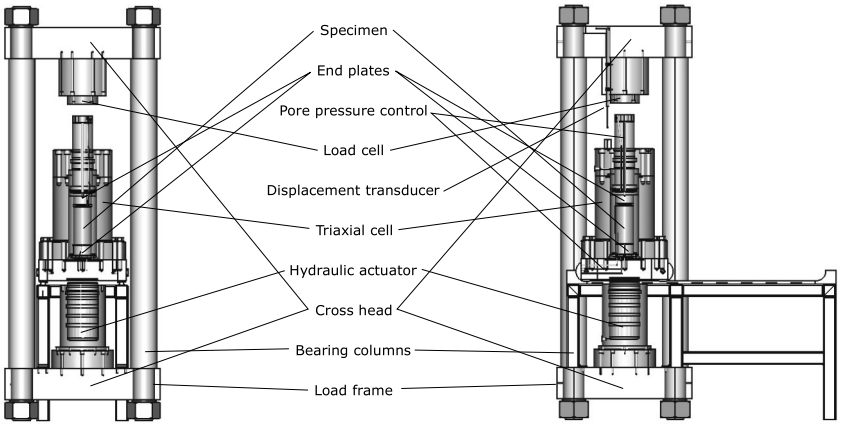


Figure 2: Outline of a typical triaxial apparatus.

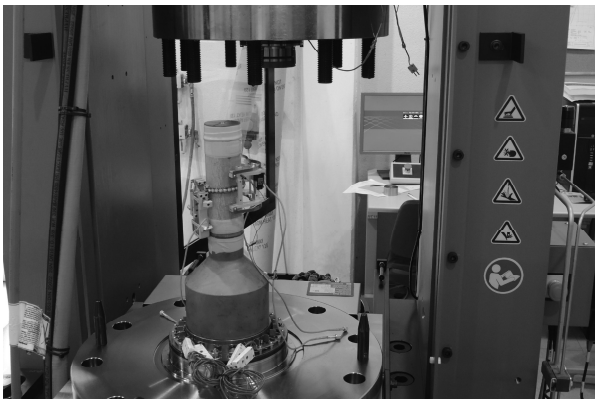


Figure 3: Instrumented specimen on pedestal with triaxial cell open.

and without leakage. Most depictions of a triaxial apparatus only contain the load cell and its immediate vicinity.

The axial load is applied in the apparatus depicted in figure 2 via a hydraulic actuator below the specimen. A hydraulic actuator is similar to a hydraulically controlled piston. When the oil pressure is increased in the chamber the piston moves upwards, applying load over the loading plates on the specimen. An alternative to the hydraulic actuator is the electromechanical or linear actuator, an example is shown in figure 1d. A linear actuator is operated via a motor, instead of a pump, and the quantity controlled directly is the speed of the actuator, rather than the pressure of the oil in the hydraulic actuator.

The hydraulic or linear actuator is supported by the bottom cross head, as shown in figure 2. The vertical load applied on the specimen is carried over the top load plate and piston to the top cross head. This means that the compressive force applied on the specimen leads to a tensile force reaction, that needs to be carried by the loading frame, and more specifically by the load columns. The cross heads themselves are subjected to bending. As the specimen is compressed, the whole loading frame lengthens slightly.

Often it is necessary to control or measure the pore pressure of the specimen. Control of the pore pressure is achieved as a rule using syringe pumps connected to the pore pressure inlet and outlet, located in the load plates. For highly permeable materials, such as gravel or sand, a pipette system may be adequate. For materials with a low permeability it is important to maintain the dead volume, meaning the volume of the tubing and pressure transducers, to a minimum [EFD+26]. Though permeability measurement is most common with water, other fluids can be used, such as oil for materials that tend to dissolve in water [BPFL06], or gas for tight materials [CBB09].

The control of the triaxial test can be performed in varying ways. Most commonly the confining pressure is maintained constant and the axial load or the axial displacement are controlled. If the axial load is controlled, the axial displacement is measured and vice versa. The end result is a curve displaying the axial stress (or equivalently the stress deviator) as a function of the axial strain. If the axial load is controlled, control of the test is lost when the specimen fails. If the axial displacement is controlled, the post yield behavior of the specimen can be captured.

The bare minimum of quantities that need to be monitored via sensors during the test are thus the confining pressure, the axial load on the specimen and the axial displacement. Often additional quantities are monitored, such as the pore pressure evolution and the circumferential strain of the specimen. The confining pressure and the pore pressure are monitored using pressure transducers. Displacement transducers used to measure the axial displacement may be located inside or outside the triaxial cell. Placement outside the cell is easier, as there is no need for a feed-through to transfer the signal of the sensor outside the cell. It is at the same time less accurate, as the measurement is not performed directly in the vicinity of the sample and is influenced by the deformation of the frame. Such an example is shown in figures 1b and 2. In

such case, the stiffness of the frame needs to be high, to minimize the error. The same is true for the measurement of the axial load: it is possible to install the load cell outside the triaxial cell, as shown in figure 2, or inside it, with the second option presenting higher technical difficulties. In the second case the measurement is more accurate, as friction in the hydraulic actuator, if present, and between top piston and cell is not influencing the measurement. Such error contributions may be very small or significant, depending on the conditions of the test, the properties of the specimen and the properties of the apparatus.

As can be seen from the above, applications for triaxial tests can vary widely and the mechanical parts and acquisition should be dimensioned differently, depending on the goals of the proposed measurements. In the next section the dimensioning of single components will be discussed in more detail, not including the pore pressure system.

3 Dimensioning of a triaxial apparatus

3.1 General Design Considerations for Experimental Apparatus

Given that the whole of the apparatus is placed under mechanical and possibly thermal loads, the first and more obvious requirement is that the apparatus can withstand the loads without damage or permanent deformation. It is common however for additional requirements to be placed on different parts, such as on the stiffness of the frame. Such requirements will be considered here with the help of simple analytical solutions, which can serve as a valuable first approximation. In special cases, especially for complicated geometries, the possibility to resort to numerical simulations is a good option.

The design process begins with the specification of requirements. The following questions need to be answered:

- What is the range of specimen sizes to be tested?
- What is the range of axial loads that will need to be applied?
- What is the range of axial displacements to be expected?
- What is the range of confining pressures required?
- What is the range of temperatures required?
- Where will the load cell be placed?
- Which measurements are needed inside the cell and what are their space requirements?

The above list represents rather a minimum. Further questions may arise based on the application and the design choices.

Answering the above questions is followed by conceptual design, where the main characteristics of the apparatus are determined. These depend on the requirements

determined above, but also on practical considerations, such as available laboratory infrastructure (space, power, compressed air etc.), available budget and safety regulations and standards (for example pressure vessel regulations).

Detailed design and dimensioning are followed by construction. The final steps before normal, routine operation are verification of operability and calibration. Calibration is not limited to sensors, who often come calibrated from the manufacturer, but also to the control of the apparatus itself [SI17].

In order to render it easier to follow the dimensioning considerations, a specific example will be used in parallel to the more generic explanations. In the rest of the chapter it will be assumed that a triaxial apparatus for the testing of rock is planned. The specimen diameter is expected to range from 25 mm to 50 mm. Testing should be possible for temperatures up to 100^oC. The maximum confining pressure is 100 MPa and the maximum axial load is 200 MPa.

3.2 Loading frame

The role of the loading frame is to provide the support for the axial load applied on the specimen. It also houses either the linear or the hydraulic actuator for the generation of that load. Because the loading frame is not heated as a rule, even when heated tests are performed, it is not necessary usually to consider the influence of temperature on the strength and stiffness of the loading frame.

3.2.1 Frame stiffness and strength

Most loading frames are equipped with two or with four loading columns. Here it will be assumed that four columns are planned. Since it is planed to apply a maximum load of 200 MPa, the maximum force that is expected to be carried by the frame is

$$F_{ax} = \sigma_{max} \cdot A_{max}, \tag{1}$$

where A_{max} is the maximum specimen cross-section. The resulting force in the specific case is about equal to 400 kN. Dividing by the number of columns yields the force to be carried by each column, namely here 100 kN.

Given the high stresses, it is reasonable to select a high strength steel, with AISI 4340 / DIN EN 36NiCrMo4 being a common choice. It is characterized by a stiffness of about 200 GPa and, in the annealed state, by an ultimate tensile strength of 700 MPa and a 0.2% yield strength of 500 MPa. The last point means that a permanent strain of 0.2% is to be expected at a load of 500 MPa. Hardening can increase the strength and the hardness significantly. Another, less costly option, would be the use of AISI 4140 / DIN EN 42CrMo4, with a yield strength of 415 MPa and an elastic modulus of 200 MPa.

Since the columns should not deform permanently, it is reasonable to use the yield rather than the ultimate strength. For the bearing columns is should then hold that

$$n_c \cdot \sigma_y \cdot A_c = F_{ax}, \tag{2}$$

where n_c is the number of columns, σ_y is the yield strength of the selected construction material, A_c is the column cross-section and F_{ax} is the maximum axial load for the apparatus. In the specific example a column diameter of about 16 mm results for 36NiCrMo4 and 18 mm for 42CrMo4.

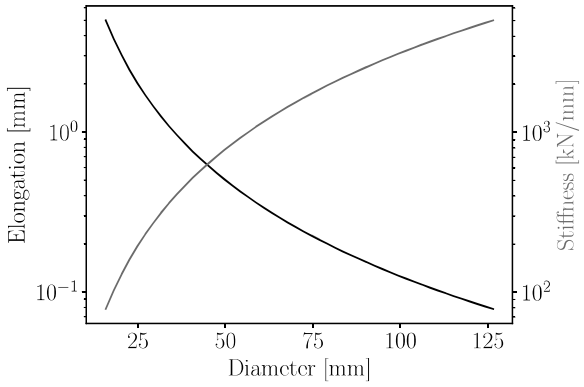


Figure 4: Frame stiffness and safety factor as a function of bearing column diameter.

In addition to the fact that it is generally not advisable to use a safety factor of one, the loading frame is not just expected to bear the load, but also to exhibit a low deformation while doing so. In figure 4 the elongation and stiffness of a frame with a column height of 2 m is shown as a function of the comumn diameter used. It can be easily observed that a significantly higher column diameter than the one resulting from safety considerations is required to achieve a reasonable stiffness. For rock testing the required stiffness is as a rule much higher than for soil as a result of the higher stiffness of the specimens and the lower total deformation. Considering a typical Bentheim sandstone specimen failing at about 1% strain [KBRW01] with a diameter of 25 mm and a height of 50 mm, failure is expected to take place at a displacement of 0.4 mm, meaning that the measured displacements are small, requiring high accuracy in the measurement. A too low frame stiffness can mask spontaneous unloadings [LGT25], lead to premature specimen failure or lead to erroneous measurements [HCF72].

The cross heads need to be dimensioned similarly, considering their being loaded in bending. A first approximation may be achieved by the Euler-Bernoulli beam theory, calculating deflection for a centrally loaded simply supported beam as

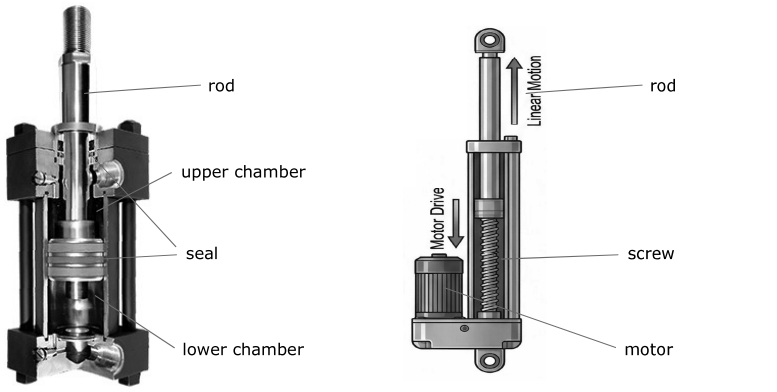
$$\delta_{max} = \frac{F_{ax} \cdot L^3}{48 E_s \cdot I}, \tag{3}$$

where L is the length of the beam and I is the moment of inertia of its cross-section, equal to $b \cdot h^3/12$ for a rectangular cross section with width w and height h. Based on this calculation, a cross head thickness of 100 mm would lead to a maximum deflection of about 0.1 mm for a span L of 800 mm, while a thickness of 200 mm would yield a

maximum deflection of 0.01 mm. This calculation makes use of crude simplifications and should be used only as a starting point. It is advisable to use numerical simulation to verify the suitability of the dimensions.

3.2.2 Control considerations

To control the axial load two alternatives are commonly used: hydraulic actuators (figure 5a) or electromechanical linear actuators (figure 5b). A hydraulic actuator has



(a) Hydraulic actuator (Cowan Dynamics) (b) Linear actuator (Firgelli Automation)

Figure 5: Axial load control.

two fluid chambers, an upper and a lower one. These are separated by the piston with a seal. A seal is also installed to avoid leakage at the point of exit of the rod from the upper chamber. Increasing the oil pressure at the bottom chamber pushes the piston upwards, moving the rod to compress the specimen. Increasing the oil pressure in the upper chamber retracts the rod, unloading the specimen. To control the oil pressure a hydraulic aggregate is necessary, with the corresponding valves and lines. Hydraulic actuators are capable of very high forces based on the dimensioning of the piston and rod and in general very durable. Their main disadvantages are the more complicated and noisy setup compared to linear actuators and the increased difficulty of control. The presence of the seals results in friction and the pressure of the oil cannot directly be converted to force on the specimen. Load control therefore requires a servo controller, as does displacement control.

Most laboratory testing for research is performed in displacement control in the axial direction. For a hydraulic actuator a servo controller will read the values from the axial displacement sensors, compare these to the expected value and correct the oil pressure to the hydraulic actuator accordingly. This may result to undesirable fluctuations of the actual displacement value around the target value. An example for a calibration experiment on a machine operated with a hydraulic actuator is shown in figure 6. The

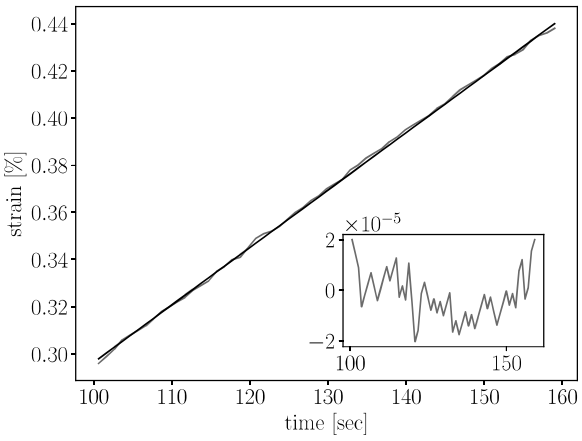


Figure 6: Strain oscillations due to imperfect control.

target strain value as a function of time is the black line, while the red line is the measured value. In the insert the absolute strain error is shown. In the specific case it amounts to about 20 microstrain. Depending on the application this may be significant or unimportant, and in some cases may be beyond the measurement precision of the displacement sensor.

An electromechanical linear actuator, or often just linear actuator, uses an electric motor to rotate a screw. Via this rotation the rod is moved upwards or downwards as shown in figure 5b. The electrical signal provided by the control system to the motor controls the rotation velocity of the motor and with it of the screw. In this way the velocity of the rod is controlled directly. Because the inclination of the thread is rather small, large angle rotations (comparatively) correspond to small vertical displacements, making it possible to control displacement with high accuracy. Given that the rod itself, the specimen and the whole apparatus in general may deform, it is advisable to make use of servo control in this case as well, but control of displacement rate is more straightforward and can be achieved with higher precision. A further advantage of linear actuators is that they are practically noiseless, something that is relevant when it is not possible to place hydraulic aggregates in a separate location. On the downside, high loads are not possible with linear actuators, with the limit usually lying in the vicinity of 250 kN.

3.2.3 Loading system

Given the high load required in the specific example, for the loading system the hydraulic actuator is the preferred option. This is also selected for demonstration purposes, as linear actuators are generally acquired with the dimensions needed and do not require dimensioning.

The loading piston needs to have a sufficient cross-section to avoid both yield and significant deformation. Assuming a maximum load of 200 MPa on a specimen with a diameter of 50 mm, any rod diameter larger than this will have a safety factor of more than two for both steel alloys considered. Large diameters are also possible, increasing the stiffness of the rod.

It is assumed that a hydraulic aggregate is availabe with a hydraulic pressure p_h of 400 bar, amounting to 40 MPa. The surface on which this maximum hydraulic pressure will act is equal to the cross-section of the piston A_p minus the cross-section of the rod A_r. The force on the rod will be equal to this product of aggregate pressure with the surface A_p - A_r, when the friction of the seals is subtracted. Since the friction is close to impossible to assess in advance, a small margin is included in the calculation to account for it. Making use of force equilibrium

$$\sigma_{max} \cdot A_{max} = p_h \cdot (A_p - A_r) \Rightarrow$$

$$A_p - A_r = A_{max} \cdot \frac{\sigma_{max}}{p_h} \tag{4}$$

yielding a radius of 150 mm for the piston, if the rod has a diameter of 100 mm.

The thickness of the flange of the piston also needs to be dimensioned for bending. Given the somewhat more complicated axisymmetric geometry, no analytical solution is presented here.

The wall of the hydraulic actuator can be dimensioned using the theory of the thick walled cylinder [Mic99]. As this will be used also to determine the wall thickness for the triaxial cell, it is omitted here.

The pressure in the lower chamber of the hydraulic aggregate is controlled by a valve controlling the flow from the hydraulic aggregate to the lower chamber of the actuator. The provided signal can for example have a precision of 0.1% of the full scale. This means that for 200 MPa of axial pressure on a specimen with a diameter of 50 mm the applied load precision is 0.2 MPa or 200 kPa, not taking into account piston friction. As a result, while this frame is suitable for the testing of rocks, it does not provide the necessary resolution in control to test soils. This is a frame characteristic that cannot be rectified by changing the used sensors. Correspondingly an electromechanical cylinder has a given displacement resolution, which depends on the minimum smooth velocity the motor can supply and the screw lead, meaning the linear travel the nut makes per revolution.

3.3 Triaxial cell

The triaxial cell is the heart of the apparatus. A typical geometry is shown in figure 7. The depicted triaxial cell features no internal load cell and provides little space for transducers in the cell. The considerations behind this choice are discussed bellow.

The axial load acting on the specimen is not transferred to the cell, because the loading rod is free to move in the vertical direction - ignoring the friction at the seal -. It is

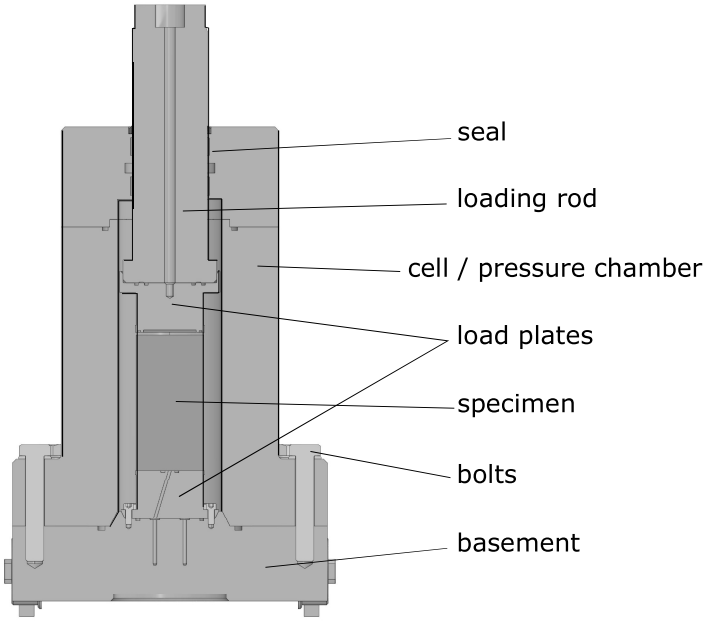


Figure 7: Typical triaxial cell geometry for rock.

however transferred to the basement, which in turn is supported from below by the piston of the hydraulic actuator.

The main load acting on the cell is the confining pressure, acting in the horizontal direction on the walls of the cell and in the vertical direction on the roof and basement.

3.3.1 Cell dimensions

Dimensions will be determined here for the thickness of the cell and for the bolts used to close it. The thickness of the cell is determined by its internal and external radius. While the choice of the external radius is relatively flexible, the internal radius is determined by the space necessary for the specimen itself, including the sleeve, and potential sensors, for example to measure temperature or deformation. The expected radial sample deformation during the test should also be taken into account, especially when tests with larger deformations are planned. For our specific example a maximum specimen diameter of 50 mm is considered. Intending to place sensors inside the cell, the inner radius is set to at least 100 mm.

To assess the necessary thickness of the cell, the thick walled cylinder theory [Mic99] can be used, see also figure 8. When the external pressure p_2 is equal to zero and the

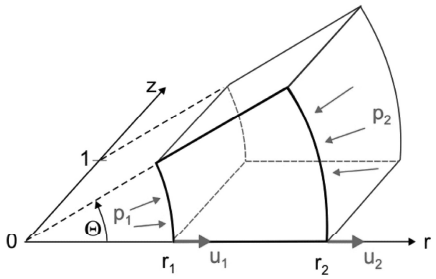


Figure 8: Thick walled cylinder.

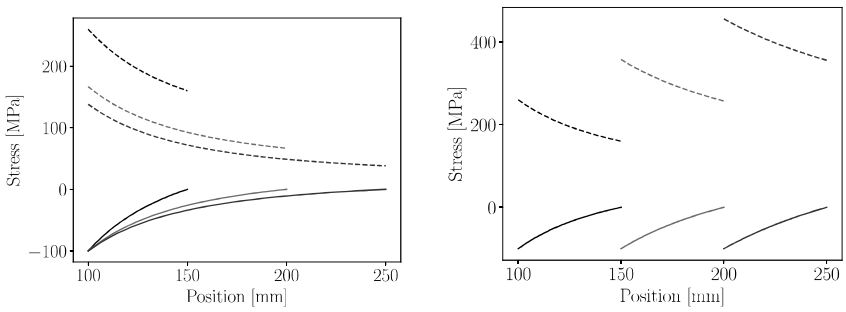
internal is equal to the confining pressure p, the radial and circumferential stress at a distance r from the axis of symmetry can be calculated as

$$\sigma_{rr} = \frac{pr_1^2}{r_2^2 - r_1^2}\left(1 + \frac{r_2^2}{r^2}\right) \tag{5}$$

$$\sigma_{\theta\theta} = \frac{pr_1^2}{r_2^2 - r_1^2}\left(1 - \frac{r_2^2}{r^2}\right) \tag{6}$$

with $\sigma_{r\theta}$ = 0. Since the vessel has closed ends, for the vertical stress force balance dictates that

$$\sigma_{zz} = \frac{pr_1^2}{r_2^2 - r_1^2} \tag{7}$$



(a) Variation of the thickness)

(b) Variation of the inner radius

Figure 9: Stresses in a thick walled cylinder.

The radial stress is compressive, while the circumferential and axial stresses are tensile.

A small parametric analysis is performed in figure 9. The radial (continuous lines) and circumferential (dashed lines) stresses in a thick walled cylinder are shown as a function of the distance from the axis of symmetry, assuming that tension is positive and compression negative. In figure 9a the thickness of the cell is varied maintaining the inner radius constant. It can be observed that increasing wall thickness has little influence on the radial stress. Its maximum value in absolute terms remains at the inner boundary, as one could expect from equilibrium consideration. The circumferential stress on the other hand decreases as the wall thickness is increased and its maximum absolute value is always found at the internal boundary. Examining the effect of the increase of the inner radius shown in figure 9b leads to the observation that the maximum circumferential stress is increasing as the inner radius increases, while the radial stress shows no variation.

The conclusion can be drawn, that the inner wall of the cell is the most likely location for failure and it suffices to consider it. The stress state at the inner wall is:

$$\sigma_{rr} = -p, \quad \sigma_{\theta\theta} = p\frac{r_2^2 + r_1^2}{r_2^2 - r_1^2}, \quad \sigma_{zz} = \frac{pr_1^2}{r_2^2 - r_1^2}, \tag{8}$$

where the radial stress is compressive and the tangential and axial stresses are tensile. To assess the strength of the cell, the Tresca failure criterion is used, with the distortional stress calculated as the difference of the maximum stress minus the minimum one, in the specific case

$$\sigma_{\mathrm{v}} = p\frac{r_2^2 + r_1^2}{r_2^2 - r_1^2} + p = 2p\frac{r_2^2}{r_2^2 - r_1^2}. \tag{9}$$

For safety factor one this yields a value of 39 mm for 42CrMo4 and 29 mm for 36NiCrMo4 for the thickness of the cell. A safety factor of one is of course inadvisable. In addition the fact should be considered, that the triaxial cell is intended to

be heated to 100 ^{o}C. Making use if a safety factor of 1.5 and assuming a reduction of 20% on the strength of steel yields values of 222 mm and 100 mm for 42CrMo4 and 36NiCrMo4 respectively. It should be noted that the reaction to temperature of high strength low grade alloys is overestimated here at 100 ^{o}C, though the effect is measurable and should not be underestimated [Ste90]. Seals and O-rings are much more sensitive to elevated temperatures and their choice needs to be carefully considered, including thermal expansion effects.

Only strength has been used as a consideration here, but other factors may be relevant. For example, the cell depicted in figure 7 has been designed to measure the dilatancy (volume change) of the specimen during testing by monitoring the amount of oil in the cell. In this case it is of advantage that the volume of oil is small in the cell, so that changes are easier to monitor. It is further of paramount importance that the cell does not deform during testing, leading to an increased wall thickness. An alternative to the same end is the use of double walled cells, where the pressure applied on the external wall of the internal cell limits its deformation, as shown in figure 10. The inner and outer pressure of the inside cell are equal to each other, leading to zero cell deformation.



Figure 10: Double walled triaxial cell for soils and soft rocks (Controls).

The necessary number and dimension of bolts is considered next. It is assumed that bolts with a diameter of 24 mm are used, see [DIN13]. The proof load for a single screw amounts to 342 kN for a class of 12.9 and to 293 kN for a class of 10.9 for ISO metric coarse pitch thread, so that failure of the bolts themselves is highly unlikely. At the same time, the failure of the material of the cell (42CrMo4 or 36NiCrMo4) should also be taken into account.

Assuming the use of 12 screws with a metric size of 24 and coarse threading and assuming that the confining pressure is applied on the whole of the inner diameter of a cell (which is an exaggeration), the load carried per screw is

$$F_s = \pi \cdot r_1^2 \cdot p/12 = 65.5kN, \tag{10}$$

leading to a safety factor of more than 6. The screws need to be preloaded. Assuming a torque of 250 Nm and ignoring the friction, the additional tensile load on the screws is

$$F_{\mathrm{p}} = \alpha_{\mathrm{v}} \frac{2M}{d_s}, \tag{11}$$

where α_{v} is a factor included to compensate for unequal tensioning, here 2.5. This yields a value of about 35 kN for a head diameter d_s of 36 mm, so that the total tensile force equals about 100 kN, significantly below the yield load.

A further important factor to consider is the pullout resistance, to avoid stripping at the thread. The DIN recommends a minimum engagement length of 1.5 times the bolt diameter, here 36 mm. This is to be understood as the minimum engagement depth in the basement plate. The maximum resisting force depends on the yield strength of the material of the plate, as this is lower than that of the bolts at 415 MPa. The resisting force is equal to

$$F_r = \pi \cdot d \cdot h \cdot \sigma_y, \tag{12}$$

where d is the diameter of the bolt, here 24 mm, h is the engagement depth and σ_y is the yield strength of 42CrMo4. It is usual to apply a safety factor to account for imperfect engagement. Even for a factor of 0.5, the force resisting thread stripping is more than 5 times larger than the tensile force on the bolts.

The pressure of the oil in the cell is as a rule also controlled with a hydraulic actuator, whose dimensioning is similar to the one described in the previous section for the actuator controlling the axial load. Capacity is an additional consideration, as the volume of the actuator should be large enough to increase the cell pressure to the desired limit, taking into account the compressibility of the oil. If a heated triaxial cell is planned, the oil expansion with temperature increase and its increased compressibility at elevated temperatures should also be taken into account.

3.4 Selection of materials

In the above example we have selected steel as a working material, aiming at dimensioning an apparatus for relatively high loads. Other considerations may come into play, affecting material selection. In soil mechanics acrylic cells are often used to allow visual contact to the specimen. Where loads are not so high and chemical effects are a concern, or the part is expected to come into contact with water often, stainless steel may be a more suitable option. Temperature ranges also play an important part, especially when considering seals and gaskets, which have not been discussed here. Other considerations may play a part in special cases. An example are miniaturized apparatus for *in situ* tomography.

4 Soft oedometer

The triaxial machine is arguably the most commonly used apparatus in geomechanics, which is why its dimensioning has been discussed here. At the same time it is a rather complicated construction with high requirements. For this reason the dimensioning of a soft ring oedometer is also presented in this chapter. Though it is relatively simple, its dimensioning includes aspects of technical mechanics, sensors and calibration.

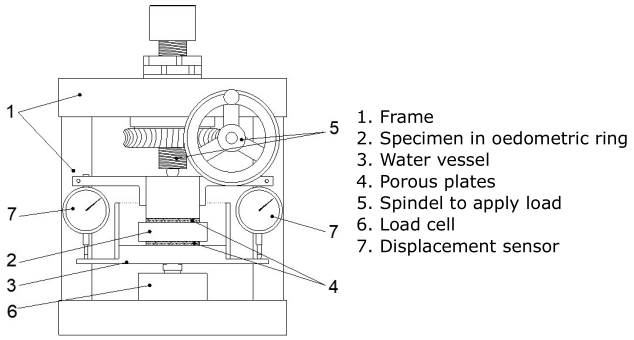


Figure 11: Oedometric setup.

An oedometric setup is usually similar to the apparatus shown in figure 11. The setup depicted here is designed for constant strain and assumes a sufficiently high frame stiffness. Various setup types exist, where loading can be performed in different modes, for example through a frame or through dead weights. An oedometric test can be also performed in the absence of water, depending on its aim.

The purpose of the metal ring in which the specimen is placed is to inhibit radial deformation of the specimen. Thus the boundary condition is

$$\varepsilon_{rr} = 0 \tag{13}$$

This means that in the radial direction the total strain is known, but the radial stress is unknown. This makes it difficult to determine the stress path, useful for model development and calibration. To overcome this difficulty the soft oedometer was proposed by Kolymbas and Bauer [KB93]. The underlying idea is to allow small but measurable strains in the ring, from which the radial stress can be determined. Strains induced by the lateral pressure in the ring are measured on its outer surface using strain gauges, as shown in figure 12 with a gasbeton specimen.

The radial strain permitted in the soft oedometer creates a deviation from the usual conditions of an oedometric test. This deviation is inevitable but usually undesirable. The aim of the dimensioning of the ring is to select its material and thickness so that the radial strain is small enough to be considered close to negligible, but large enough to yield an adequate resolution for the measurement of the radial stress.

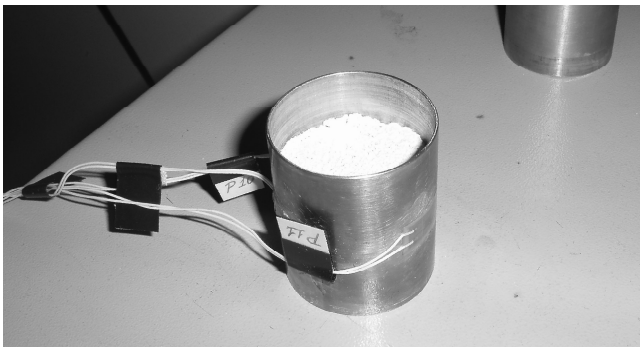


Figure 12: Soft oedometer ring, Politecnico di Milano.

Two examples will be considered to illustrate the effect of different targets in the measurement: a soft ring for an artificial weak rock (maximum radial stress 1000 kPa) and a soft ring for the oedometric testing of highly compacted bentonite (maximum radial stress 50 MPa). In both cases the influence of water will not be considered, even though water is present in the second case.

4.1 Strength and stiffness considerations

The first point to consider is of course that the ring should not plastify under load. The calculation can be performed using the thin walled cylinder theory, which is valid when the thickness of the ring is less than one tenth of its radius. Given that the thick walled cylinder theory yields the same result, it will be used here, even when the assumptions of the thin walled cylinder theory are satisfied.

The calculation of the stresses is the same as for the triaxial cell, with the only difference being that the ring is not loaded in the axial direction. The Tresca stress remains the same at

$$\sigma_{\mathrm{v}} = 2p\frac{r_2^2}{r_2^2 - r_1^2}. \tag{14}$$

Three different materials are considered for the contruction of the ring, stainless steel (AISI 304) with a yield strength of 205 MPa, 7076 aluminium with a yield strength of 120 MPa and brass (UNS C28000) with a yield strength of 140 MPa. For the different materials and the two different rings the minimum thickness of the rings is given in the table, assuming an inner diameter of 50 mm. It can be seen that for the soft oedometer designed for the cemented soil with a maximum radial stress of 1000 kPa or 1 MPa the thickness required is so small that it is of the order of tenths of mm.

A further consideration is the radial deformation. The radial strain permitted to the specimen is a deviation from oedometric conditions. In [KB93] it is suggested to use the strains measured with the strain gauges to assess the magnitude of the deviation. While this is possible, it is preferable to calibrate or at least check the calibration of

Table 1: Minimum ring thickness to avoid plastification.

Material Yield strength	Steel (AISI 304) 205 MPa	Aluminium (7076) 120 MPa	Brass (UNS C28000) 140 MPa
Stiffness	200 GPa	67 GPa	100 GPa
Ring 1 (1 MPa)	0.13 mm	0.21 mm	0.18 mm
Ring 2 (50 MPa)	10 mm	36 mm	22 mm

strain gauges after gluing them. In [CGN09] it is selected instead to calibrate directly for the radial stress. In any case, the radial displacement arising from the use of a thinner, more flexible ring can be calculated from the tangential strain

$$u_r = R \cdot \varepsilon_{\theta\theta} = r_1 \cdot \frac{\sigma_{\theta\theta} - \nu \cdot \sigma_{rr}}{E} \tag{15}$$

with

$$\sigma_{\theta\theta} = p\frac{r_2^2 + r_1^2}{r_2^2 - r_1^2}. \tag{16}$$

If the radial strain is zero, the radial stress is equal to

$$\sigma_{rr,0} = \frac{\nu_m}{1-\nu_m}\sigma_{\text{vv}} \Rightarrow \sigma_{\text{vv}} = \frac{1-\nu_m}{\nu_m}\sigma_{rr,0} \tag{17}$$

assuming the rock or soil to be linearly elastic. In the above, E and ν are the elastic modulus and Poisson's ration of the metal and E_m and ν_m those of the tested material. If that is not the case, the tangential strain at the interface between the soil or rock and the ring will be continuous, yielding

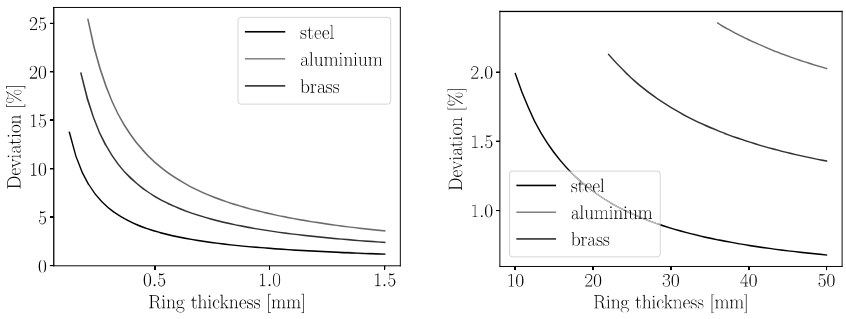
$$\varepsilon_{\theta\theta,m} = \frac{\sigma_{\theta\theta,m} - \nu_m\left(\sigma_{\text{vv}} + \sigma_{rr}\right)}{E_m} = \frac{\sigma_{\theta\theta} - \nu\sigma_{rr}}{E} = \varepsilon_{\theta\theta}, \tag{18}$$

which can be simplified to

$$(1-\nu_m)\frac{\sigma_{rr} - \sigma_{rr,0}}{E_m} = \left(\frac{r_2^2 + r_1^2}{r_2^2 - r_1^2} - \nu\right)\frac{\sigma_{rr}}{E} \Rightarrow \tag{19}$$

$$\frac{\Delta\sigma_{rr}}{\sigma_{rr}} = \frac{\frac{r_2^2+r_1^2}{r_2^2-r_1^2} - \nu}{(1-\nu_m)}\frac{E_m}{E} \tag{20}$$

For the sake of simplicity, it is assumed here that both the geomaterial and the metal have a Poisson ratio of 0.3. The elastic modulus of a hard compacted soil is assumed to be equal to 100 MPa and that of the compacted bentonite to equal 1000 MPa. The deviation from oedometric conditions expressed as a stress percentile, see equation (20), is shown as a function of the ring thickness in figures 13a and 13b for the bonded



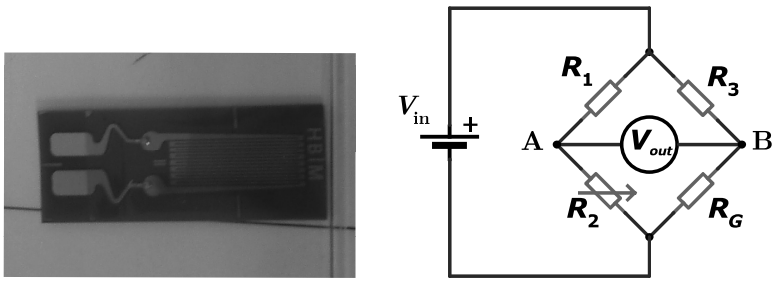
(a) Bonded soil) (b) Compacted bentonite

Figure 13: Deviation from oedometric conditions due to soft ring.

soil and the compacted bentonite respectively. It can be seen that for the bonded soil the ring thickness needs to be adjusted well beyond the value required when considering yielding to achieve a reasonable error, while the choice of material for the ring has a much higher influence for the compacted bentonite. This means that such an analysis needs to be performed for each case, as the stiffness of the tested material has a significant influence on the deviation from oedometric conditions.

4.2 Sensor selection and resolution

The radial stress is measured indirectly by measuring the tangential strain at the outer surface of the ring using strain gauges. Usually three strain gauges are used at 120 degrees angles, but other configurations are possible.



(a) Strain gauge) (b) Wheatstone bridge, courtesy of A. Tengattini

Figure 14: Strain gauge and Wheatstone bridge.

Strain gauges consist of a metallic foil embedded in an insulating backing, as shown in figure 14a. They can be glued on the object whose deformation is to be measured. As the object deforms, so does the metallic foil, changing its electrical resistance. These

changes in electrical resistance can in turn be measured to measure the deformation of the instrumented object. To measure the change in resistance of the measuring strain gauge R_G, a constant voltage V_{in} is applied to a Wheatstone bridge, in figure 14b, and the voltage V_{out} at the other leg of the bridge is measured. Assuming all resistances of the Wheatstone bridge to be initially equal, the relationship between voltage change and strain is

$$\frac{V_{out}}{V_{in}} = \frac{1}{4} k \cdot \varepsilon, \tag{21}$$

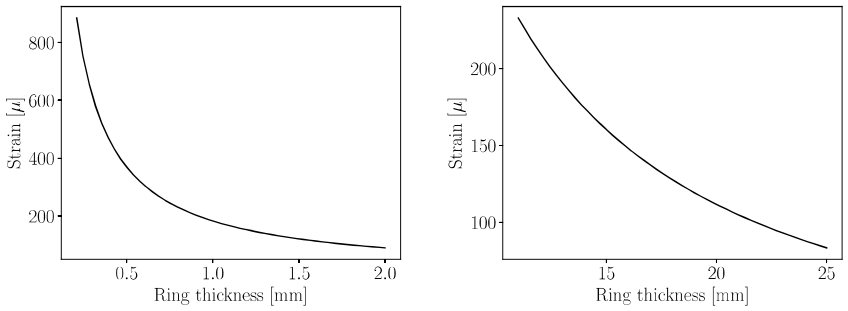
where k is a characteristic of the strain gauge commonly known as k-factor.

To apply the voltage V_{in} and read the response V_{out} a measurement amplifier can be used. It is assumed here that the available amplifier provides an input voltage of 1 Volt and can read in the $\pm$ mV interval with a resolution of 0.1% of the full scale, meaning with a resolution of 1 μV. This is a further consideration in dimensioning the ring. The circumferential strain at the outer surface of the ring, which is equal to

$$\varepsilon_{\theta\theta} = \frac{1}{E} \frac{r_1^2}{r_2^2 - r_1^2} p, \tag{22}$$

needs to be such that

- the strain gauges are not overextended, the limit usually being 0.3% or 3000 μstrain,
- the stress resolution is adequate, at best ensured by using as large as possible a part of 1 mV,
- the limit of the amplifier is respected, i.e. the 1 mV is not exceeded.



(a) Bonded soil

(b) Compacted bentonite

Figure 15: Maximum circumferential strain for different ring thicknesses.

Selecting brass for the bonded soil and steel for the compacted bentonite, the maximum circumferential strain is shown in figure 15 for different ring thicknesses. Settling on a maximum circumferential strain of 200 μstrain for both (corresponding to a thickness of 0.9 mm for the bonded soil and 12.5 mm for the compacted bentonite),

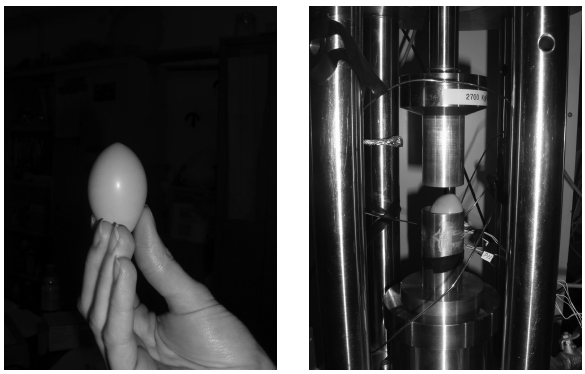
as not resulting in large deviations from the oedometric state and being well within the limits of the strain gauges, it remains to examine the resolution it is possible to achieve in terms of stress.

The resolution depends clearly on the k-factor of the strain gauges. Commonly its value is about 2. Making use of this value and the 200 μstrain fixed upon above, the maximum voltage measured would be equal to 0.1 mV, making use of a small range of the amplifier only. The resolution of 1 μV would amount to a stress resolution of 10 kPa for the bonded soil and one of 500 kPa for the compacted bentonite. While this may be acceptable, it is not optimal. If one would wish to improve the resolution, it would be possible to reduce the thickness of the ring in order to increase the range of the circumferential strain. Another option would be to use semiconductor strain gauges for small strains, for example with a k-factor of 100. In this case the maximum circumferential strain of 200 μstrain would result in a voltage of 5 mV, which is too high for the amplifier. To remedy this, a thicker ring would be required.

On the whole, in this case determining the ring thickness does not only take the stability into account, but also the acceptable error margin and the desired resolution of the measurement.

4.3 Calibration

For the calibration of the apparatus, it is suggested in [KB93] to measure the radial strain using the strain gauges and calculate the radial stress. This can be achieved by using equation (21) to determine the strain from the measured signal and equation (22) to determine radial stress p from the measured strain. This method ignores the vertical strain of the ring, resulting as a reaction to the radial and circumferential stresses.



(a) Water 'specimen' (b) Ring ready for calibration

Figure 16: Soft oedometer ring calibration.

In [CGN09] on the other hand, it is suggested to use water, for example in a thin balloon. The applied axial stress will then be equal to the radial stress, as the Poisson ratio

of water is equal to 0.5. In that way it is possible to calibrate the ring for measuring the radial stress without the error resulting from the vertical deformation or geometric factors.

5 Conclusions

The dimensioning of an apparatus has a direct influence on its range of applicability and is therefore of interest, whether one is constructing it or only using it. Requirements of high stresses come as a rule at the expense of resolution in stress control for example. When constructing an apparatus it is important to determine at the outset the range over which it should be used. When using an apparatus it is important to verify that the tests planned lie within its range of applicability and the precision in control is adequate. Precision in measurement is easier to improve by changing the corresponding sensors.

The dimensioning of a testing apparatus itself is a balancing act between safety considerations, precision requirements, costs and, often, technical and legal constraints, taking into account for example norms.

References

[Bea72] Jacob Bear. *Dynamics of Fluids in Porous Media*. American Elsevier Publishing Company, New York, 1972.

[BPFL06] Theocharis Baxevanis, Euripides Papamichos, Olav Flornes, and Idar Larsen. Compaction bands and induced permeability reduction in Tuffeau de Maastricht calcarenite. *Acta Geotechnica*, 1(2):123–135, Sep 2006.

[CBB09] X. Cui, A. M. M. Bustin, and R. M. Bustin. Measurements of gas permeability and diffusivity of tight reservoir rocks: different approaches and their applications. *Geofluids*, 9(3):208–223, 2009.

[CGN09] R. Castellanza, E. Gerolymatou, and R. Nova. Experimental Observations and Modelling of Compaction Bands in Oedometric Tests on High Porosity Rocks. *Strain*, 45(5):410–423, October 2009.

[DIN13] Mechanical properties of fasteners made of carbon steel and alloy steel - Part 1: Bolts, screws and studs with specified property classes - Coarse thread and fine pitch thread (ISO 898-1:2013); German version EN ISO 898-1:2013. Standard, DIN Deutsches Institut für Normung e. V. / Beuth Verlag GmbH, Berlin, Germany, 5 2013.

[EFD+26] R. Ewy, E. Fjær, P. Delage, D. Dewhurst, J. Dudley, A. Ferrari, S. Giger, M. Soldal, J. Stenebråten, B. Crawford, S. Fontoura, and L. Grande.

ISRM suggested methods for triaxial compression testing of shales and mudstones. *Rock Mechanics and Rock Engineering*, Jun 2026.

[HCF72] John A. Hudson, Steven L. Crouch, and Charles Fairhurst. Soft, stiff and servo-controlled testing machines: a review with reference to rock failure. *Engineering Geology*, 6(3):155–189, October 1972.

[HF68] E. Hoek and J.A. Franklin. Simple triaxial cell for field or laboratory testing of rock. *Transactions of the Institution of Mining and Metallurgy*, 77:A22– 26, 1968.

[KB93] D Kolymbas and E Bauer. Soft Oedometer—A New Testing Device and Its Application for the Calibration of Hypoplastic Constitutive Laws. *Geotechnical Testing Journal*, 16(2):263–270, June 1993.

[KBRW01] E. Klein, P. Baud, T. Reuschlé, and T-f. Wong. Mechanical behaviour and failure mode of Bentheim sandstone under triaxial compression. *Physics and Chemistry of the Earth, Part A: Solid Earth and Geodesy*, 26(1-2):21–25, January 2001.

[LGT25] Julia Leuthold, Eleni Gerolymatou, and Theodoros Triantafyllidis. Experimental Investigation and Constitutive Description of Mechanical Anisotropy in Soft, Porous Rock. *Journal of Geophysical Research: Solid Earth*, 130(5):e2024JB030075, May 2025.

[Mic99] J. H. Michell. On the Direct Determination of Stress in an Elastic Solid, with application to the Theory of Plates. *Proceedings of the London Mathematical Society*, s1-31(1):100–124, April 1899.

[Shi81] Mtsuhiko Shimada. The method of compression test under high pressures in a cubic press and the strength of granite. *Tectonophysics*, 72(3):343–357, 1981.

[SI17] T. Sabaliauskas and L.B. Ibsen. Improved PID control for triaxial testing liquefied specimen. DCE report 232, Department of Civil Engineering, Aalborg University, 2017.

[Ste90] R. Steiner. *ASM Handbook, Volume 1: Properties and Selection: Irons, Steels, and High-Performance Alloys*. ASM International, Materials Park, OH, 10th edition, 1990. Volumes 1-2 originally published as part of the Metals Handbook series.

[Wag13] J.F. Wagner. Chapter 9 - mechanical properties of clays and clay minerals. In Faïza Bergaya and Gerhard Lagaly, editors, *Handbook of Clay Science*, volume 5 of *Developments in Clay Science*, pages 347–381. Elsevier, 2013.

Unsaturated soils: experimental techniques

Alessandro Tarantino

University of Strathclyde, Glasgow, Scotland, UK

Abstract

Experimental investigation of unsaturated soils requires the measurement of hydraulic and mechanical state variables that are not encountered in conventional saturated soil mechanics. In particular, the determination of the (negative) pore-water pressure (suction), degree of saturation, and volumetric water content is essential for the characterisation of flow, water retention, and stress-strain behaviour. This chapter presents the fundamental principles underlying the measurement of these variables and reviews the experimental techniques most commonly adopted in laboratory and field investigations. The hydraulic and mechanical variables governing unsaturated soil behaviour are first introduced, together with the phase relationships required for their evaluation. Methods for suction measurement are subsequently examined, including direct techniques based on tensiometers and indirect techniques relying on porous block sensors, psychrometers, filter paper methods, and axis-translation procedures. The chapter discusses the physical principles, operating ranges, advantages, and limitations of each technique. Particular attention is devoted to dielectric methods for volumetric water content measurement, including Time Domain Reflectometry (TDR) and capacitance sensors. The relationship between soil dielectric permittivity, water content, electrical conductivity, and soil density is examined, highlighting the assumptions underlying commonly used calibration equations and the conditions under which corrections become necessary. This chapter aims to provide new users with a coherent framework for understanding the principles of unsaturated soil measurement, to help systematise the extensive information available in the literature and to support the selection of appropriate experimental techniques for laboratory and field applications.

1 Introduction

Unsaturated soils are encountered in a wide range of natural and engineered geosystems, including slopes, embankments, earth dams, pavements, landfill covers, and near-surface foundations. Their behaviour differs fundamentally from that of saturated soils because the pore space contains both water and air.

This gives rise to negative pore-water pressures, commonly expressed in terms of suction. The experimental complexity in unsaturated soil mechanics arises from the difficulty of measuring pore-water pressure in the negative range. As a result, multiple techniques, including both direct and indirect methods, have been developed. The experimental techniques discussed in this chapter, together with their principal advantages and limitations, include conventional tensiometers, high-capacity tensiometers, axis-translation technique, filter paper method, porous-block sensors, and psychrometers.

A special class of indirect methods is based on the establishment of equilibrium through the vapour phase between the soil water and the measuring instrument. The interpretation of these measurements requires the application of thermodynamic principles, which are often outside the traditional geotechnical engineering background and may therefore be difficult for the neophyte geotechnical researchers to fully appreciate. This chapter seeks to make these thermodynamics concepts more accessible and to provide readers with the necessary foundations to access the specialist literature.

A second class of measurements that extends beyond the traditional boundaries of saturated soil mechanics concerns the determination of the (volumetric) water content. In saturated soils, the pore space is completely occupied by water, and changes in water content coincide directly with changes in void ratio. Consequently, measurements of soil deformation are sufficient to characterise the water-content variations relevant to water-flow processes. In unsaturated soils, however, water and air coexist within the pore space, and changes in water content may occur independently of changes in volume. The measurement of water content therefore becomes an important aspect of experimental investigations in unsaturated soil mechanics.

The working principles of water-content sensors are largely based on the dielectric properties of the soil-water-air mixture, which, once again, lie outside the traditional geotechnical engineering background. This chapter therefore seeks to make these concepts related to the electrical behaviour of water and geomaterials more accessible and to provide readers with the necessary foundations for understanding and navigating the specialist literature on the measurement of water content in unsaturated soils. The experimental techniques discussed in this chapter, together with their principal advantages and limitations, include capacitance-based sensors and Time Domain Reflectometry (TDR) techniques.

2 Relevant variables for representing hydraulic and mechanical behaviour

2.1 Phase variables

Unsaturated soils contain two fluid phases: an aqueous solution, referred to as water, and an air-water vapour mixture, referred to as air. Different phase variables are used to quantify the pore space and the respective fractions of the pore space occupied by water and air. Table 1 provides a list of the phase variables commonly used

to describe and model the hydraulic and mechanical behaviour of unsaturated soils, together with their definitions and a breakdown of the measurements required for their determination.

Variables associated with the amount of water present in the pore space can be divided into two classes. The first class includes variables that require only mass measurements, such as the gravimetric water content and the water ratio. The second class includes variables that additionally require measurements of soil volume, such as the degree of saturation and the volumetric water content. These variables incorporate both mass and volumetric information and provide a richer description of the hydraulic state of an unsaturated soil. Selected phase relationships that are frequently used are summarised in Table 2.

Table 1. Phase variables for unsaturated soils

Variable	Definition	Measurement	
Gravimetric water content	$w = \frac{M_w}{M_s}$	$w = \frac{M}{M_s} - 1$	(1)
Degree of saturation	$S_r = \frac{V_w}{V_v}$	$S_r = \frac{M - M_s}{\rho_w} \frac{1}{V - \frac{M_s}{\rho_s}}$	(2)
Water ratio	$e_w = \frac{V_w}{V_s}$	$e_w = G_s \left(\frac{M}{M_s} - 1 \right)$	(3)
Void ratio	$e = \frac{V_v}{V_s}$	$e = \left(V \frac{\rho_s}{M_s} - 1 \right)$	(4)
Volumetric water content	$\theta = \frac{V_w}{V}$	$\theta = \frac{M - M_s}{\rho_w} \frac{1}{V}$	(5)
Porosity	$n = \frac{V_v}{V}$	$n = 1 - \frac{1}{V} \frac{M_s}{\rho_s}$	(6)

where:

V_w = volume of pore water

V_v = volume of voids

V = total volume

M_s = mass of solids

M_t = total mass (solids + water)

M_w = mass of water

ρ_s = solid density

ρ_w = water density

G_s = specific gravity

Table 2. Useful phase relationships

$$S_r = \frac{e_w}{e} = \frac{\theta}{n} \tag{7}$$

$$S_r\, e = w\, G_s \tag{8}$$

$$\theta = S_r\, n \tag{9}$$

2.2 Mechanical behaviour

The complete constitutive description of the mechanical behaviour of an unsaturated soil generally requires two independent effective stress variables, in contrast to saturated soils, whose behaviour can be described using a single effective stress.

Saturated soils comprise two phases, the soil skeleton and water respectively, and are characterised by two 'measurable' stress variables: the total stress and the pore-water pressure. Their constitutive behaviour can be formulated in terms of a single effective stress variable embodied in Terzaghi's effective stress postulate:

$$\sigma' = \sigma - u_w \tag{10}$$

where σ' is the effective stress, σ is the total stress, and u_w is the pore-water pressure. This indicates that the number of independent stress variables required to describe the mechanical behaviour of a saturated soil is reduced by one relative to the number of measurable stress variables.

Unsaturated soils comprise three phases, namely the soil skeleton, water, and air. Consequently, three 'measurable' stress variables exist: total stress, pore-air pressure, and pore-water pressure. Consistent with the case of saturated soils, the number of independent stress variables is reduced from three to two, resulting in the need for two independent effective stress variables to describe the mechanical behaviour of the soil (Figure 1).

Various choices of stress variables have been proposed for the constitutive modelling of unsaturated soils, and the reader is referred to [Hou97] and [Gal18] for a more detailed discussion. In most formulations, at least one of the effective stress variables incorporates the degree of saturation, either explicitly or implicitly. Consequently, both pore-water pressure, u_w, and degree of saturation, S_r, must be monitored or controlled during experimental testing.

It should be noted that, while pore-water pressure can be controlled relatively straightforwardly using axis-translation or other suction-control techniques, direct control of the degree of saturation remains challenging. In practice, the degree of saturation is generally treated as a response variable whose evolution is monitored during testing rather than prescribed independently.

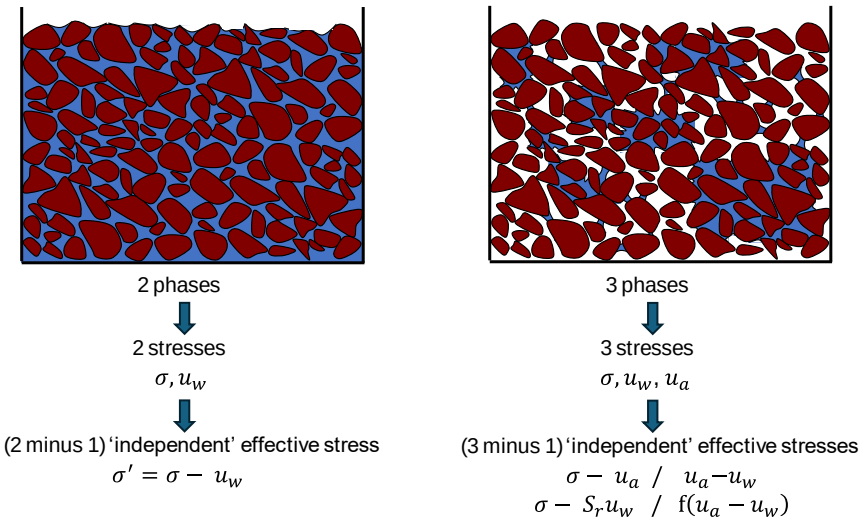


Figure 1: (a) Saturated soil. (b) Unsaturated soil.

2.3 Hydraulic behaviour

For the sake of simplicity, the water flow equation is presented here for one-dimensional (1D) conditions. The water mass balance can be written as follows:

$$\frac{\partial v_z}{\partial z} = -\frac{\partial \theta}{\partial t} \tag{11}$$

where v_z is the flow velocity, θ is the volumetric water content (volume of water per total volume), and t is the time. Considering Eq. (7), the term on the right-hand side of Eq. (11) can be re-written as follows:

$$\frac{\partial \theta}{\partial t} = n\frac{\partial S_r}{\partial t} + S_r\frac{\partial n}{\partial t} \tag{12}$$

where S_r is the degree of saturation and n is the porosity. The first term represents the storage capacity associated with changes in the degree of saturation, while the second term accounts for storage arising from changes in porosity. The former vanishes under saturated conditions, whereas the latter is often negligible in unsaturated soils [Mar20].

In Eq. (11), the flow velocity is given by the Darcy-Buckingam law ([Fre93], [Lu06]):

$$v_z = -k\frac{\partial h}{\partial z} = -k\frac{\partial}{\partial z}\left(\frac{u_w}{\gamma_w} + z\right) \tag{13}$$

where u_w is the pore-water pressure (the opposite of the pore-water tension), z is the vertical coordinate increasing upward, γ_w is the specific weight of water, and k is the hydraulic conductivity, which depends on void ratio e and degree of saturation S_r [Mit93]. Eq. (13) neglects diffusive and advective transport of water vapour. By combining Eqs. (11), (12), and (13), we can derive the water flow equation under 1-D conditions

$$\frac{\partial}{\partial z}\left[k\frac{\partial}{\partial z}\left(\frac{u_w}{\gamma_w}+z\right)\right]=n\frac{\partial S_r}{\partial u_w}\frac{\partial u_w}{\partial t}+S_r\frac{\partial n}{\partial u_w}\frac{\partial u_w}{\partial t} \tag{14}$$

For the case of saturated soils, k ≅ constant and S_r=1=constant, and Eq. (14) reduces to the Terzaghi's 1D consolidation equation

$$\frac{k}{\gamma_w}\frac{\partial^2 u_w}{\partial z^2}=\frac{\partial n}{\partial u_w}\frac{\partial u_w}{\partial t} \qquad \left[m_v=\frac{\partial n}{\partial u_w}\right] \tag{15}$$

where m_v is the compressibility coefficient.

For the general case of unsaturated soils given by Eq. (14), the solution of the water flow requires the definition of two functions, the water retention function $S_r = S_r(u_w)$ and the hydraulic conductivity function $k = k(u_w)$, in addition to the compressibility function $n = n(u_w)$.

The experimental techniques enabling the determination of the water retention and hydraulic conductivity functions are discussed in the following sections.

3 Measurement of negative pore-water pressure (suction)

Pore-water pressure in unsaturated soils is defined operationally in the same manner as in saturated soils. Specifically, it is defined as the water pressure measured by an instrument in hydraulic equilibrium with the soil water through liquid phase, provided that the solute concentration in the instrument water is the same as that in the soil water. Under these conditions, no osmotic gradients exist between the instrument and the soil. The condition of identical solute concentration between the instrument and the soil water is rarely stated explicitly in saturated soil mechanics textbooks; however, it is implicit in the classical operational definition of pore-water pressure.

Although pore-water pressure in unsaturated soils is operationally defined in the same way as in saturated soils, its measurement is considerably more challenging because pore-water pressures are negative. To overcome the difficulty of measuring negative pore-water pressures directly, a range of indirect measurement techniques has historically been developed. The interpretation of these measurements requires the application of thermodynamic principles, and it is within this context that the concept of suction is introduced.

This section reviews the definitions of suction and presents an overview of the techniques available for the direct and indirect measurement of negative pore-water pressure. Techniques for suction measurement in the laboratory and in the field have

widely been reviewed in the literature [Rid98], [Sca02], [Dur05], [Bul08], [Mar08], [Tar08], [Del08]) and the reader may refer to these publications for a comprehensive discussion of these techniques.

3.1 Definitions

Matric and total suction can be quantified by measuring the pressure that needs to be applied to water in a measurement system to establish equilibrium through liquid and vapour phase respectively.

If the measurement system is connected to the soil water through the liquid phase (left-hand side in Figure 2), solutes will rapidly diffuse toward the measurement system [Tar04]. As the solute concentration is the same in the soil and measurement system, the negative pore-water pressure in the measurement system is only generated by the action of the solid matrix. The negative pressure measured by the instrument relative to atmospheric air pressure is referred to as '*matric suction*', s_m (Figure 2). For consistency, the pore-water pressure measured in saturated soils should also be referred to as *matric* pore-water pressure, even though this qualifier is generally omitted.

If the measurement system is connected to the soil water through the vapour phase (right-hand side in Figure 2), solutes cannot diffuse toward the measurement system. '*Total suction*' is defined as the negative pressure that needs to be applied to liquid water in the measurement system to establish equilibrium through the vapour phase.

However, this pressure is never measured directly. Instead, total suction is determined from measurements of the water vapour pressure in equilibrium with the soil water. This is subsequently converted into total suction using a thermodynamic relationship derived by considering that the chemical potential of water is the same in the liquid and gaseous phases [Tar10]:

$$s_t = \frac{RT}{v_w} ln \frac{p_v}{p_v^0} \tag{16}$$

In summary, the factor discriminating between the measurement of total and matric suction is the presence of solutes in the measurement system (at the same concentration as the soil water). Matric suction is measured when solutes are allowed to diffuse towards the measurement system whereas total suction is measured when pure water is present in the measurement system (typically in the vapour phase).

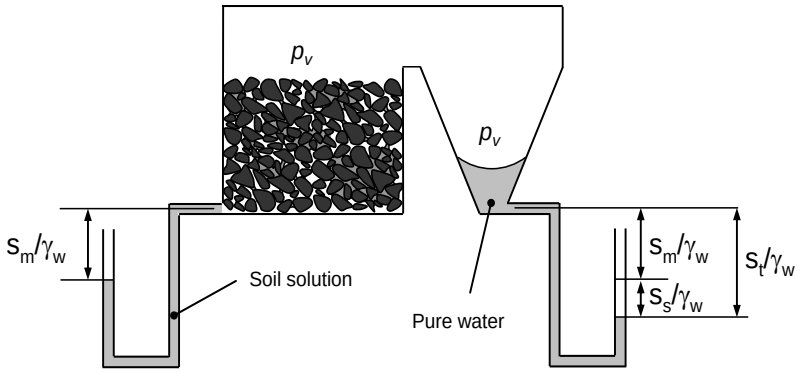


Figure 2: Definition of total and matric suction.

3.2 Direct measurement of suction

Matric suction is measured directly using tensiometers. The essential components of a tensiometer are a high air-entry porous ceramic, a liquid reservoir (filled with water), and a pressure-measuring device, such as the strain-gauged diaphragm used in the instrument shown in Figure 3. When the porous ceramic is brought into contact with an unsaturated geomaterial, water is drawn from the reservoir into the soil, resulting in the development of a negative pressure within the reservoir. This negative pressure causes the diaphragm to deflect towards the porous ceramic and can therefore be quantified from the change in electrical resistance of the strain gauge bonded to the rear surface of the diaphragm.

Water within the reservoir and ceramic remains under tension because of the menisci formed at the air-water interfaces within the ceramic pores (Figure 3). These menisci sustain the pressure difference between the external air pressure (typically atmospheric pressure) and the negative water pressure in the reservoir. The maximum sustainable pressure differential depends on the maximum curvature of the menisci, which is controlled by the pore size of the ceramic. This limiting pressure differential is known as the air-entry value of the ceramic and defines the maximum water tension that can be measured by the tensiometer.

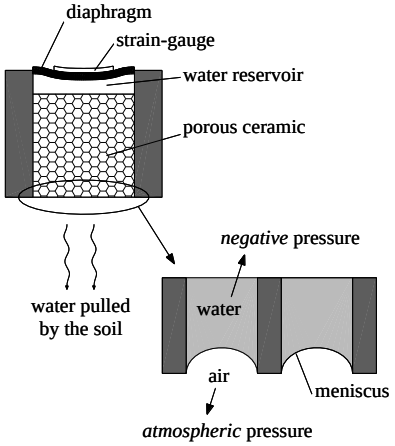


Figure 3: Working principle of tensiometer

Water tensions lower than the air-entry value of the ceramic can be sustained, but not indefinitely. Under tension, pre-existing air cavities trapped within crevices in the reservoir walls and the porous ceramic tend to expand, causing the air pressure within these cavities to decrease below atmospheric pressure. Owing to this pressure differential, air diffuses from outside the tensiometer towards the cavities, which gradually enlarge until they occupy the entire cross-section of the water reservoir. This phenomenon is referred to as tensiometer *cavitation.*

The rate at which air cavities grow depends on their initial number and size. By minimising the presence of such cavities through (i) the use of a small water reservoir, (ii) filling the tensiometer under vacuum with deaired water, and (iii) pre-pressurising the water within the ceramic filter and reservoir to high pressures, cavity growth can be significantly slowed. Under these conditions, even negative absolute water pressures (gauge pressures lower than −100 kPa) can be sustained for relatively long periods, ranging from hours to weeks, as first demonstrated by Ridley and Burland [Rid93]. Tensiometers capable of measuring negative absolute pore-water pressures are known as *high-capacity* tensiometers.

Cavitation is readily detected during measurements at negative absolute pressures. Once an air cavity expands to occupy the entire cross-section of the reservoir, negative absolute pressures can no longer be transmitted to the pressure-sensing device, since gases cannot sustain tensile stresses. Consequently, the measured pressure rises rapidly towards zero absolute pressure (approximately −100 kPa gauge pressure) as the air cavity expands throughout the reservoir, as illustrated in Figure 4.

When tensiometers (i) have relatively large water reservoirs, (ii) are filled with ordinary tap water, and (iii) are not preconditioned through high-pressure pressurisation, air cavities grow rapidly as the water pressure approaches zero absolute pressure. As a result, the measurement range is effectively limited to positive absolute pore-water pressures, corresponding to gauge pressures between 0 and −100 kPa.

Tensiometers that can measure only positive absolute pore-water pressures are commonly referred to as *conventional* tensiometers. In these devices, cavitation is more difficult to detect because air-filled cavities are still capable of transmitting positive absolute pressures. Consequently, the pressure response may remain apparently valid even after cavitation has occurred, potentially leading to erroneous measurements.

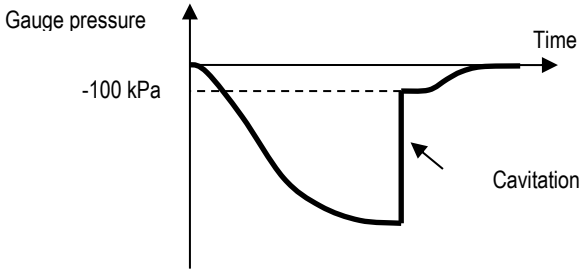


Figure 4: Cavitation in high-capacity tensiometer

3.2.1 Conventional tensiometers (positive absolute pressure)

Conventional tensiometers may differ in the relative arrangement of the porous ceramic filter and the pressure-sensing device, the method adopted for re-saturating the porous filter, and the procedure used to establish and maintain hydraulic contact between the soil and the tensiometer. One of the most common designs comprises a water-filled reservoir tube, a differential pressure transducer connected to the upper end of the tube, and a porous ceramic cup attached to its lower end (Figure 5).

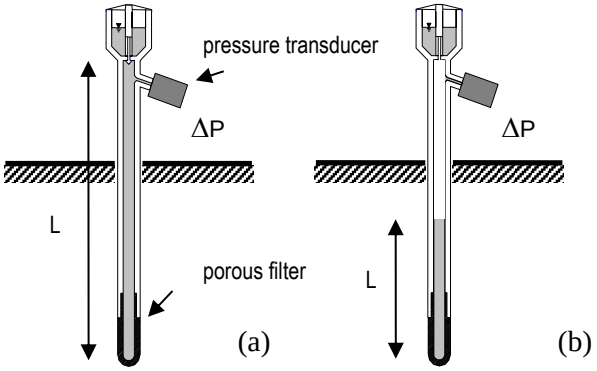


Figure 5: Schematic layout of tensiometer with sensing device at the ground surface and manual re-filling (Jet- fill vacuum gauge tensiometer, Soilmoisture Equipment Corp., Santa Barbara, CA, USA). (a) Fully saturated water reservoir. (b) Partially saturated water reservoir)

The suction measured at the tensiometer tip for a fully saturated tube end (Figure 5a) is given by

$$s = \Delta P - L \cdot \gamma_w \tag{17}$$

where ΔP is the differential pressure reading, γ_w is the unit weight of water, and L is the tube length. Equation (2) shows that the useful measurement range of a tensiometer decreases with increasing tube length by an amount $L\gamma_w$. Theoretically, the minimum pressure that can be measured by a conventional tensiometer is approximately −100 kPa. In practice, however, measuring pressures below approximately −60 to −70 kPa is difficult because air rapidly forms within the water-filled tube at these suctions. Ridley [Rid98] reported that the practical measurement range of a 1.5 m long tensiometer was only about 0–50 kPa, as air formation became too rapid and difficult to remove manually at higher suctions.

If air formation is not arrested, the tensiometer can eventually become completely dry, causing the pressure gauge to return towards zero. This can easily be mistaken for a genuine zero-suction measurement, corresponding to wet soil conditions, and can therefore lead to significant measurement errors.

When air forms in the upper portion of the tube (Figure 5b), the suction at the tensiometer tip is given by

$$s = \Delta P - L_w \cdot \gamma_w \qquad (L_w < L) \tag{18}$$

where L_w is the height of the water column. If suction is instead calculated using Equation (17), which assumes a fully saturated tube, significant measurement errors can result. Frequent maintenance is therefore required to keep the tensiometer fully saturated.

Saturation is generally restored by injecting water into the reservoir at the top of the tube and allowing water to flow out through the porous tip. This process temporarily increases the water content of the soil surrounding the tensiometer tip, and some time is therefore required for the soil to re-establish moisture equilibrium.

Figure 6 shows a typical measurement in which the recorded suction decreases with time after installation. In practice, it can be difficult to determine whether this decrease represents a genuine reduction in soil suction or progressive desaturation of the tensiometer. If the tensiometer is refilled, two typical responses may be observed. If the suction continues to decrease along the same trend (solid line in Figure 6), the tensiometer was fully saturated before refilling and the previous measurements were therefore representative of the actual soil suction. Conversely, if the post-refilling measurements deviate from the previous trend (dashed line in Figure 6), the actual soil suction was higher than that measured before refilling, and the apparent decrease in suction during this period was caused by progressive cavitation within the tensiometer.

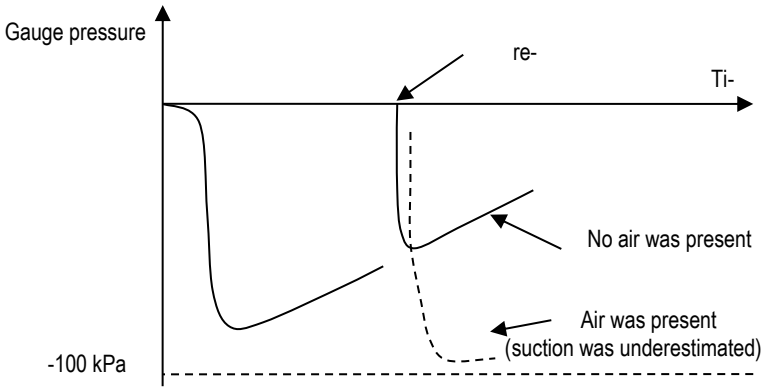


Figure 6: Re-saturation of conventional tensiometer

To overcome the limitations associated with long water reservoirs, tensiometers have been developed in which the pressure sensor is positioned close to the porous ceramic filter, thereby reducing the length of the water reservoir to a few centimetres (Figure 7). In this configuration, the formation of air within the water reservoir does not necessarily affect measurement accuracy, provided that the ceramic filter remains saturated and the negative pressure is still transmitted to the water in the reservoir. However, the presence of air substantially increases the response time because the compressibility of air is much greater than that of water. For reliable field operation, these tensiometers therefore require a means of removing air from the water reservoir when it forms.

Self-filling tensiometers have become commercially available, such as the TS1 (METER Group). Following dry periods, when the soil is rewetted by rainfall, an integrated micropump controlled by an onboard controller draws water from the soil into the tensiometer until the internal reservoir is completely refilled [DUR05].

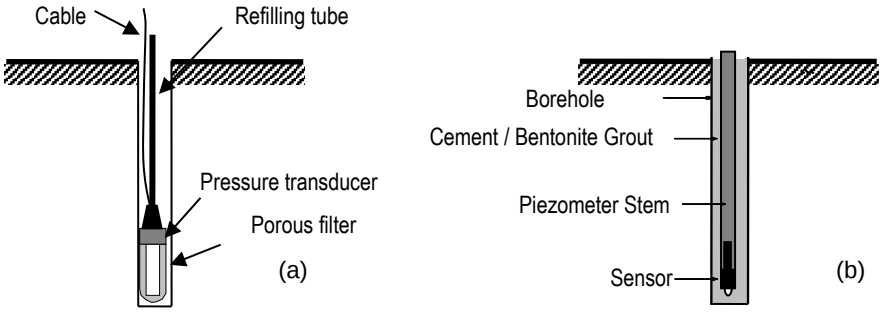


Figure 7: Schematic layout of tensiometer with sensing device close to the porous tip (a) pressed in pre-drilled hole; (b) in borehole filled with cement-bentonite grout ([RID 03]

Good hydraulic contact between the tensiometer cup and the surrounding soil is essential for reliable operation. When the tensiometer is installed by pressing the cup into a predrilled hole that is slightly smaller than the cup diameter, adequate hydraulic contact is generally achieved. In coarse-grained soils, however, this approach may not be feasible. In such cases, hydraulic contact can be established by filling a larger-diameter predrilled access hole with either a slurry prepared from sieved local soil or a suitable silty contact material.

Alternatively, the tensiometer can be installed in a borehole that is subsequently backfilled with a cement–bentonite grout. The grout acts as a secondary filter, transmitting negative pore-water pressures from the surrounding soil to the tensiometer. When appropriately designed, the grout remains saturated up to suctions of approximately 100 kPa or higher and therefore does not significantly restrict the suction range measurable by the tensiometer [Rid03].

3.2.2 High-capacity tensiometers (negative absolute pressure)

Ridley [Rid93] introduced the concept of measuring soil suctions exceeding 100 kPa using high-capacity tensiometers. Subsequently, Ridley and Burland [Rid96] presented an integral strain-gauged tensiometer capable of measuring suctions of up to 1500 kPa; the basic design of this tensiometer is illustrated in Figure 3. The instrument combines a fine porous filter, capable of remaining saturated at suctions of up to approximately 1,500 kPa, with a preconditioning procedure in which the water within the tensiometer is pressurised to very high pressures (e.g. 4,000 kPa). Ridley and Burland [Rid96] also developed an installation technique that allowed these tensiometers to be installed at depths of up to 5 m (Figure 8).

A major limitation of high-capacity tensiometers for field measurements is that, once cavitation occurs, the instrument generally needs to be removed from the ground and resaturated using the high-pressure procedure. Cui et al. [Cui08] presented a tensiometer designed to monitor suction changes within the relatively low suction range of 20–160 kPa at shallow depths (25 and 45 cm) over periods of up to three weeks. The installation system allowed the tensiometer to be readily removed and replaced when resaturation by pressurisation was required following cavitation.

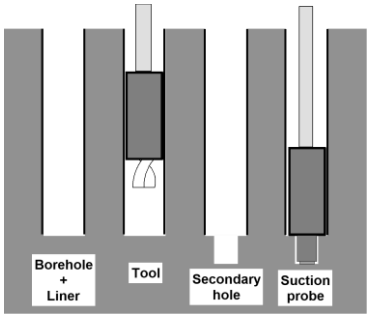


Figure 8: Installation of high-capacity tensiometer [RID 96].

3.3 Indirect measurement of suction

To monitor suctions greater than approximately 70 to 80 kPa, that is, beyond the measurement range of conventional tensiometers, a range of devices has been developed to measure suction indirectly. Indirect suction measurement techniques are based on equilibrium through either the liquid phase or the vapour phase.

3.3.1 Equilibrium through liquid phase – Porous block sensors

These devices are based on the measurement of water content or water content-related properties within porous blocks that are allowed to reach hydraulic equilibrium with the surrounding soil. A porous block is a rigid porous medium characterised by its own water retention behaviour, which is typically described by main drying and wetting curves, together with a series of scanning curves spanning the region between these bounding curves (Figure 9).

When the porous block is placed in contact with the soil, water flows into or out of the block until suction within the porous block equals that in the surrounding soil. Owing to water retention hysteresis, the equilibrium water content is not uniquely related to suction. However, when the hysteresis domain is relatively narrow, a relationship between water content and suction can be established with an acceptable degree of confidence (Figure 9). Consequently, if the water content, or a property related to water content, is measured, suction can be inferred from an appropriate calibration curve, with an inherent uncertainty arising from the hysteretic behaviour of the porous block material.

Common water content-related properties used for indirect suction measurement include electrical resistance (electrical resistance sensors), thermal conductivity or heat dissipation (heat dissipation sensors), and dielectric permittivity (dielectric equitensiometers). *Electrical conductivity sensors* have porous element made of gypsum or a granular matrix of silt size (Watermark™ sensors). Such devices are generally inexpensive but are more suitable for trend measurement rather than accurate determinate of suction. Electrical conductivity is affected by soil salinity ([AIT 51]), so calibrations for these devices are needed to take account of saline soils. Gypsum blocks have the advantage that they tend to buffer the soil salinity thereby decreasing this effect. They do this by dissolution of the gypsum, which means that gypsum block sensors have a limited life (up to 5 years in alkaline or neutral soils).

Thermal conductivity sensors, also known as heat dissipation sensors, determine suction by monitoring the temperature rise generated by a heating element embedded within the centre of the porous block. Because the thermal conductivity of the block varies with its water content, the measured temperature response can be related to suction through an appropriate calibration relationship.

Dielectric equitensiometers employ specially formulated porous matrix materials designed to minimise hysteresis between drying and wetting paths. The porous matrix is allowed to reach hydraulic equilibrium with the surrounding soil, after which its water content is determined using a dielectric permittivity sensor embedded in porous matrix (Figure 10). The measured water content is then converted into matric suction through a calibration curve that conceptually represents the water retention behaviour of the porous matrix material.

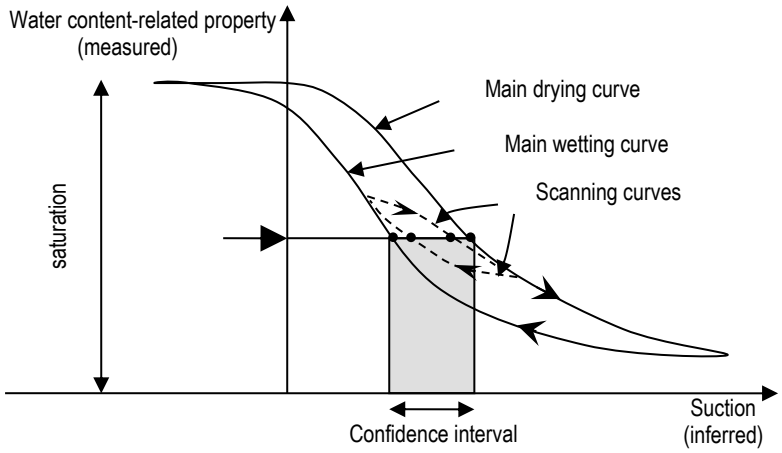


Figure 9: Working principle of porous block sensors

A common feature of all porous block devices is their relatively slow response time. When suction in the surrounding soil changes, water must flow into or out of the porous block until hydraulic equilibrium is re-established. However, because the porous block is typically unsaturated, its hydraulic conductivity is relatively low. Consequently, equilibration may require days or even weeks.

For example, [BER02] reported that Watermark electrical resistance sensors respond more slowly than tensiometers, exhibiting a lag of approximately two days. Similarly, [SHU00] found that the equilibration time of thermal conductivity sensors may be as long as two weeks, although a dry sensor may reach equilibrium within approximately four days. [NG03] also observed that thermal conductivity sensors exhibited a slower response than tensiometers, with delays of around two days.

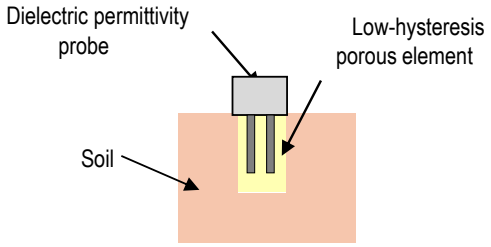


Figure 10: Schematic layout of dielectric equitensiometer

3.3.2 Equilibrium through liquid phase – Axis-Translation

The historical limitation of traditional tensiometers to measure matric suctions up to approximately 80 kPa prompted the development of an alternative laboratory technique by Richards ([Ric41], [Ric47]). This technique overcomes the limitation by artificially increasing the air pressure surrounding the soil specimen.

The principle of the method can be illustrated using the idealised model of a capillary pore. Figure 11a depicts the typical case in which the pore is subjected to atmospheric air pressure (i.e. zero-gauge air pressure), resulting in a water pressure lower than atmospheric pressure within the capillary. If the same capillary system is enclosed and subjected to an elevated air pressure under laboratory conditions, its behaviour changes as illustrated in Figure 11b. In this case, the increase in air pressure is transmitted to the pore-water, causing its pressures to rise while maintaining the same pressure difference across the air-water interface.

Let us consider the relationship between air and water pressure within the capillary tube.

$$u_a - u_w = \frac{4T\cos\theta}{d} \tag{19}$$

where u_a and u_w are the air and water pressure respectively, d is the diameter of the capillary, T is the surface tension, and θ is the contact angle.

Figure 11b assumes that the water and solid phases are sufficiently incompressible that the curvature of the meniscus is not significantly affected by the increase in air pressure [Ols65]. If this is true, Equation (19) predicts that the pressure difference u_a-u_w, otherwise known as the matric suction, also does not change. The result is that the water pressures within the capillary tube have now risen to positive gauge pressures and can be easily measured or imposed. If the elevated air pressure is also measured or imposed, the matric suction can be therefore inferred.

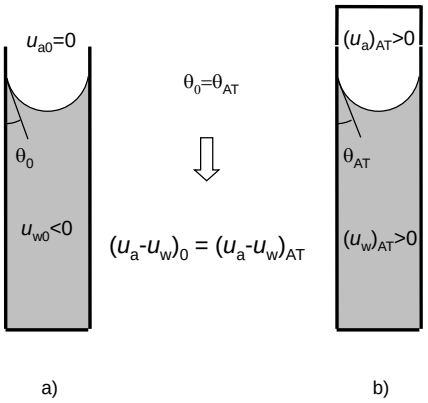


Figure 11:Working principle of axis translation technique [Mar08]

The significance of this elevation in water pressure is illustrated in Figure 12 for the measurement of matric suction in unsaturated soils. In Figure 12a, a sample of soil has a matric suction (u_a-u_w) in excess of 100 kPa. As a result, if this suction is to be quantified a pore-water pressure lower than -100 kPa must be recorded. However, if this same sample is subjected to a large positive air pressure, the water pressure in the soil can be raised to an easily measurable positive gauge pressure. If drainage of the pore water is prevented from the sample, the matric suction in the soil can now

be calculated as the difference of these two known pressures (Figure 12b). Thus, this technique is referred to as the 'axis translation technique' as water pressure has been translated upwards with the air pressure origin and away from the region of metastable states.

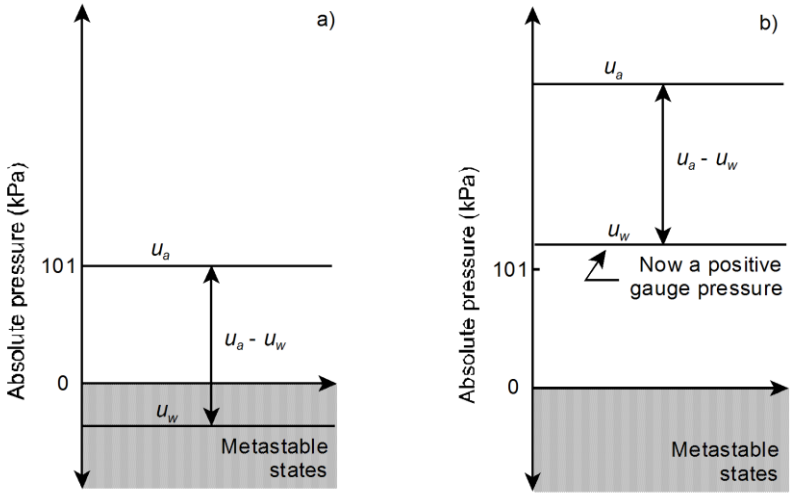


Figure 12: Use of the axis translation technique to avoid metastable states [Mar08]

The axis translation technique has been used to measure or control suction in triaxial tests, oedometers, and in direct shear tests. However, by far the most common application of the axis translation technique is in the pressure plate apparatus, which is used either to measure the suction of a given soil sample or to determine the soil-water retention curve (SWRC) of a soil (e.g. [Boc80], [Leo04], [Wan04]).

The conceptual procedure for measuring soil suction using the axis translation apparatus is illustrated in Figure 13. The apparatus comprises a high-air-entry ceramic plate underlain by a water reservoir connected to a water level control system, which is used to impose a constant zero water pressure within the reservoir. A null indicator moves towards or away from the water reservoir depending on whether water enters or leaves the reservoir, respectively (Figure 13a).

If an unsaturated soil sample is placed on the ceramic plate (Figure 13b), water will flow from the reservoir into the sample due to the suction within the soil. As a result, the null indicator will shift to the left. If the space above the sample is finally enclosed within a pressure chamber and the air pressure is increased, the direction of water flow is reversed, causing water to flow from the sample back into the reservoir. Consequently, the null indicator shifts towards the right. The air pressure required to restore the null indicator to its original position (Figure 13c) represents a quantitative measure of the suction of the soil sample.

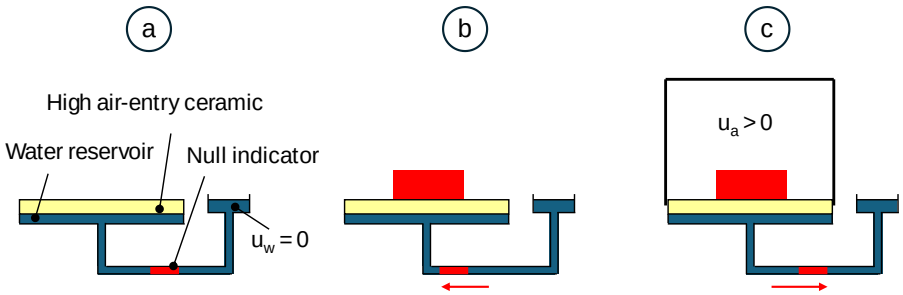


Figure 13: Axis translation technique for suction measurement

3.3.3 Equilibrium through vapour phase

Total suction s_t can be inferred from the measurement of relative humidity of the air in equilibrium with the soil water according to the 'psychrometric law' [TarR10]:

$$s_t = -\frac{RT}{v_w} ln \frac{p_v}{p_{v0}(T)} = -\frac{RT}{v_w} ln\, RH \tag{20}$$

where T is the absolute temperature, R is the universal gas constant, v_w. is the molar volume of liquid water, p_v is the pressure of the vapour in equilibrium with the liquid, p_{v0} is the saturated vapour pressure at the same temperature, and RH is the relative humidity. The reader can find a complete thermodynamic derivation of Equation (20) in [Tar10]. In this section, the equation is instead elucidated through its physical interpretation.

Let us consider the classical phase diagram of water, which describes the equilibrium conditions between the solid, liquid and vapour phases as a function of temperature and pressure (Figure 14a). Although rarely stated explicitly, the classical phase diagram of water implicitly refers to the case of a flat air-water interface. Under these conditions, surface curvature effects are absent and the pressure in the water phase is equal to that in the gas phase.

If the air-water interface is curved, as is the case in unsaturated soils, the pressure in the water phase becomes lower than that in the air phase as a result of capillary effects. This negative water pressure reduces the chemical potential of the pore water and, consequently, the equilibrium vapour pressure above the interface. As a result, the vapour pressure is lower than that corresponding to a flat air-water interface at the same temperature (Figure 14b). The relative humidity, RH, therefore decreases to values below 100%. The lower the liquid water pressure, or equivalently the higher the suction, the lower the equilibrium relative humidity. In other words, an increase in suction corresponds to a reduction in the vapour pressure of water relative to that of free water at the same temperature. This relationship is expressed mathematically by Equation (20). This phenomenon forms the basis of suction measurement through vapour-phase equilibrium.

Unfortunately, a second mechanism can also cause a reduction in vapour pressure, namely the presence of dissolved electrolytes in the aqueous solution. An increase in electrolyte concentration lowers the chemical potential of the water, which

in turn reduces the equilibrium vapour pressure. Consequently, the relative humidity, *RH*, decreases as the electrolyte concentration increases (Figure 14c).

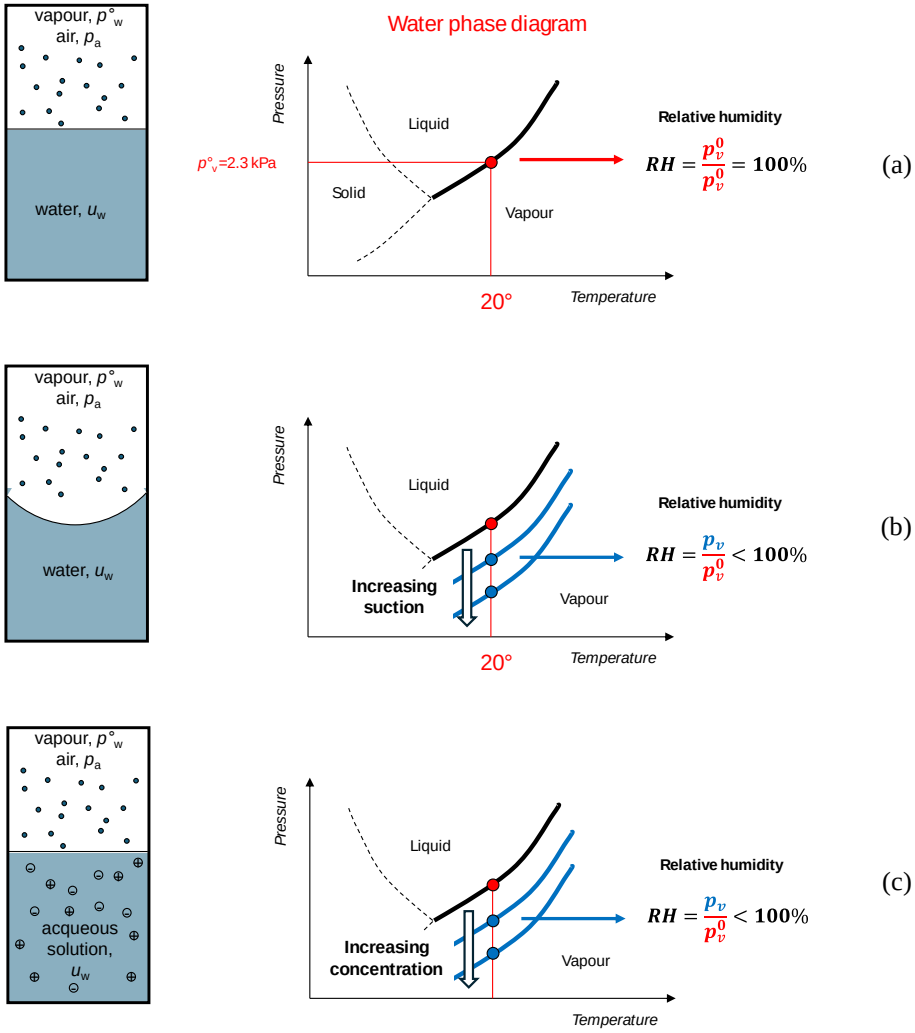


Figure 14: Working principle of suction measurement through vapour-phase equilibrium. (a) Free pure water at atmospheric pressure. (b) Pure water subjected to negative pressure. (c) Free aqueous solution at atmospheric pressure.

It is impossible to discriminate between the effects of negative pore-water pressure and electrolyte concentration from a single measurement of relative humidity. Both mechanisms reduce the chemical potential of water and therefore lead to a decrease in equilibrium vapour pressure and relative humidity.

For this reason, the concept of total suction is introduced. Total suction represents the combined contribution of matric effects associated with negative pore-water pressure and osmotic effects associated with dissolved electrolytes in the pore water.

Thermocouple Psychrometer

Relative humidity can be measured using a thermocouple psychrometer (Figure 15). Psychrometers operate by measuring the temperature difference between a dry bulb and a wet bulb. The dry bulb is maintained at the temperature of the surrounding soil, whereas the wet bulb is cooled by evaporation from a wetted surface. As the relative humidity decreases, the rate of evaporation from the wet bulb increases, producing a larger temperature depression relative to the ambient temperature. This temperature difference can be related to the relative humidity of the surrounding air through psychrometric relationships.

Because water vapour diffuses through the air phase while dissolved solutes remain confined to the liquid phase, the equilibrium relative humidity reflects the overall reduction in the chemical potential of the pore water. Consequently, the suction inferred from psychrometric measurements includes both the matric and osmotic components of suction. Psychrometers therefore provide a measure of the total suction of the soil rather than matric suction alone.

A thermocouple consists of two junctions formed by joining two dissimilar metals. When the two junctions are maintained at different temperatures, a voltage difference is generated between them due to the Seebeck effect. Conversely, when an electrical current is passed through the junction, heating or cooling occurs depending on the direction of the current, a phenomenon known as the Peltier effect [Dur05].

In soil applications, one junction of the thermocouple is suspended within a thin-walled porous ceramic or stainless-steel screen cup placed in the soil, while the reference junction is embedded in an insulated body located nearby to measure the ambient soil temperature. By applying an electric current, the suspended junction is cooled below the dew-point temperature, causing water vapour to condense on its surface. The current is then interrupted, and the condensed water begins to evaporate. This evaporation extracts latent heat from the junction, lowering its temperature below that of the surrounding air until a wet-bulb temperature is reached.

The temperature difference between the wet-bulb and dry-bulb junctions is a function of the relative humidity of the surrounding air. This relationship is established through calibration, typically by exposing the thermocouple to salt solutions of known relative humidity. Once the relative humidity has been determined, the corresponding total suction can be calculated using the psychrometric law. Because the measurement is based on vapour-phase equilibrium, the resulting suction incorporates both matric and osmotic contributions and therefore represents the total suction of the soil.

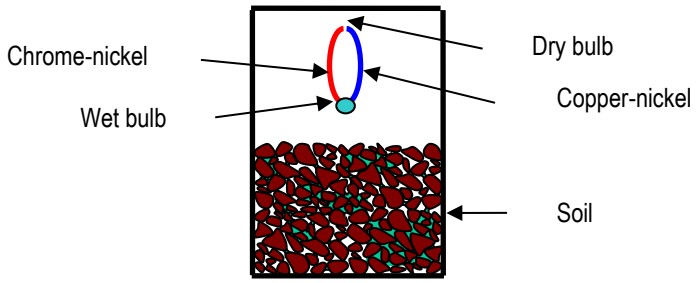


Figure 15: Working principle of thermocouple psychrometer

One of the limitations of the psychrometer is the need for equilibrium to be established through the vapour phase, which results in a relatively slow response time. In addition, psychrometers are highly susceptible to thermal gradient effects and do not perform well at shallow soil depths. For the same reason, suctions below approximately ~1000 kPa are difficult to measure reliably, and psychrometers should therefore be used primarily for measurements in the high-suction range.

To clarify this point, consider the effect of small temperature fluctuations on relative humidity. If temperature changes rapidly, it can be assumed that the water vapour pressure, p_v, remains constant, whereas the saturated vapour pressure, p_{v0}, changes in response to the temperature variation.

By deriving the Clausius-Clapeyron equation representing the vapour-liquid branch of the phase diagram of water, we can write:

$$\frac{dp_{v0}}{dT} = \frac{M_w L p_{v0}}{RT^2} \tag{21}$$

where M_w is the molar weight of water (M_w=18.016 g mol^{-1}), R is the universal gas constant (R=8.314 J K^{-1} mol^{-1}), L is the latent heat of evaporation (L= 2,453,000 J/kg at 20°C) and T is the absolute temperature, we obtain:

$$\frac{\partial s_t}{\partial T} = (s_t + \rho_w L)\frac{1}{T} \cong \frac{\rho_w L}{T} \tag{22}$$

where ρ_w is the water density. According to Equation (22), a temperature fluctuation of only ±0.01°C produces a change in suction of about ±80 kPa at 20°C. This is the reason why it is difficult to accurately measure suction lower than ~1000 kPa and the response may be highly inaccurate when the psychrometer is installed at shallow depths.

Chilled-mirror dew-point psychrometer

This method operates according to the working principle shown in Figure 16. Once the water vapour equilibrates in a sealed chamber with the soil water at the temperature T_0, the chamber is cooled until condensation is detected on a mirror. The temperature at which condensation occurs is referred to as the dew-point temperature, T_d. The vapour pressure corresponding to the dew-point temperature, T_d, obtained

from the liquid–vapour equilibrium curve of the phase diagram of water, corresponds to the vapour pressure that was in equilibrium with the soil water prior to cooling the chamber (at the temperature T_0). This enables the relative humidity of the vapour in equilibrium with the soil water to be quantified.

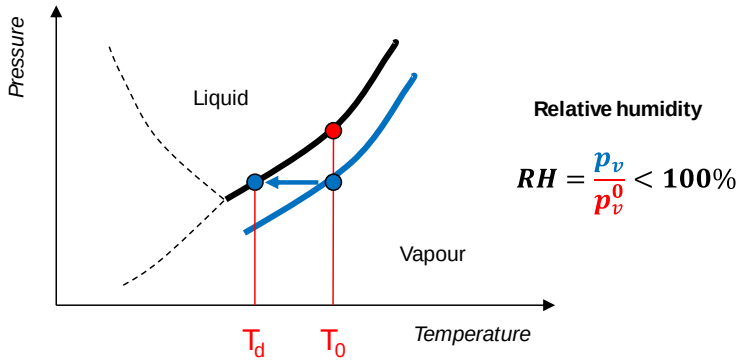


Figure 16: Working principle of chilled-mirror dew-point psychrometer

3.3.4 Equilibrium through liquid or vapour phase – Filter paper

The filter paper method operates on the same principle as the porous block sensor. When the filter paper is brought into equilibrium with the soil water, either through direct liquid contact or via the vapour phase, water flows into or out of the filter paper until the suction within the paper becomes equal to that of the surrounding soil (Figure 17). The soil suction can then be inferred from the water content of the filter paper using a calibration curve, which essentially represents the water retention curve of the filter paper material. The filter paper measures matric suction when it is in direct contact with the soil (Figure 17a) and total suction when is it suspended above the soil sample (Figure 17b).

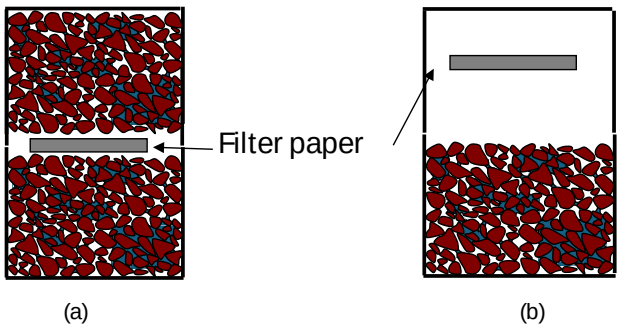


Figure 17: Filter paper measurement. (a) Contact filter paper for matric suction measurement. (b) Non-contact filter paper for total suction measurement.

After equilibrium has been attained, the water content of the filter paper is determined post-mortem by removing and weighing the paper. Consequently, the method is destructive and is therefore not suitable for continuous monitoring of soil suction.

[Leo02] and [Leo16] provide extensive reviews of the filter paper method using the standard Whatman No. 42 filter paper. The accuracy of suction measurements depends far more on the calibration methodology and equilibration conditions than on the filter paper itself. Much of the variability reported in the literature can be attributed to differences in the suction sources used during calibration, uncertainty in the reference suction values, and insufficient time allowed for moisture equilibrium to be established between the soil and the filter paper. Consequently, careful control of the experimental procedure is essential for obtaining reliable measurements.

Hysteresis effects are generally small when adequate equilibration time is provided. Although hysteresis is present, its influence on the measured water content of the filter paper is limited and does not significantly affect practical suction determinations. Reported differences in water content are typically small and are insufficient to explain the large scatter observed in some published calibration datasets.

4 Measurement of (volumetric) water content

Volumetric water content is commonly monitored using dielectric methods, which have been widely reviewed in the literature ([Gar01], [Nor01], [Jon02], [Rob03], [Tar08]). The reader is referred to these publications for comprehensive discussions of the underlying principles, instrumentation, and applications of dielectric measurement techniques.

The aim of this chapter is not to provide an exhaustive review, but rather to present the fundamental principles of dielectric water content measurement in a concise and systematic manner. The objective is to help new users understand the physical basis of these techniques and to navigate the extensive body of information available in the literature.

The dielectric permittivity of the soil mixture depends on the permittivities of the individual soil constituents (solid, liquid, and gas) and on their respective volumetric fractions. Since the relative permittivity of air is approximately 1, that of most soil minerals ranges between 3 and 5, and that of water is approximately 80 at 20°C, the dielectric response of the soil is largely controlled by the water phase and, therefore, by its volumetric fraction. Soil dielectric permittivity can thus be related to volumetric water content (the volume of water per unit total volume of soil) through suitable calibration relationships. This forms the basis of dielectric methods for water content measurement.

In practice, soil dielectric permittivity is not measured in a static electric field but in an alternating electromagnetic field that propagates in the form of waves. Under these conditions, the dielectric permittivity of water is frequency dependent and is described by both a real component, associated with energy storage, and an imaginary component, associated with energy dissipation. A proper understanding of soil dielectric behaviour and of wave propagation in transmission lines is therefore essential for the interpretation of dielectric measurements.

These topics are not commonly covered in undergraduate or graduate geotechnical engineering curricula and are therefore introduced in this chapter. The dielectric methods considered herein include broadband high-frequency techniques, such as Time Domain Reflectometry (TDR), and single-frequency techniques, such as Amplitude Domain Reflectometry (ADR) and capacitance-based sensors.

4.1.1 Dielectric-based method: working principle

For convenience, the working principle behind dielectric-based methods is illustrated by considering the case of capacitance sensors. In this configuration, two needles act as the electrodes of a capacitor, as illustrated in Figure 18.

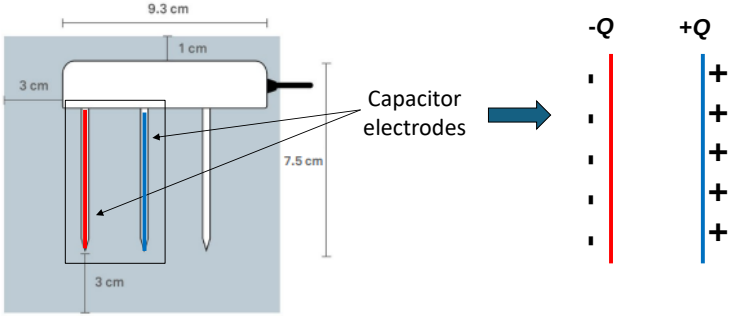


Figure 18: Capacitive sensor (METER Group TEROS 1) and equivalent capacitor.

Let us consider first the capacitor with vacuum separating the plates, where the plates have an area S and are separated by a distance d (Figure 19), For a given surface charge, Q, an electrical potential difference, ΔV_0, develops between the electrodes. This potential difference is determined by the capacitor geometry and the permittivity of vacuum, ε_0. The capacitance, C, is defined as:

$$C_0 = \frac{Q}{\Delta V_0} = \frac{\varepsilon_0 S}{d} \qquad d \ll \sqrt{A} \tag{23}$$

Let us now consider the case in which the space between the electrodes is filled with water. The asymmetric distribution of charge within a water molecule gives rise to a permanent electric dipole moment. As a result, when subjected to an electric field, the water molecules tend to align with the field direction.

The opposite electric charges associated with adjacent dipoles cancel each other, except at the electrode surfaces, where an imbalance of charge gives rise to an additional surface polarization charge, ΔQ_{water}. This polarization charge partially neutralizes the original charge on the electrodes. Consequently, the electric potential difference between the electrodes, ΔV, is reduced compared with that in vacuum, ΔV_0.

At the macroscopic scale, this effect is accounted for by introducing the relative permittivity, ε_r, such that the dielectric permittivity is given by the product of the vacuum permittivity, ε_0, and the relative permittivity. The capacitance C can then be expressed as

$$C = \frac{Q}{\Delta V} = \frac{\varepsilon_r \varepsilon_0 S}{d} \qquad \varepsilon_r \geq 1 \tag{24}$$

The greater the degree of polarisation within the dielectric, the higher its relative permittivity.

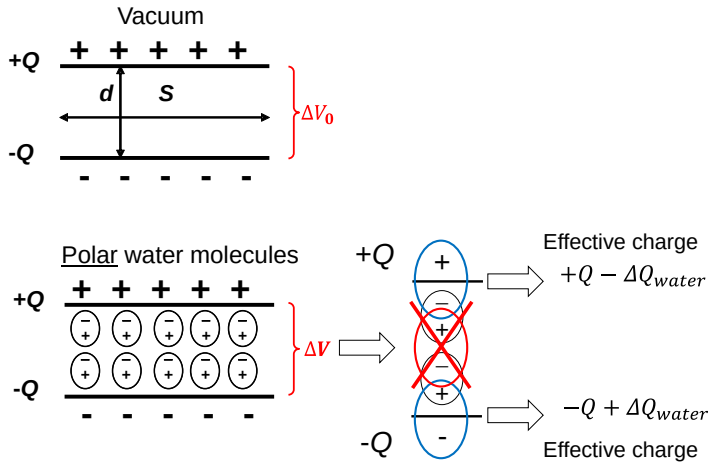


Figure 19: Effect of polar molecules on capacitance.

If ions are present between the electrodes, they migrate towards electrodes carrying the opposite charge, further reducing the effective charge on the capacitor plates (Figure 20). As a result, the capacitance increases further.

At the macroscopic scale, this phenomenon is accounted for by introducing an apparent relative permittivity, K_a, such that the effective dielectric permittivity is given by the product of the vacuum permittivity, ε_0, and the apparent relative permittivity. The capacitance C can then be expressed as

$$C = \frac{Q}{\Delta V} = \frac{K_a \varepsilon_0 S}{d} \qquad K_a \geq \varepsilon_r \geq 1 \tag{25}$$

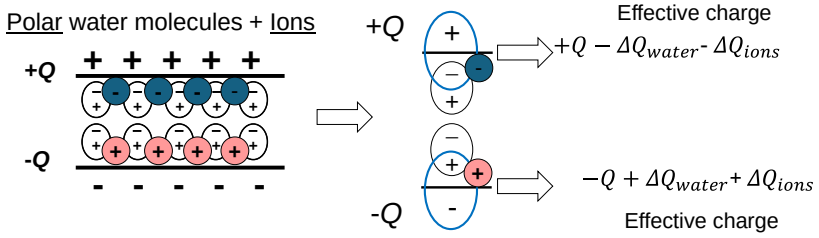


Figure 20: Effect of additional ions on capacitance.

4.1.2 Soil 'apparent' dielectric permittivity K_a in an alternating electric field

Owing to the inevitable presence of dissolved ions in soil water, the application of a DC voltage would cause ions to migrate towards electrodes of opposite charge and accumulate at the electrode interfaces. This process would give rise to electrode polarisation, whereby the resulting space-charge distribution would progressively screen the electric field within the medium. At equilibrium, the electric field in the bulk solution would be negligible, and the majority of the applied potential would drop across the polarised interfacial regions adjacent to the electrodes.

To avoid the charge accumulation associated with DC excitation, a time-harmonic electric field is applied. The oscillating electric field induces the alignment of molecular dipoles within the material, giving rise to a polarisation that varies in time with the applied field. At sufficiently low frequencies, the dipoles are able to follow the oscillations of the electric field closely. This dipole alignment contributes to the real (in-phase) component of the relative permittivity, ε_r'.

As the excitation frequency increases, the dipoles can no longer reorient rapidly enough to keep pace with the alternating field, a phenomenon known as dipole relaxation. Consequently, the magnitude of the polarisation decreases, and a time lag develops between the applied electric field and the polarization response. This phase lag is represented by the imaginary (out-of-phase) component of the relative permittivity, ε_r'', and is associated with the dissipation of electromagnetic energy as heat, as exploited in microwave heating.

The real and imaginary part of dielectric permittivity of pure water, ε_r' and ε_r" respectively, is plotted in Figure 21 The figure also reports the upper bound of TDR bandwidth (~1.5 GHz) showing that the TDR frequencies are well below the relaxation frequency of free water (~17 GHz) and are therefore associated with negligible dielectric losses.

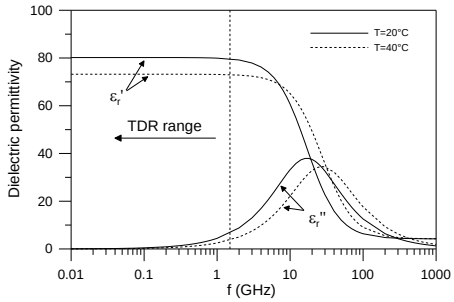


Figure 21: Real and imaginary part of water relative permittivity for two different temperatures

Water in soils is rarely pure and usually contains charge carriers such as ions. Ionic conductivity causes a loss of energy (*conductive loss*) in addition to loss due to dipole relaxation (*relaxation loss).* The effects of electrical conductivity and dielectric relaxation losses can be combined into the apparent permittivity, K_a:

$$K_a = \frac{\varepsilon_r^{'}}{2}\left[\sqrt{1+\left(\frac{\varepsilon_r^{''}+\frac{\sigma}{2\pi f \varepsilon_0}}{\varepsilon_r^{'}}\right)^2}+1\right] \tag{26}$$

where σ is the direct current electric conductivity, and f is the frequency

For the operating frequency range of sensors used to measure volumetric water content (approximately 0.5-1 GHz for Time Domain Reflectometry, TDR, and around 100 MHz for Amplitude Domain Reflectometry, ADR, and capacitance sensors), $\varepsilon_r^{''} \cong 0$ and the apparent permittivity can be then expressed as:

$$K_a = \frac{\varepsilon_r^{'}}{2}\left[\sqrt{1+\left(\frac{\frac{\sigma}{2\pi f \varepsilon_0}}{\varepsilon_r^{'}}\right)^2}+1\right] \tag{27}$$

The apparent permittivity, K_a, is the quantity actually measured by volumetric water content sensors. In contrast, the real part of the dielectric permittivity, $\varepsilon_r^{'}$, is the component that accounts for the presence of polar molecules and, consequently, for the amount of water present in the soil.

If conductive losses are negligible, which occurs at low values of electrical conductivity (σ) and/or at high operating frequencies (f), the apparent dielectric permittivity, K_a, can be directly related to the soil water content. However, when conductive losses are significant, a correction procedure must be applied to the measured K_a in order to derive the real part of the dielectric permittivity, $\varepsilon_r^{'}$.

Equation (27) also explains why high-frequency techniques, such as Time Domain Reflectometry (TDR), are less sensitive to electrolyte-induced electrical conductivity than techniques operating at much lower frequencies, such as Amplitude Domain Reflectometry (ADR) and capacitance sensors.

The effects of measurement frequency and electrical conductivity on the apparent dielectric permittivity are illustrated in Figure 22. Figure 22a shows the apparent permittivity of moderately saline water (σ~0.5 S/m) at different temperatures. It can be noticed that the apparent permittivity in high frequency range of TDR bandwidth is fairly constant and equal to the static permittivity of pure water.

Figure 22b shows the apparent permittivity for saline water having electrical conductivity of about 5 S/m (sea water) at different temperatures. In this case, the apparent permittivity in the high frequency range of TDR bandwidth is significantly higher than static permittivity of pure water due to the contribution of the term the $\sigma/2\pi f\varepsilon_0$. In addition, the apparent permittivity increases with temperature in contrast to the moderately saline water.

The TDR bandwidth is 0.5-1 GHz and this frequency falls in the range where apparent permittivity K_a is not affected by both relaxation and conductive losses (with the exception of high conductivity pore-water or very active clays). On the other hand, single frequency methods (ADR and Capacitance methods) operate at lower frequencies (~100 MHz) and are therefore more sensitive to electrical conductivity of soils.

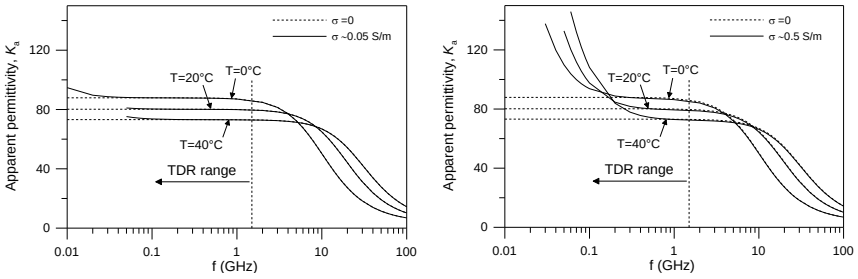


Figure 22: Apparent permittivity K_a of aqueous solution water having σ~0.5 S/m (moderately saline) and σ~5 S/m (sea water)

4.1.3 Flow chart for dielectric permittivity-based measurement

The measurement of volumetric water dielectric permittivity-based sensor involves two stages as illustrated in Figure 23:

1. Derive the real part of the dielectric permittivity, ε_r', from the measured apparent dielectric permittivity K_a
2. Derive the volumetric water content θ from the real part of the dielectric permittivity, ε_r'.

These two stages are discussed separately in the following sections.

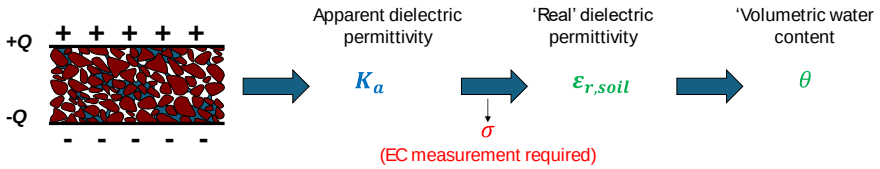


Figure 23: Dielectric permittivity measurement flow chart

4.1.4 From apparent dielectric permittivity K_a to real part of dielectric permittivity ε'_r

Different empirical or semi-empirical equations have been proposed to derive the real part of the dielectric permittivity, ε_r', from the measured apparent dielectric permittivity K_a. These are listed below for the cases of Capacitance and TDR measurements.

CAPACITANCE

$$\sqrt{\varepsilon_{r,soil}} = \sqrt{K_a} - 6.28\,\sigma \qquad [\sigma = S\,m^{-1}\,] \qquad \text{[Rob99]} \qquad (28)$$

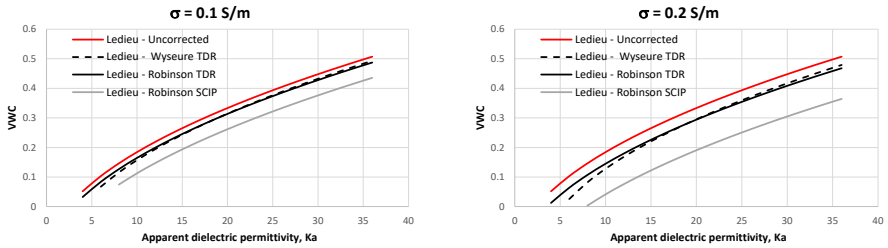
TDR

$$\sqrt{\varepsilon_{r,soil}} = \sqrt{K_a} - 1.72\,\sigma \qquad [\sigma = S\,m^{-1}\,] \qquad \text{[Wys97} \qquad (29)$$

$$\varepsilon_{r,soil} = K_a - 14.32\,\sigma \qquad [\sigma = S\,m^{-1}\,] \qquad \text{[Rob99]} \qquad (30)$$

$$\varepsilon_{r,soil}^{'} = K_a - \frac{1}{4K_a}\left(\frac{\sigma}{2\pi f_{eff}\varepsilon_0}\right)^2 \qquad \text{[Chu09]} \qquad (31)$$

To illustrate the effect of electrical conductivity correction, Figure 24 presents the estimated volumetric water content obtained without correcting the apparent dielectric permittivity and after applying the correction based on Equations (28)-(30). The comparison is made using the calibration equation proposed by Ledieu [Led86] presented later on in this chapter. The figure shows that the correction becomes relevant when the electrical conductivity exceeds 0.1 S/m.



(a) (b)

Figure 24: Effect of electrical conductivity on apparent dielectric permittivity and estimation of volumetric water content

4.1.5 From real part of dielectric permittivity to volumetric water content θ

The (real part) of the dielectric permittivity of a mixture ε_m can be expressed via the Lichtenecker equation [Lic26]

$$\sqrt{\varepsilon_m} = \frac{V_s}{V}(\varepsilon_s)^\alpha + \frac{V_a}{V}(\varepsilon_a)^\alpha + \frac{V_w}{V}(\varepsilon_w)^\alpha \qquad (32)$$

where V_s, V_a, and V_w, are the volumes of the solids, air, and liquid water respectively, V is the total volume of the mixture, ε_s, ε_a, and ε_w are the values of dielectric permittivity of the solids, air, and liquid water, and α an exponent that depends on the spatial arrangement of the mixture with the respect to the applied electromagnetic field. For a heterogeneous layered medium, the exponent varies between α=-1 for an electromagnetic field orthogonal to the layers, and α= 1 for a parallel field [Zak98].

The Lichtenecker model for α=0.5 is referred to as 'refractive index' mixing model (RIMM). It is associated with an isotropic distribution of the four phases and has been found to capture satisfactorily experimental data for mineral soils ([Rob99], Rot90]).

The volume fractions in Equation (32) can be expressed in terms of phase relationship as follows:

$$\begin{aligned} \frac{V_w}{V} &= \theta \\ \frac{V_s}{V} &= \frac{\rho_d}{\rho_s} \\ \frac{V_a}{V} &= 1 - \frac{\rho_d}{\rho_s} - \theta \end{aligned} \tag{33}$$

where θ is the volumetric water content of the liquid water, ρ_d is the dry density of the soil, ρ_s is the density of the solids.

By combining Eqs. (32) and (33) and considering α=0.5, the calibration equation to derive the volumetric water content θ from the dielectric permittivity ε_m of the soil mixture can be derived as:

$$\theta = a\sqrt{\varepsilon_m} - b \tag{34}$$

where:

$$\begin{aligned} a &= \frac{1}{\sqrt{\varepsilon_w} - \sqrt{\varepsilon_a}} \\ b &= \frac{\frac{\rho_d}{\rho_s}\sqrt{\varepsilon_s} + \left(1 - \frac{\rho_d}{\rho_s}\right)\sqrt{\varepsilon_a}}{\sqrt{\varepsilon_w} - \sqrt{\varepsilon_a}} \end{aligned} \tag{35}$$

Equations (34) and (35) provide a general calibration equation for unsaturated soils. It is worth noticing that the intercept *b* depends on the dry density of the soil

4.1.6 Empirical calibration equations

Empirical equations have been widely adopted to infer the volumetric water content from the apparent dielectric permittivity, i.e. Topp [Top80] and Ledieu [Led86] equations:

Topp's equation

$$\theta = -5.3 \cdot 10^{-2} + 2.92 \cdot 10^{-2} K_a - 5.5 \cdot 10^{-4} K_a^2 + 4.3 \cdot 10^{-6} K_a^3 \tag{36}$$

Ledieu's equation

$$\theta = 0.1138\sqrt{K_a} - 0.1758 \tag{37}$$

These two empirical equations derive the volumetric water content from the apparent dielectric permittivity K_a. In the light of the discussion in the previous sections, these empirical equations implicitly assume that

i) The apparent dielectric permittivity K_a is equal to the (real part of the) dielectric permittivity ε_m as is the case for soils with negligible electrical conductivity.

ii) The dry densities of the soils from which these equations were empirically derived fall within a relatively narrow range, making the equations practically independent of dry density.

Figure 25 shows the calibration curve derived from the refractive index mixing model for two different soil dry densities (ρ_d=1.3/1.5 g/cm^3) against the empirical equations by Topp and Ledieu. The curves are essentially overlapping up to $\theta = 0.4$ with slight deviation for $\theta > 0.4$.

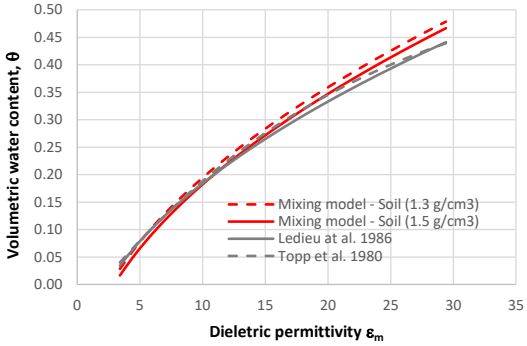


Figure 25: Calibration curve derived from the 'refractive' mixing model compared to the empirical models

Equations (34) and (35) show that the calibration equation for the volumetric water content depends on the soil dry density. When the soil dry density falls outside the range investigated by Topp [Top80] and Ledieu [Led86] when developing their empirical equations, Equations (36) and (37) are no longer applicable.

For the case of low density (ρ_d<0.8g/cm^3) organic soils, Malicki *et al.* [Mal96] have developed the following empirical equation:

$$\theta = \frac{\sqrt{Ka} - 0.819 - 0.168\rho_d - 0.159\rho_d^2}{7.17 + 1.18\rho_d} \tag{38}$$

where the dependency of the volumetric water content, θ, on the apparent dielectric permittivity, K_a, is corrected for the dry density, ρ_d.

Figure 26 shows the Malicki's model compared to the RIMM for the case of ρ_d=0.8 g/cm^3. For comparison, the Ledieu's equation is also shown in the figure. The lower dry density shifts the calibration curve upward, for both the RIMM and Maliki's equation. This shows once again that the traditional Ledieu's and Topp's empirical equations only apply to a relatively narrow range of dry density, typically encountered in agricultural soils. These equations are no longer valid for lower dry densities, as encountered in organic soils, or for very high dry densities, as encountered in highly compacted soils.

It should be noted that there is a discrepancy between the Malicki's and the RIMM models. This may partly be attributed to the likely non-negligible electrical

conductivity of the organic soils that makes $\varepsilon_m \neq K_a$. A discussion on the effect of the soil electrical conductivity is, however, outside the scope of this chapter.

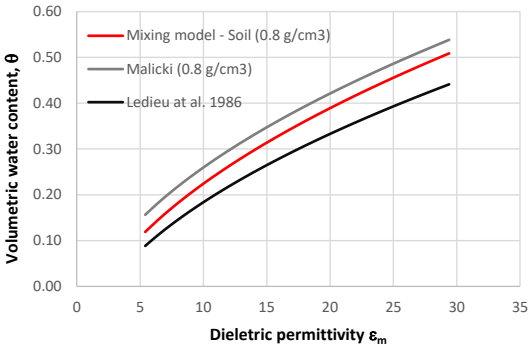


Figure 26: Calibration curve derived from the 'refractive' mixing model compared to the empirical models by [Mal96]

4.1.7 TDR applied to volumetric water content measurement

A TDR system consists of a step pulse generator, an oscilloscope, a coaxial cable, and a probe, in turn consisting of a head incorporating two or three rods (Figure 27). The step pulse generator launches a fast-rise time voltage step associated with a bandwidth up to 1.5 GHz and the reflection waveform is recorded by an equivalent time sampling oscilloscope. The highest frequencies are sufficiently lower than relaxation frequency of water and fall in the range where the effect of electrical conductivity is often negligible.

TDR working principle may be illustrated following [Nis 95]. Let us assume that impedance of segment AB, Z_C, is greater than that of segment BC, Z_P. This is the case of probe inserted in water or wet soil.

At time t=0, the step pulse generator starts to launch electromagnetic waves to produce a voltage step, V_0. At time $t=t_A$, the front of the voltage step reaches the oscilloscope that records an instantaneously rise in voltage, V_0 (stage 1).

At point B, some of the voltage step is reflected back towards the sampler, $U_{r,1}$, and some is transmitted further on, $U_{t,1}$. Since $Z_C > Z_P$, the reflection coefficient ρ is negative ($\rho<0$) and a negative reflected step is observed (the reflected wave travels in counterphase with the wave transmitted by the pulse generator). The superposition of these two waves causes a drop in voltage amplitude with respect to the original wave (stage 2).

At time $t=t_B$, the front of the reflected step has reached the oscilloscope, which detects a drop in voltage. On the other side, the transmitted voltage step $U_{t,1}$ is totally reflected in phase at the end of the transmission line (open ended circuit) because $Z_L \rightarrow \infty$ and the reflection coefficient $\rho=1$ (stage 3). The reflection of the transmitted voltage step $U_{t,1}$ reaches back point B. Here it is partly reflected in phase ($\rho>0$) towards point C, $U_{r,}2$, and partly transmitted in phase toward the sampler, $U_{t,2}$ (stage 4).

The transmitted voltage step $U_{t,2}$ reaches the sampler at $t=t_C$. Because it is in phase with the waves transmitted by the pulse generator, the sampler measures a rise in voltage (stage 5). Multiple reflections will then take place in the system until a stable level is reached.

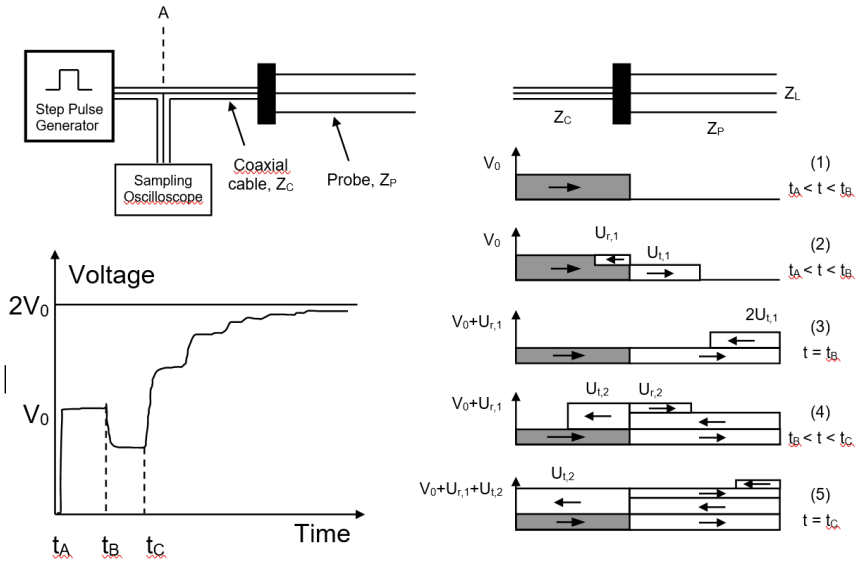


Figure 27: Voltage step reflections in an open-ended transmission line having an impedance discontinuity (after [NIS 95]).

The apparent permittivity K_a of the medium in which the probe is inserted can be obtained from the propagation velocity of the pulse in the probe according to:

$$K_a = \left(\frac{c}{V_p}\right)^2 = \left(c\frac{t_C - t_B}{2L_{BC}}\right)^2 \tag{39}$$

The time t_B at which the signal enters the probe and the time t_C at which the signal is reflected at the end of the rods can be derived from the reflection waveform as illustrated in Figure 28. In this figure, the time t_{head} represents the time at which the signal enters the head of the probe and Δt is the tame taken by the signal to travel along the head and reach the top of rods (refer to [Tar08] for a detailed discussion on the procedures to determine t_{head}, t_B and t_C).

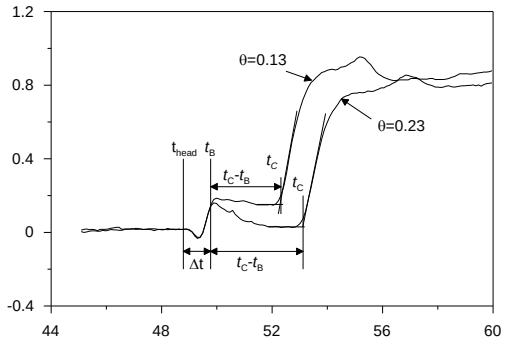


Figure 28: Reflection waveforms in fine sand samples and travel time determination.

4.1.8 Water content measurement using Capacitance sensors

Due to installation difficulties, TDR systems are not always adapted for determination of water content at relatively high depths. Depth capacitance probes have then been designed to sense the soil from within an access tube or directly 'dropped' into a pre-drilled hole (Figure 29). These probes are relatively inexpensive and easy to operate and are becoming a popular choice for routine monitoring purposes.

The depth capacitance installation probe consists of an electrode pair separated by a plastic dielectric. The upper and lower electrodes and the plastic separator are in the shape of a cylinder that fits closely inside the plastic access tube. The lines of force between the capacitor plates intersect the soil outside the tube (the length of the plates is of the same order of magnitude as plate distance). A resonant *LC* circuit (*L*= inductance, *C*= capacitance) in the probe includes the ensemble of the soil outside the access tube, the access tube itself, plus the air space between the probe and the access tube, as one of the capacitive element. The LC circuit is included in the tuned circuit of an oscillator to measure the resonant frequency F_{res} of the LC circuit. The resonant frequency depends on the capacity of the soil-access tube system *C*, which in turn linked to the soil apparent permittivity K_a. Water content measurements can be performed by directly relating the resonant frequency F_{res} to the water content ([Pal97]) or by developing a calibration between the resonant frequency F_{res} and the apparent permittivity K_a which can be in turn related to water content using the empirical TDR relationships ([Rob98]). The major disadvantage of the single step calibration is that one cannot separate errors due to the instrument from errors due to the calibration between capacitance and soil water content.

Surface capacitance insertion probes (SCIP) have also been developed and may be an interesting alternative to TDR when measurements at few locations in the field have to be made.

It should be noted that the operating frequency of the capacitance probe is in the range 70-150 MHz. In this frequency range, the apparent permittivity is more sensitive to electrical conductivity with respect to TDR.

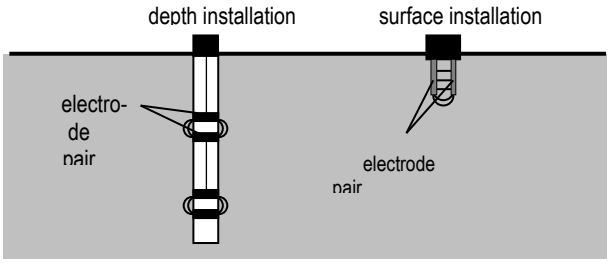


Figure 29: Surface and depth installation capacitance probes and relative electric fields.

5 Conclusions

The accurate characterisation of unsaturated soils relies on the measurement of hydraulic and mechanical state variables that have no direct counterpart in saturated soil mechanics. Among these, suction, degree of saturation, and volumetric water content play a central role in governing flow processes, water retention, and mechanical behaviour. This chapter has reviewed the fundamental principles underlying the measurement of these variables and has examined the most widely adopted laboratory and field techniques for their determination.

The discussion has shown that no single measurement method is universally applicable, as each technique operates within specific ranges and is subject to distinct assumptions and limitations. Direct and indirect approaches to suction measurement, including tensiometers, porous block sensors, psychrometers, filter paper methods, and axis-translation techniques, each provide valuable information when selected and implemented appropriately. Similarly, dielectric methods such as Time Domain Reflectometry (TDR) and capacitance sensors offer powerful tools for water content determination, although their accuracy depends on factors including soil density, electrical conductivity, and the validity of calibration relationships.

A sound understanding of the physical principles governing these measurement techniques is essential for the correct interpretation of experimental data and for the design of reliable testing programmes. By bringing together the theoretical background, operational characteristics, and practical limitations of the most commonly used methods, this chapter provides a structured framework to support informed technique selection and to promote more consistent and rigorous investigation of unsaturated soil behaviour in both laboratory and field environments.

References

[Ait51] Aitchison GD, Butler PF, Gurr CG. 1951. Techniques associated with the use of gypsum block soil moisture meters. Aust. J. Appl. Sci., 2: 57–75.

[Ber02] Bertolino AVFA, Souza AP, Fernandes NF, Rangel AM, de Campos TMP, Shock CC 2002. Monitoring the Field Soil Matrix Potential using Mercury Tensiometer and Granular Matrix Sensors. In Unsaturated Soils (eds. Jucá, J.F.T, de Campos, T.M.P. and Marinho, F.A.M.), Proc. 3rd Int. Conf. on Unsaturated Soils, Recife, Lisse: Balkema, Vol. 1, p. 335-338.

[Boc80] Bocking KA, Fredlund DG 1980. Limitation of the axis translation technique. In: Proc. 4th Int. Conf. on Expansive Soils, Vol. 1, Colorado: 117–135.

[Bul08] Bulut R, Leong EC 2008. Indirect measurement of suction. Geotechnical and Geological Engineering, 26(6): 1573-1529.

[Chu09] Chung C-C, Lin C-P 2009. Apparent dielectric constant and effective frequency of TDR measurements: Influencing factors and comparison. Vadose Zone Journal, 8: 548–556.

[Del98] Delage P, Romero E, Tarantino A 2008. Recent developments in the techniques of controlling and measuring suction in unsaturated soils. First International Conference on Unsaturated Soils, Jul 2008, Durham, United Kingdom. p. 33-52.

[Dur05] Durner W, Or D 2005. Soil Water Potential Measurement. In: Encyclopedia of Hydrological Sciences, (ed. Anderson M.G. and J. J. McDonnell), John Wiley & Sons, p. 1089-1102.

[Fre93] Fredlund D, Rahardjo H 1993. Soil Mechanics for Unsaturated Soils. John Wiley and Sons, New York.

[Gal18] Gallipoli D, Grassl P, Wheeler S, Gens A 2018. On the choice of stress–strain variables for unsaturated soils and its effect on plastic flow. Geomechanics for Energy and the Environment, 15: 3-9. https://doi.org/10.1016/j.gete.2018.02.002.

[Gal18] Gallipoli D, Grassl P, Wheeler S, Gens A 2018. On the choice of stress–strain variables for unsaturated soils and its effect on plastic flow. Geomech. Energy Environ., 15: 3–9.

[Gar01] Gardner CMK., Robinson DA, Blyth K, Cooper JD 2001. Soil water content measurement. In: Soil and Environmental Analysis: Physical Methods: Second Edition. (Ed. Smith K.and Mullins C.). Marcell Dekker, Inc., 270 Madison Ave, New York, p. 1-64.

[Hou97] Houlsby GT 1997. The work input to an unsaturated granular material. Géotechnique, 47(1): 193–196.

[Jon02] Jones SB, Wraith JM, Or D 2002. Time domain reflectometry measurement principles and applications. Hydrol. Process. 16: 141–153.

[Kel04] Kelleners TJ, Soppe RWO, Ayars JE, Skaggs TH 2004. Calibration of capacitance probe sensors in a saline silty slay. Soil Soil Sci. Soc. Am. J., 68: 770–778.

[Led86] Ledieu J, De Ridder P, De Clerck P, Dautrebande S 1986. A method of measuring soil moisture by time domain reflectometry. Journal of Hydrology, 88: 319–328.

[Leo02] Leong EC, He L, Rahardjo H. 2002. Factors affecting the filter paper method for total and matric suction measurements. Geotech. Test. J., 25(3): 322–333.

[Leo04] Leong EC, Tripathy S, Rahardjo H 2004. A modified pressure plate apparatus. Geotech. Test. J. 27(3): 322–331.

[Leo16] Leong EC, Kizza R, Rahardjo H 2016. Measurement of soil suction using moist filter paper. E3S Web Conf., 9: 10012.

[Lic26] Lichtenecker K 1926. Die Dielektrizitätskonstante natürlicher und künstlicher Mischkörper. Physikalische Zeitschrift, 27: 115–158.

[Lu06] Lu N, Likos WJ 2006. Suction Stress Characteristic Curve for Unsaturated Soil. J. Geotech. Geoenvironmental Eng. 132.

[Mal96] Malicki MA, Plagge R, Roth CH 1996. Improving the calibration of dielectric TDR soil moisture determination taking into account the solid soil. Eur. J. Soil Sci., 47: 357–366.

[Mar08] Marinho FAM., Take A, Tarantino A 2008. Tensiometeric and axis translation techniques for suction measurement. Geotechnical and Geological Engineering, 26(6): 615-631.

[Mar20] Martini M, Tarantino A, Sloan A 2020. Suction drains as a low-carbon ground improvement technique: proof of concept at the laboratory scale. Tunnelling and Underground Space Technology, 99: 103361.

[Mit93] Mitchell JK 1993. Fundamentals of Soil Behavior. Wiley Inter-Science, New York.

[Ng03] Ng CWW, Zhan LT, Bao CG, Fredlund DG, Gong BW 2003. Performance of an unsaturated expansive soil slope subjected to artificial rainfall infiltration. Geotechnique, 53(2): 143-157

[Ng03] Ng CWW, Zhan LT, Bao CG, Fredlund DG, Gong BW. 2003. Performance of an unsaturated expansive soil slope subjected to artificial rainfall infiltration. Géotechnique, 53(2): 143–157.

[Nis95] Nissen HH, Moldrup P 1995. Theoretical Background for the TDR Methodology. Proceedings of the Symposium: Time Domain Reflectometry Applications in Soil Science, 16 September 1994, Tjele, Denmark. SP report no. 11, Vol. 3, p. 9-23.

[Nor01] Noborio K 2001. Measurement of soil water content and electrical conductivity by TDR: a review. Computers and Electronics in Agriculture, 31: 213-237.

[Ols65] Olson RE, Langfelder LJ 1965. Pore water pressure in saturated soils. J. Soil Mech. Found. Div., ASCE. SM4: 127–150.

[Pal97] Paltineanu IC, Starr JL 1997. Real-time soil water dynamics using multisensor capacitance probes: Laboratory calibration. Soil Sci. Soc. Am. J., 61: 1576–1585.

[Ric41] Richards LA 1941. A pressure-membrane extraction apparatus for soil solution. Soil Sci. 51(5): 377–386.

[Ric47] Richards LA 1947. Pressure-membrane apparatus – Construction and use. Agric. Eng.: 451–460.

[Rid03] Ridley AM, Dineen K, Burland JB, Vaughan PR 2003. Soil Matrix Suction: some examples of its measurement and application in geotechnical engineering. Géotechnique, 53(.2): 241-253.

[Rid96] Ridley AM, Wray WK 1996. State of the art report - Suction measurement: A review of current theory and practices. Proc. 1st International Conference on Unsaturated Soils, Unsaturated Soils, Alonso & Delage (eds), Paris, vol.3, p. 1293-1322.

[Rid98] Ridley AM., Patel AR, Marsland F 1998. Tensiometers: their design and use for civil engineering purposes. Geotechnical Site Characterisation, Balkema, Rotterdam, p. 851-856.

[Rob03] Robinson DA, Jones SB, Wraith JM, Or D, Friedman SP 2003. A review of advances in dielectric and electrical conductivity measurement in soils using TDR. Vadose Zone Journal, 2: 444-475.

[Rob98] Robinson DA, Gardner CMK, Evans J, Cooper JD, Hodnett MJ, Bell JP 1998. The dielectric calibration of capacitance probes for soil hydrology using an oscillation frequency response model. Hydrology and Earth System Sciences, 2(1): 111-120.

[Rob99] Robinson DA, Gardner CMK, Cooper JD 1999. Measurement of relative permittivity in sandy soils using TDR, capacitance and theta probes: Comparison, including the effects of bulk soil electrical conductivity. Journal of Hydrology, 223: 198–211.

[Rot90] Roth K, Schulin R, Flühler H, Attinger W 1990. Calibration of TDR for water content measurement using a composite dielectric approach. Water Resour. Res., 26: 2267–2273.

[Sca02] Scanlon BR, Andraski BJ, Bilskie J 2002. Miscellaneous methods for measuring matric or water potential. In Methods of Soil Analysis, Part 4, Physical Methods, SSSA Book Series No. 5, Dane J.H. and Topp G.C. (Eds.), Soil Science Society of America, Madison, p. 643–670.

[Shu00] Shuai F, Fedlund DG 2000. Use of a New Thermal Conductivity Sensor to Measure Soil Suction". In Advances in Unsaturated Geotechnics (eds. Shackleford, C.D., Houston, S.L. and Chang, N.Y.), Geotechnical Special Publication No. 99, Reston: American Society of Civil Engineers, p. 1-12.

[Shu00] Shuai F, Fredlund DG. 2000. Use of a new thermal conductivity sensor to measure soil suction. In: Shackelford CD, Houston SL, Chang NY, editors. Advances in Unsaturated Geotechnics. Geotechnical Special Publication No. 99. Reston, VA: American Society of Civil Engineers, pp. 1–12.

[Tar04] Tarantino A 2004. Panel Lecture: Direct measurement of soil water tension. Proc. 3rd Int. Conf. on Unsaturated Soils, Recife, Brasil, vol.3, p. 1005-1017.

[Tar08] Tarantino A, Ridley AM, Toll DG 1998. Field measurement of suction, water content, and water permeability. Geotechnical and Geological Engineering, 26(6): 751-782.

[Tar10] Tarantino A. 2010. Basic concepts in the mechanics and hydraulics of unsaturated geomaterials. In: Laloui L, editor. Mechanics of Unsaturated Geomaterials. London: ISTE–John Wiley & Sons, pp. 3–28.

[Top80] Topp GC, Davis JL, Annan AP 1980. Electromagnetic determination of soil water content: Measurements in coaxial transmission lines. Water Resour. Res., 16: 574–582.

[Wan04] Wang X, Benson CH 2004. Measuring the soil water characteristic curve with the leak-free pressure plate extractor. Geotech. Test. J. 27(2): 1–10.

[Wys97] Wyseure GCL, Mojid MA, Malik AI 1997. Measurement of volumetric water content by TDR in saline soils. European Journal of Soil Science, 48: 347–354.

[Zak98] Zakri T, Laurent JP, Vauclin M 1998. Theoretical evidence of the Lichtenecker's mixture formulae based on the effective medium theory. J. Phys. D: Appl. Phys., 31: 1589–1594.

Physical modelling: From abstraction to experiment design

Miguel Angel Cabrera

Delft University of Technology

> "The purpose of [physical] models is not to give a mirror image of reality, not to include all its elements in their exact sizes and proportions, but rather to single out and make available for intensive investigation those elements which are decisive."
>
> *David Muir Wood*
> [Woo03]

1 Introduction

In general terms, experiments are often conducted to explore, estimate, or confirm our understanding of a given behaviour or process [Ant23]. Exploration refers to understanding the collected data, while estimation refers to determining the effects of independent variables on an output observation, and confirmation implies contrasting the predicted results with a theory, or even set the foundations for a new one. In this line of experimentation, sand castles provide a rich example into the complex behaviour of soils and the importance of initial an boundary conditions. To some extent, we can improve our sand castle construction skills by iterating on the degree of compaction and water content, limiting to the available beach sand and water, but we may not achieve to live in a sand castle as it may simply collapse by self-weight after a certain threshold height. This rather dramatic example illustrates the relevance of physical modelling as a crucial tool for understanding the soil behaviour through experimentation, while maintaining close attention to the interdependencies between independent and dependent variables. A physical model then allows the exploration of the associated interdependencies of soil when interacting with a structure or with a set of environmental loads, while connecting with an idealized prototype, often of larger dimensions.

This chapter aims to provide an overview on how to design a physical model in the context of geomechanics and geotechnical engineering, while defining a clear experimental programme. It starts by giving an introduction to the reasoning behind physical modelling. It then moves to the abstraction exercise that allows capturing the complexity of a "real" life problem to an idealized system. And then, it presents the use of dimensional analysis as an strategy to identify the dominant interactions and aid in the design of a experiment. This chapter is not meant to be an exhaustive review of all the intricacies of physical modelling, but to serve as a reference to the interested reader and provide the resources to move in depth in each of these topics.

2 What is physical modelling?



Figure 1: Physical modelling of a pile bearing capacity at (a) large scale [Duf25], (b) medium-size scale [LKZ+24], (c) small scale [QAGC25]. Note that through all these scales, both boundary and initial conditions are key in capturing the representative soil-structure interaction, requiring the use of a geotechnical centrifuge for small scale models.

Soil behaviour is highly non-lineal, with strong dependencies on confinement stress, relative density, degree of saturation, grain shape, among others. Capturing this behaviour is crucial in physical modelling. A physical model refers to an experimental model that allows the study of a given geomechanical process (e.g., consolidation, internal erosion) or geotechnical structure (e.g., foundation systems, retaining walls, tunnels) under, in principle, well defined boundary and initial conditions. This definition of a physical model is often referred as well as a *boundary value problem*. In this context, a boundary condition refers to the set of constraints, i.e., degrees of freedom, or specifications applied to the sides or boundaries of a soil mass or a soil model domain; while the initial conditions refer to the state or characteristics of the soil mass at the beginning of a particular analysis or reference period. Note that boundary conditions may include factors such as fixed or free boundaries, applied loads, prescribed

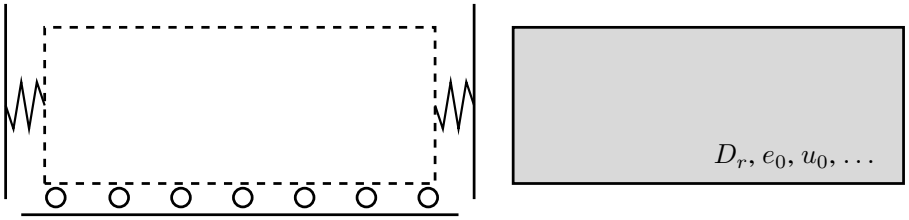


Figure 2: Common boundary (left) and initial conditions (right) in a physical model.

displacements, fluid flow rates, or temperature gradients at the sides of the soil domain, while, initial conditions may include parameters such as initial stress states, initial pore water pressures, initial temperatures, initial void ratios, or initial moisture contents.

In civil engineering, a range of scales is explored by means of physical modelling (see Fig. 1), often starting from a full-scale prototype and moving towards scaled-down versions that focus on particular aspects of the prototype behaviour [Woo04]. Large-scale modelling is a type of physical modelling where the prototype is reproduced at a workable dimension [BBB$^+$20], such that available actuators or a comprehensive network of sensors can detail the soil and structure response [AAS18]. However, smaller models are often used because they are faster, more economgic, easier to control, and better suited for parametric studies. Scaling principles at $1g$ share similarities to structural and mechanical engineering physical models, extensively detailed in the book of Harris and Sabnis [HS99]. Furthermore, the geotechnical centrifuge offers the posibility of scaling up the stresses in the physical model providing a complementary set of scaling principles [GGS$^+$07] or by two-stage scaling approaches as in [ITN05]. The interested reader is refered to the books of Taylor [Tay18] and Madabushi [Mad17] for more information on centrifuge modelling.

In this sense, the goal of physical modelling can be defined as to obtain information on the dominant soil deformation patterns, the soil response when interacting with a given structure or surrounding environmental actions, or the role of a soil body in accelerating or delaying a given mechanical, hydraulic, thermal, chemical, or biological process. In order to achieve this, it is posited that the physical model must:

- Use the same or equivalent soil and structural materials,
- identify the process dominant geometrical features (e.g., shape, height, width, diameter, length),
- replicate field conditions, i.e., prototype, in a “small” scale model, and
- match the controlling physical actions, for example by dimensional analysis, such that the interpretation of the output observation becomes equivalent.

Physical modelling can also provide crucial information to validate or improve the

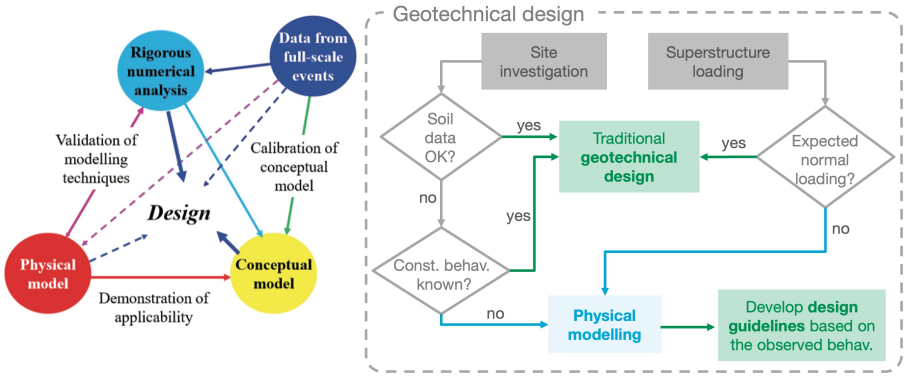


Figure 3: Physical modelling in geotechnical design as a complementary modelling tool (from [RH01]) (left), or as a modelling tool for challenging designs (adapted from [Mad14]) (right).

confidence of a particular geotechnical design (see Fig. 3). In this sense, a physical model provides an alternative modelling tool to validate a numerical technique (e.g., DEM-CFD, MPM, SPH, PFEM) or to demonstrate the applicability of a conceptual model (e.g., novel pile impact hammer [QIC$^+$24]), or to corroborate full-scale observations [RH01]. In this role, the physical model serves as an independent tool for the exploration of soil behaviour. Moreover, a physical model can also provide an opportunity to explore the soil behaviour when a challenging design needs to be addressed [Mad14]. Such case is formulated for situations when the soil behaviour is unknown for a specific set of initial conditions or when the loading conditions fall outside the range previously explored. In both cases, the abstraction of the full scale process is crucial in isolating the dominant features of the specific geotechnical design under consideration.

3 Abstraction in geotechnical engineering

In geotechnical engineering it is common to simplify a process by its planes of symmetry or under a given set of mechanical, thermal, hydraulic, chemical, or biological constraints. A plane of symmetry is a plane that divides a three-dimensional object into equal parts that are mirror images of each other. By taking advantage of this symmetry, one can simplify the analysis and design of a structure, and reduce the number of calculations required (e.g., axial symmetry of a CPT [TVGCS$^+$23]). The geometrical simplifications often guide the interpretation of a failure plane and are connected to the configuration of a geotechnical structure (i.e., embankments, piles, shallow foundations). These planes of symmetry are often related with the given strain or stress constraint, leading to a simplified stress or strain field, e.g., plane strain, plane stress. A similar degree of abstraction is found in the shapes of element test samples (i.e.,

cylinder, cuboid) and loading directions (i.e., axial, radial).

The abstraction of a physical model is not unique and requires the specification of additional constraints or assumptions. These may include physical constraints (e.g., basal drainage) or process scales (e.g., consolidation time). The adequate definition of these assumptions will lead to a closer representation of the large prototype process under interest. In this sense, the main difference between an element test and a physical model is the level of complexity of the system being tested. An element test focuses on a soil element and provides detailed information on its mechanical properties and behaviour, while a physical model focuses on the coupled behaviour of a given soil layer or soil-structure configuration, providing an overall perspective of its response to various loading and environmental conditions.

Physical models can be grouped in: Processes controlled by *failure*, like in landslides, earthquakes, and pile installation; processes controlled by *deformation*, like in retaining walls, foundations, and tunnels; and processes controlled by the *soil-structure interface*, like in cyclic loading of piles or geotextile reinforcement. The degree of abstraction behind capturing the fundamental processes of these applications depends on the definition of the dominant process of interest, the model scale, and the measurable quantities. The following sections detail further on how to address these when designing a physical model by means of dimensional analysis.

4 Dimensional analysis

Dimensional analysis is a method for reducing complex physical problems to their simplest and most economical form, setting the stage for either a numerical or experimental model. Dimensional analysis is formalized mathematically by Buckingham's Π theorem [Buc14]. The goal of dimensional analysis is to reduce a problem's degrees of freedom and suggest appropriate scaling principles [Son04].

Buckingham's Π theorem states that if a quantity Q_0 (a dependent variable) is completely determined by the values of a set of n independent quantities, of which a number k form a complete, dimensionally independent subset, then a suitable dimensionless Q_0/k will be completely determined by $(n-k)$ dimensionless similarity parameters. In other words, the number of independent variables (the problem's inherent "degrees of freedom") may be reduced by the number of k characteristic dimensions, such as a characteristic length L^*, a characteristic time T^*, a characteristic mass M^*, and a characteristic temperature Θ^* [Son04]. This relationship can be expressed as

$$Q_0 = f(Q_1, Q_2, Q_3, ..., Q_n). \tag{1}$$

Note that two categories of variables are possible. Variables that can be interpreted as dimensionless (i.e., friction coefficient), and variables that are measured and require a scale with a defined unit (i.e., length, time, mass, temperature). It is theorized that keeping the set of dimensionless groups Π_i equal between model and prototype leads

to the same value, or order of magnitude, of the dependent dimensionless quantity Q_0/k, irrespective of the scale, granting a successful scaling.

The following procedure has been suggested by Sonin for identifying the dimensionless variables by means of Buckingham's Π theorem [Son04]. In this approach, a single set of $[L^*, M^*, T^*, \Theta^*]$ is required.

> Step 1: Describe the dependent variable Q_0 as a function of the n independent quantities Q_n (see Eq. 1)
>
> Step 2: Select from the set of n independent quantities in Eq. 1 a complete and dimensionally independent subset of k quantities (e.g., $[L^*, M^*, T^*, \Theta^*]$).
>
> Step 3: Normalize Eq. 1 by each of the k quantities resulting in a set of Π_i dimensionless variables.

By following these steps, Eq. 1 can be rewritten as

$$\frac{Q_0}{k} = f(\Pi_1, \Pi_2, \Pi_3, ..., \Pi_n). \tag{2}$$

where each Π_i is a dimensionless group linked to the response of Q_0/k. Note that the formulation of a dimensionless variable, based on the Π-theorem, leads to non-unique answers, as various combinations are equally valid. However, some forms are more useful than others, making useful an a priori understanding of the process to be explored.

It is often convenient to understand a dimensionless variable as a ratio of two physical processes or two physical scales. Typical examples of these are the Stoke's number St or the Reynold's number Re, both showing the ratio between inertial and viscous forces. In the context of geomechanics, applications where adhesive forces between grains appear due to a bonding force or due to partial saturation, the Bond and Capillary numbers are useful.

$$\text{Bond number} = \mathrm{Bo} = \frac{\rho g \ell^2}{\sigma} = \frac{\text{inertial effects}}{\text{capillary effects}} \tag{3}$$

$$\text{Capillary number} = \mathrm{Ca} = \frac{\mu_f \sqrt{g\ell^3}}{\sigma \ell} = \frac{\text{viscous effects}}{\text{surface tension effects}} \tag{4}$$

where ℓ refers to a characteristic length, σ to the fluid surface tension, and μ_f is the fluid dynamic viscosity.

In the interpretation of granular flows, multiple dimensionless numbers become useful [CKBW18]. Some examples of these are

$$\text{Savage number} = \mathrm{Sa} = \frac{\dot{\gamma}^2 \rho d}{P} = \frac{\text{grain collisions}}{\text{macroscopic friction}} \tag{5}$$

$$\text{Bagnold number} = \mathrm{Ba} = \frac{\upsilon_s}{1-\upsilon_s}\frac{\rho d^2 \dot{\gamma}}{\mu_f} = \frac{\text{internal grain stress}}{\text{viscous shear}} \tag{6}$$

$$\text{Inertial number} = \mathrm{I} = \mathrm{Sa}^2 = \frac{\dot{\gamma} d}{\sqrt{P/\rho}} = \frac{\text{macroscopic timescale}}{\text{microscopic timescale}} \tag{7}$$

where $\dot{\gamma}$ is the shear strain rate, d the grains diameter, P the geostatic pressure, and υ_s is the solid volume fraction [Ive97]. Note that I can also be interpreted as a ratio between the grains inertia and the acting confinement, allowing accounting for additional stress contributions like viscous and cohesion interactions into the rheology of complex granular flows [VNM+20].

Finally, at the grains scale, erosion is often interpreted through the lens of the Shields number

$$\text{Shields number} = \Psi = \frac{\tau}{(\rho_s - \rho_f) g d} = \frac{\text{shear stress}}{\text{grain's weight}} \tag{8}$$

where τ is the shear stress due to the flow, and the subscripts s and f refer to the soil and fluid fractions, respectively.

Exercise: Dimensional analysis of a laterally loaded pile

Let's review the dimensional analysis procedure for the case of a pile embedded in sand and being loaded laterally. In this case, the dependent variables of interest Q_0 are the pile maximum lateral capacity P and its maximum displacement y_0 (see Fig. 4). These in turn would be a function of the pile's length L, diameter D, thickness t_p and bending stiffness EI, also known as flexural rigidity, as well as to the sand-pile interface friction angle δ, and the soil stiffness K. Completing this list requires to account for the role of gravity g and the material densities ρ_p and ρ_s for both pile and sand, respectively.

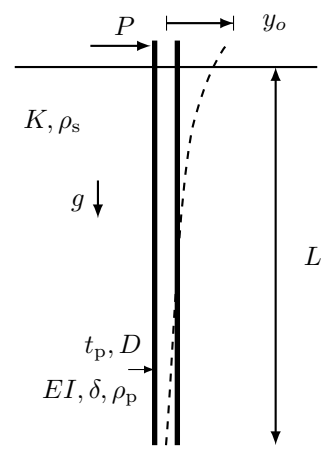


Figure 4: Lateral load capacity of a pile

Formulating Eq. 1 with these variables leads to a system of two dependent variables and eight independent variables ($n = 9$), for which three characteristic dimensions are possible ($k = 3$).

$$(P, y_0) = f(L, D, t_\mathrm{p}, EI, \delta, K, g, \rho_\mathrm{p}, \rho_\mathrm{s}) \tag{9}$$

The exercise of identifying the characteristic dimensions of this problem starts by assuming a characteristic length as $L^* \equiv D$, and then elaborate further until all terms in Eq. 9 are dimensionless. For this example, this is completed by assuming $M^* \equiv \rho_\mathrm{s} D^3$ and $T^* \equiv \sqrt{\rho_\mathrm{s} D^2/K}$. The elaboration of this approach can be tabulated, moving from one characteristic dimension to the next, from left to right in the columns of Table 1, and always extracting those instances where a dimensionless quantity is reached. The output of this exercise leads to the expected set of five dimensionless groups ($n - k = 6$) shown in Eq. 10.

	$L^* \to D$	$M^* \to \rho_\mathrm{s} D^3$	$T^* \to \sqrt{\rho_\mathrm{s} D^2/K}$
P [ML/T^2]	P/D [M/T^2]	$P/(\rho_\mathrm{s} D^4)$ [1/T^2]	P/D^2K [$-$]
y_0 [L]	y_0/D [$-$]	–	–
L [L]	l/D [$-$]	–	
D [L]	–	–	–
t_p [L]	t_p/D [$-$]	–	
EI [ML^3/T]	EI/D^3 [M/T]	$EI/(\rho_\mathrm{s} D^6)$ [1/T]	$EI/(D^4K)$ [$-$]
δ [$-$]	–	–	–
K [M/T^{2}L]	KD [M/T^2]	$K/(\rho_\mathrm{s} D^2)$ [1/T^2]	–
g [L/T^2]	g/D [1/T^2]	g/D [1/T^2]	$g\rho_\mathrm{s} D/K$ [$-$]
ρ_p [M/L^3]	$\rho_\mathrm{p} D^3$ [M]	$\rho_\mathrm{p}/\rho_\mathrm{s}$ [$-$]	–
ρ_s [M/L^3]	$\rho_\mathrm{s} d^3$ [M]	–	–

Table 1: Tabulated form of the dimensional analysis exercise of a laterally loaded pile on sand.

$$\left(\frac{P}{D^2K}, \frac{y_0}{D}\right) = f\left(\frac{L}{D}, \frac{t_\mathrm{p}}{D}, \frac{EI}{D^4K}, \delta, \frac{g\rho_\mathrm{s} D}{K}, \frac{\rho_\mathrm{p}}{\rho_\mathrm{s}}\right). \tag{10}$$

Note that the higher order in the prefactors involving D in Eq. 10 might be distributed by accounting for complementary lengths, like L, t_p, or the grain's size.

The right-hand side independent variables in Eq. 10 show the pile slenderness ratio L/D and t_p/D, the interface friction coefficient δ, and the pile-soil density ratio ($\rho_\mathrm{p}/\rho_\mathrm{s}$) as the typical modelling parameters. Moreover, two interesting relationships that could be further explored state the ratio between the pile bending stiffness and the soil stiffness ($EI/(D^4K)$), and between the soil geo-static stresses and its stiffness ($g\rho_\mathrm{s}D/K$). The latter requires a close match of the stress state in order to capture the non-lineal soil behaviour.

This dimensional analysis exercise allows to formulate the expected dependency between the physical model initial conditions, e.g., ρ_s, and the pile lateral capacity P and displacement y_0, suggesting that by keeping a close match between the prototype and model scales, in the right-hand side in Eq. 10, an equivalent response of the soil-structure process at a prototype scale should be expected. For example, let us consider a prototype tubular pile 20 m long, of 5 m diameter, wall thickness of $t_\mathrm{p} = 50$ mm and made from steel with a Young's modulus $E = 210$ GPa. An equivalent physical model could be downscaled by a factor of 100, i.e., $L = 20$ cm and $D = 5$ cm, but it would also require that K scales accordingly and that a model decision is made regarding t_p. Scaling K can be achieved by keeping the proportionality with the effective stress σ, i.e., $K \propto \sigma^\alpha$ where α might be of the order of 0.5 for sands and 1.0 for clays [Woo04], or by preparing the soil model up to a stiffness that matches that of the prototype, e.g., overconsolidated clay at the prototype stress level.

Calibration chambers and centrifuge modelling are alternatives for achieving the first strategy, while the second strategy implies changing the soil bulk density and potentially its interaction with the pile and expected non-lineal behaviour. Caution must be taken when following the second strategy. Moreover, t_p has a clear influence in soil-pile interaction, being recommended to have a pile thickness larger than 10 times the grains diameter, while maintaining a practical dimensioning in the resulting model pile [FBR21]. Finally, the model pile can share the same material as the prototype, or use an alternative material, while matching EI, while keeping in mind the expected interaction mechanism, relative to a "deformable" or "infinitely" rigid pile.

An example where this configuration is studied is the multi-facility benchmarking study evaluating centrifuge modelling of a prototype pile in dry sand under monotonic lateral loading [LKZ$^+$ss]. In this work, a prototype test conducted in large test pit (see Fig. 1) was replicated through eight centrifuge tests at five European facilities using identical sand and model piles at two scaling levels. Comparisons focused on pile head force–displacement–rotation response and bending-moment distributions. All centrifuge tests qualitatively captured the main features of the prototype behaviour, but consistently exhibited a softer response and reduced lateral capacity. Statistical analyses identified sand dry density and proximity to lateral container boundaries as the only factors with a strong and significant influence on pile response. Other potential sources of variability, including pile installation method, gravity-field variation, and scaling effects related to pile cross-section and grain size, were of secondary or inconclusive influence.

The decision on the scaling method for studying the selected process needs to consider the experimental capabilities, e.g., model containers, actuators, and the instrumentation resolution, e.g., load cells, video recording cameras, fiber optics. The experimental capabilities are specific to each laboratory, but the use of dimensional analysis could help in dimensioning future facilities with a clear modelling goal. Moreover, instrumentation advances over the last decades have shown substantial leaps in miniaturization and high sampling frequencies, increasing the range of observation in physical modelling. It is advised to keep a close look to technology developments and proven applications in fields like rheology, nanotechnology, biophysics to name a few.

Dimensional analysis and its link to scaling principles has been further elaborated in the previous Alert Doctoral School as a tool for defining the similarity principles for experiments in geomechanics for the energy transition [RSA25]. There, two approaches are presented for this purpose, a equation-based and a variable-based dimensional analysis. This section reviews the transition from dimensional analysis and scaling principles as a means for orienting the experiment design. The interested reader is referred to book of Wood on Geotechnical Modelling [Woo04] to Alert's 2025 doctoral school [RSA25], and to the paper of Butterfield [But99] for further information on dimensional analysis.

5 Experiment design

The design of an experiment involves planning, designing, and analysing the most feasible physical model so that reliable and objective conclusions can be reached [Ant23]. The process of abstraction and dimensional analysis discussed in this chapter serve as a starting point in the design of an experiment. It is often desirable to match the dimensionless dependent and independent variables such that a close link between the prototype scale and the model scale is possible. The relationship between these di-

mensionless groups might be direct or approximated by an order of magnitude. Some examples of centrifuge geotechnical models where this is achieved are the excavation of a tunnel [IAWB11], the case of landslide-generated waves [CPTM20], or the influence of pile installation with a vibro-hammer [SOVQ$^+$ss], to name a few.

The experiment planning starts by formulating a hypothesis on the influence of a set of independent variables on the process under study, being aware of their interconnectedness, variability, and modelling capabilities (i.e., instrumentation resolution). Their interconnectedness must be evaluated from the understanding of the specific process, considering its associated conservation principles or governing equations. The variability and modelling capabilities then relate with the inherent soil variability and the measurement error and model uncertainty, respectively [PK99]. Moreover, the design of an experiment requires the consideration of the range and possible combinations to be explored of the selected independent variable or variables. For example, a slope stability model can explore the role of saturation degree as an isolated variable, or the combined effect of saturation degree and soil relative density.

Once the set of variables is defined, for example trough dimensional analysis, it is necessary to consider the model replicability. Note that replications relate to the repetitions of an entire experiment, or a portion of it, under more than one set-up configuration, while a repetition refers to a process of running the experiment under the same set-up configuration [Ant23]. In this sense, replications allow to address the model experimental error Δ (i.e., size of the effect to detect) and obtain a more precise estimate of the process variability σ (i.e., noise level). Once this is known, the number of experiments N of a given physical model, with a sound statistical basis, can be estimated as

$$N \approx (4n)^2 \left(\frac{\sigma}{\Delta}\right)^2 \tag{11}$$

where n is number of independent variables under consideration and Δ/σ refers to the signal-to-noise ratio of the specific physical model, considering both its instrumentation, boundary and initial conditions and process constraints. Considering this, a physical model dealing with three independent variables (i.e., $n = 3$) and a $\Delta/\sigma = 2$ would require at least 36 experiments. Clearly, as n increases, the desired number of experiments may not be affordable in some situations. Nevertheless, its correct implementation may yield better results in the long run and increase the confidence on the physical model and its observations. Notably, the biggest alternative to reduce the number of repetitions is by increasing Δ/σ, achievable by increasing the precision in the measuring techniques or reducing the model variability through, for example, sample preparation and well defined and well controlled boundary conditions.

In industrial process engineering, a strategy to optimize the number of experiments and orientate the design of experiments involving a set of multiple variables is known as *factorial design*. Although this approach is rather rare in geomechanics and geotechnical engineering, its implementation could turn advantageous when studying complex processes with multiple interdependencies. Factorial design could help in screening the interdependencies and then identify those considered dominant for further un-

derstanding. A detailed description of factorial design lays outside the scope of this chapter, but the interested reader is referred to the books of Wu & Hamada [WH11] and Antony [Ant23].

A factorial design enables the study of the joint effect of the independent variables n on an expected output. An example of this approach is that of the weld strength, being regarded as a function of independent variables such as weld speed, voltage, welding time, and weld position [Ant23]. In such a case, the isolated exploration of a single variable at a time may turn unreliable, inefficient and time consuming. Therefore, accounting for the combined interactions of multiple variables could turn more efficient than the isolated exploration of a single variable at a time [Ant23]. With this reasoning, the design of an experiment may benefit from the combined (i.e., full factorial) or partial (fractional factorial) assessment of the possible combinations of the independent variables, termed in this field as factors. The combinations to be explored are often tabulated, as in Table 5, with the -1 and $+1$ representing the $\min(x_i)$ and $\max(x_i)$, respectively. The statistics from the repetitions on each combination, e.g., mean, standard deviation, allow identifying those dominant effects and guide the design of an experimental campaign that focuses on a wider set of levels for a single combination or dominant variable. The output from each combination can then be analysed through statistical tools, aiming at identifying the dominant contributions and their variability.

A	**B**	**AB**	**Mean**	**Standard deviation**
-1	-1	1	·	·
-1	1	-1	·	·
1	-1	-1	·	·
1	1	1	·	·

Table 2: Coded matrix in a full factorial design with two variables (A,B), their combination factor AB, evaluated at two levels (+1,-1).

The number of combinations in a full factorial design is ξ^n, where ξ is the number of values to be considered for each variable n, termed as levels. For example, assuming low and high values leads to $\xi = 2$, while assuming low, middle, and high values leads to $\xi = 3$. Clearly, the more values are assumed, the more combinations are possible, making appealing the idea of either reducing the number of variables or limiting the number of values to be explored in the physical model.

In the full factorial design, the number of experiments N is then distributed evenly among these combinations. For example, in an experiment involving $n = 2$ and $\Delta/\sigma = 2$, requires 16 experiments evaluating two combinations at low and high values, i.e., $\xi = 2$. If each variable is evaluated separately, a total of 64 experiments would be needed, i.e., $Nn\xi$. However, if the variable combinations are distributed in four groups, i.e., 2^2, only 4 repetitions per combination would be necessary and still reach the total of 16 experiments estimated as a function of Δ/σ (Eq. 11). Alternatively, in a fractional factorial design the total number of experiments may be further

reduced by excluding some of the combinations considered not to have a significant effect on the output. In this example, excluding one combination would lead to three combinations and a total of 12 experiments.

Exercise: Full factorial design of grain-size-effects in the residual strength of granular matter

The residual shear strength is of primary importance for understanding the behaviour of granular materials subjected to large deformations and for characterizing granular flows. It is well known that the shear strength depends on material properties such as grain shape and the interparticle friction coefficient μ. Furthermore, the grain size distribution is known to influence the packing fraction ϕ, with the void ratio defined as $e = (1 - \phi)/\phi$, and is therefore expected to affect the resulting shear strength. This exercise aims at designing an experimental programme that enables the assessment of the effect of the grain size distribution on the residual shear strength of a granular material in a triaxial test configuration.

We can start the design of this experiment by identifying the dependent variable, i.e., residual shear strength q_{res}, and the independent variables. For simplicity, variables like the grain shape, the sample size, and loading rate $\dot{\varepsilon}_z$ are kept constant, allowing focusing on the grain size distribution alone. The grain size distribution can be captured by two descriptors, the polydispersity ratio $\lambda = d_{\max}/d_{\min}$, equivalent to the uniformity coefficient, and a characteristic diameter d_c. Therefore, the following function relates the dominant factors for consideration in the dimensional analysis:

$$(q_{\mathrm{res}}) = f(D, d_c, \lambda, \rho, p_0, g) \tag{12}$$

where, D is the sample diameter, ρ is the grain density, p_0 is the initial mean stress, and g is the Earth's gravity.

The following dimensionless factors are obtained by assuming $L^* \equiv d_c$ as the characteristic length, $M^* \equiv \rho d_c^3$ as the characteristic mass, and $T^* \equiv \sqrt{d_c/g}$ as the characteristic time.

$$\left(\frac{q_{\mathrm{res}}}{\rho d_c g}\right) = f\left(\frac{D}{d_c}, \lambda, \frac{p_0}{\rho d_c g}\right) \tag{13}$$

Note that the denominator of the dependent variable could be changed by p_0, leading to the well known stress ratio $\eta_{\mathrm{res}} = q_{\mathrm{res}}/p$. The resulting set of variables can be further reduced by keeping p_0 constant.

The experimental design for this case is to identify the effect of D/d_c and λ on the residual stress ratio η_{res}. This means the exploration of two variables, i.e., d_c, λ, studied in combination. The experimental error in dry triaxial tests can be assumed to be $\Delta \approx 10\%$, due to end restraint friction, and area changes, while the variability in the estimated residual stress can be $\sigma \approx 5\%$, due to limitations in maintaining ideal kinematic boundary conditions at large strains. Considering these, the total number of tests is $N = 16$, which could be significantly reduced if a factorial experiment design is implemented. Note that inter-laboratory programmes, also known as round robins, are a good exercise for estimating the signal to noise ratio of this type of element tests. Some examples can be found in [RFA$^+$21, RMGO$^+$24, RFD$^+$25, PMYU99, QDP$^+$26].

The work of Polanía et al. explores the effect of λ and d in the range of $d \in [0.35 : 1.9]$ mm and $\lambda \in [1.0 : 12.7]$ [PCR$^+$23]. In this work, the role of grain shape, the grains interparticle friction and density remained constant by using ceramic beads, while the initial packing fraction ϕ_0 varied with λ by a common sample preparation method. Overall, this experimental work confirms that the residual shear strength of granular materials is independent of the grain size, of the level of polydispersity (see Fig. 5, and of ϕ_0, confirming numerical observations with the Discrete Element Method [VRDEY09, NASR15, Est16, CASR18, LMAE$^+$19]. Moreover, in a following work, the same group have shown that the mean grain size $d_c = d_{50}$ does not correlate strictly with η_{res}, but with the Sauter-mean diameter as a better characteristic length $d_c = \Sigma d_i^3 / \Sigma d_i^2$ [PRC$^+$25].

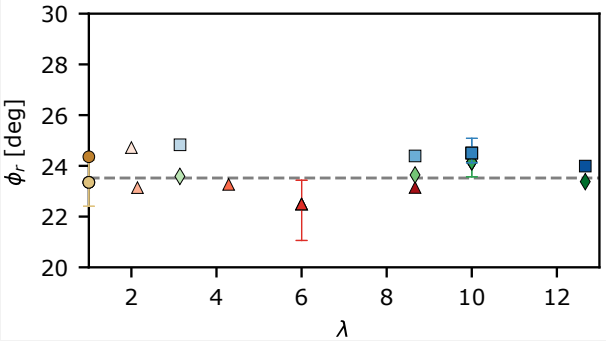


Figure 5: Residual friction angle $\varphi_r = \text{asin}(3\eta_{\text{res}}/(6 + \eta_{\text{res}}))$ as a function of the size span λ and for d_c. The dashed line shows the mean value for all experiments. Vertical bars indicate the maximum and minimum values between repetitions for monodisperse samples (circles), bidisperse samples (triangles), polydisperse samples with uniform distributions by volume fraction (diamonds), and polydisperse samples with Fuller and Thompson distributions (squares). (taken from [PCR$^+$23])

6 Conclusions

This chapter has presented how physical modelling can be used to explore, estimate, or validate a given behaviour or process through experimentation. Physical models may be developed at different scales; however, their effective use requires the selection of similar or equivalent soil and structural materials, the identification of the dominant geometric features of the process, the replication of field conditions as closely as possible, and the reproduction of the governing physical actions. It is important to emphasize that a physical model is an abstraction of the complex site conditions and loading combinations associated with a full-scale prototype process. This abstraction is achieved through the adoption of geometric symmetries together with well-defined boundary and initial conditions.

In this chapter, dimensional analysis has been introduced as a tool for identifying the governing dimensionless variables of a physical model. The definition of these variables enables the establishment of a link between the small-scale model and the prototype process. The resulting dimensionless groups can then be used to design experimental programmes and to evaluate their influence on the dependent dimensionless response variables.

The design of an experiment that effectively addresses the effect of the independent variables can be explored by the isolated testing of a single variable at a time, or by accounting for their combined effects. In either case, special attention has been given to accounting for repeatability and to the number of tests required to obtain statistically meaningful and conclusive observations. Taken together, this framework provides a useful and strategic approach for investigating the key variables governing geomechanical processes and the behaviour of geotechnical structures across different experimental scales.

References

[AAS18] Amin Askarinejad, Devrim Akca, and Sarah M Springman. Precursors of instability in a natural slope due to rainfall: a full-scale experiment. *Landslides*, 15(9):1745–1759, 2018.

[Ant23] Jiju Antony. *Design of experiments for engineers and scientists*. Elsevier, 2023.

[BBB+20] Harvey J Burd, William JAP Beuckelaers, Byron W Byrne, Kenneth G Gavin, Guy T Houlsby, David JP Igoe, Richard J Jardine, Christopher M Martin, Ross A McAdam, Alastair Muir Wood, et al. New data analysis methods for instrumented medium-scale monopile field tests. *Géotechnique*, 70(11):961–969, 2020.

[Buc14] Edgar Buckingham. On physically similar systems; illustrations of the use of dimensional equations. *Physical review*, 4(4):345, 1914.

[But99] R Butterfield. Dimensional analysis for geotechnical engineers. *Geotechnique*, 49(3):357–366, 1999.

[CASR18] David Cantor, Emilien Azéma, Philippe Sornay, and Farhang Radjai. Rheology and structure of polydisperse three-dimensional packings of spheres. *Phys. Rev. E*, 98:052910, Nov 2018.

[CKBW18] Miguel Cabrera, Patrick Kailey, Elisabeth T Bowman, and Wei Wu. Effects of viscosity in granular flows simulated in a centrifugal acceleration field. In *Physical Modelling in Geotechnics, Volume 2*, pages 1075–1080. CRC Press, 2018.

[CPTM20] M. A. Cabrera, G. Pinzon, W. A. Take, and R. P. Mulligan. Wave generation across a continuum of landslide conditions from the collapse of partially submerged to fully submerged granular columns. *Journal of Geophysical Research: Oceans*, 125(12):e2020JC016465, 2020.

[Duf25] K Duffy. *Axial capacity of piles in sand: A field investigation using distributed fibre optic sensing*. PhD thesis, 2025.

[Est16] Nicolas Estrada. Effects of grain size distribution on the packing fraction and shear strength of frictionless disk packings. *Phys. Rev. E*, 94:062903, Dec 2016.

[FBR21] Shengsheng Fan, Britta Bienen, and Mark F Randolph. Centrifuge study on effect of installation method on lateral response of monopiles in sand. *International Journal of Physical Modelling in Geotechnics*, 21(1):40–52, 2021.

[GGS+07] Jacques Garnier, Christophe Gaudin, Sarah M Springman, PJ Culligan, D Goodings, D Konig, B Kutter, R Phillips, MF Randolph, and Luc Thorel. Catalogue of scaling laws and similitude questions in geotechnical centrifuge modelling. *International Journal of Physical Modelling in Geotechnics*, 7(3):01–23, 2007.

[HS99] Harry G Harris and Gajanan Sabnis. *Structural modeling and experimental techniques*. CRC press, 1999.

[IAWB11] G. Idinger, P. Aklik, W. Wu, and R. I. Borja. Centrifuge model test on the face stability of shallow tunnel. *Acta Geotechnica*, 6(2):105–117, 2011.

[ITN05] S Iai, T Tobita, and T Nakahara. Generalised scaling relations for dynamic centrifuge tests. *Geotechnique*, 55(5):355–362, 2005.

[Ive97] R.M. Iverson. The physics of debris flows. *Reviews of Geophysics*, 35(3):245–296, 1997.

[LKZ+24] Joaquin Liaudat, Alexander Kochnev, Hauke Zachert, William Ovalle-Villamil, Stefano Muraro, Miguel Cabrera, Matthieu Blanc, Luc

Thorel, Alexandru Marin, Liam Jones, et al. Assessing repeatability, scale effects, and consistency in geotechnical physical modelling: a collaborative benchmark exercise on horizontally loaded piles in dry sand. In *5th European Conference on Physical Modelling in Geotechnics-ECPMG 2024*, 2024.

[LKZ+ss] Joaquin Liaudat, Alexander Kochnev, Hauke Zachert, Athanasios Agalianos, Liam Jones, Alexandru Marin, Max Sieber, Ioannis Anastasopoulos, Matthieu Blanc, Luc Thorel, William F. Ovalle, Stefanno Muraro, Miguel A. Cabrera, Shechuan Liu, Stuart Haigh, Dirk de Lange, Koen Castelein, and Suzanne J.M. van Eekelen. Benchmark exercise on centrifuge modelling: Piles under monotonic lateral loading. *International Journal of Physical Modelling in Geotechnics*, In press.

[LMAE+19] S. Linero Molina, E. Azema, N. Estrada, S. Fityus, J. Simmons, and A. Lizcano. Impact of grading on steady-state strength. *Géotechnique Letters*, 9(4):328–333, 2019.

[Mad14] Gopal Madabhushi. *Centrifuge modelling for civil engineers*. CRC press, 2014.

[Mad17] Gopal Madabhushi. *Centrifuge modelling for civil engineers*. CRC press, 2017.

[NASR15] Duc-Hanh Nguyen, Emilien Azéma, Philippe Sornay, and Farhang Radjai. Effects of shape and size polydispersity on strength properties of granular materials. *Phys. Rev. E*, 91:032203, Mar 2015.

[PCR+23] Oscar Polanía, Miguel Cabrera, Mathieu Renouf, Emilien Azéma, and Nicolas Estrada. Grain size distribution does not affect the residual shear strength of granular materials: An experimental proof. *Physical Review E*, 107(5):L052901, 2023.

[PK99] Kok-Kwang Phoon and Fred H Kulhawy. Characterization of geotechnical variability. *Canadian geotechnical journal*, 36(4):612–624, 1999.

[PMYU99] Tej BS Pradhan, Tamotsu Matsui, Kazuya Yasuhara, and Kazunori Uchida. Cyclic undrained triaxial strength of clay by a round robin test. *Soils and foundations*, 39(4):121–129, 1999.

[PRC+25] Oscar Polanía, Mathieu Renouf, Miguel Cabrera, Nicolas Estrada, and Emilien Azéma. Monodisperse behavior of polydisperse flows. *Physical Review E*, 111(4):L043401, 2025.

[QAGC25] TO Quinten, AA Askarinejad, Kenneth Gavin, and MA Cabrera. Hpmc viscous fluid for centrifuge modelling. *Canadian Geotechnical Journal*, 62:1–20, 2025.

[QDP+26] Santiago Quinteros, Rune Dyvik, Ingrid Peikli, Diana CA Silva, Ali Seiphoori, Zack Westgate, Mussie Kidane, Danilo Zepilli, Kenny K Sørensen, Sumin Song, et al. Interface friction angle from ring shear tests on sand: A round robin. *Journal of Geotechnical and Geoenvironmental Engineering*, 152(6):04026024, 2026.

[QIC+24] TO Quinten, C Ioannou, MA Cabrera, A Askarinejad, KG Gavin, and J van Wijk. Performance of the blue blow generator for centrifuge modelling at delft university of technology (dut). In *Proc. 5th Eur. Conf. Phys. Mod. Geotech*, 2024.

[RFA+21] David Reid, Andy Fourie, Juan Luis Ayala, Simon Dickinson, Felipe Ochoa-Cornejo, Riccardo Fanni, Juan Garfias, António Viana Da Fonseca, Mason Ghafghazi, Carlos Ovalle, et al. Results of a critical state line testing round robin programme. *Géotechnique*, 71(7):616–630, 2021.

[RFD+25] David Reid, Andy Fourie, Simon Dickinson, Thavakumaran Shanmugarajah, Riccardo Fanni, Kyle Smith, Juan Garfias, Bin Yuan, Mason Ghafghazi, and Adam Duyvestyn. Results of a dilatancy round robin. *Geotechnical Research*, 12(1):2–28, 2025.

[RH01] MF Randolph and AR House. The complementary roles of physical and computational modelling. *International Journal of Physical Modelling in Geotechnics*, 1(1):1–8, 2001.

[RMGO+24] Juan Carlos Ruge, Fausto Molina-Gómez, María C Olarte, Javier Camacho-Tauta, Óscar Reyes-Ortiz, Joan M Larrahondo, Hermes A Vacca, Luis F Prada, Alfonso Ramos-Cañón, Yezid A Alvarado, et al. Inter-laboratory testing program for the physical characterization of guamo sand. *Ingeniería e Investigación*, 44(3), 2024.

[RSA25] Hadrien Rattez, Luc Simonin, and Pauline André. Physical model experiments in geomechanics for the energy transition. In Anne-Catherine Dieudonné, Martin Lesueur, Jean-Michel Pereira, Hadrien Rattez, and Manolis Veveakis, editors, *ALERT Doctoral School 2025, The Role of Geomechanics in the Energy Transition*, pages 105– 120. Alert Geomaterials, 2025.

[Son04] Ain A Sonin. A generalization of the π-theorem and dimensional analysis. *Proceedings of the National Academy of Sciences*, 101(23):8525–8526, 2004.

[SOVQ+ss] Luc E.J. Simonin, William F. Ovalle-Villamil, Tristan Quinten, Benoît Herman, Stijn François, George Anoyatis, Miguel A. Cabrera, and Hadrien Rattez. Influence of vibro-driver parameters on vibrodriveability: A geo-centrifuge study. *Journal of Geotechnical and Geoenvironmental Engineering*, in press.

[Tay18] RN Taylor. *Centrifuges in modelling: principles and scale effects*. CRC Press, 2018.

[TVGCS+23] Ruben D Tovar-Valencia, Ayda Galvis-Castro, Rodrigo Salgado, Monica Prezzi, and Daniel Fridman. Experimental measurement of particle crushing around model piles jacked in a calibration chamber. *Acta Geotechnica*, 18(3):1331–1351, 2023.

[VNM+20] Thanh Trung Vo, Saeid Nezamabadi, Patrick Mutabaruka, Jean-Yves Delenne, and Farhang Radjai. Additive rheology of complex granular flows. *Nature communications*, 11(1):1476, 2020.

[VRDEY09] C. Voivret, F. Radjaï, J.-Y. Delenne, and M. S. El Youssoufi. Multiscale force networks in highly polydisperse granular media. *Phys. Rev. Lett.*, 102:178001, Apr 2009.

[WH11] CF Jeff Wu and Michael S Hamada. *Experiments: planning, analysis, and optimization*. John Wiley & Sons, 2011.

[Woo03] David Muir Wood. *Soil Behaviour and Critical State Soil Mechanics*, chapter A particular elastic-plastic model: Cam-Clay, pages 112–138. Cambridge University Press, 2003.

[Woo04] David Muir Wood. *Geotechnical modelling*. CRC press, 2004.

©ALERT Geomaterials
Laboratoire 3SR / Bâtiment Galilée
CS 40700
38 058 Grenoble cedex 9
France

ISBN **978-2-9584769-7-7**

Fon: +33 (0) 456 528 621
Fax: +33 (0) 476 827 043
president@alertgeomaterials.eu
https://alertgeomaterials.eu

All rights reserved. No part of this book may be reproduced in any form without written permission from the publisher or author.

ALERT Doctoral School 2026

Experimental Geomechanics for Beginners

Editors: N. Benahmed, M. Cabrera, J. Dijkstra, E. Gerolymatou, A. Tarantino & A. Tengattini

Dijkstra, Jelke & Cheng, Xiaoyang
Introduction to geotechnical testing

Tengattini, Alessandro
Sensors: fundamentals of measurement and electronics for experimentalists

Benahmed, Nadia
Triaxial Testing of Geomaterials

Gerolymatou, Eleni, Düsterloh, Uwe & Castellanza, Riccardo
Dimensioning and construction of experimental apparatus with examples

Tarantino, Alessandro
Unsaturated soils: experimental techniques

Cabrera, Miguel Angel
Physical modelling: From abstraction to experiment design